Acoustic charge and spin transport in sidewall quantum wires on GaAs (001) substrates

DISSERTATION

zur Erlangung des akademischen Grades

doctor rerum naturalium (Dr. rer. nat.)
im Fach Physik

eingereicht an der
Mathematisch-Naturwissenschaftlichen Fakultät
Humboldt-Universität zu Berlin

von
Paulus Leonardus Joseph Helgers, M.Sc.

Präsidentin der Humboldt-Universität zu Berlin:
Prof. Dr.-Ing. Dr. Sabine Kunst

Dekan der Mathematisch-Naturwissenschaftlichen Fakultät:
Prof. Dr. Elmar Kulke

Gutachter:

1. *Prof. Dr. Henning Riechert*
2. *Prof. Dr. Hubert Krenner*
3. *Prof. Dr. Oliver Benson*

eingereicht am:	*09.03.2021*
Tag der mündlichen Prüfung:	*12.08.2021*

This project has received funding from the European Union's Horizon 2020 research and innovation program under Grant Agreement No. 642688.

Abstract

Fast and efficient computation devices can be developed by complementing conventional electronics with quantum mechanical spin. A common example for such a building block is the Datta-Das spin transistor. In this thesis, an acoustically driven spin transistor based on acoustic spin transport in quantum wires is investigated. These quantum wires (QWRs) are defined by molecular-beam epitaxy (MBE) growth. They form on the sidewalls of ridges which are prepatterned along the [110] direction of GaAs (001) substrates. The edges of the ridges contain deviations from a straight line (LER: line-edge roughness), originating from the photolithography process. LER is, however, much smaller than the typical width of a QWR, which implies that it does not play a dominant role for acoustic transport. Optically injected electrons and holes in the QWR are laterally confined by a potential barrier between the QWR and the surrounding QW of 25.4 meV and 4.8 meV, respectively.

The application of a surface acoustic wave (SAW) enables the transport of electrons and holes over long distances along the QWR. For high acoustic powers, the charge carriers are transported by the strong SAW potential over distances of up to 90 µm, where a metal stripe is deposited to screen the SAW potential and induces carrier recombination. The acoustic transport time of QWR carriers for a fixed distance corresponds to the one expected from the acoustic velocity, indicating a high transport efficiency. For lower acoustic powers, unintentional trapping centers lead to additional hotspots of carrier recombination along the transport path. These trapping potentials are overcome by the SAW for high acoustic powers.

The intrinsic spin lifetimes of the QWR carriers are approximately 2 ns to 3 ns. Acoustic spin transport in the QWR is observed over distances of at least 15 µm. It is shown that the spin-orbit field, around which the spins rotate during transport, strongly depends on the acoustic power for the QWR carriers. For high acoustic powers, the QWR spin precession frequency is enhanced by 3.5 times with respect to the intrinsic one.

The results presented in this thesis demonstrate that the strain field of a SAW acts as a strain gate for QWR spins which are transported over a fixed distance. Therefore, the sidewall quantum wire on GaAs (001) substrates is a promising concept to be used in an acoustically driven spin transistor.

Keywords:
spin transport, surface acoustic waves, quantum wires, semiconductor spectroscopy

Zusammenfassung

Die Ergänzung der konventionellen, ladungsbasierten Elektronik durch die quantenmechanischen Spin Eigenschaften der Elektronen ermöglicht die Entwicklung von schnellen und effizienten Rechnersystemen. Ein bekannter Baustein für solch ein System ist der Datta-Das Spin-Transistor. In dieser Arbeit wird ein akustisch angetriebener Spin-Transistor untersucht, basiert auf Quantendrähten definiert mittels Molekularstrahlepitaxie. Diese Quantendrähte (QWRs: quantum wires) bilden sich während des epitaktischen Überwachsens an den Flanken von Barrenstrukturen, welche entlang der [110] Richtung auf GaAs (001) Substraten prozessiert wurden. Die Ränder dieser Barrenstrukturen weisen Abweichungen vom geradlinigen Verlauf auf (LER: line-edge roughness), die auf die Fotolithographie zurückzuführen sind. Die große QWR Breite impliziert jedoch, dass LER keine dominierende Rolle beim akustischen Transport spielt. Elektronen (Löcher), die optisch in den QWR injiziert werden, sind lateral durch eine Potenzialbarriere von 25.4 meV (4.8 meV) zum umgebenden QW eingesperrt.

Die Verwendung einer akustischen Oberflächenwelle (AOW) ermöglicht den Transport von Elektronen und Löchern über große Entfernungen. Im Fall von hohen akustischen Leistungen werden die Ladungsträger vom starken AOW Potenzial über Distanzen von bis zu 90 µm bis zu einer Stelle transportiert, wo ein Metallstreifen das AOW Potenzial abschirmt und die Rekombination der Ladungsträger bewirkt. Die akustische Transportdauer der QWR Ladungsträger bis zu einer festgelegten Entfernung entspricht der Dauer, die man aufgrund der akustischen Geschwindigkeit erwartet, d.h. dass die Ladungsträger sehr effizient transportiert werden. Im Fall von niedrigen akustischen Leistungen führen unbeabsichtigte Einfangzentren zu zusätzlichen Hotspots der Ladungsträgerrekombination auf dem Transportweg. Der Effekt diesen Einfangzentren ist abwesend für hohe akustische Leistungen.

Die intrinsischen Spinlebenszeiten der QWR Ladungsträger betragen ungefähr 2 ns bis 3 ns. Akustischer Spintransport im QWR wird über Entfernungen von mindestens 15 µm beobachtet. Es wird gezeigt, dass für Ladungsträger im QWR das Spin-Bahn Feld, um welches die Spins während des Transportes rotieren, stark von der akustischen Leistung abhängt. Im Fall von hohen akustischen Leistungen wird die QWR Spin-Präzessionsfrequenz gegenüber der Eigenfrequenz 3,5-fach erhöht.

Die Ergebnisse, die in dieser Arbeit präsentiert werden, demonstrieren, dass das Verspannungsfeld einer AOW als Verspannungs-Gate auf QWR Spins wirkt, welche über eine festgelegte Entfernung transportiert werden. Daher stellen Flanken-QWRs auf GaAs (001) Substraten ein vielversprechendes Konzept für die Verwendung in einem akustisch betriebenen Spin-Transistor dar.

Schlagwörter:
Elektronenspin Transport, Akustische Oberflächenwellen, Quantendrähte, Halbleiter Spektroskopie

List of Abbreviations

AFM	atomic force microscopy
BAP	Bir-Aronov-Pikus
BIA	bulk inversion asymmetry
CB	conduction band
CL	cathodoluminescence
CW	continuous wave
DP	Dyakonov-Perel
DQD	dynamic quantum dot
EBL	electron-beam lithography
EY	Elliott-Yafet
FWHM	full-width-at-half-maximum
hh	heavy-hole
IDT	interdigital transducer
LER	line-edge roughness
lh	light-hole
LHCP	left-hand circularly polarized
MBE	molecular-beam epitaxy
MEE	migration-enhanced epitaxy
MOKE	magneto-optical Kerr effect
NIA	natural inversion asymmetry
PL	photoluminescence
PLE	photoluminescence excitation
PSH	persisent spin helix
QD	quantum dot
QW	quantum well
QWR	quantum wire
rf	radio-frequency
RHCP	right-hand circularly polarized
RHEED	reflection high-energy electron diffraction
SAW	surface acoustic wave
SEM	scanning electron microscopy
SIA	structural inversion asymmetry
SO	spin-orbit
STEM	scanning transmission electron microscopy
TRKR	time-resolved Kerr rotation
TRPL	time-resolved photoluminescence
UHV	ultra-high vacuum
VB	valence band

Contents

chapter 1

Introduction

By 2025, the digital universe will contain about 175 zettabytes (10^{21} bytes*) of data [1], which clearly emphasizes the need of high storage densities and fast information processing devices with low power consumption. In the center of conventional processing devices lies the field-effect transistor [2]. In 1975, George Moore predicted that the number of transistors on a computer chip doubles every two years, which is now a famous vision known as Moore's law [3]. However, with the conventional silicon-based devices reaching limiting dimensions, Moore's law is expected to come to an end within the next five years [4], thus requiring the development of new and innovative computation concepts.*

Many research efforts have been devoted to the revolutionary concept of quantum computation, where a two-level quantum system is used as a quantum bit (qubit). In contrast to classical bits, a qubit is neither '1' nor '0', but represents a superposition of these states. Quantum computing is expected to lead to much faster [5] and more secure [6] computations. Promising candidates for semiconductor-based qubits are photonic qubits [7] and spin qubits [8]. Whereas the former are favourable for information transmission, the latter are preferable for information processing. It is evident that future quantum technologies require the conversion between different qubits and that the qubit information is kept for times long enough for information transmission and processing.

There are major challenges to be overcome for the development of a quantum computer [9]. For near-future improvements of computational devices, a solution may be to complement modern technologies with new functionalities. Such an advancement of current technologies can come from combining conventional charge-based electronic devices with quantum mechanical spin: a research field called spintronics. This chapter provides a brief introduction of three important topics for this thesis: spintronics, growth-defined quantum wires and surface acoustic waves. In the final section, the contents of this thesis are laid out.

1.1 Spintronics and the spin transistor

Quantum mechanical spin was put forward by Goudsmit and Uhlenbeck in 1926 to explain anomalies in the hydrogen spectrum [10]. They considered that besides charge, electrons carry a quantized spinning motion. The concept of spin is not only interesting from a fundamental viewpoint. The technological use of spin as an information carrier has been investigated for many purposes such as data storage, information processing, quantum computation and sensitive magnetic sensors [11]. One pivotal spin-based concept integrated in devices is giant magnetoresistance (GMR) [12, 13]. GMR describes the dependency of

the electrical resistance on the mutual magnetization alignment of two ferromagnetic (FM) thin films, which are separated by a conductive thin film. The application of GMR as a read head in hard-disk drives (HDD) enabled increases in data densities to Tbit/in^2 these days [14]. A further integration of GMR into magnetic random access memories (MRAM) [15], where each databit has its own GMR structure (commonly known as spin valve), allows the manufacturing of low-power and stable memory devices. While GMR has led to significant improvements of read heads, writing data in both HDD and MRAM is still based on current-induced magnetic fields, thereby limiting their down-scaling [15]. A promising solution to this problem is another spintronic device: spin-transfer-torque (STT) MRAM. In this device, data writing is carried out by the spin-transfer-torque exerted by a spin-polarized current onto the FM magnetization [15].

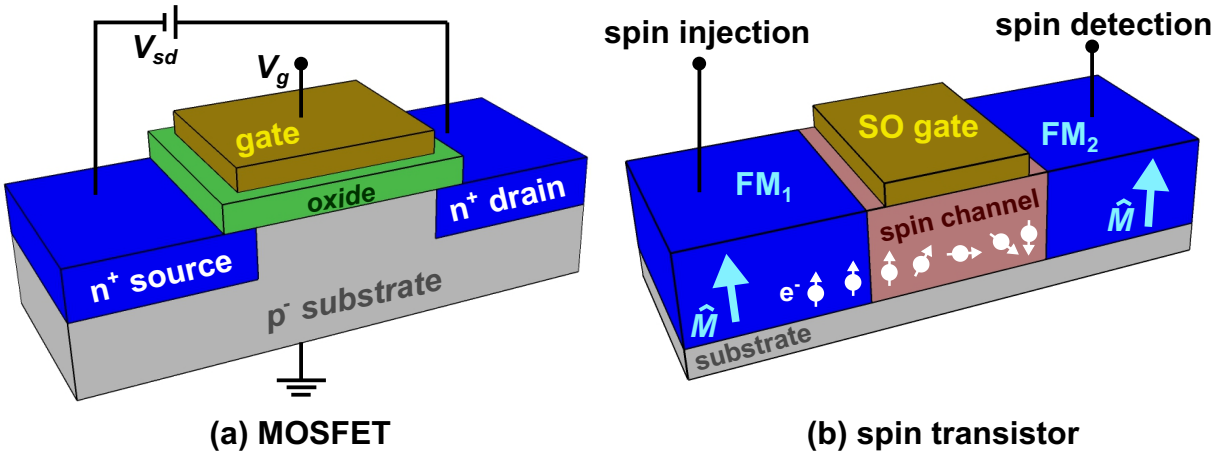

Figure 1.1: (a) Illustration of a MOSFET. The grey, green and brown areas represent the substrate, oxide and metal gate, respectively. The blue areas depict the n-type source and drain. (b) Illustration of a spin transistor. The grey area corresponds to the substrate. The blue areas display ferromagnetic regions, whereas the red area depicts the transport channel of electron-spins (white). The brown layer represents a spin-orbit gate, which may be induced by means of various concepts.

In the field of data processing, a key concept was proposed by Datta and Das [16], which is widely interpreted as a spin transistor. In order to understand the working principle of this device, first consider a conventional charge-based metal-oxide-semiconductor field-effect transistor (MOSFET) [2], as illustrated in fig. 1.1(a). This MOSFET consists of a p-type silicon substrate (grey) with an oxide layer (green) and a metal gate (brown) deposited onto its surface. At the left and right sides of the gate, n-type regions (blue) implemented in the substrate define the source and drain, respectively. When the gate potential V_g is zero (as in the figure), no current flows from source to drain and the MOSFET is in its 'off' state. To switch the MOSFET to its 'on' state, a potential $V_g > 0$ is applied. As a result, an inversion layer forms at the interface between the oxide layer and the substrate, attracting electrons from the source and drain regions and eventually defining an n-type channel. An additional voltage V_{sd} between source and drain creates an electron flow, which defines the 'on' state.

The spin transistor is entirely based on electron-spin, as illustrated in fig. 1.1(b). The spin transistor consists of a semiconductor spin channel (red) laterally sandwiched between two ferromagnetic areas (blue). The region FM_1 is used for spin injection: as a result of spin-dependent scattering, current is spin-polarized after passing through the region. The spin current then traverses the spin channel. Within this channel, the orientation of the spin polarization is actively controlled by spin-orbit (SO) effects. The state of the

transistor is defined by the spin orientation at the end of the spin channel: if the spin orientation is parallel (opposite) to the FM_2 magnetization $\hat{M}$, the spin transistor is 'on' ('off'). Some of the advantages of spin transistors over the charge-based transistors are their easy integration with spin-based memory devices, low-power circuits and non-volatile logic systems [17].

The key concept on which the spin transistor is based is the spin-orbit coupling: a coupling between the electron's orbital motion and its spin. This coupling is mediated by the magnetic field arising in the reference frame of a moving electron due to the electric field between atoms in the crystal. The intrinsic SO coupling emerges from the crystal structure, as described by Dresselhaus [18]. Extrinsic contributions emerge from, for example, the application of electric fields, as described by Rashba [19]. In both cases, the SO coupling can be interpreted as an internal magnetic field, around which the spin rotates.

Inspecting fig. 1.1(b), two major challenges for the development of the spin transistor become clear: (i) active control of the spin orientation and (ii) sustainability of the spin polarization. In their proposal, Datta and Das proposed electrical control of the spin orientation by the Bychkov-Rashba effect as an approach to the first challenge (this effect is similar to the Rashba effect, but applies for 2D systems). The control of the spin orientation by an electric gate was demonstrated for the first time by *Nitta et al.* in an (In,Ga)As/(In,Al)As quantum well (QW) structure [20]. During the last two decades, various other possibilities were suggested, including stray magnetic fields [21], spin lifetime control [22], the spin Hall effect [23] and a photonic SO gate [24]. Be that as it may, experimental realizations of the spin transistor have been scarce. Here, the SO field resulting from strain [25] is promising as a convenient means for active spin control, compatible with common fabrication processes.

The second challenge is mainly associated with two spin relaxation mechanisms. Under the condition of optical excitation of carriers (as typically used throughout this thesis), electron-hole exchange interaction is an important spin relaxation mechanism. At low temperatures, the electron and hole bind into excitons [26]. Under such conditions, the exchange interaction leads to an effective magnetic field, which leads to Maialle spin relaxation [27]. Exchange interaction is also active at high temperatures for p-doped semiconductors, leading to Bir-Aronov-Pikus spin relaxation [28]. This mechanism is caused by spin flips when an electron scatters with a free hole. The second spin relaxation mechanism arises due to the momentum-dependency of the SO field. Spins moving along distinct trajectories between two fixed locations experience different spin rotations along their trajectories. This leads to Dyakonov-Perel (DP) spin relaxation [29]. The DP spin relaxation time is inversely proportional to the momentum scattering time: fast momentum scattering averages the SO field and leads to slower spin relaxation.

Several ways to suppress DP spin relaxation are proposed in literature. The momentum scattering rate can be increased by introducing impurities or doping [30]. Another way of suppressing the DP mechanism is by special sample design. For example, spins oriented along the growth axis of a (110) quantum well are immune against spin dephasing by the intrinsic SO field [31, 32]. In (111) QWs the intrinsic SO field can even be compensated for by a Bychkov-Rashba field, so that the total SO field vanishes for all spin orientations [33, 34]. In (001) QWs, the emergence of a persistent spin helix (PSH) is observed [35]. The PSH arises when the intrinsic and extrinsic SO coupling parameters have equal magnitude. As a result, the SO field aligns along a single axis, leading to an enhancement of the spin lifetime.

A different pathway to suppress DP spin relaxation is to confine the motion of the spins in two or three dimensions [36]. Experimental demonstrations of enhanced spin

lifetimes in quasi-one-dimensional channels are reported in channels etched in a QW [37], gate-fitted channels in QWs [38], free standing nanowires [39] and acoustically induced moving potential dots [40]. However, these structures have several disadvantages: (i) etch-defined quantum wires (QWRs) contain free surfaces, which can be detrimental for optical and electrical purposes, (ii) gate-defined QWRs need to be close at the surface, since the effect of the surface gate diminishes away from the surface, hence prohibiting their convenient integration in epitaxial structures and (iii) the trajectory of moving potential dots is not flexible, as it is determined by the requirement of piezoelectricity. A type of growth-defined QWRs fabricated by molecular-beam epitaxy (MBE) offer great advantages, since they do not have detrimental free surfaces, can easily be embedded in epitaxial structures and they can be routed towards essentially any position on a chip.

1.2 Growth-defined quantum wires

Growth-defined QWRs are wires with nanometer-scale dimensions, which form in specially designed samples under certain growth conditions. At the basis of growth-defined quantum wire fabrication is the anisotropic MBE overgrowth of a QW structure on a substrate prepatterned with ridges. MBE is a thin film deposition technique, where a beam consisting of atoms or molecules of the desired material impinges on a hot substrate. The growth is carried out with low growth rates and in an ultra-high vacuum environment, which provides excellent growth control of samples with a high purity. The epitaxial nature of the growth results in a high crystalline quality [41].

The prepatterned ridges on the substrate are fabricated by an etching process. The specific shapes and surface orientations of the ridge areas depend on the etching process. Likewise, the diffusion and incorporation processes of adatoms during epitaxial growth depend strongly on the atomic surface configuration. Since the ridges contain a combination of different surface orientations, certain ridge areas have a faster growth rate as compared to other ridge areas. If a QW structure is overgrown on the ridges, its thickness will be larger at the fast growing surfaces. Consequently, the quantum confinement energy in this thicker region is smaller than the one in the surrounding QW, which leads to the formation of a QWR on the fast growing surface. A variety of growth-defined QWRs are reported on GaAs substrates [42, 43, 44, 45, 46, 47]. These can be categorized in two groups: (i) those which form at the ridge bottom or top and (ii) those which form on the ridge sidewalls.

In the first group, QWRs have been fabricated on (001) substrates prepatterned with V-grooves [42]. Here, V-shaped grooves oriented along the $[\bar{1}10]$ crystal direction are etched into the substrate. In the grooves, the overgrowth of AlAs cladding layers forms a very sharp corner between two (111)A sidewalls. Subsequent overgrowth by MBE of a GaAs/AlAs QW structure leads to the formation of a QWR region in this sharp corner. Vertical stacking of these QWRs is reported by growing multiple QW structures on top of each other. In contrast to etching grooves into the substrate, the grating can also be defined by ridges sticking out of the surface. One of the earliest QWRs on ridges was reported by *Nakamura et al.* [43] on (001) substrates. Here, ridges along the [110] crystal direction with a height of several micrometers are defined by photolithography and reactive ion etching. The subsequent overgrowth of a GaAs cladding layer creates a flattened pyramid structure, with a narrow (001) top surface and (111)B sidewalls. The width of the top surface depends on the cladding layer thickness, which, therefore, needs to be considered carefully. The ridge top is a fast growing surface, while the sidewalls are slow growing ones. Thus, the growth-defined quantum wires form at the ridge top. In later reports, similar QWRs are reported on ridges along the [100] direction [44] and on e-beam lithographically defined ridges along the $[\bar{1}10]$ direction [45].

In this thesis, QWRs are fabricated on the sidewalls of nanometer-height ridges prepatterned on GaAs (113)A and (001) substrates. The fabrication of QWRs on the sidewalls of the ridges is more convenient than those discussed above, since one needs neither to tune the thickness of cladding layers nor to define very narrow lateral dimensions of the ridges. The fabrication method for sidewall QWRs on (113)A substrates was introduced by *Nötzel et al.* [46]. Ridges oriented along $[\bar{1}10]$ are defined by photolithography and wet chemical etching. Due to the anisotropic MBE overgrowth of a QW structure, the thickness of the QW layer increases at the ridge sidewall (which has a $[\bar{1}\bar{1}3]$ facet), thereby defining the QWR region. This anisotropic overgrowth results from differences in the incorporation rates of Ga adatoms on the ridge sidewall as compared to the top and bottom. It was later shown that the QWR properties do not change for a deviation of the ridges away from the $[\bar{1}10]$ direction up to 20° [48], providing a means of routing the QWR charge carriers between any two distant locations on a chip. Further engineering of this type of structures proved fruitful for the development of a quantum system containing interconnected quantum wells, quantum wires and quantum dots [49].

A similar type of quantum wire is fabricated on (001) substrates at the sidewalls of ridges oriented along the [110] direction [47]. One of the key concepts for QWR formation for these QWRs is the (2x4) surface reconstruction: a change of the atomic configuration at the surface with respect to the one in bulk material [50]. MBE growth is better studied and preferred on (001) substrates due to this surface reconstruction, which for GaAs only occurs on the (001) surface orientation. Consequently, (001) substrates are more commonly found in large-scale applications. The QWRs fabricated on (001) substrates are, therefore, easily integrated in existing processes and, hence, desirable over those on (113)A substrates.

1.3 Surface acoustic waves

In a spin transistor, the spin population is transported through a spin channel between the FM regions. Surface acoustic waves (SAWs), propagating vibrations on a surface, offer a convenient way of transporting carriers. The spatial separation of electrons and holes by the piezoelectric potential accompanying the SAW reduces their wavefunctions overlap, resulting in a strong enhancement of their recombination lifetimes. Knowledge of SAWs dates back to the 19th century with their mathematical description by Lord Rayleigh [51]. The initial interest in SAWs for device application starting in the 1960s [52, 53] was sparked by their low propagation velocities as compared to electromagnetic waves: typical acoustic velocities are five orders of magnitude smaller than those for electromagnetic waves. The corresponding small wavelengths result in much smaller resonator dimensions as compared to those required for electromagnetic fields. Acoustic resonators allow for the down-scaling of delay lines and frequency filters in the MHz-GHz range, which are still used in modern communication devices. A typical smartphone nowadays has tens of acoustic devices. The great advantage of surface over bulk acoustic waves is that SAWs can easily be accessed by convenient surface contacts [52] and are controlled by simply modifying the surface over which they travel.

Surface acoustic waves also offer the possibility to modify the behaviour of carefully designed solid-state nanostructures. For example, optical microcavity resonances have been modulated using the periodic displacement of the cavity interfaces [54]. A second example is the modulation of the electronic energy levels in quantum systems by the strain fields of a SAW [55]. Other examples are acoustically induced magnetization switching [56], superconducting qubit circuiting [57] and the acoustic transport of charge carriers by the piezoelectric potential accompanying a SAW [58]. Acoustic charge transport was

in later studies recognized as a way to store light [59]. The storage of light is possible due to ambipolar acoustic transport of optically injected electrons and holes, which are brought to recombine by a metal stripe, positioned at a well-defined remote location. This method was subsequently employed to study the dynamics of acoustic ambipolar transport in quantum wells [60], quantum wires [61] and dynamic quantum dots (DQD) [62]. The extended investigation of ambipolar transport has resulted in proof-of-concepts for acoustically driven single-photon detectors [63], as well as single-photon emitters [64].

The spatial separation of charge carriers by the piezoelectric potential also reduces the exchange interaction between electrons and holes, because it strongly reduces their wavefunctions overlap. Since the exchange interaction is a major spin relaxation mechanism, this enables acoustic spin transport over micrometer scales [65]. An even further increase of the spin transport length can be reached when utilizing SAWs in sample designs as discussed in sec. 1.1 to reduce DP spin relaxation, such as (110) QWs [66]. In gate-fitted QWRs, acoustic spin information transfer between two distant QDs was shown using acoustic transport of individual electrons [67]. DQDs formed by the interference between two SAWs suppresses spin diffusion in all three dimensions and resulted in an acoustic spin transport length exceeding 100 µm [40]. Surprisingly, carrier confinement in narrow sidewall QWRs fabricated on (113)A GaAs substrates resulted in only small spin transport lengths below 2 µm [68]. The strong spin decay in these QWRs was attributed to Elliott-Yafet spin-flip scatterings [69] during momentum relaxation. It is shown in this thesis, that this type of spin relaxation can be reduced by increasing the QWR width.

1.4 Contents of this thesis

As compared to the narrow sidewall QWRs on GaAs (113)A substrates investigated in ref. [68], wider QWRs on GaAs (001) substrates promise longer spin transport lengths, as well as easier integration into common epitaxial structures. However, the properties of these QWRs have not been widely studied: the state of knowledge is restricted to structural analysis. In this thesis, a detailed study of sidewall QWRs on prepatterend GaAs (001) substrates is conducted, including the fabrication method, their optical properties and their acoustic transport behaviour. For the development of a spin transistor, the combination of these QWRs with SAWs promises an efficient way of tackling the spin conservation challenge, while simultaneously providing a convenient way for active control of the spin orientation. The experiments in this thesis will show that the precession frequency of spins transported in the sidewall QWRs can be controlled by the acoustic amplitude over a wide range, which is a contrast to previous reports on (001) QWs [70].

The first part of the thesis provides the necessary theoretical background to understand the experimental findings, whereafter the second part discusses the experimental results and summarizes the main conclusions. The thesis is constructed by the following chapters:

- *Chapter 2* briefly lays down the mathematical framework used to describe surface acoustic waves. It then describes the modulation of the electronic bands of a semiconductor by the SAW and possible trapping mechanisms, which lead to unintentional carrier trapping along the transport path. The chapter concludes with a simulation procedure to extract numerical values for related SAW-induced quantities.

- *Chapter 3* derives the electronic states in a QW, briefly introduces spin-orbit coupling and the optical selection rules. It then proceeds with a discussion of the main spin relaxation mechanisms in GaAs QW structures and describes how a SAW affects the spin dynamics during acoustic transport.

- *Chapter 4* provides an overview of the experimental methods. It starts with a short review of the MBE equipment and the equipment used to analyze the structural properties of prepatterned GaAs substrates, as well as the QWR dimensions. The main experiments of this thesis are conducted by optical means. Two experimental optical setups for studies of photoluminescence (PL) and acoustic charge transport are introduced. The chapter ends with a description of the optical setups used to study spin dynamics by means of polarization-resolved PL and Kerr rotation measurements.

- *Chapter 5* studies in detail the fabrication method of sidewall quantum wires on prepatterned GaAs substrates, evaluates the structural quality of the ridges and analyzes the formation of the QWRs by MBE overgrowth.

- *Chapter 6* presents the results of PL studies revealing the optical properties of QWRs on both (113)A and (001) substrates. The complex carrier dynamics between QWRs and their surrounding QW is revealed by a time-resolved PL experiment. The chapter finishes with a brief discussion of the (Al,Ga)As barrier on prepatterned substrates, showing that these barrier layers are affected by the substrate prepatterning as well.

- *Chapter 7* addresses acoustic charge transport in the QWR and the surrounding QW on (001) substrates, as revealed by PL studies. The characteristics of the ambipolar transport are disclosed by a study of remote recombinations along the transport path for different excitation conditions. Subsequently, it is demonstrated that carriers may escape out of the QWR into the surrounding QW during acoustic charge transport.

- *Chapter 8* extends the examinations of chap. 7 with a study of spin dynamics. Using Kerr rotation measurements, it is shown that the QWR dimensions lead to an enhancement of the spin lifetimes with respect to the surrounding QW. It is then demonstrated by polarization-resolved PL studies, that the spins are acoustically transported over several micrometers along the QWR axis, while their precession frequency can actively be controlled by choosing the appropriate acoustic power.

- *Chapter 9* finally summarizes the main conclusions of this thesis and provides some future perspectives.

chapter 2

Surface acoustic waves

This chapter reviews the basic properties of surface acoustic waves (SAW). Such waves were first described theoretically by Lord Rayleigh [51]. A sketch of the atomic positions in an elastic medium (green dots) subjected to a SAW is shown in fig. 2.1. The propagation direction of the SAW is along the horizontal axis, indicated by a purple arrow. Tension and compression occurs when atoms move away from and towards each other, respectively. The distance between two positions of maximum tension defines the acoustic wavelength λ_{SAW}*, which is of the order of micrometers in the nanostructures studied in this thesis. This chapter is divided in five sections. The first section introduces the piezoelectric effect, a key concept in the study of acoustic charge and spin transport. The second section starts with a mathematical description of bulk acoustic waves, introduces the boundary conditions applied to derive the mathematics of surface acoustic waves and introduces interdigital transducers, which are used to excite and detect acoustic waves. The third section discusses the modulation of the electronic states in an elastic semiconductor by a SAW. The fourth section gives a brief overview of mechanisms of carrier trapping along the transport path. The final section provides an overview of the properties of a SAW propagating along the* [110] *crystal direction on the GaAs (001) surface by means of simulations of the SAW fields.*

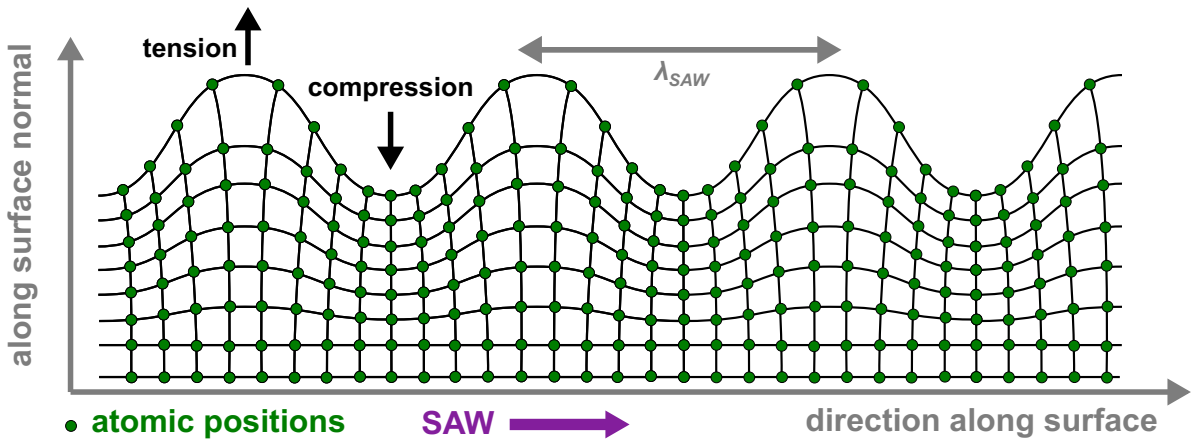

Figure 2.1: Schematic drawing of the SAW strain field, with specified positions of tension and compression. The SAW propagation direction is indicated by a purple arrow. The green dots represent the atomic positions.

2.1 The piezoelectric effect

In crystal structures without an inversion center, the application of mechanical forces induces an internal electric field. This phenomenon was discovered in 1880 by the brothers Curie and called the piezoelectric effect [71, 72]. Consider a two-dimensional toy crystal without inversion center, as illustrated in fig. 2.2(a). This toy crystal consists of atoms charged with either $-e$ (red) or $+e$ (blue), where e is the elementary charge. Under the condition without mechanical forces, d_1 defines the distance between nearest neighbours, as well as the distance between an arbitrary atom and the virtual centerpoint of the system. The lines interconnecting the atoms define a grid consisting of equilateral triangles, as marked by dashed grey lines. If all negative charges would be replaced by an equivalent charge of $Q_\Sigma^- = -3e$, that charge would be located at the virtual centerpoint of the system to resemble the configuration of the negatively charged atoms. Likewise, a charge $Q_\Sigma^+ = +3e$ replacing all positive charges would be located in the virtual centerpoint of the system as well. Clearly, the system has a zero net electric dipole and accordingly, no electric field appears in the unperturbed state.

If the system is subjected to mechanical stresses, the atomic charges are redistributed. Figure 2.2(b) displays the reorganized crystal model under external compressional force. In this new configuration, $d_2 < 2d_3$, where d_2 and d_3 are the lengths as depicted in fig. 2.2(b) (in fig. 2.2(a) $d_2 = 2d_3 = d_1$). In this case, Q_Σ^- is shifted upwards from the virtual centerpoint of the system, as indicated in the figure. Similarly, Q_Σ^+ is shifted downwards from the virtual centerpoint of the system. As a result of the separation between Q_Σ^- and Q_Σ^+, an electric dipole $\mathbf{P}$ arises as indicated in the figure by a black arrow, leading to the emergence of a piezoelectric field $\mathbf{F}$.

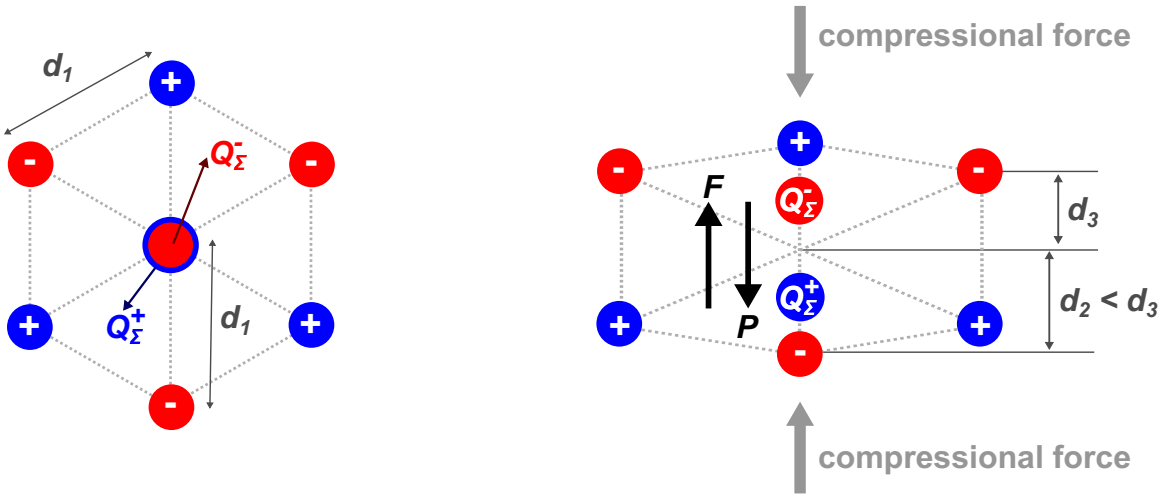

Figure 2.2: Crystallic toy model to explain the piezoelectric effect. (a) In the equilibrium state, the average position of the charges is in the virtual centerpoint of the system for both negative (red dots) and positive (blue dots) charges. In this situation, no electric dipole emerges. (b) The charge is redistributed when the crystal is deformed by compressional forces (grey arrows). As a result, a net electric dipole moment $\mathbf{P}$ and piezoelectric field $\mathbf{F}$ arise as indicated by black arrows.

In addition to the piezoelectric effect, the inverse piezoelectric effect [72] is another key concept in the field of acoustic waves. In this case, an inversion asymmetric crystal structure is subjected to an external electric field. The charged atoms are displaced from

their equilibrium position due to the external electric field. Since the atoms have opposite charge, the atomic displacements are in opposite directions, leading to a deformation of the crystal, similar to deformation resulting from a mechanical force.

Throughout this thesis, both effects are utilized in GaAs-based structures. Since the Ga and As atoms in the alloy are charged with opposite polarity, the crystal directions containing both Ga and As atoms are piezoelectric. Note that certain crystal directions contain only one type of atom (i.e. Ga or As) per atomic layer: these directions are not piezoelectric. The piezoelectric effect is crucial for the transport of carriers by the surface acoustic wave, which will be discussed in sec. 2.3.1. The excitation of a surface acoustic wave relies on the inverse piezoelectric effect and is the topic of sec. 2.2.3.

2.2 Fundamentals of acoustic waves

The vibrational motion of atoms in a crystal is described by quasi-particles known as phonons. In compound semiconductors such as GaAs, two types of phonons exist: acoustic phonons, for which the Ga and As atoms of the unit cell vibrate in the same direction and optical phonons, for which the Ga and As atoms vibrate in opposite directions. Surface acoustic waves are low-frequency acoustic phonons, which are restricted to the vicinity of the surface of an elastic medium. However, bulk acoustic waves, which propagate far away from the surface, can exist as well. In this section, the equations describing the properties of bulk acoustic waves in an infinite elastic medium are considered. The discussion is then extended to surface acoustic waves by introducing appropriate boundary conditions at the surface of the elastic medium. This medium is assumed to be an elastic semiconductor, while the surface is assumed to be the interface with the vacuum space. After providing the mathematical framework describing (surface) acoustic waves, interdigital transducers, used for SAW generation, are briefly introduced. An elaborate discussion of the theory in this section can be found in, for example, the book by *Auld* [73].

2.2.1 Bulk acoustic waves

Consider a bulk acoustic wave propagating through an unbounded semiconductor. For this thesis, an acoustic wavelength on the micrometer scale is relevant, which is typically about a factor 10^4 larger than the lattice constant of semiconductors (for GaAs, the lattice constant is 5.7 Å [74]). The semiconductor in which the acoustic wave propagates may, therefore, be considered as a continuous solid consisting of a collection of infinitesimal volumes, rather than as a discrete grid of individual atoms. The mechanical displacement $\mathbf{u}(\mathbf{r}', t)$ of such a volume exerts a stress force on the neighbouring volumes and depends on the position $\mathbf{r}' = (r_{x'}, r_{y'}, r_z)$ of the volume within the solid and the time coordinate t. The prime accents denote the crystallographic axes $x'||[100]$, $y'||[010]$ and $z||[001]$. In elasticity theory, stress is represented by the stress tensor $\mathbf{T}$ with components T_{ij}, where lowercase subscripts such as i and j are assumed to denote the (x', y', z) axes. The component T_{ij} expresses the force per unit area exerted along the r_i direction on a surface with the normal vector pointing in the r_j direction, as is illustrated in fig. 2.3.

The mechanical displacement resulting from the stress forces can be related to the stress tensor via Newton's second law of motion:

$$\frac{\partial T_{ij}}{\partial r_j} = \rho \frac{\partial^2 u_i(\mathbf{r}', t)}{\partial t^2}, \tag{2.1}$$

where ρ is the mass density of the semiconductor. Since the displacement field $\mathbf{u}$ is a function of $\mathbf{r}'$, the displacement is different for each infinitesimal volume. As a result, the

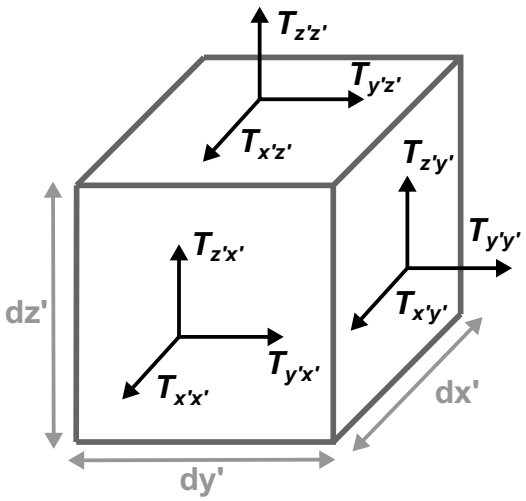

Figure 2.3: Sketch of an infinitesimal volume element in a solid with the definitions of the stress tensor components.

semiconductor deforms while it is subjected to stress. The deformation is characterized by a strain field represented by the strain tensor $\mathbf{S}$. The components of the strain tensor are defined by the gradients of $\mathbf{u}(\mathbf{r}', t)$ [73]:

$$S_{kl}(\mathbf{r}', t) = \frac{1}{2}\left[\frac{\partial u_k(\mathbf{r}', t)}{\partial r_l} + \frac{\partial u_l(\mathbf{r}', t)}{\partial r_k}\right]. \tag{2.2}$$

Here, it is assumed that quadratic terms are negligible, which applies for small displacement gradients of the order of 10^{-3} to 10^{-4}. Fracture of the material occurs for displacement gradients with larger orders. Examining eq. 2.2, it is clear that the strain tensor is symmetric: $S_{kl} = S_{lk}$. The total number of uniquely defined strain components reduces, therefore, to the six elements S_I of a strain vector defined by:

$$\mathbf{S} = \begin{bmatrix} S_{x'x'} \\ S_{y'y'} \\ S_{zz} \\ 2S_{y'z} \\ 2S_{x'z} \\ 2S_{x'y'} \end{bmatrix} = \begin{bmatrix} S_1 \\ S_2 \\ S_3 \\ S_4 \\ S_5 \\ S_6 \end{bmatrix}, \tag{2.3}$$

where the notational system is constructed by introduction of the following subscript relations:

$$\begin{aligned} x'x' &\to 1, \qquad y'y' \to 2, \qquad zz \to 3, \\ y'z &\to 4, \qquad x'z \to 5, \qquad x'y' \to 6. \end{aligned} \tag{2.4}$$

In the remainder of this chapter, the uppercase subscripts I and J are assumed to take the values from 1 to 6 corresponding to the notations of eq. 2.4.

Along with the strain components defined above, a hydrostatic strain component S_0 can also be defined. The effect of the strain components S_1 to S_6 is a deformation of the semiconductor, while S_0 changes the volume of the semiconductor but leaves the original shape of the semiconductor unaffected. The total hydrostatic strain is given by a summation of the strain along the x', y' and z axes:

$$S_0 = S_1 + S_2 + S_3. \tag{2.5}$$

For small deformations, the strain scales linearly with the applied stress forces. In this regime of linear elastic deformation, the relation between stress and strain is described by Hooke's law:

$$T_I = c_{IJ} S_J. \tag{2.6}$$

Here, the tensor $\mathbf{c}$ with the components c_{IJ} represents the elastic stiffness tensor. Since the subscripts I and J both denote six pairs, the elastic stiffness tensor is described by the 36 elements of a 6 x 6 matrix. Thermodynamical considerations lead to a reduction of the tensor to 21 elements [73]. The symmetry of the crystal imposes further restrictions on the elastic stiffness tensor. For anisotropic cubic crystals like the (Al,Ga)As structures used throughout this thesis, the total number of independent components of the elastic stiffness tensor reduces to three, namely c_{11}, c_{12} and c_{44}. The elastic stiffness tensor for the physical systems studied throughout this thesis then becomes [73]:

$$\mathbf{c} = \begin{bmatrix} c_{11} & c_{12} & c_{12} & 0 & 0 & 0 \\ c_{12} & c_{11} & c_{12} & 0 & 0 & 0 \\ c_{12} & c_{12} & c_{11} & 0 & 0 & 0 \\ 0 & 0 & 0 & c_{44} & 0 & 0 \\ 0 & 0 & 0 & 0 & c_{44} & 0 \\ 0 & 0 & 0 & 0 & 0 & c_{44} \end{bmatrix}. \tag{2.7}$$

The strain field from the acoustic wave results in the storage of strain energy E_S, which is related to the strain tensor as follows. A particle velocity can be defined by the time derivative of the strain tensor. Realizing that the stress tensor $\mathbf{T}$ represents elastic forces, the rate of work done on an infinitesimal volume by the stress tensor (rate of strain energy) is calculated by (implying summation over the subscripts I and J):

$$\frac{\partial E_S}{\partial t} = \mathbf{T} : \frac{\partial \mathbf{S}}{\partial t} \rightarrow E_S = \frac{1}{2} c_{IJ} S_I S_J. \tag{2.8}$$

Here, eq. 2.6 is used to express the stress tensor in terms of the strain tensor. By integrating over time, one arrives at the given expression for E_S [73].

In a piezoelectric semiconductor, the strain field induces a piezoelectric field $\mathbf{F}$. The stress tensor as defined by Hooke's law in the absence of piezoelectricity (eq. 2.6) is modified in the piezoelectric case to include the electrical forces arising from $\mathbf{F}$:

$$T_I = c_{IJ} S_J - e_{Jk} F_k, \tag{2.9}$$

where e_{Jk} are the components of the piezoelectric tensor of the semiconductor. Due to the particular symmetry of the cubic crystallic structure of (Al,Ga)As systems, there is only one independent component of the piezoelectric tensor: e_{14}. The full form of the piezoelectric tensor for such systems reads:

$$\mathbf{e} = \begin{bmatrix} 0 & 0 & 0 & e_{14} & 0 & 0 \\ 0 & 0 & 0 & 0 & e_{14} & 0 \\ 0 & 0 & 0 & 0 & 0 & e_{14} \end{bmatrix}^T. \tag{2.10}$$

The piezoelectric field defines a piezoelectric displacement field $\mathbf{D}$:

$$D_i = e_{kJ} S_J + \epsilon_{ij} F_j, \tag{2.11}$$

where ϵ_{ij} represents the components of the dielectric permittivity matrix of the semiconductor. Due to piezoelectricity, the acoustic wave appears to be more stiffened in a piezoelectric semiconductor as compared to a non-piezoelectric semiconductor. Thus, a

smaller deformation occurs as compared to a non-piezoelectric semiconductor and the effective elastic stiffness tensor is modified by the piezoelectric effect according to:

$$c_{IJ} \rightarrow c_{IJ}\left(1 + K_{IJ}^2\right). \tag{2.12}$$

The stiffening of the piezoelectric semiconductor is quantified by the factor K^2, which characterizes the strength of the electromechanical coupling in the semiconductor.

Additionally, it is assumed that there are no free charges in the solid. In this case, the first Maxwell equation dictates that the divergence of the piezoelectric displacement field vanishes: $\nabla \cdot \mathbf{D} = 0$. The piezoelectric field can be expressed in terms of a piezoelectric potential ϕ by $F_j = -\partial\phi/\partial r_j$. Combining eq. 2.9 with eq. 2.1 then leads to the constitutive equations describing acoustic wave propagation in a solid:

$$c_{ijkl}\frac{\partial^2 u_k\left(\mathbf{r}', t\right)}{\partial r_j \partial r_l} + e_{kij}\frac{\partial^2 \phi\left(\mathbf{r}', t\right)}{\partial r_j \partial r_k} = \rho\frac{\partial^2 u_i\left(\mathbf{r}', t\right)}{\partial t^2}, \tag{2.13a}$$

$$e_{ijk}\frac{\partial^2 u_j\left(\mathbf{r}', t\right)}{\partial r_i \partial r_k} - \epsilon_{ij}\frac{\partial^2 \phi\left(\mathbf{r}', t\right)}{\partial r_i \partial r_j} = 0. \tag{2.13b}$$

2.2.2 Surface acoustic waves

The previous discussion provides a general description of bulk acoustic waves. In this thesis, surface acoustic waves are utilized for acoustic charge and spin transport. The mathematical framework for bulk acoustic waves can be extended to surface acoustic waves by introducing the appropriate boundary conditions at the interface between the semiconductor and vacuum space. In the following discussion, the vacuum occupies the half-space $z > 0$ and the semiconductor occupies the half-space $z < 0$. The surface has to be stress-free, since the vacuum does not apply stress to the surface. Since vacuum space can hold an electromagnetic wave, the boundary condition for the piezoelectric displacement field on the charge-free surface follows from Gauss's law, which implies that the normal component of the electric displacement field should be continuous. In terms of the stress tensor and the piezoelectric displacement field $\mathbf{D}$ the boundary conditions can be stated as:

$$T_{x'z} = T_{y'z} = T_{zz} = 0 \tag{2.14a}$$

$$D_z(z = 0^{\uparrow}) = D_z(z = 0^{\downarrow}), \tag{2.14b}$$

where $0^{\uparrow}$ and $0^{\downarrow}$ indicate that one approaches the surface from its lower side (semiconductor side) and upper side (vacuum side), respectively. Furthermore, the fact that a SAW is confined at the surface enforces the acoustic wave amplitude to decay when $z \rightarrow -\infty$. In semiconductors like (Al,Ga)As, where piezoelectricity is weak, the mechanical properties of the surface acoustic wave are dominated by the elastic properties of the material. The problems of finding the mechanical displacement functions and the corresponding piezoelectric potential can therefore be separated.

The particular form of eq. 2.13(a) in the absence of piezoelectricity ($e_{ijk} = 0$) motivates a trial function of plane waves travelling in the (x', y')-plane at an angle of θ_{SAW} with the x' axis, with a SAW wavevector $\mathbf{k_{SAW}} = (k_{x'}, k_{y'})$ and SAW angular frequency ω_{SAW}:

$$\mathbf{u}\left(\mathbf{r}', t\right) = \begin{bmatrix} \hat{u}_{x'} \\ \hat{u}_{y'} \\ \hat{u}_z \end{bmatrix} e^{k_z z} e^{i\left[k_{x'}x' + k_{y'}y' - \omega_{SAW}t\right]}. \tag{2.15}$$

Here, $\hat{u}_{x'}$, $\hat{u}_{y'}$ and $\hat{u}_z$ are amplitudes and k_z is related to the evolution of the wave when it penetrates through the semiconductor. For convergence of the SAW solution when $z \to -\infty$, the real part of k_z should be positive. Additionally, k_z is allowed to have a finite imaginary part, representing an oscillation of the SAW amplitudes with depth. The in-plane wavevector components are related to θ_{SAW} by $k_{x'} = k_{SAW}\cos(\theta_{SAW})$ and $k_{y'} = k_{SAW}\sin(\theta_{SAW})$. Substituting the trial function (eq. 2.15) into eq. 2.13(a) yields an equation of the form $\mathcal{M}\mathcal{A} = 0$, where

$$\mathcal{A} = \begin{bmatrix} \hat{u}_{x'} \\ \hat{u}_{y'} \\ i\hat{u}_z \end{bmatrix} \tag{2.16}$$

and the matrix $\mathcal{M}$ is defined by:

$$\begin{bmatrix} c_{11}k_{x'}^2 + c_{44}\left[k_{y'}^2 - k_z^2\right] - \rho\omega_{SAW}^2 & k_{x'}k_{y'}\left[c_{12}+c_{44}\right] & -k_{x'}k_z\left[c_{12}+c_{44}\right] \\ k_{x'}k_{y'}\left[c_{12}+c_{44}\right] & c_{11}k_{y'}^2 + c_{44}\left[k_{x'}^2 - k_z^2\right] - \rho\omega_{SAW}^2 & -k_{y'}k_z\left[c_{12}+c_{44}\right] \\ -k_{x'}k_z\left[c_{12}+c_{44}\right] & -k_{y'}k_z\left[c_{12}+c_{44}\right] & c_{11}k_z^2 - c_{44}k_{SAW}^2 + \rho\omega_{SAW}^2 \end{bmatrix}. \tag{2.17}$$

In regular algebra calculations, non-trivial solutions of $\mathcal{A}$ are found for those values of k_z for which $\det\mathcal{M} = 0$, which is an equation of sixth order in k_z with three roots for k_z^2. Thus, three sets of plane waves exist, each corresponding to a different acoustic mode, where each mode has a distinctive value of k_z^2 and consists of distinct mechanical displacement functions for the x', y' and z directions. Within each set, denoted by the subscript m, the amplitudes can be related to a constant K_m corresponding to that set [75]:

$$K_m = \frac{u_{nm}}{\zeta_{nm}}, \tag{2.18}$$

where the constants ζ_{nm}; $n = x'$, y', z; $m = 1$, 2, 3; can be extracted from the matrix defined by eq. 2.17: they can be expressed in terms of the wavevector components, material density, elastic stiffness tensor components and the SAW frequency. Since K_m is a constant, it can be used to determine the relation between $\hat{u}_{x'}$, $\hat{u}_{y'}$ and $\hat{u}_z$. A superposition of the three sets describes the surface acoustic wave:

$$(u_{x'}, u_{y'}, u_z)(\mathbf{r}', t) = \sum_{m=1,2,3} (\zeta_{x'm}, \zeta_{y'm}, -i\zeta_{zm}) K_m e^{k_z z} e^{i\left[k_{x'}x' + k_{y'}y' - \omega_{SAW}t\right]} \tag{2.19}$$

As introduced in chap. 1, the quantum wires studied in this thesis form along the [110] crystal direction on GaAs (001) substrates. Due to the atomic configuration along this direction, it is piezoelectric, which is a prerequisite for acoustic transport of separated electrons and holes. Therefore, the remainder of this chapter focusses on the properties of SAWs propagating along this direction. The projections of the corresponding SAW wavevector on the crystallographic axes are $k_{x'} = k_{y'} = k_{SAW}/\sqrt{2}$. Inserting this in the matrix $\mathcal{M}$ and subtracting the second row from the first row reveals that $\hat{u}_{x'} = \hat{u}_{y'}$. In other words, the mechanical displacement field has components along the $x||[110]$ and $z||[001]$ axes. In this reference frame, the matrix $\mathcal{M}$ defined by eq. 2.17 reduces to a 2 x 2 matrix $\mathcal{M}_{110}$ for the displacement functions u_x and u_z with amplitudes $\hat{u}_x$ and $\hat{u}_z$, respectively:

$$\begin{bmatrix} \frac{k_{SAW}^2}{2}\left[c_{11}+c_{12}+2c_{44}\right] - c_{44}k_z^2 - \rho\omega_{SAW}^2 & -\frac{k_{SAW}k_z}{\sqrt{2}}\left[c_{12}+c_{44}\right] \\ -\sqrt{2}k_{SAW}k_z\left[c_{12}+c_{44}\right] & c_{11}k_z^2 - c_{44}k_{SAW}^2 + \rho\omega_{SAW}^2 \end{bmatrix}. \tag{2.20}$$

As in the previous case, non-trivial solutions for $\hat{u}_x$ and $i\hat{u}_z$ are found by solving $\det \mathcal{M}_{110} = 0$, resulting in two sets of waves with different values for k_z^2. The final explicit solutions for the mechanical displacements are:

$$u_x = A_S e^{k_z z} \cos\left(k_{SAW} x - \omega_{SAW} t\right) \tag{2.21a}$$

$$u_z = r_{xz} A_S e^{k_z z} \sin\left(k_{SAW} x - \omega_{SAW} t\right). \tag{2.21b}$$

Here, A_S is the amplitude of the displacement along the x axis. The parameter r_{xz} relates the amplitude of u_z with A_S and can be calculated using the matrix $\mathcal{M}_{110}$ [75]:

$$r_{xz} = \frac{\sqrt{2} k_{SAW} k_z \left[c_{12} + c_{44}\right]}{c_{11} k_z^2 - c_{44} k_{SAW}^2 + \rho \omega_{SAW}^2}. \tag{2.22}$$

The mechanical displacement functions of eqs. 2.21(a) and (b) describe a Rayleigh wave with displacement components u_x and u_z, which is the SAW mode utilized for the experiments on acoustic transport in this thesis. For this acoustic mode, the non-zero strain components are S_1, S_3 and S_5. Equations 2.21 show that the atoms vibrate along the SAW propagation direction and along the surface normal, while no transverse mechanical displacement occurs in the surface. The trajectory of the atoms in the Rayleigh wave is elliptic with an eccentricity determined by r_{xz}. It can be shown that k_z is complex. As a result, r_{xz} is a function of depth, meaning that the eccentricity of the atomic trajectory depends on the depth of the atom [75]. Inserting the explicit equations for the mechanical displacement functions (eqs. 2.21) in the constitutive equation 2.13(a), the dispersion of the SAW is given by:

$$\omega_{SAW} = v_{\mathrm{SAW}} k_{SAW}, \tag{2.23}$$

where v_{SAW} is the acoustic velocity. This velocity can be calculated by solving $\det \mathcal{M} = 0$ while applying the boundary conditions (eqs. 2.14). For a SAW propagating along the [110] direction of a GaAs (001) surface, this results in a velocity of approx. $3 \times 10^3\,\mathrm{m/s}$ [75].

When the mechanical solution is found for the non-piezoelectric semiconductor, the piezoelectric potential ϕ_{SAW} can be determined by considering the mechanical solution and the boundary condition defined by eq. 2.14(b). In vacuum, the piezoelectric displacement field is simply given by the vacuum permittivity and the piezoelectric field, which can be expressed in terms of the piezoelectric potential: $\mathbf{D_{vac}} = -\epsilon_0 \nabla \phi_{\mathrm{SAW}}$. From Poisson's equation ($\Delta \phi_{\mathrm{SAW}} = 0$) and the confinement of the wave to the surface, the piezoelectric displacement field in the vacuum space can be derived to be $\mathbf{D_{vac}} = -\epsilon_0 k_{SAW} \phi_{\mathrm{SAW}}$. The electric boundary condition at the surface of the medium gives in combination with eq. 2.11:

$$\left(e_{zjk} \frac{\partial u_j}{\partial r_k} - \epsilon_{zj} \frac{\partial \phi_{\mathrm{SAW}}}{\partial r_j} + \epsilon_0 k_{SAW} \phi_{\mathrm{SAW}} \right)_{z=0} = 0. \tag{2.24}$$

From this equation, the piezoelectric potential can be derived to be [76]:

$$\phi_{\mathrm{SAW}} = i\hat{\phi} \mathcal{F}\left(k_{SAW} z\right) e^{i(k_{SAW} x - \omega_{SAW} t)} \quad \text{semiconductor (z<0)} \tag{2.25a}$$

$$\phi_{\mathrm{SAW}} = i\hat{\phi} \mathcal{F}\left(0\right) e^{k_{SAW} z} e^{i(k_{SAW} x - \omega_{SAW} t)} \quad \text{vacuum (z>0)} \tag{2.25b}$$

The decay of the potential with depth is governed by a function $\mathcal{F}\left(k_{SAW} z\right)$, given by:

$$\mathcal{F} = 2\left|A_1\right| \mathrm{Re}\left(e^{k_z z + i\xi}\right) + A_3 e^{\mathrm{Re}(k_z) z}, \tag{2.26}$$

where ξ is a phase which can be expressed in terms of v_{SAW}, k_z, ρ, c_{11}, c_{12} and c_{44}. The constants A_1 and A_3 can be expressed in those terms as well [76]. Typically, the acoustic and piezoelectric fields of a SAW decay within one SAW wavelength.

In experiments on acoustic charge transport, detection may be achieved by means of remote photoluminescence (PL), as will be described in secs. 7.1 and 7.2. To induce the recombination of transported carriers, the piezoelectric potential can be screened by a metallic stripe on the surface. Since metal is a conductor, its potential should be constant inside and may be set to zero. The potential should be continuous when crossing the interface between the semiconductor surface and the metal stripe. Consequently, the piezoelectric potential inside the semiconductor should be zero in the vicinity of the interface between semiconductor and metal stripe. This screening of the piezoelectric potential leads to recombination of transported carriers. The electromechanical coupling can be determined by short-circuiting the surface with a perfect conductor. The K^2 factor (see eq. 2.12) can be estimated by comparing the SAW velocities in the semiconductor with and without the metal stripe [77]:

$$K^2 = 2\frac{v_{SAW,f} - v_{SAW,g}}{v_{SAW,f}}, \tag{2.27}$$

where $v_{SAW,f}$ is the SAW velocity for the free surface and $v_{SAW,g}$ is the SAW velocity for the surface with a metal stripe.

2.2.3 Interdigital transducers

The (inverse) piezoelectric effect is employed to (generate) detect surface acoustic waves using an interdigital transducer (IDT). A single-finger IDT consists of two spatially periodic metallic electrodes deposited on top of the semiconductor surface. Per period, each electrode contains one finger. The two electrodes are connected to an output port of an external radio-frequency (rf) source. The rf source applies an alternating voltage which induces the strain field required to excite a surface acoustic wave. The single-finger IDT is subjected to scattering of the SAW within the IDT to the substrate, because the electrode grating periodicity fulfils the conditions for a Bragg grating. In the current thesis, unless stated otherwise, the SAWs are generated by split-finger IDTs, as illustrated in fig. 2.4(a). Here, each single IDT finger is split into two fingers. This transforms the metallic Bragg grating into a second-order one, thereby reducing scattering of the SAW within the IDT. Consequently, this increases the conversion efficiency of electrical energy into an acoustic mode propagating outside the IDT region [78]. Figure 2.4(a) shows a sketch of the deformation of the solid (grey) under operation of the IDT. The rf voltage induces an electric field $\mathbf{F}$ as sketched in the figure. The field direction reverses between two consecutive finger pairs. Combined with the inverse piezoelectric effect, this results in xz shear strain, and therefore, in an oscillating upwards and downwards movement of the surface. The wavelength of the SAW λ_{SAW} is determined by the periodicity of the metallic grating (characterized by the finger separation Δx_f) and the width of the fingers w_f. For a split-finger type IDT, these are related by:

$$w_f = \Delta x_f = \lambda_{SAW}/8. \tag{2.28}$$

A SAW generated by the rf voltage travels along two opposite surface directions, as illustrated in the figure. As a result, the total acoustic power supplied by the IDT from conversion of electrical energy into mechanical energy is divided over these two SAW modes.

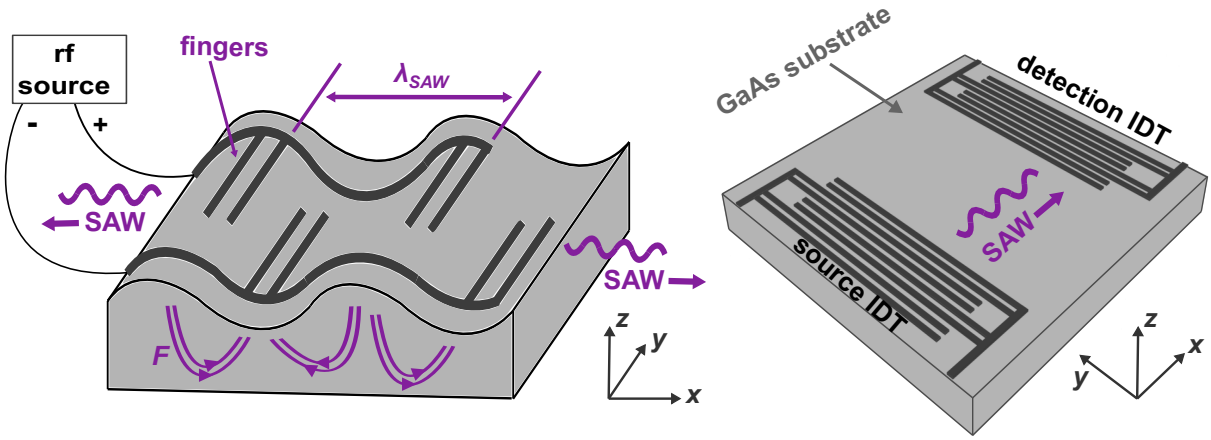

(a) interdigital transducer with rf source **(b) delay line device**

Figure 2.4: Split-finger interdigital transducers (IDT). (a) Sketch of the IDT (black) in operation. An rf source applies an alternating voltage to the IDT, resulting in deformation of the semiconductor surface, as sketched in the figure. The purple lines in the front view depict the electric field lines, resulting from the rf voltage. The wavelength of the SAW λ_{SAW} is determined by the periodicity of the electrode, as indicated in the figure. (b) A typical delay line consists of two IDTs (black) on top of the semiconductor (grey), where the source IDT excites a surface acoustic wave and a detection IDT is used for detection of the SAW.

A common acoustic device is a delay line consisting of two opposing IDTs, as illustrated in fig. 2.4(b). Here, a source IDT is used to generate a SAW towards the detection IDT, which converts the mechanical energy carried by the SAW into an electrical signal. The conversion efficiency between electrical and acoustic energy depends on the rf frequency f_{rf} and is described by four scattering parameters (S-parameters), which describe the scattering behaviour of electrical signals in electrical circuits. In the case of an acoustic delay line, they can be related to the characteristics of the IDTs. Two of these parameters (S_{12} and S_{21}) depict the transmission of the SAW: a SAW is excited by the source IDT and transmitted to the detection IDT, whereafter the electric signal coming from the detection IDT is then recorded as the S_{12} parameter. The reverse case, where the SAW is generated by the detection IDT and back converted by the source IDT, results in the S_{21} parameter. In a typical device, the SAW amplitude can be considered to be maintained over the distance between the IDTs (of the order of $10^2\,\mu\text{m}$). Under this condition, the S_{12} and S_{21} parameters can be characterized by a sinc function, specified by the number of finger pairs N_f and the center frequency of the IDT $f_0 \equiv \omega_{SAW}/(2\pi)$ (determined by eq. 2.28) [78]:

$$S_{12}, S_{21} \propto \frac{\sin(f')}{f'} \tag{2.29a}$$

$$f' = \frac{N_f}{f_0}\pi\left[f_{rf} - f_0\right]. \tag{2.29b}$$

The remaining two parameters S_{11} and S_{22} correspond to the reflection of rf power at the source and detection IDT, respectively. Away from f_0, the rf power can not be converted efficiently into acoustic modes, since the condition of eq. 2.28 is not met. If the rf frequency corresponds to f_0, the conversion is most efficient and the reflection parameter has a minimum. The linewidth of the minimum is determined by the IDT design.

A common application of the acoustic device described above is as a signal delay line.

Here, an electromagnetic signal is converted by the IDT into a SAW. Since the acoustic velocity is three orders of magnitudes smaller than the electromagnetic velocity, transmission over the distance between the two IDTs is delayed with respect to electromagnetic transmission over an equal distance. The detection IDT converts the SAW back into an electromagnetic signal for further processing. A related use of the device is that of a frequency filter. In such a filter, an electromagnetic signal containing multiple frequencies is guided to the input of the source IDT. The frequency dependency of the IDT means that only a narrow band of frequencies is converted into acoustic modes, which are converted back into an electromagnetic signal by the detection IDT. As a result, the output signal of the acoustic device only contains the frequencies selected by the delay line. Since the SAW properties are easily adjusted by modifications of the top surface, a third usage of this device is that of material sensors or pressure sensors.

In this thesis, excitations in nanostructures (such as charge carriers or spins) are controlled by surface acoustic waves. The nanostructures are located between the two IDTs of a typical delay line. In order to avoid reflections of the SAW, the IDTs are of the split-finger type. SAW reflections off a single-finger IDT may result in a standing-wave pattern, which is unfavourable for acoustic transport. The use of delay lines rather than single IDTs is motivated by experimental reasons. The detection IDT can be used to probe SAW generation by the source IDT. In addition, if the source IDT is defect, one may perform similar experiments using the detection IDT as a source. Finally, for experiments where a standing wave is actually desired (not included in this thesis), one needs to excite a SAW using both the source and the detection IDT.

2.3 Acoustic modulation of the electronic states

Consider the optical injection of electrons (solid brown dots) in the conduction band (CB) and holes (open brown dots) in the valence band (VB) by a laser in a thin GaAs QW layer, sandwiched between two thick (Al,Ga)As barrier layers, as illustrated by the bright red arrow in fig. 2.5(a). The electronic properties of this system will be discussed in detail in sec. 3.1. In a QW layer, the valence band splits into a heavy-hole (hh) state and a light-hole (lh) state, which have a small energetic splitting. After excitation, the flat band-edges in space mean that the electrons and holes are located at similar positions. If the transition is dipole allowed, the carriers recombine due to the overlap of their wavefunctions. The transition energy E_{e-hh} released upon recombination is emitted in the form of a photon (dark red arrow). The piezoelectric potential and the strain fields of the SAW modulate the semiconductor band-edges in the spatial and temporal dimensions, which is the topic of this section. In general, two modulation types can be distinguished. The 'type-I' modulation describes a situation where the conduction and valence band-edge modulation is out-of-phase: a minimum in the conduction band corresponds to a maximum in the valence band. In contrast, the 'type-II' describes a situation where the modulation is in-phase, e.g. the minima of the conduction and valence bands correspond to the same spatial or temporal coordinate.

2.3.1 Modulation by the piezoelectric potential

The spatial separation of optically excited electrons and holes by the SAW prevents their recombination and supports acoustic carrier transport over distances of the order of $10^2\,\mu$m. The separation of the carriers is achieved via the piezoelectric potential accompanying a SAW propagating along a piezoelectric surface direction [59]. The potential energy $-e\phi_{\mathrm{SAW}}$ supplemented by the piezoelectric potential can be of the order of $10^2\,$meV. This energy

is large enough to ionize optically injected excitons in (Al,Ga)As-based QW structures, which typically have binding energies below 10 meV [79], into free electrons and holes. The band-edge modulation by the piezoelectric SAW potential in a QW layer is illustrated in fig. 2.5(b). Here, the grey dashed lines indicate the band-edges without acoustic modulation, whereas the green lines depict the band-edges along the SAW direction with piezoelectric modulation. The piezoelectric modulation follows from superposing the potential energy $-e\phi_{\mathrm{SAW}}$ onto the flat (unmodulated) band-edges. The figure shows that all band-edges are modulated in an in-phase fashion: the positions of the minima and maxima of all band-edges coincide. This is known as a 'type-II' modulation. The corresponding positions of electrons and holes is displayed with solid and open brown dots, respectively. Clearly, the separation between the oppositely charged carriers is $\lambda_{SAW}/2$. Note that the SAW wavelength is three orders of magnitude larger than the low-temperature carrier deBroglie wavelengths. The piezoelectric modulation should, therefore, not lead to an acoustically induced quantum shift of E_{e-hh}.

In the case of a Rayleigh wave, the piezoelectric potential results in piezoelectric fields along the SAW propagation direction (longitudinal field F_x) and along the surface normal (transverse field F_z). The efficiency of acoustic carrier transport can be evaluated by considering how well the charge carriers are able to follow the modulation of F_x. The velocity of the carriers is dictated by their drift velocity $v_d = \mu F_x$, where μ is the carrier mobility. In order for the carriers to follow the band extrema, v_d should at least match the acoustic velocity. Efficient acoustic charge transport requires, therefore, the following conditions to be fulfilled:

$$F_x > \frac{v_{\mathrm{SAW}}}{\mu_e}, \tag{2.30a}$$

$$F_x > \frac{v_{\mathrm{SAW}}}{\mu_h}, \tag{2.30b}$$

where μ_e and μ_h are the electron and hole mobilities, respectively. As is shown in sec. 2.5.2, typical field strengths of F_x are large enough to transport both electrons and holes. The use of a GaAs QW promises efficient carrier transport, since its piezoelectricity is sufficiently strong to induce the required F_x and the carrier mobilities are much larger than comparable materials such as nitride-based structures.

The vertical piezoelectric field F_z squeezes the carriers towards either the upper or lower interfaces between the QW and the barriers. The direction of F_z depends on the SAW propagation direction and is discussed in sec. 2.5.2. Another effect of F_z is an acoustically induced quantum-confined Stark effect [80]. In fig. 2.5(c), the CB and VB of an unperturbed QW structure are schematically drawn. The energy of the electrons (solid brown dots) and holes (open brown dots) is depicted by green and blue dashed lines, respectively. Their approximate wavefunctions are displayed with solid lines in the corresponding colours. The transition energy is given in this case by E_{e-hh}. In fig. 2.5(d), the electronic bands are drawn for the same QW structure, which is now subjected to F_z. Since the QW thickness is much smaller than the SAW wavelength, F_z can be considered to be constant over the QW thickness. The electronic bands are now bent and electrons move towards the QW minimum of the conduction band, while holes move towards the QW maximum of the valence band. The new transition energy E_{St} is, consequently, red-shifted with respect to E_{e-hh}. Moreover, the recombination rate decreases because electrons and holes are squeezed towards opposite interfaces of the QW layer, reducing their spatial overlap of the wavefunctions.

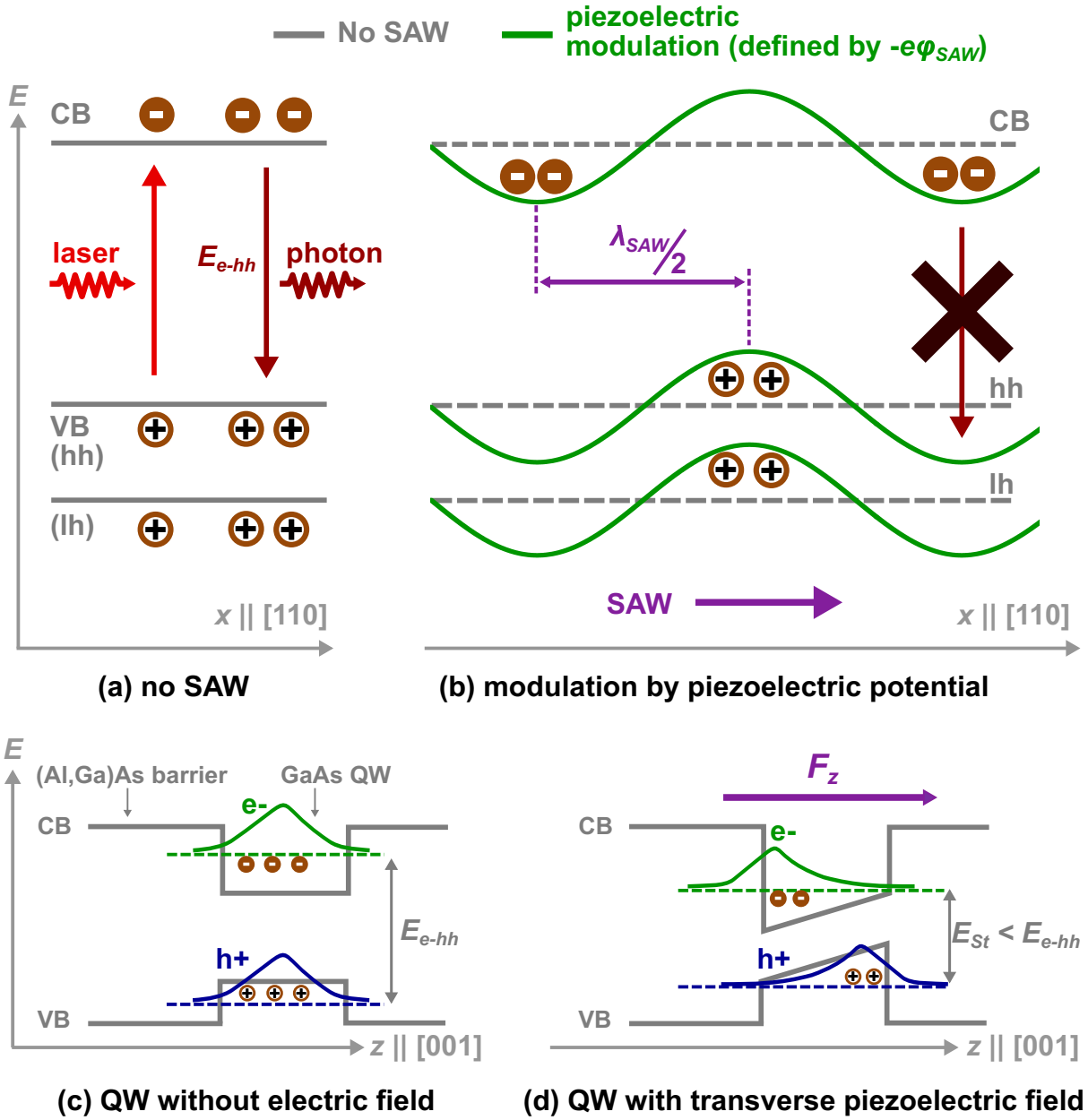

Figure 2.5: Piezoelectric modulation of the band-edge states by the SAW. (a) Band-edges in space without SAW. Under this condition, electrons (brown solid dots) and holes (open brown dots), optically injected by a laser (bright red), are located at similar positions and are allowed to recombine upon emission of a photon with energy E_{e-hh} (dark red). (b) The type-II modulation of the electronic bands by the piezoelectric potential (green lines) spatially separates electrons and holes by half a SAW wavelength: recombination is drastically suppressed. The dashed grey lines indicate the band-edges without SAW (conform fig. (a)). (c)-(d): Quantum-confined Stark effect. (c) Electronic states in a QW structure. The wavefunctions and energy levels of the electrons and holes are depicted in green and blue, respectively. The transition energy of an electron recombining with a hole is given by E_{e-hh}. (d) The electronic bands are modified, when the QW is subjected to an electric field along its growth axis. The electrons move towards the minimum of the conduction band, while holes move towards the maximum of the valence band. As a result, the recombination rate decreases and the transition energy is red-shifted to E_{St}.

2.3.2 Modulation by the SAW strain field

The strain field induces local variations of the volume and symmetry of the crystal structure and leads, like the piezoelectric field, to a modulation of the electronic band-edge states in the semiconductor. Since the states of the conduction and valence bands exhibit different spatial symmetries, they respond in different ways to the strain field of the SAW.

The band-edge states of the conduction band of a compound III-V semiconductor have an s-like character. These s-like states are primarily affected by the volume changes induced by the hydrostatic component of the strain field. The shift of the conduction band energy can be expressed as $\Delta E_{CB} = a_{CB} S_0$, where a_{CB} is the hydrostatic deformation potential for the conduction band of the solid.

In contrast to the s-type conduction band states, the band-edge states of the valence band of a compound III-V semiconductor mainly have a p-like character. The hydrostatic deformation potential a_{VB} is small for these states. The valence band states are more sensitive to the uniaxial components S_1 and S_3. These uniaxial strains cause an energy shift of the valence band states and a mixing of the heavy-hole and light-hole states. In case of a QW with a large splitting of the heavy-hole and light-hole bands, the corresponding energy shift is expressed as $b_{VB}\,(S_3 - S_1/2)$, with b_{VB} the uniaxial deformation potential of the valence band. The strain modulation of the transition energy is given by [81]:

$$\Delta E_{e-hh} = (a_{CB} + a_{VB})\, S_0 \pm b_{VB} \left(S_3 - \frac{S_1}{2} \right). \tag{2.31}$$

In this expression, the positive (negative) sign corresponds to the heavy-hole (light-hole).

The modulation of the band-edge states by the strain field is schematically drawn in fig. 2.6. Here, the grey dashed lines indicate the band-edge modulation by the piezoelectric potential only, whereas the green solid lines also include the modulation by the strain field. The difference between the two lines corresponds to the modulation by the strain field only. For a SAW propagating along the [110] direction, the electron and heavy-hole (hh) bands are strain modulated in-phase: this is again a type-II modulation. In addition, the induced shifts of the conduction and valence bands are usually not equal, as was the case for the piezoelectric modulation. As a result, the transition energy E_{e-hh} varies within a SAW period. Since the band-edge shift for the electrons is larger than the shift for the holes, the minimum (E^{min}_{e-hh}) and maximum (E^{max}_{e-hh}) transition energies appear at positions where the strain field induces a lowering and raise of the electron energy, respectively. Twice every SAW period, at the positions of zero strain, the transition energy takes its original value E^{0}_{e-hh}.

The modulation of the light-hole (lh) band-edge is shown in fig. 2.6 as well. Contrarily to the heavy-hole states, the light-hole modulation appears in an out-of-phase fashion with respect to the conduction band (note that this is again for a SAW propagating along the $x||[110]$ direction): this is known as the 'type-I' modulation. Due to the type-I modulation, the variation of the electron to light-hole transition energy is stronger than the one for the electron to heavy-hole transition. However, the positions where the minimum, maximum and original transition energies appear do not change, because they are determined by the stronger strain-induced modulation of the conduction band.

Note that the amplitudes of the band-edge shifts due to the piezoelectric potential and the strain field as depicted in fig. 2.6 are not scaled to real values. In fact, it is shown in sec. 2.5.2 that for the QW systems studied in this thesis, the modulation induced by the piezoelectric potential is much stronger than the one induced by the strain field. Additionally, it is worthwhile to take into consideration the SAW propagation direction. The scheme as illustrated in fig. 2.6 holds for a SAW propagating along the [110] crystal direction. For SAW propagation along $[\bar{1}10]$, a phase shift between the strain field and the

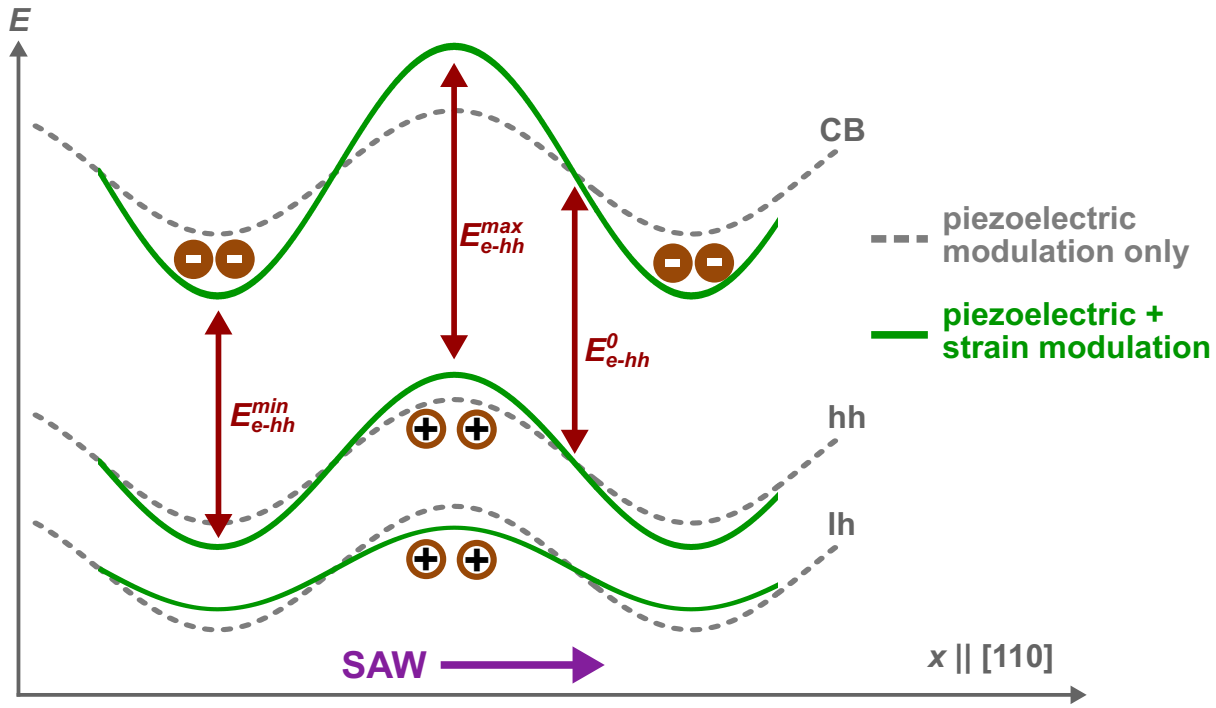

Figure 2.6: Modulation of the electronic bands by the strain field. The dashed grey lines indicate the piezoelectric modulation, the solid green lines include the strain modulation as well. The positions of electrons and holes are indicated by solid and open brown dots, respectively. Twice every SAW period, the transition energy takes its original value E^0_{e-hh}. Recombination at positions of the electrons (holes) in the piezoelectric potential leads to the transition energy E^{min}_{e-hh} (E^{max}_{e-hh}).

piezoelectric potential arises. For that direction, the position of electrons corresponds to E^{max}_{e-hh} and not to E^{min}_{e-hh}.

2.4 Carrier trapping mechanisms

In the previous section, it is discussed how the piezoelectric potential leads to acoustic carrier transport. The carriers are transported as long as they are not forced to recombine. Ideally, the recombination can be induced on-demand, for example, by depositing a metal stripe onto the transport path. In real structures, however, trapping centers along the transport path lead to unintended carrier trapping and recombination. In this section, three mechanisms of carrier trapping are discussed.

Trapping centers can arise due to potential fluctuations along the transport path [64]. These fluctuations result from random variations of the QW(R) dimensions or alloy fluctuations of the (Al,Ga)As barriers. Figure 2.7(a) illustrates the effect of QWR thickness variations on the electron energy. Here, the dashed grey lines indicate the ideal QWR interfaces with the lower and upper (Al,Ga)As barriers. The solid green lines depict the real QWR boundaries. The resulting modifications of the electron energy around its ideal value $E_{e,0}$ is drawn in the upper panel. Fluctuations of the QWR width may induce similar effects. Note that neither the magnitudes of the thickness fluctuations nor of the energy variation is scaled to real values. As is shown by the upper panel, at different places, an increase of the electron energy induces a lateral barrier for electrons along the SAW propagation direction. The local minima of E_e act as trapping centers for electrons. A similar situation may occur in the valence band, which results in trapping of holes. This

type of carrier trapping is reported to result in quantum dot (QD) like states with sharp PL lines [64] in 12 nm thick QWRs on GaAs (113)A substrates. In that report, the QD states are attributed to monolayer fluctuations of the QWR thickness. The thickness of the QWRs studied in this thesis is much larger (25 ± 5 nm, as will be shown in sec. 5.3.2). Therefore, the effect of thickness fluctuations is smaller in the experiments conducted in this thesis. Due to the large QWR thickness, the QWR transition energy fluctuations should be small. Therefore, the PL from the trapping centers related to QWR thickness fluctuations in the QWRs studied in this thesis should essentially be the same as the one observed at the excitation location.

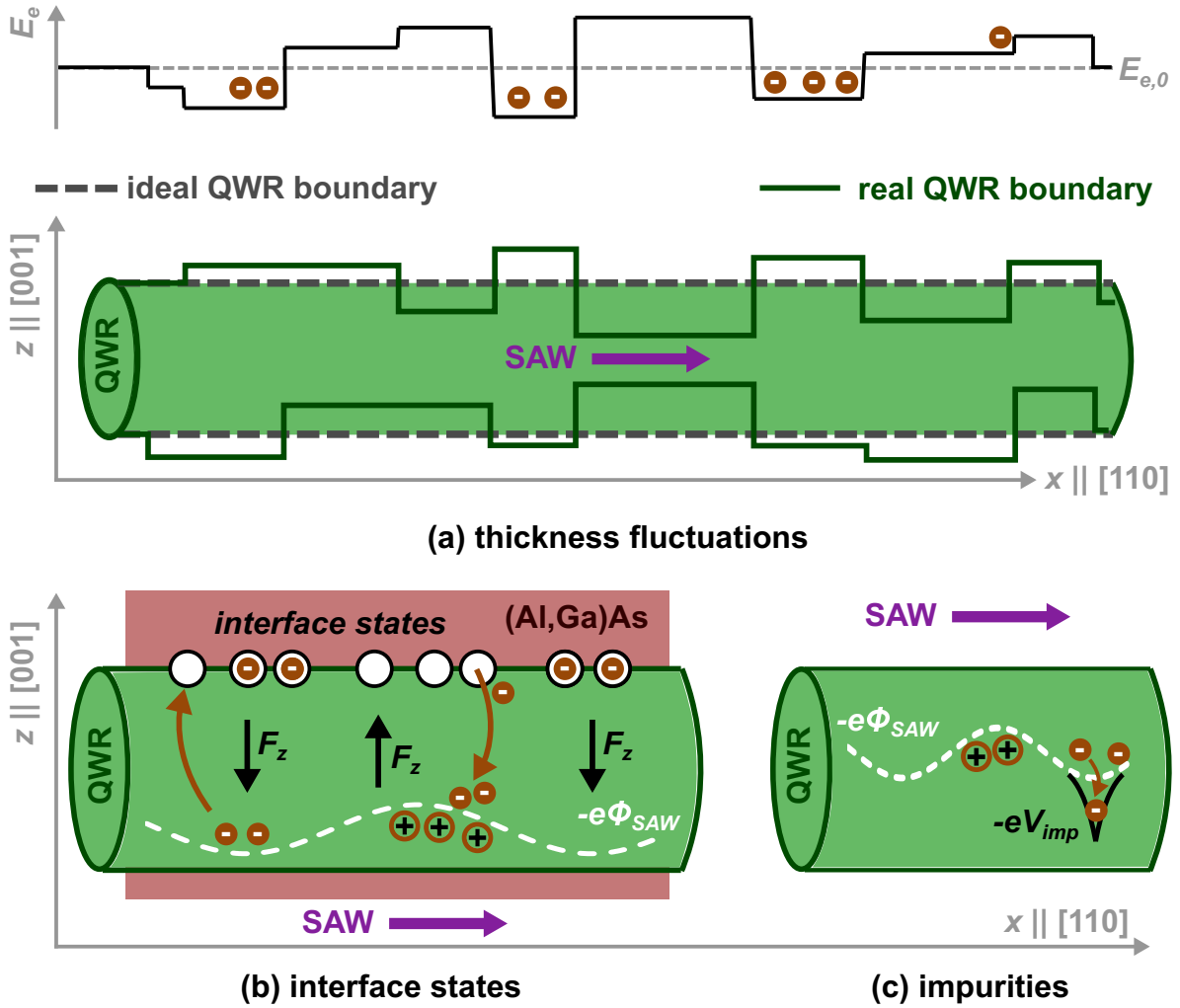

Figure 2.7: Carrier trapping mechanisms. (a) Potential fluctuations: the ideal boundaries (dashed grey lines) of the QWR are rough in reality (solid green lines). The upper panel indicates the corresponding modulation of the electron energy. The electrons are depicted as solid brown dots. (b) Interface states: white circles represent states at the interface between the QWR and the upper (Al,Ga)As layer. Electrons (holes) are sketched by solid (open) brown dots. The brown arrows indicate the movement of electrons due to the transverse piezoelectric field (black arrows). The dashed white line indicates the shape of the piezoelectric potential energy. The red areas represent the (Al,Ga)As barriers. (c) Impurities: the black solid line illustrates a possible trapping potential energy arising from an impurity. The purple arrow in figs. (a)-(c) indicates the SAW propagation direction.

A second trapping mechanism arises due to the presence of interface states [82], as illustrated in fig. 2.7(b). At the interface between the QWR (green) and the (Al,Ga)As

barrier (red), interface states with a typical density of 10^{10}-$10^{11}/\mathrm{cm}^2$ [83] may trap carriers moving in the SAW potential. Consider the situation for electron trapping, as illustrated in the figure. At the position of electron storage by the SAW, the transverse piezoelectric field F_z (black arrow) is oriented downwards. This means that electrons (solid brown dots) stored by the SAW are squeezed towards the upper QWR interface and are easily trapped into the interface states. In contrast, at the position of hole storage, F_z is oriented upwards. Thus, electrons may escape from the interface states and move back into the QWR under influence of F_z. Since this situation corresponds to the SAW phase of hole storage, the released electrons recombine with the holes stored by the SAW. The mobility of holes is one order of magnitude smaller than the one for electrons. This means that the holes are less susceptible to such a mechanism, because one requires larger electrical fields to move the holes as compared to the electrons. The trapping of carriers into the interface states can, thus, be assisted by the piezoelectric field. Therefore, the trapping dynamics depends on the acoustic power. Since for this trapping mechanism recombination takes place in the QWR itself, the PL spectrum induced by such a trapping and recombination event should essentially be equal to the one at the excitation location.

A third trapping mechanism is illustrated in fig. 2.7(c). In this case, a local impurity or defect results in a local trapping potential. In GaAs, a variety of impurities have been found to emit within the GaAs bandgap [84]. Since the energy of these states is smaller as those in the QWR, they correspond to local energy minima. Thus, carriers stored by the SAW may be trapped by the impurity and recombine with the passage of carriers of opposite polarity. Since the transition energies of these impurities are smaller than the GaAs bandgap, the PL from such a trapping center should, in general, be red-shifted with respect to the transition energy of the QWR.

2.5 Simulations of the SAW fields on GaAs (001)

Having laid down the fundamental equations to describe a SAW, the properties of the SAW mode propagating along [110] on GaAs (001) surfaces are studied in this section by means of numerical simulations. Firstly, the numerical procedure to obtain the SAW modes is introduced in sec. 2.5.1, after which simulation results of the SAW properties are presented in sec. 2.5.2.

2.5.1 Simulation method

Since the SAW propagation direction for the experiments in this thesis is [110], it is convenient to reconsider the mathematical framework introduced in sec. 2.2 for a reference frame constructed by $x||[110]$, $y||[\bar{1}10]$ and $z||[001]$. The transformation from the crystallographic axes to this new reference frame can be performed by rotating the matrices involved in the calculations by the Euler angles. The only rotation necessary is a rotation by an angle θ_{eu} in the (x', y')-plane, as depicted in fig. 2.8. From this figure, it is clear that for a SAW propagating along the [110] direction, $\theta_{eu} = 0.25\pi$, so that after rotation the SAW propagation direction corresponds to the new x axis. The simulations can then be carried out by appropriate transformation of the involved tensors.

In this thesis, (Al,Ga)As quantum wire structures grown by molecular-beam epitaxy (MBE) are investigated. The layer sequence of a typical structure is summarized in table 2.1. For simulation purposes, the QWR will be regarded as a 25 nm thick QW layer, since the QWR width is much larger than the QWR thickness (as will be shown in sec. 5.3). Unless stated otherwise, the simulation results presented in the next section apply to the QWR. Along the vertical axis, $z = 0$ corresponds to the upper sample surface, while the

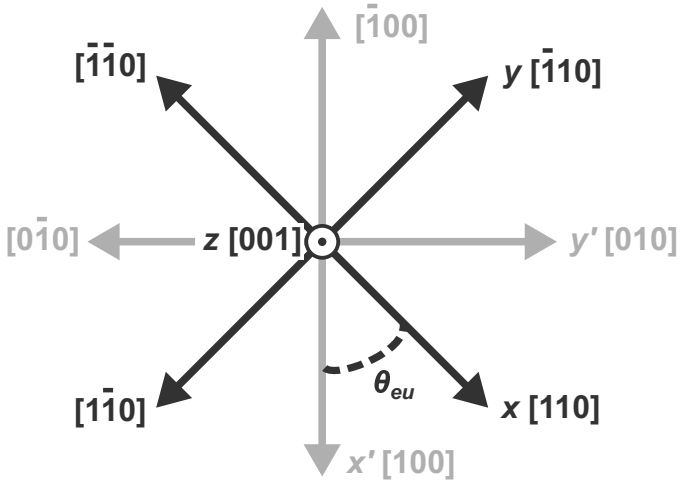

Figure 2.8: Overview of the crystal directions on the GaAs (001) surface. The bright grey reference frame depicts the crystallographic axes, while the dark grey axes construct the convenient reference frame for the studies in this thesis. The angle θ_{eu} denotes the Euler angle to transform the crystallographic axes into the convenient axes.

Layer	**Thickness (nm)**
GaAs caplayer	2
$Al_{0.15}Ga_{0.85}As$ barrier	200
GaAs quantum wire	*25*
$Al_{0.15}Ga_{0.85}As$ barrier	117
$Al_{0.15}Ga_{0.85}As$ smoothening layer	13
GaAs substrate	1

Table 2.1: A typical QWR structure grown by MBE on a GaAs (001) substrate as studied in this thesis. For computational reasons, the substrate is described by its upper interface with a thickness of 1 nm. In reality, the substrate thickness is 350 µm.

Material	$\mathbf{c_{11}}$ (N/m^2)	$\mathbf{c_{12}}$ (N/m^2)	$\mathbf{c_{44}}$ (N/m^2)	$\mathbf{e_{14}}$ (C/m^2)	ρ (kg/m^3)
GaAs	11.90×10^{10}	5.38×10^{10}	5.95×10^{10}	0.160	5318
AlAs	12.02×10^{10}	5.70×10^{10}	5.89×10^{10}	0.120	3760
$Al_{0.15}Ga_{0.85}As$	11.92×10^{10}	5.43×10^{10}	5.94×10^{10}	0.154	5084

Table 2.2: Overview of the room temperature parameters for tensor components and material densities used in the simulation of the SAW fields. The values for the elastic tensor components, as well as the densities, are taken from ref. [74]. The piezoelectric components are taken from ref. [85].

GaAs substrate corresponds to $z \to -\infty$. If not specified otherwise, the SAW wavelength is assumed to be 4 µm and the acoustic linear power density P_{SAW} to be 10 W/m. The value for P_{SAW} is within the order of magnitude as typically used in an experiment. The simulation method is as follows:

- Choose a value for the acoustic frequency, ω_{trial}. Considering that the SAW propagation direction is known and along x, an in-plane SAW wavector for the new axes can be defined taking into account eq. 2.23: $\mathbf{k_{SAW}} = (|k_{SAW}|, 0)$. This in-plane wavevector is conserved throughout the various layers.

- Having defined the acoustic wavevector and frequency, the solutions for the constitutive equations 2.13 are determined for each layer separately. These solutions correspond to the eigenvalues of the matrix $\mathcal{M}$ defined in eq. 2.17 and can be found by solving the equation $\det \mathcal{M} = 0$ (after appropriate Euler rotation). Connected to every eigenvalue is an acoustic mode, with a corresponding complex wavevector component along the z-axis given by k_z. The related solution for $\mathbf{u}$ can be combined with the piezoelectric potential in eigenvectors $\mathbf{u_{eig}}$ with four elements $\mathbf{u_{eig}} = (u_x, u_y, u_z, \phi_{\mathrm{SAW}})^T$.

- Subsequently, the eigenvectors $\mathbf{u_{eig}}$ are correlated to each other by imposing boundary conditions at the interfaces between the layers in the structure. The conditions are determined by considering that the z-components of the interface stress and piezoelectric displacement field should be continuous. The result is a description of $\mathbf{u_{eig}}$ corresponding to the surface layer in terms of the (known) parameters of the substrate.

- Finally, SAW modes are found by evaluating whether the solution corresponding to a certain value of ω_{trial} complies with the boundary conditions defined by eqs. 2.14 at the upper interface, as well as with a decaying SAW amplitude in the substrate (that is, for $z \to -\infty$, meaning that the real part of k_z must be positive. The value of ω_{trial} for such a solution corresponds to a SAW mode with angular frequency $\omega_{SAW} = \omega_{trial}$.

The first and the second rows of table 2.2 summarize the values for the components of the elastic stiffness tensor, piezoelectric tensor and material density used in the calculations. The values for $Al_{0.15}Ga_{0.85}As$ are obtained by interpolation of the values between GaAs and AlAs and are presented in the third row.

2.5.2 SAW propagation along the [110] direction

A SAW propagating along the [110] direction of the structure depicted in table 2.1 is a Rayleigh wave, for which the mechanical displacement and the piezoelectric potential are

derived in sec. 2.2.2. Figure 2.9(a) displays the simulated dispersion curve for this SAW mode. As expected from eq. 2.23, the dispersion curve can be fitted by a linear function. From this fit, a SAW velocity of $v_{\mathrm{SAW}} = 2918\,\mathrm{m/s}$ is extracted, which is consistent with values for v_{SAW} for similar QW structures as reported in literature [86].

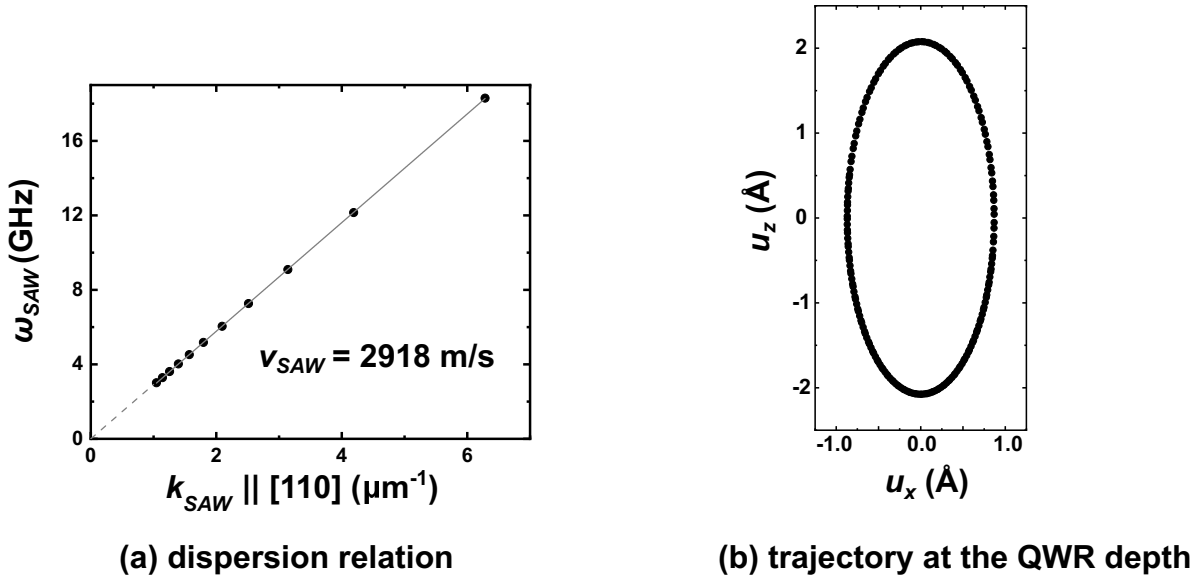

Figure 2.9: (a) Dispersion of the SAW angular frequency as function of SAW wavevector, for the structure described in table 2.1. A linear fit depicts that the SAW velocity is 2918 m/s. (b) Trajectory of a QWR atom in the (x, z)-plane. The scales of the axes are 1:1, emphasizing the elliptical trajectory of an atom in the SAW.

The simulated trajectory of an infinitesimal volume in the SAW is depicted in fig. 2.9(b). Here, the longitudinal (u_x) and transverse (u_z) mechanical displacements are shown as extracted at the QWR depth of z = -215 nm. The plot confirms that the movement is elliptical, with the long axis along the vertical axis and the short axis in the surface plane. The eccentricity of the ellipse, which varies with depth due to a complex k_z, is 0.87 at the QWR depth.

Figure 2.10(a) displays the simulated piezoelectric potential as function of depth in the sample. The decay of the piezoelectric potential is governed by the function $\mathcal{F}$ given by eq. 2.26. The green line marks the depth of the QWR. At the QWR depth, the piezoelectric potential energy is approximately 150 meV, which is much larger than the binding energy of the excitons in the QWR (which is typically below 10 meV [79]). Consequently, the photo-excited excitons are ionized into free electrons and holes and stored in the maxima and the minima of the SAW piezoelectric potential, respectively. The black curve in fig. 2.10(b) displays the piezoelectric potential at the QWR depth as function of position along the SAW path. The positions of the free electrons and holes are denoted by brown solid and open dots, respectively. Clearly, the simulation results confirm that the electrons and holes are spatially separated by half a SAW wavelength. Since this length corresponds to 2 µm, the overlap of the electron and hole wavefunctions is negligible. Consequently, for ideal acoustic charge transport, the corresponding carrier lifetimes should essentially be infinite.

The red curve in fig. 2.10(b) shows the simulated transverse piezoelectric field F_z along the SAW path, at the QWR depth. At the position of electron storage, F_z is oriented along the $-z$ direction. Since the force exerted on electrons by F_z is given by $-eF_z$, the electrons are squeezed against the interface between the QWR and the upper (Al,Ga)As barrier. At the position of hole storage, F_z is reversed. This means that the holes (carrying

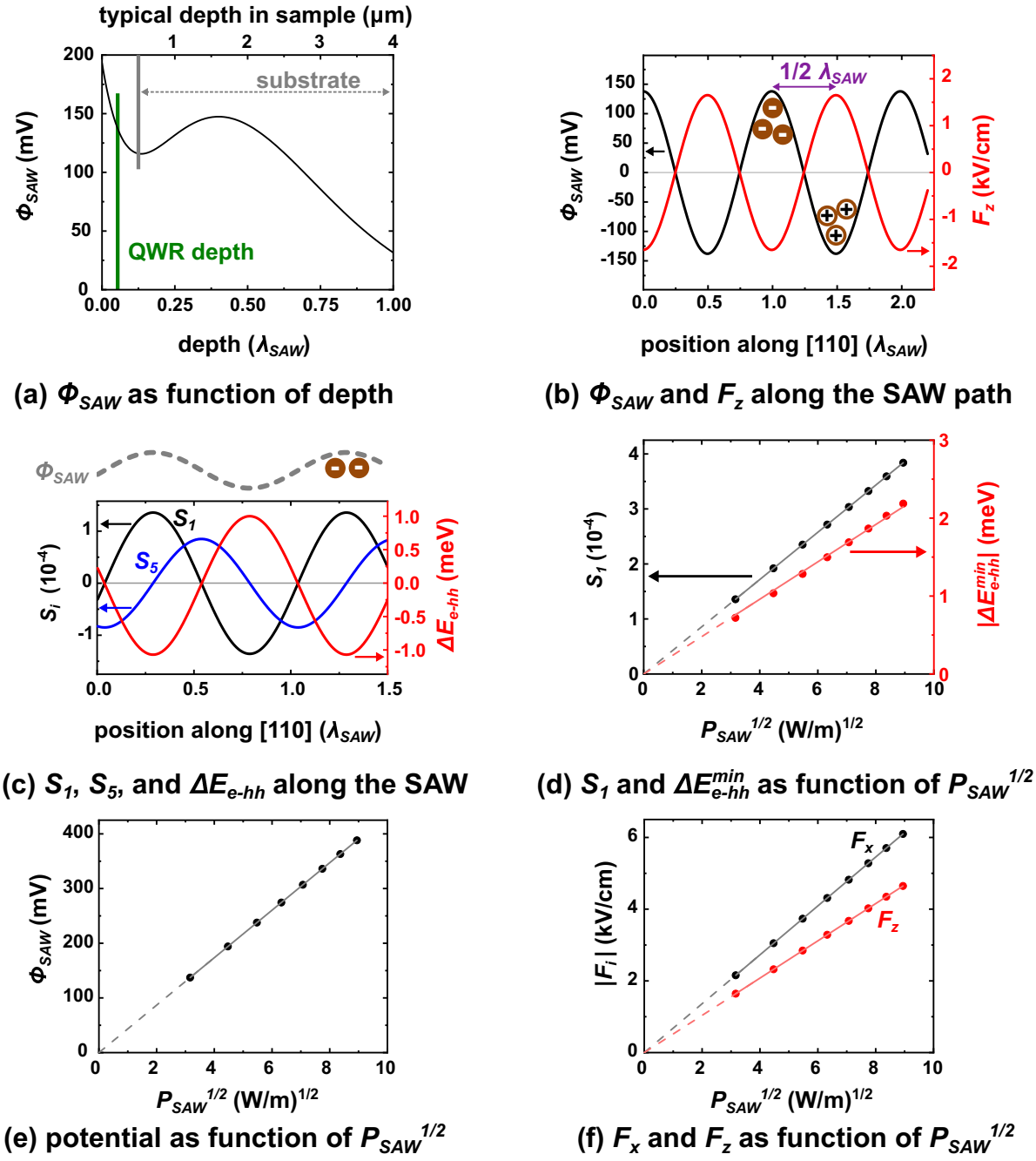

Figure 2.10: (a): Piezoelectric potential as function of depth. The green and grey lines mark the depths of the QWR and substrate, respectively. (b) Plot of the piezoelectric potential (black) and transverse piezoelectric field (red) along the SAW path, simulated at the QWR depth. The solid (open) brown dots indicate the positions of electrons (holes). (c) Plot of strain components S_1 (black) and S_5 (blue), and the corresponding modulation of the electron to heavy-hole transition energy (red) along the SAW path, at the QWR depth. The upper panel indicates the shape of the piezoelectric potential, conform fig. (b). (d) Dependency of strain component S_1 and the modulation of ΔE^{min}_{e-hh} on $\sqrt{P_{SAW}}$, at the QWR depth and at a SAW phase corresponding to electron storage. (e) Amplitude of the piezoelectric potential at the QWR depth as function of $\sqrt{P_{SAW}}$. (f) Dependency of the amplitudes of F_x (black) and F_z (red) on $\sqrt{P_{SAW}}$, at the QWR depth. The solid lines in figs. (d)-(f) depict linear fits of the simulation results.

positive charge) are squeezed against the same interface (note that the charge of holes is $+e$).

Figure 2.10(c) displays the strain components S_1 (black) and S_5 (blue), and the corresponding modulation of the electron to heavy-hole transition energy by the strain field (red) along the SAW path, at the QWR depth. The upper panel indicates the shape of the piezoelectric potential and the positions of electron storage. The figure shows that for electrons, $S_1 > 0$, $S_5 = 0$ and $\Delta E_{e-hh} < 0$. Thus, electrons are stored at positions of maximum tensile strain along the x axis, while the bandgap is reduced to its minimum value. The strain component S_1 contributes to the spin dynamics in the QWR and is, therefore, an important SAW property, as will be discussed in sec. 3.5. Furthermore, recombination at the SAW phase of electron storage leads to emission of a photon with energy $E^{min}_{e-hh} = E^0_{e-hh} - \Delta E^{min}_{e-hh}$, while recombination at the SAW phase of hole storage leads to emission of a photon with $E^{max}_{e-hh} = E^0_{e-hh} + \Delta E^{max}_{e-hh}$. This knowledge can be used to extract the SAW phase of recombination, if the splitting between E^{min}_{e-hh} and E^{max}_{e-hh} can be resolved in the experiment. For large acoustic power, ΔE^{min}_{e-hh} may differ from ΔE^{max}_{e-hh} due to the mixing of the heavy-hole and light-hole bands [87].

Equation 2.8 shows that the strain energy carried by the SAW depends quadratic on the strain field. Conversely, this means that the externally applied power (given by P_{SAW}) converted to strain energy should result in a strain amplitude which is proportional to the square root of P_{SAW}. Figure 2.10(d) shows the dependencies of S_1 and ΔE^{min}_{e-hh} on $\sqrt{P_{SAW}}$, simulated at the QWR depth. Indeed, the linearity of S_1 predicted by eq. 2.8 is clearly visible. Furthermore, eq. 2.31 shows that ΔE^{min}_{e-hh} is proportional to strain, and therefore, to $\sqrt{P_{SAW}}$. The following equations describe the evolution of the uniaxial strain S_1 and the transition energy E^{min}_{e-hh} with acoustic power density:

$$S_1 = r_{SP}\sqrt{P_{SAW}}, \tag{2.32}$$

$$E^{min}_{e-hh} = E^0_{e-hh} - \Delta E^{min}_{e-hh} = E^0_{e-hh} - r_{EP}\sqrt{P_{SAW}}. \tag{2.33}$$

From linear fits of the data presented in fig. 2.10(d), the values $r_{SP} = 4.3 \times 10^{-5}\,(\mathrm{m/W})^{1/2}$ and $r_{EP} = 0.24\,\mathrm{meV(m/W)}^{1/2}$ are extracted. Note that the band mixing of heavy-holes and light-holes at large acoustic power causes a slight deviation of the linearity between ΔE^{min}_{e-hh} and $\sqrt{P_{SAW}}$. Nevertheless, fig. 2.10(d) shows that the proportionality approximately holds up to $P_{SAW} = 80\,\mathrm{W/m}$, which is the maximum acoustic linear power density used in the experiments conducted for this thesis.

In fig. 2.10(e), the amplitude of the piezoelectric potential is shown as function of $\sqrt{P_{SAW}}$. The amplitudes of the resulting longitudinal and transverse piezoelectric fields are plotted in fig. 2.10(f) with black and red colours, respectively. The figures reveal a linear dependency of ϕ_{SAW}, F_x and F_z on $\sqrt{P_{SAW}}$:

$$\phi_{\mathrm{SAW}} = r_{PP}\sqrt{P_{SAW}}, \tag{2.34}$$

$$F_x = r_{FXP}\sqrt{P_{SAW}}, \tag{2.35}$$

$$F_z = r_{FZP}\sqrt{P_{SAW}}, \tag{2.36}$$

where the fits in figs. 2.10(e) and (f) depict that $r_{PP} = 43\,\mathrm{mV(m/W)}^{1/2}$, $r_{FXP} = 68\,\mathrm{kV/(mW)}^{1/2}$ and $r_{FZP} = 52\,\mathrm{kV/(mW)}^{1/2}$. As explained in sec. 2.3.1, the efficiency of acoustic transport can be evaluated by considering the condition of eq. 2.30, which, using eq. 2.35, can be expressed as conditions for the acoustic power density:

$$P_{SAW} \geq \left(\frac{v_{\mathrm{SAW}}}{\mu_e r_{FXP}} \right)^2, \tag{2.37a}$$

$$P_{SAW} \geq \left(\frac{v_{\mathrm{SAW}}}{\mu_h r_{FXP}} \right)^2. \tag{2.37b}$$

Typical low-temperature electron mobilities are of the order of $\mathrm{m}^2/(\mathrm{V\,s})$ [74]. Due to their larger effective mass, (heavy) hole mobilities are one order of magnitude smaller. Equation 2.37 depicts a minimum acoustic power density of the order of $10^{-3}\,\mathrm{W/m}$ and $10^{-1}\,\mathrm{W/m}$ for electrons and holes, respectively. Since typical acoustic power densities used in the experiments are between $1\,\mathrm{W/m}$ and $10^2\,\mathrm{W/m}$, the piezoelectric potential in the QW structures studied in this thesis is expected to be very efficient.

Note that the linearities of S_1 and F_z in figs. 2.10(d) and (f) imply that the transverse piezoelectric field can be expressed as function of the uniaxial strain component S_1:

$$F_z = r_{FZS} S_1, \tag{2.38}$$

where r_{FZS} = -1.2 $\times$ $10^9\,\mathrm{V/m}$. This will prove to be useful in the analysis of the experimental data on acoustic spin transport.

chapter 3

Spin dynamics in GaAs (001) quantum well structures

The concept of spin was introduced by Goudsmit and Uhlenbeck to explain the splitting of spectral lines of hydrogen [10]. The fact that this discovery was not only important from a fundamental point of view, but also from an application viewpoint is clear by the emergence of the field of spintronics [88]. For example, spin valve structures as introduced in chap. 1 are an important part of present-day memory devices. Another key concept introduced in chap. 1 is the Datta-Das spin transistor [16]. It is thus evident that understanding of spin dynamics is of utmost importance.

A key concept in understanding spin dynamics in semiconductors is the coupling of the spin with the orbital motion of the electron. The theory of spin-orbit coupling is introduced in sec. 3.2, after a brief overview of the electronic properties of semiconductors in sec. 3.1. The optical injection of a spin population relies on the conservation of angular momentum, which is the topic of sec. 3.3. The strong interaction between the spin and its environment causes spin relaxation through various mechanisms, which are the subject of sec. 3.4. Section 3.5 discusses how a surface acoustic wave affects the spin dynamics. Finally, sec. 3.6 gives a brief overview of the procedure to simulate the spin dynamics using Monte Carlo simulations and sec. 3.7 introduces how the interference between two SAWs results in the formation of dynamic quantum dots.

3.1 Electronic properties of quantum well structures

The theory provided in this section can be found in several books on quantum mechanics and semiconductor physics, such as those in refs. [89, 90, 91]. In the experiments of this thesis, a spin population is optically injected in a quantum well (QW) structure, as schematically drawn in fig. 3.1(a). The QW structure consists of a thin GaAs layer, sandwiched between two $Al_{0.15}Ga_{0.85}As$ barrier layers. For the structures studied in this thesis, the QW layer thickness d_{QW} is 10 nm. Due to the smaller bandgap of GaAs (1.519 eV) as compared to $Al_{0.15}Ga_{0.85}As$ (1.731 eV), the carrier motion in the GaAs layer is confined in the growth direction between $z = -d_{QW}/2$ and $z = +d_{QW}/2$. As indicated in the figure, the alignment of the GaAs and $Al_{0.15}Ga_{0.85}As$ bandgaps is such that it creates a potential barrier in the conduction band ($V_{0,CB}$) and valence band ($V_{0,VB}$) of 146 meV and 66 meV, respectively. In the experiments, a laser beam (bright red arrow) impinging along the growth axis excites electrons carrying a charge $-e$ (solid brown dot) from the valence band to the conduction band and creates holes carrying a charge $+e$ (open brown dot) in

the valence band. Here, e is the elementary charge. If the laser is circularly polarized, the optically injected carriers carry a well-defined spin, as will be pointed out in sec. 3.3.

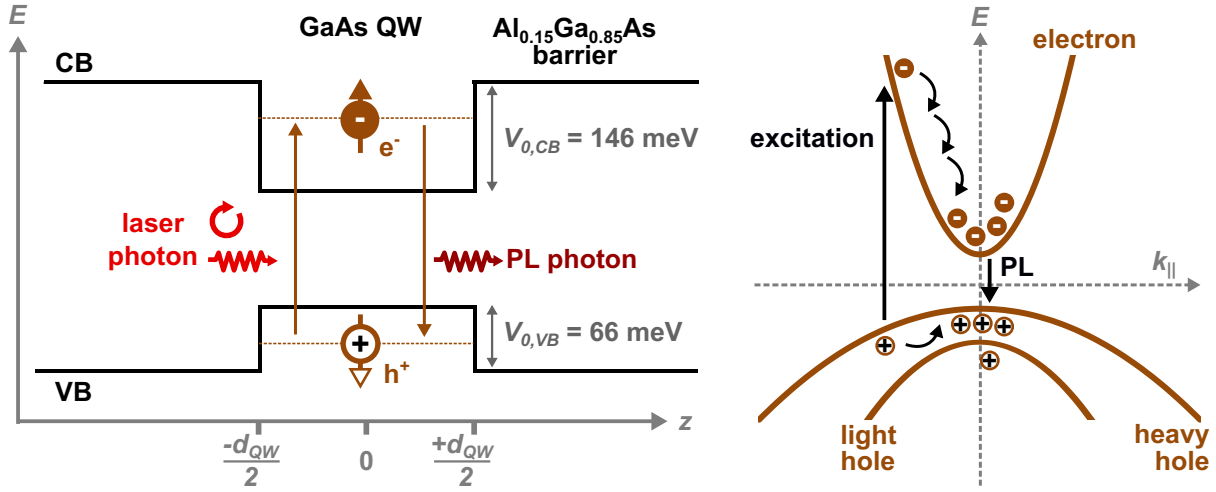

Figure 3.1: (a) Schematics of a quantum well geometry. A GaAs layer with a small bandgap is enclosed between two $Al_{0.15}Ga_{0.85}As$ layers with larger bandgap. $V_{0,CB}$ and $V_{0,VB}$ denote the potential barriers for the conduction and valence bands, respectively. In optical excitation, a photon (bright red arrow), which may be polarized, excites an electron (solid brown dot) in the valence band to the conduction band and leaves behind a hole (open brown dot) in the valence band. (b) Dispersion curves for the electron, heavy-hole and light-hole states in a symmetric quantum well. For off-resonant excitation (left black arrow), the electron and hole have an excess energy, relax towards a state with $\mathbf{k} = 0$, recombine and emit a photon (right black arrow).

In order to find the energy levels of electrons in the conduction band, first consider the dynamics of the electron travelling through bulk material, as described by the Schrödinger equation:

$$\mathcal{H}(\mathbf{r},t)\,\Psi(\mathbf{r},t) = i\hbar\frac{\partial\Psi(\mathbf{r},t)}{\partial t}, \tag{3.1}$$

where $\mathcal{H}(\mathbf{r},t)$ is the Hamiltonian, $\mathbf{r}$ the position of the electron, t the time coordinate, $\Psi(\mathbf{r},t)$ the electron wavefunction and $\hbar$ the reduced Planck's constant. In physical systems with inversion symmetry, the Hamiltonian is defined by its kinetic and potential energy:

$$\mathcal{H}(\mathbf{r},t) = \frac{p^2}{2m_e} + \phi_{crys}(\mathbf{r},t), \tag{3.2}$$

where m_e is the effective mass of the electron, p the momentum operator of the electron and ϕ_{crys} represents a potential describing the crystal. Solving the Schrödinger equation for a free electron in bulk material results in the following dispersion curve for the electron energy E_e versus electron wavevector $\mathbf{k} = (k_x, k_y, k_z)$:

$$E_e = \frac{\hbar^2|\mathbf{k}|^2}{2m_e}. \tag{3.3}$$

The spatial wavefunction ψ of a free electron is constructed from plane waves in all three dimensions:

$$\psi = Ae^{i\mathbf{k}\cdot\mathbf{r}} + Be^{-i\mathbf{k}\cdot\mathbf{r}}, \tag{3.4}$$

where A and B are arbitrary constants.

For the QW structure, the motion of the electron is confined along the growth axis z. The electron in a QW is, therefore, only free to move in the QW plane (which coincides with the (x, y)-plane). Consequently, the energy of the electron is quantized into multiple subbands, characterized by the quantum number n_z and $k_z = n_z\pi/d_{QW}$. In a typical QW, transitions between the states corresponding to $n_z = 1$ are dominant. In the remainder of this chapter, it is, therefore, assumed that $n_z = 1$. In an infinite QW ($V_{0,CB}, V_{0,VB} \to \infty$), the energy and wavefunction become:

$$E_e = \frac{\hbar^2\left[k_x^2 + k_y^2\right]}{2m_e} + \frac{\hbar^2\pi^2}{2m_e d_{QW}^2}. \tag{3.5a}$$

$$\psi = \sqrt{\frac{2}{d_{QW}}}\cos\left(\frac{\pi}{d_{QW}}z\right)e^{ik_y y}e^{ik_x x}. \tag{3.5b}$$

The first term of eq. 3.5a is associated with the free motion of the electron in the QW plane, with zero energy for $k_x, k_y = 0$. The second term is associated with the confinement of the electron along the growth axis and results in a quantum shift of its energy at $k_x, k_y = 0$. A further confinement of the electron into a 1D channel with axis along x, such as a quantum wire (QWR), results in $k_y = n_y\pi/w_{QWR}$, where w_{QWR} is the width of the QWR. Again, transitions corresponding to $n_y = 1$ are dominant and this condition is assumed in the following discussion. The lateral confinement leads to an additional quantum shift, so that the electron energy and wavefunction in the QWR are given by:

$$E_e = \frac{\hbar^2 k_x^2}{2m_e} + \frac{\hbar^2\pi^2}{2m_e}\left[\frac{1}{w_{QWR}^2} + \frac{1}{d_{QWR}^2}\right], \tag{3.6a}$$

$$\psi = \frac{2}{\sqrt{d_{QWR}\cdot w_{QWR}}}\cos\left(\frac{\pi}{d_{QWR}}z\right)\cos\left(\frac{\pi}{w_{QWR}}y\right)e^{ik_x x}. \tag{3.6b}$$

A 1D channel has electron energies as depicted by eq. 3.6a. However, as will be shown in sec. 5.3.2, a typical QWR fabricated for this thesis has a much larger width than its thickness. Therefore, the electronic behaviour in these QWRs can be approximated by the description of a QW.

In real structures, the determination of the energy levels is more complicated, because $V_{0,CB}$ is finite. In this case, high-energy states with $E_e > V_{0,CB}$ become unbound. Low-energy states with $E_e < V_{0,CB}$ are bound to the QW layer. The energy for these bound states can not be found analytically, but have to be determined by numerical methods. For the states symmetric with respect to the QW center (like $n_z = 1$), this can be done by finding solutions for the following equation [90]:

$$\tan(k') = \sqrt{\frac{k_0^2}{k'^2} - 1}, \tag{3.7a}$$

$$k' = \frac{|\mathbf{k}|\, d_{QW}}{2}, \tag{3.7b}$$

$$k_0 = \frac{m_e d_{QW}^2 V_{0,CB}}{2\hbar^2}. \tag{3.7c}$$

The solution of eq. 3.7a yields a value for $|\mathbf{k}|$, which is inserted in eq. 3.3 to find the electron energy in the finite potential well. Since the dispersions for the infinite and the finite QW have similar $|\mathbf{k}|$-dependencies near the band-edge, the remainder of this chapter assumes an infinite QW. However, whenever the discussions provided in the experimental

part of this thesis refer to the QW energy, that energy is calculated using the finite potential well model.

Equation 3.5a shows that the subbands are described by parabolas with an energy minimum at $\mathbf{k}_{||} = 0$. Here, $\mathbf{k}_{||}$ denotes the in-plane wavevector $\mathbf{k}_{||} = (k_x, k_y)$. These dispersion curves are symmetric in momentum space upon an spatial inversion operation: $E_e\left(+\mathbf{k}_{||}\right) = E_e\left(-\mathbf{k}_{||}\right)$. Since electrons are fermions, Pauli's exclusion principle states that every state with energy E_e can be occupied by at most two electrons which carry opposite spin angular momentum $\pm\hbar/2$. In the remainder of this thesis, an electron carrying spin angular momentum characterized by the quantum spin number $s = +1/2$ will be called a spin-up electron, denoted by the spin state $|\uparrow\rangle$. An electron carrying the quantum spin number $s = -1/2$ will be called a spin-down electron, denoted by the spin state $|\downarrow\rangle$. The subbands of the QW described by eq. 3.5a are also symmetric under a time-inversion operation and, therefore, two-fold degenerate in the spin quantum number (Kramer's theorem [92]). In systems with momentum and time inversion symmetries, $E_\uparrow\left(+\mathbf{k}_{||}\right) = E_\downarrow\left(-\mathbf{k}_{||}\right)$.

The discussion above did not include orbital momentum characterized by the quantum number L. For the s-like orbitals of the conduction band, $L = 0$. In the valence band, the orbital momentum is characterized by $L = 1$ and the $n_z = 1$ subband splits into two bands with azimuthal quantum numbers $l = 0$ and $l = 1$, respectively. The band exhibiting $l = 1$ is further split into two bands described by the heavy-hole and the light-hole. The energies of the heavy- and light-holes E_h can be described in a similar way as those for the electron by substituting m_e with either the effective mass for the heavy-hole m_{hh} or the light-hole $m_{lh} < m_{hh}$. In bulk material without spin-orbit coupling, the bands in the valence band are six-fold degenerate for $\mathbf{k}_{||} = 0$. The confinement of the QW lifts the degeneracy of the heavy- and light-hole, with the light-hole shifted deeper into the valence band, as can be seen by considering its smaller mass in eq. 3.5a. In a semiconductor without spin-orbit coupling, all electronic bands are occupied by two carriers carrying opposite spins.

The most relevant bands in a typical quantum well structure are illustrated in fig. 3.1(b). Here, the dispersion curves of the electron, heavy-hole and light-hole are schematically drawn as function of $k_{||} = |\mathbf{k}_{||}|$. The effective masses of the bands can be calculated from the band curvature. The left black arrow indicates a transition for off-resonant excitation. Since the momentum of the photon is much smaller than the momentum of the charge carriers, conservation of energy and momentum dictates that the transition is approximately vertical, i.e. the transition is between electronic states carrying roughly the same momenta.

For off-resonant excitation, the electron and the hole are initially unbound. As a result, they can be considered to be free particles, meaning that their movements is not correlated to each other. However, after excitation, the electron and the hole may quickly bind into a neutral quasi-particle called the exciton, mediated by the Coloumb interaction. In this case, the energy of the exciton is lowered by an amount equal to the binding energy E_{bind}, which is in the range 5 meV to 10 meV for the QW structures studied in this thesis [79]. When the thermal energy of the physical system is larger than this binding energy, it may break the exciton into free electrons and free holes (exciton ionization). For the systems studied in this thesis, the corresponding temperature to ionize the exciton is approx. 60 K-120 K. Therefore, photoluminescence studies in this thesis are performed below these temperatures. Under the condition of off-resonant excitation, the laser energy is larger than the transition energy associated with $\mathbf{k}_{||} = 0$. As a result, the electron in the conduction band and the hole in the valence band both carry a non-zero in-plane momentum. In undoped samples, the PL originates from states within the vicinity of $\mathbf{k}_{||} = 0$. Generally, relaxation of high-momentum states towards the state with $\mathbf{k}_{||} = 0$ is

much faster than recombination of the electron-hole pair [26]. Thus, the electron in the conduction band relaxes towards a lower energy, while the hole relaxes upwards in the valence band. Once the momentum of the exciton approaches zero, the pair decays upon emission of a photon with an energy of:

$$E_{PL} = E_g + E_e + E_h - E_{bind}, \tag{3.8}$$

where E_{PL} is the energy of the emitted photon and E_g the bandgap energy. The emission resulting from the process of optical carrier excitation, relaxation and recombination is called photoluminescence (PL).

3.2 Spin-orbit coupling

In the reference frame of the electron, its motion around the nucleus translates into an effective magnetic field $\mathbf{B_{SO}}$ due to the transformation of the electric field of the nucleus $\mathbf{F} = -\nabla\phi_{crys}$ [93]:

$$\mathbf{B_{SO}} = -\frac{\nabla\phi_{crys} \times \mathbf{v_e}}{c^2}, \tag{3.9}$$

where $\mathbf{v_e}$ is the electron velocity, c the speed of light and it is assumed that $|\mathbf{v_e}| \ll c$. Since the electron's magnetic moment is determined by its spin, the magnetic field as described by eq. 3.9 acts on the electron-spin, thereby coupling the electron motion to the electron-spin. Hence, the interaction is termed spin-orbit (SO) coupling. The strength of the potential ϕ_{crys} is determined by the charge of the nucleus and thus increases with atomic number. Accordingly, the spin-orbit coupling increases its strength with increasing atomic number.

The SO coupling enters the Schrödinger equation through its associated energy ΔE_{SO}. The complete Hamiltonian becomes [94]:

$$\mathcal{H}(\mathbf{r}, t) = \frac{p^2}{2m_e} + \phi_{crys}(\mathbf{r}, t) - \frac{\hbar^2}{4m_e^2c^2}\sigma \cdot [\mathbf{k} \times \nabla\phi_{crys}(\mathbf{r}, t)], \tag{3.10}$$

where σ denote the Pauli spin matrices. Due to the spin-orbit coupling, the orbital (characterized by L) and spin (characterized by S) angular momenta are no longer conserved separately, but only the total angular momentum, given by $J = L + S$. Since $L = 0$ in the conduction band, J is solely determined by the electron spin. However, in the valence band $L \neq 0$ and the orbital angular momentum affects J. In semiconductors with inversion symmetry, the effect of the SO term in the Schrödinger equation is to induce an energy separation between the valence bands carrying $J = 1/2$ (split-off band, not included in fig. 3.1(b)) and $J = 3/2$ (heavy- and light- holes). The energy splitting is equal to the spin-orbit energy Δ_{SO}, which is approx. 340 meV in GaAs [74]. For inversion symmetric semiconductors, the electronic bands are degenerate in spin: $E_\uparrow = E_\downarrow$. This spin degeneracy is lifted in all electronic bands of a semiconductor with spatial inversion asymmetry and, consequently, $E_\uparrow \neq E_\downarrow$ for $\mathbf{k}_{||} \neq 0$, as schematically drawn in fig. 3.2 for the conduction band. As this figure shows, the energy difference ΔE_{SO} between a $|\uparrow\rangle$ electron and a $|\downarrow\rangle$ electron with equal momenta changes with momentum. The precise form of the momentum-dependency depends on the type of inversion asymmetry and will be discussed in sec. 3.4.3.

There are three types of inversion asymmetries. Firstly, bulk inversion asymmetry (BIA) is the intrinsic asymmetry related to the crystal structure of the semiconductor. In a zinc-blende semiconductor like GaAs, BIA arises due to the presence of two distinct

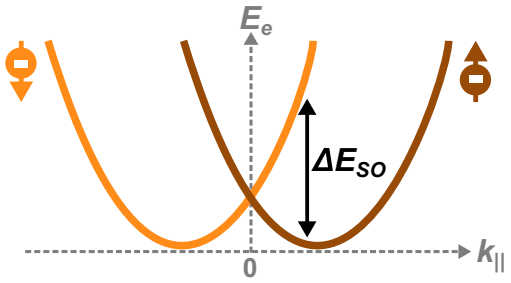

Figure 3.2: Spin-orbit splitting of the conduction band. The orange and brown curves show the dispersion curves for $|\downarrow\rangle$ and $|\uparrow\rangle$ electrons, respectively.

atoms within the lattice unit cell. Due to the biatomic unit cell, the crystal potential felt by electrons depends on the crystallographic direction and is, therefore, asymmetric. The spin-splitting energy of the conduction band resulting from BIA in zinc-blende crystals was theoretically studied by Dresselhaus [18].

Secondly, for specific sample geometries structural inversion asymmetry (SIA) exists due to an asymmetric potential. This asymmetry arises, for example, when an external electric field is applied across the structure. In the experiments throughout this thesis, the transverse piezoelectric field accompanying the SAW (see sec. 2.3.1) causes a contribution to SIA. The spin-splitting energy due to SIA in 2D systems was studied by Bychkov and Rashba [95].

Finally, if the interfaces of the QW layer with the barriers are asymmetric, additional contributions to asymmetry may arise (natural interface asymmetry, NIA) [96]. These terms can result from fabrication inhomogeneities or interfaces without common atoms. NIA can partially be cancelled by compensating the two opposite interfaces of a QW layer. In this thesis, the QW-barrier interfaces are expected to be symmetric due to the low Al content and NIA will therefore be neglected.

The spin-splitting energies arising from the different types of asymmetry can be regarded as an internal magnetic field, for which the magnitude B_{SO} is given by $\Delta E_{SO} \sim \mu_0 B_{SO}$, where ΔE_{SO} is the spin-splitting energy and μ_0 Bohr's magneton. As will be discussed in sec. 3.4.3, this magnetic field can lead to spin relaxation. Additionally, mixing of spin states due to the additional SO term in the Hamiltonian leads to another spin relaxation mechanism, as will be discussed in sec. 3.4.2. Spin relaxation is detrimental for the application of electron-spin in a spin transistor. Before addressing the different spin relaxation mechanisms, the next section describes optical orientation, the process by which a spin population is optically injected in a semiconductor.

3.3 Optical selection rules

A spin population can be optically injected by circularly polarized light due to the conservation of momentum [97]. Note that the electric field of the light only directly acts on the electron orbital motion, so that spin-orbit coupling is a crucial ingredient in the process of optical spin injection.

As discussed above, the inclusion of angular momentum has profound effects on the physics of the semiconductor system. In the conduction band, the orbital angular momentum $L = 0$ and the total angular momentum $J = L + S$ is determined only by the spin part S. Thus, the projections of J on the quantization axis z are given by $j_z = -1/2$ and $j_z = +1/2$. In the valence band, the orbital angular momentum is given by $L = 1$. The heavy-hole and light-hole bands carry an orbital angular momentum characterized

by $l = 1$. The heavy-hole band has a projection of $l_z = 1$, resulting in $j_z = \pm 3/2$. The light-hole has a projection of $l_z = 0$: $j_z = \pm 1/2$. Since in the experiments for this thesis the excitation energy is too small to excite the split-off band, the discussion here does not consider the split-off band.

Absorption of light is subjected to the law of momentum conservation. Right-hand circularly polarized (RHCP) light carries a momentum of $-\hbar$ and is denoted by σ^-, whereas left-hand circularly polarized (LHCP) light carries a momentum of $+\hbar$ and is denoted by σ^+. Conservation of momentum dictates, therefore, that the electronic transition is only allowed if $\Delta j_z = -1$ for RHCP light or if $\Delta j_z = +1$ for LHCP light. This is the basis for the optical selection rules, as illustrated in fig. 3.3. In the figure, the energy levels for the electron, heavy-hole and light-hole are indicated. The momentum of the states is denoted by j_z for the hole states, while it is indicated by spin s for the electron, since for the latter $j_z = s$. For clarity reasons, the split-off band is not shown in fig. 3.3. The bright red arrows represent excitation with σ^- light, while the dark red arrows represent excitation with σ^+ light. As the arrows show, excitation of the heavy-hole and light-hole with equal polarization result in opposite spin orientation of the electron in the conduction band. For example, heavy-hole or light-hole excitation with σ^- results in excitation of a $|\uparrow\rangle$ of $|\downarrow\rangle$ electron, respectively. A calculation of the transition elements using Fermi's golden rule depicts the transition probabilities T as denoted in the figure [98]. Based on the transition probabilities, the expected spin polarization can be calculated. The spin polarization ρ_z is defined as the net electron-spin, normalized to the total number of electrons.

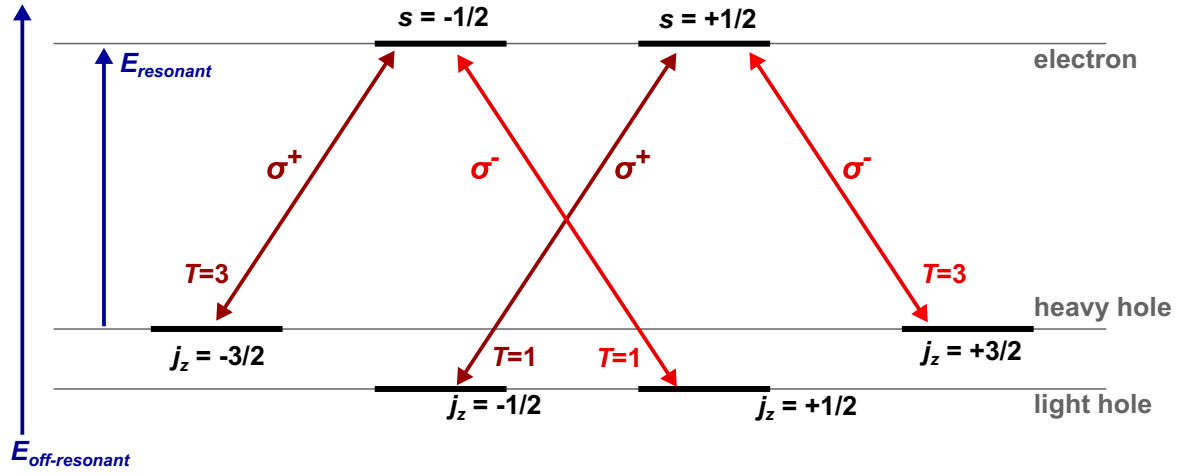

Figure 3.3: Optical selection rules in a semiconductor. Illustrated are the energy levels of an electron, heavy-hole and light-hole in a quantum well structure, with associated total angular momentum characterized by j_z (holes) or s (electrons). The left blue arrows show optical excitation. The bright red arrows depict the possible transitions for RHCP light, while the dark red arrows depict the possible transitions for LHCP light. T represents the transition probabilities with respect to the light-hole, for which $T = 1$.

A full spin polarization may be induced by exciting the QW structure using light with a specific circular polarization and energy $E_{resonant}$, resonant with the heavy-hole exciton transition. However, in a typical experiment the excitation energy is tuned to $E_{off-resonant}$. Under this condition, heavy-hole and light-hole excitations take place with relative transition probabilities 3:1. The spin polarization of the conduction band electrons is thus 50 %. The transition probabilities for recombination are the same as those for excitation. In this way, if the initial spin polarization of 50 % is preserved, one expects the polarization of the photoluminescence to be 25 %. In real physical systems however, several spin relaxation mechanisms cause the initial spin population to decay. Additionally,

any magnetic field (internal or external) cause the spins to precess. Both effects mean that after some time interval the spin is not in a pure $|\uparrow\rangle$ or $|\downarrow\rangle$ state, but in a linear combination of these two states. The spin polarization ρ_z can be expressed by the following equation:

$$\rho_z = \frac{I_R - I_L}{I_R + I_L}, \tag{3.11}$$

where I_L and I_R represent LHCP PL and RHCP PL, respectively. The optical orientation process turns out to be a powerful tool for both the injection and probing of a spin population in a semiconductor. Note that from the definition of eq. 3.11, ρ_z in fact describes the degree of PL polarization, which is related to the component of the spin along the z-axis. However, for convenience, it will be regarded as being the spin polarization.

3.4 Spin relaxation processes

As discussed in the previous section, a spin population is optically injected in the QW structure via the optical selection rules. Generally, the spins are not very well isolated from the environment and interact strongly with the system in which they are contained. On one hand, this opens up a convenient way of manipulating the spin state, while on the other hand it induces effective ways of spin relaxation. One important spin relaxation mechanism originates from interaction of the electrons with holes and is described in sec. 3.4.1. Spin-orbit coupling has a detrimental effect on the spin polarization and generally results in two main types of spin relaxation: on one hand, Elliott-Yafet spin relaxation is very effective under fast momentum relaxation, while on the other hand, Dyakonov-Perel spin relaxation is very effective under slow momentum relaxation.

A fourth source of spin relaxation is the hyperfine interaction of electron spins with the nuclear spins of the hosting material, as first described by Overhauser for transition metals [99]. For delocalized electrons as studied in the current thesis, the large number of nuclei the electrons interact with results in a very long spin lifetime as compared to the other mechanisms [100, 36, 101]. The hyperfine interaction will, therefore, not be considered here.

3.4.1 Exchange interaction

The wavefunction $\psi^s_{\mathbf{k}}$ of an electron with momentum $\mathbf{k}$ and spin state s can be expressed as the product of its electronic state $|\psi_{\mathbf{k}}\rangle$ and spin state ($|\uparrow\rangle$ or $|\downarrow\rangle$). Electrons are indistinguishable fermions, so that the total wavefunction describing a system with multiple electrons is required to be antisymmetric with respect to an exchange of the electrons. The spin state can be either in the symmetric singlet or in the antisymmetric triplet state. The symmetry of the electronic state depends, therefore, on the spin state of the system. Conversely, for a given symmetry of the electronic state, the required spin state symmetry depends on the electronic state. As discussed in sec. 3.1, optical injection of carriers involves both the creation of an electron in the conduction band (CB) and a hole in the valence band (VB). Considering that the hole describes a quasi-particle of the missing electron in the VB, exchange interaction between the CB electron and the remaining electrons in the VB may be described by the interaction between the CB electron and the VB hole. Due to the requirement of antisymmetry, a change of the electronic state symmetry leads to a change of the spin state. A change of the electronic state symmetry may result from scattering.

As discussed in sec. 3.1, the excited electron-hole pair may be either unbound as free particles or bound into an exciton. Bir, Aronov and Pikus [28] studied the spin relaxation of electron-spins due to the exchange interaction with free holes (BAP spin relaxation). Such a situation is the case for unbound electron-hole pairs or for p-doped semiconductors. The Hamiltonian for the exchange interaction $\mathcal{H}_{ex}$ is expressed in terms of the exchange parameter A_{exch} (characterizing the electron-hole exchange coupling strength) and the volume of the crystal V_{crys} [102]:

$$\mathcal{H}_{ex} = A_{exch} V_{crys} \quad \mathbf{J_h} \cdot \mathbf{S_e}, \tag{3.12}$$

where $\mathbf{J_h}$ represents the angular momentum of the hole and $\mathbf{S_e}$ the angular momentum of the electron. A spin-flip scattering event of an electron-spin with a hole corresponds to a transition between two states of the electron, where the initial state is characterized by spin $\mathbf{S_e}$ and the final state by spin $\mathbf{S'_e}$. Intuitively, the probability of a spin-flip transition increases with hole density and decreases with the Bohr radius a_0 (which defines the spatial extent of the exciton), since the former leads to stronger electron-hole interaction and the latter leads to a weaker electron-hole interaction. In fact, the spin relaxation rate Γ_s is proportional to the hole density N_p and inversely proportional to a_0^3: $\Gamma_s \propto a_0^{-3} N_p$ [97]. In systems like a QW where the electrons and holes are confined, the exchange interaction is enhanced because there is a larger overlap of the electron and hole wavefunctions as compared to bulk material. Consequently, one can expect faster spin relaxation in confined systems.

If the confinement dimensions are comparable to a_0, the electron-hole pairs bind together into excitons rather than forming unbound electron-hole pairs. In this case, the electron-spin can not be separated from the hole-spin and the description should rather involve the total angular momentum of the bound exciton. The spin dynamics changes in this case and belongs to the motional narrowing regime, where more frequent scattering leads to a slow down of the spin relaxation, which is a contrast to the BAP mechanism. In the exciton system, the exchange interaction leads to an internal magnetic field $\mathbf{B_{ex}}$ [27]. The exciton-spins rotate in this field, which depends on the exciton momentum. Different exciton trajectories lead, therefore, to spin relaxation of the excitonic spin vector. This process is similar to spin relaxation due to the Dyakonov-Perel mechanism, which will be discussed in more detail in sec. 3.4.3.

If temperature rises, a transition from exciton spin relaxation to the BAP mechanism can be observed, since the increasing thermal energy ionizes a considerable amount of the excitons into unbound electron-hole pairs. In the latter regime, one may consider the holes to be unpolarized, because the relaxation times for hole-spins in both bulk material and confined systems are several orders of magnitude smaller than the corresponding relaxation time for electron-spins [103, 104].

3.4.2 Elliott-Yafet spin relaxation

Besides the scattering of electrons by holes, electrons may scatter with phonons, defects and impurities in a crystal. Reflection of the electron at the boundaries of a channel may be regarded as a scattering event as well. Consider an electron in the state $|\psi^{s_1}_{\mathbf{k_1}}\rangle$ with momentum $\mathbf{k_1}$ and spin s_1. The transition rate Γ from this state to a state with momentum $\mathbf{k_2}$ and spin s_2, due to a scattering event represented by the Hamiltonian operator $\hat{\mathcal{H}}_{sc}$, can be calculated using Fermi's golden rule [105]:

$$\Gamma = \frac{2\pi}{\hbar} \left| \langle \psi^{s_2}_{\mathbf{k_2}} | \, \hat{\mathcal{H}}_{sc} \, | \psi^{s_1}_{\mathbf{k_1}} \rangle \right|^2 D(E_e), \tag{3.13}$$

where $D(E_e)$ is the density of states at electron energy E_e. In crystals without spin-orbit coupling, the electron can be in a pure spin state $|\uparrow\rangle$ or $|\downarrow\rangle$. The probability of a spin flip due to a spin-independent scattering event is given by eq. 3.13 by replacing $\mathcal{H}_{sc}$ with the Identity operation $\hat{\mathcal{I}}$, $\psi^{s1}_{\mathbf{k_1}} = |\uparrow\rangle$ and $\psi^{s2}_{\mathbf{k_2}} = |\downarrow\rangle$. The identity operator leaves the state upon which it acts unaffected. The spin-flip probability is given by the mutual product of the spin states, which vanishes without spin-orbit coupling due to the orthogonality of $|\uparrow\rangle$ and $|\downarrow\rangle$.

The additional term in the Hamiltonian due to spin-orbit coupling (see eq. 3.10) leads to mixing of the spin states in the electron wave function [69, 106]. Under this condition, the electron wavefunctions contain components of both the $|\uparrow\rangle$ and $|\downarrow\rangle$ spin states. Elliott described the wavefunctions of a 'spin-up' state $\psi^{\uparrow}_{\mathbf{k}}$ and 'spin-down' state $\psi^{\downarrow}_{\mathbf{k}}$ in symmetric crystals with spin-orbit coupling taking into account the mixing [69]:

$$\psi^{\uparrow}_{\mathbf{k}} = \left[a_{\mathbf{k}} |\uparrow\rangle + b_{\mathbf{k}} |\downarrow\rangle\right] e^{i\mathbf{k}\cdot\mathbf{r}} \tag{3.14a}$$

$$\psi^{\downarrow}_{\mathbf{k}} = \left[a^*_{-\mathbf{k}} |\downarrow\rangle - b^*_{-\mathbf{k}} |\uparrow\rangle\right] e^{i\mathbf{k}\cdot\mathbf{r}}, \tag{3.14b}$$

where $a_{\mathbf{k}}$ and $b_{\mathbf{k}}$ represent the amplitudes of the spin components in the wavefunction associated with the state $\psi_{\mathbf{k}}$. In general, spin mixing due to spin-orbit coupling is only small and $a_{\mathbf{k}} \gg b_{\mathbf{k}}$. Nevertheless, the spin parts of $\psi^{s1}_{\mathbf{k_1}}$ and $\psi^{s2}_{\mathbf{k_2}}$ are now not exactly orthogonal because they are described by eqs. 3.14: both contain components of the spin-up and spin-down states. As a consequence, the matrix element in eq. 3.13 associated with the spin state is no longer determined by orthogonal states and is non-vanishing. As a result of the spin mixing, there is a finite probability that the electron-spin is flipped upon momentum scattering. Since $a_{\mathbf{k}} \gg b_{\mathbf{k}}$, this spin-flip probability is generally small. The ratio between a spin-conserving and spin-changing scattering event is a crucial parameter to calculate the spin lifetime in an Elliott-Yafet (EY) spin relaxation dominated condition.

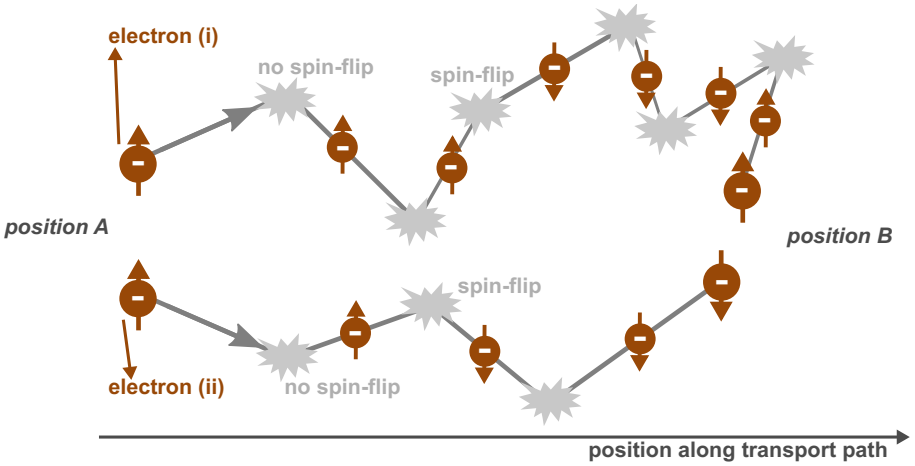

Figure 3.4: Illustration of Elliott-Yafet spin relaxation. Two electrons (i) and (ii) (brown dots) are traversing different trajectories, while their overall motion is between positions A and B. On each momentum scattering event (grey stars), the electron may flip its spin with a finite probability.

An intuitive picture of the EY spin relaxation mechanism is shown in fig. 3.4. Here, two electrons (brown dots) move along different trajectories from a position A to a position B. Electron (i) suffers many scattering events and has, therefore, a large probability of multiple spin flips along its path. In the illustrated situation, there are two scattering events which flip the spin. The spin states for electron (i) at positions A and B are therefore equal. In contrast, another electron (ii) might follow a different trajectory, with

different numbers of scattering events. Note that if the nature of the scattering event is different, the probability of a spin-flip also changes. In the figure, electron (ii) has opposite spin at position B with respect to its start position A. One can easily see that the total spin polarization of the two electrons at position B is lost over the distance A-B. For a larger electron ensemble, this can be quantified by a characteristic spin lifetime τ_S [107]:

$$\frac{1}{\tau_S} = A_{sc}\left[\frac{\Delta_{SO}}{E_g + \Delta_{SO}}\right]^2 \left[\frac{E_e}{E_g}\right]^2 \frac{1}{\tau_p}, \tag{3.15}$$

where $A_{sc} \approx 1$ is a factor depending on the nature of the scattering events and τ_p the momentum relaxation time. The spin polarization of an ensemble of electrons is described by an exponential decay with the characteristic spin lifetime τ_S. Equation 3.15 shows that Elliott-Yafet spin relaxation is mostly important for small-gap semiconductors with a large spin-orbit splitting. GaAs is considered to be a small-gap semiconductor with $E_g \approx 1.519\,\text{eV}$ and $\Delta_{SO} \approx 340\,\text{meV}$. The equation furthermore reveals an important characteristic of the EY spin relaxation mechanism: spin relaxation increases effectively with momentum scattering rate. This is in contrast to spin relaxation due to the Dyakonov-Perel mechanism, which is the subject of the next section.

3.4.3 Dyakonov-Perel spin relaxation

EY spin relaxation considers a process which occurs instantaneously during a scattering event. The spin splitting of the conduction band additionally leads to an internal spin-orbit field, which acts on the electron-spin between scattering events and depends on the electron momentum. An intuitive figure of this principle presented in fig. 3.5 reveals that the SO field leads to a decay of the spin associated to an electron ensemble: Dyakonov-Perel (DP) spin relaxation [29]. In the figure, two electrons are shown following the same trajectories as sketched in fig. 3.4. The SO field $\mathbf{B_{SO}}$ is assumed to be oriented perpendicular to the motion path of the electron. Between scattering events, the electron-spin precesses in the spin-orbit field. A scattering event changes the direction of the electron momentum and the precession axis of the spin due to the momentum-dependency of $\mathbf{B_{SO}}$. After multiple scattering events, the spin acquires a certain phase, which is related to the magnitude and orientation of the SO field, and to the number of momentum scatterings. A different trajectory, as traversed by electron (ii), may have a different number of scatterings, which also change the precession axis in a different fashion. As a result, the spin phases acquired by electrons (i) and (ii) at some position B are different. This leads to decay of the spin polarization of electrons travelling between locations over distinct trajectories.

It was shown by Dresselhaus that in bulk material, the spin splitting of the conduction band due to BIA is of cubic order in the electron momentum $\mathbf{p} = \hbar\mathbf{k}$ [18]. The spin splitting of the conduction band can be associated with a momentum-dependent internal magnetic field $\mathbf{B_{SO}}$, which substitutes the term related to spin-orbit coupling in the Hamiltonian (eq. 3.10) by the following term:

$$-\frac{\hbar}{4m_e^2c^2}\sigma\left(\nabla\phi\left(\mathbf{r}', t\right) \times \mathbf{p}'\right) = \frac{g\mu_B}{2}\left(\sigma \cdot \mathbf{B_{SO}}\right). \tag{3.16}$$

The momentum dependency of the spin-orbit field associated to the Dresselhaus term for electrons travelling in bulk materials is described by [29]:

$$\mathbf{B_D} = \frac{\gamma}{g\mu_B}\begin{bmatrix} k_{x'}\left[k_{y'}^2 - k_z^2\right] \\ k_{y'}\left[k_z^2 - k_{x'}^2\right] \\ k_z\left[k_{x'}^2 - k_{y'}^2\right] \end{bmatrix}, \tag{3.17}$$

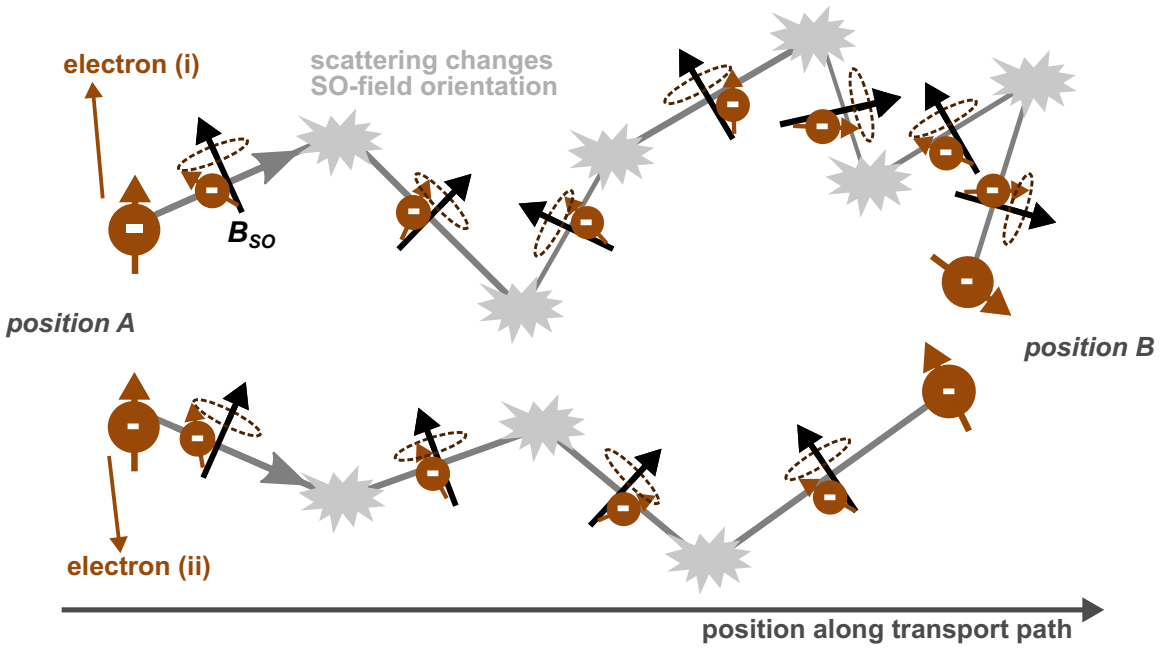

Figure 3.5: Illustration of Dyakonov-Perel spin relaxation. Two electrons (i) and (ii) (brown dots) are traversing different trajectories, while their overall motion is between positions A and B. On each momentum scattering event (grey stars), the momentum of the electron is changed. Consequently, the spin precession axis associated with the spin-orbit field changes. The electrons acquire different spin phases when arriving at position B. This leads to spin relaxation.

where the components $k_{i'}$ represent the wavevector components along the crystallographic axes $x'||[100]$, $y'||[010]$ and $z||[001]$, and γ is a parameter quantifying the Dresselhaus spin-splitting energy. In GaAs, *Stotz et al.* reported a value of $\gamma = 17 \pm 2 \times 10^{-30}\,\mathrm{eV\,m^3}$ [108]. The dot product of $\mathbf{B_D}$ and $\mathbf{k'}$ vanishes, depicting that the Dresselhaus field for electron motion in bulk materials is always perpendicular to the propagation direction of the electron. The spin precession is characterized by a Larmor vector $\mathbf{\Omega_{SO}}$:

$$\mathbf{\Omega_{SO}} = \frac{g\mu_B}{\hbar}\mathbf{B_{SO}}. \tag{3.18}$$

The precession axis coincides with the direction of this vector, while the angular precession frequency Ω_{SO} corresponds to $|\mathbf{\Omega_{SO}}|$. The spin-orbit length L_{SO}, defined as the travel distance for a rotation of 2π is given by:

$$L_{SO} = \frac{2\pi v_e}{\Omega_{SO}}. \tag{3.19}$$

The timescale associated with DP spin relaxation can be quantified by considering the spin rotation angle $\theta_S = \Omega_{SO}\tau_p$ between two scattering events [29]. Based on the value of θ_S, two regimes of spin relaxation can be distinguished. In the first regime, either the electron energies are large, leading to high precession frequencies, or momentum relaxation is slow, leading to a long momentum scattering time τ_p. In this regime $\theta_S \gg 1$ and the spin orientation is quickly lost. In the opposite regime of small energy or fast momentum relaxation, $\theta_S \ll 1$ and the spin rotation angle between two scattering events is small. In this case, spin relaxation will be considerably retarded. The spin dynamics of the QW structures studied throughout this thesis is in the latter regime of retarded spin relaxation. One can estimate the spin lifetime for this regime in the following way. After a time t the electron experienced t/τ_p scattering events. The average of the squared spin rotation angle

will be $\langle\theta_S^2\rangle = (\Omega_{SO}\tau_p)^2\, t/\tau_p$. Considering a definition of the spin lifetime τ_S derived from the condition $\langle\theta_S^2\rangle = 1$, it follows that τ_S is inversely proportional to τ_p. The constant of proportionality is determined by Ω_{SO}:

$$\frac{1}{\tau_S} = A_{sc}\,\langle\Omega_{SO}^2\rangle\,\tau_p, \tag{3.20}$$

where A_{sc} is again a constant characterizing the nature of the scattering event. This equation reveals the counterintuitive fact that momentum relaxation efficiently suppresses DP spin relaxation, in contrast to Elliott-Yafet spin relaxation. Hence, in high-quality samples (e.g. without impurities), DP spin relaxation is very effective, while for samples exhibiting many impurities or defects, DP spin relaxation should be considerably reduced.

In the experiments conducted throughout this thesis, spin transport is studied along the [110] direction. In the x, y, z reference frame constructed by $x||[110]$, $y||[\bar{1}10]$ and $z||[001]$, the Dresselhaus Larmor vector $\mathbf{\Omega_D}$ for electrons travelling in bulk material is given by:

$$\mathbf{\Omega_D} = \frac{\gamma}{\hbar}\begin{bmatrix} k_y k_z^2 + \frac{k_y}{2}\left[k_x^2 - k_y^2\right] \\ k_x k_z^2 + \frac{k_x}{2}\left[k_y^2 - k_x^2\right] \\ -2k_x k_y k_z \end{bmatrix}, \tag{3.21}$$

Besides the intrinsic Dresselhaus field, structural inversion asymmetries can be induced, for example, by introduction of asymmetrical doping or the application of an electric field $\mathbf{F} = (F_x, F_y, F_z)$. The effect of structural inversion asymmetry was studied by *Rashba* [19]. The Larmor vector $\mathbf{\Omega_R}$ in bulk material due to the Rashba term is given by:

$$\mathbf{\Omega_R} = \frac{2r_{41}}{\hbar}\begin{bmatrix} k_y F_z - k_z F_y \\ -k_x F_z + k_z F_x \\ k_x F_y - k_y F_x \end{bmatrix}, \tag{3.22}$$

where $r_{41} = -6 \pm 1 \times 10^{-20}\, e\,\mathrm{m}^2$ [109, 110] is a parameter quantifying the Rashba spin-splitting energy.

3.4.4 Dyakonov-Perel spin relaxation in confined structures

To study the effect of the spin-orbit field in confined systems [111], the value of the wavevector along the confinement axis is substituted by its average, which is vanishing: $\langle k_z\rangle = 0$. In a first, linear, approximation it can furthermore be assumed that $\langle k_z^2\rangle \gg \langle k_x^2\rangle, \langle k_y^2\rangle$. Therefore, the terms in eq. 3.21 proportional to $\langle k_z\rangle$ vanish and the terms proportional to either k_x^2 or k_y^2 are negligibly small and not of significant importance. Considering that in a QW, $\langle k_z^2\rangle = \pi^2/d_{QW}^2$, the expression for the Dresselhaus Larmor vector in a QW in the x, y, z reference frame can be derived by keeping only the terms linear in k_x and k_y [93, 100]:

$$\mathbf{\Omega_D^{2D}} = \frac{\gamma}{\hbar}\left[\frac{\pi}{d_{QW}}\right]^2\begin{bmatrix} k_y \\ k_x \\ 0 \end{bmatrix}. \tag{3.23}$$

The spin rotation angle θ_S of a spin travelling over a distance Δr with a speed $v_e = |\mathbf{v_e}|$ in the QW plane, during a time $t = \Delta r/v_e$, can then be calculated by:

$$\theta_S = \Omega_D^{2D} t = \Omega_D^{2D}\frac{\Delta r}{v_e}. \tag{3.24}$$

Since the wavevector is related to the velocity by $\mathbf{k} = \mathbf{v_e} m_e/\hbar$, eq. 3.24 can be rewritten to:

$$\theta_S = \frac{\gamma m_e \Delta r}{\hbar^2} \left[\frac{\pi}{d_{QW}}\right]^2 . \tag{3.25}$$

Equation 3.25 shows that the spin rotation angle depends only on travelling distance and not on time or velocity. In a QW plane, the trajectories of individual spins within a spin ensemble travelling from a position A to B are different. Hence, Δr varies from spin to spin. As is the case for bulk material, the different trajectories result in dephasing of the spin angles in the ensemble and as a result, to a decay of the spin polarization.

Symmetric quantum wells subjected to a transverse field F_z are also subjected to structural inversion asymmetry. The associated contribution to the Larmor vector $\mathbf{\Omega_{BR}^{2D}}$ induced by F_z in 2D systems was derived by *Bychkov and Rashba* [95] and can be derived from eq. 3.22 by realizing that in these conditions $\langle k_z \rangle = F_x = F_y = 0$. For intrinsic QWs subjected to a transverse electric field, the total Larmor vector is then given by the sum of the Dresselhaus and the Bychkov-Rashba contributions:

$$\mathbf{\Omega_{SO}^{2D}} = \begin{bmatrix} \gamma \left[\frac{\pi}{d_{QW}}\right]^2 \frac{k_y}{\hbar} + 2 r_{41} F_z \frac{k_y}{\hbar} \\ \gamma \left[\frac{\pi}{d_{QW}}\right]^2 \frac{k_x}{\hbar} - 2 r_{41} F_z \frac{k_x}{\hbar} \\ 0 \end{bmatrix}, \tag{3.26}$$

In a QWR with axis along x, the carriers are not only confined in the growth axis z, but as well in the y direction. The same arguments for k_z in the case of a QW now additionally apply to k_y. Therefore, in eqs. 3.21 and 3.22 terms proportional to k_y vanish. Since $\langle k_z^2 \rangle$ and $\langle k_y^2 \rangle$ are of the same order, only terms proportional to k_x^2 can be neglected in this case. The Larmor vector for such a one dimensional channel is then given by:

$$\mathbf{\Omega_{SO}^{1D}} = \frac{k_x}{\hbar} \begin{bmatrix} 0 \\ \gamma \left[\frac{\pi}{d_{QWR}}\right]^2 + \frac{\gamma}{2} \left[\frac{\pi}{w_{QWR}}\right]^2 - 2 r_{41} F_z \\ 0 \end{bmatrix}. \tag{3.27}$$

This equation reveals that in a one-dimensional channel, the spin-orbit field is oriented along the same axis for all electrons and its magnitude is determined by the channel thickness d_{QWR}, channel width w_{QWR} and transverse electric field F_z. Accordingly, the rotations resulting from momentum scattering commute and, the spin orientation only depends on the final position of the trajectory. Consequently, all electrons in an electron ensemble travelling to a fixed position in the QWR experience the same net spin rotation. The initial spin polarization is, therefore, maintained. Thus, DP spin relaxation is efficiently suppressed in a one-dimensional channel [112, 36].

In GaAs, the Bohr radius is approximately 12 nm. In order to fabricate truly one-dimensional channels, one needs to fabricate wires with a width comparable to, or smaller than, the Bohr radius. Such small features are subjected to inhomogeneities from the fabrication process. Monte Carlo simulations revealed, however, that one does not need to reduce the channel size to a pure one-dimensional channel to enhance spin lifetimes [36]. Since the spin lifetime is inversely proportional to the momentum scattering time, increasing the scattering rate should also enhance spin lifetimes. Consider the motion of an electron in a narrow channel. If the width of the channel is smaller than the mean free path, the channel width acts as an effective mean free path for momentum relaxation, effectively increasing the scattering rate. In fact, spin lifetimes are even enhanced for channels with a width w_{chan} of a few mean free paths, with a dependency $\tau_S \propto w_{chan}^{-2}$ [113].

For such narrow channels, the spin rotation angle between scattering events is too small to mimic the frequent changes of the precession axis. The predicted enhancement of the spin lifetime with channel widths beyond the mean free path is also observed in experimental works [112, 37, 38]. The reported spin lifetimes are on the picosecond timescale and extend to nanosecond timescale in more recent work [114, 115]. Note that in the discussion here, only linear terms of the Dresselhaus field are included. It was shown in ref. [115] that the spin lifetime in a one-dimensional channel is limited by the terms in eq. 3.21 which are cubic in $\mathbf{k}$.

3.5 Acoustically induced spin dynamics

As discussed in sec. 2.3.1, the piezoelectric potential accompanying a surface acoustic wave dissociates the optically injected excitons into free electrons and holes. These free carriers are distributed towards the piezoelectric potential maxima (electrons) and minima (holes). If the condition for efficient transport, as defined by eq. 2.30, is met, there is no overlap of the electron and hole wavefunctions. As a result, spin relaxation due to exchange interaction is suppressed [65, 100]. However, consider the situation where the high-mobility electrons are able to follow the SAW piezoelectric potential, while the low-mobility holes are spread throughout the SAW period. In this case, the electrons interact with those holes which are spread. Consequently, the suppression of the exchange interaction is weakened. It is expected that transport is very efficient for the QW structures studied in this thesis, due to the high mobilities of carriers in GaAs/(Al,Ga)As QW structures. The spins transported in the QWR are, thus, essentially confined into mobile dots defined by the SAW potential. The confinement is characterized by the QWR thickness, QWR width and SAW wavelength and should result in efficient suppression of exchange interaction and DP spin relaxation.

The previous sections introduced a brief overview of the SO field in quantum well structures. The spin dynamics may be affected by the SAW through both its strain field and piezoelectric field. As discussed in sec. 3.4.4, an electric field induces a structural inversion asymmetry, resulting in a Bychkov-Rashba SO field. The SAW induces a piezoelectric field along the transport direction F_x and along the growth axis F_z. In the conduction band minimum, where the electrons are stored, F_x is vanishing. The Bychkov-Rashba Larmor vector is, therefore, solely determined by F_z. The Larmor vector for an intrinsic QW subjected to a transverse electric field is given by eq. 3.26. Additional to the piezoelectric fields, the strain fields of the SAW induce another type of structural inversion asymmetry. For a Rayleigh wave propagating along the [110] direction, it is discussed in sec. 2.2.2 that the non-zero strain components are S_1, S_3 and S_5. For electrons acoustically transported in a QW layer ($\langle k_z \rangle = 0$), the strain contribution to the SO field is given by [97]:

$$\mathbf{\Omega_S} = \frac{S_1 C_3}{2\hbar} \begin{bmatrix} k_y \\ -k_x \\ 0 \end{bmatrix}, \tag{3.28}$$

where C_3 is the spin-orbit parameter quantifying the strain contribution to the SO field. The value of the C_3 parameter is determined in different reports using static strain. The reported values range from 0.31 eV nm in a GaAs QW to 0.81 eV nm as measured in bulk GaAs [25, 116, 117]. The experiments conducted for this thesis will show that for the QWRs studied here, the C_3 parameter is much larger. This will be discussed in sec. 8.2. Note that according to fig. 2.10(c), the shear strain S_5 is zero at the position of electron storage. This results in a zero z-component of $\mathbf{\Omega_S}$. If the electrons are transported at

a different position where S_5 has a finite value, $\Omega_{S,z} = -C_3 S_5 k_y/[2\hbar]$, which results in a change of the spin rotation plane.

The spin-orbit field experienced by electrons stored in the SAW is then determined by the Dresselhaus, Bychkov-Rashba and strain terms added together. Furthermore, eq. 2.38 depicts the fact that F_z can be expressed as S_1 by the parameter r_{FZS}. The Larmor vector for electrons acoustically transported in a QW plane is, therefore:

$$\Omega_{SO}^{SAW} = \begin{bmatrix} \frac{k_y}{\hbar}\left[\gamma\left[\frac{\pi}{d_{QW}}\right]^2 + S_1\left[2r_{41}r_{FZS} + \frac{1}{2}C_3\right]\right] \\ \frac{k_x}{\hbar}\left[\gamma\left[\frac{\pi}{d_{QW}}\right]^2 - S_1\left[2r_{41}r_{FZS} + \frac{1}{2}C_3\right]\right] \\ 0 \end{bmatrix} = \begin{bmatrix} \frac{k_y}{\hbar}\left[\beta + \alpha\right] \\ \frac{k_x}{\hbar}\left[\beta - \alpha\right] \\ 0 \end{bmatrix}, \tag{3.29}$$

where $\beta = \gamma\left[\frac{\pi}{d_{QW}}\right]^2$ and $\alpha = S_1\left[2r_{41}r_{FZS} + \frac{1}{2}C_3\right]$ are SO terms associated with BIA and SIA, respectively. In the experiments conducted for this thesis, acoustic spin transport is studied in both the quantum wires and the surrounding quantum well. As argued in sec. 3.1, the dynamics in the QWR may be described by the dynamics of a quantum well with the QWR thickness. Thus, the spin-orbit field in the QW and the QWR have the same form. For analytical purposes, a second approximation $\mathbf{k} = (k_x, 0, 0) = m_e v_{\mathrm{SAW}}/\hbar\hat{\mathbf{x}}$ will be made. This assumption is justified for the QWR spins, since the QWR width is orders of magnitudes smaller than the spin-orbit precession length. In the QW however, lateral diffusion along y means that this assumption is not strictly valid. Investigation of eq. 3.29 reveals that for $\mathbf{k} = k_x\hat{\mathbf{x}}$ the SO field has a component only along the y axis. The resulting precession frequency is determined by the balance between the Dresselhaus, Bychkov-Rashba and strain terms. As a result, the Larmor vector for electrons acoustically transported in a quasi-one-dimensional channel is:

$$\mathbf{\Omega_{SO}^{SAW}} = \frac{m_e v_{\mathrm{SAW}}}{\hbar^2}\left[\gamma\left[\frac{\pi}{d_{QW}}\right]^2 - S_1\left[2r_{41}r_{FZS} + \frac{1}{2}C_3\right]\right]\hat{\mathbf{y}}. \tag{3.30}$$

Two particular points are worthwhile mentioning here. Firstly, the spin orientation of a single spin after a time t is determined by its spin rotation angle $\theta_S = \Omega_{SO}^{SAW} t$. Under a SAW, the correlation between time and position along the transport path is fixed by $t = \Delta x/v_{SAW}$. As is the case for the spin dynamics in an intrinsic QW (see eq. 3.25), θ_S can, therefore, be rewritten as:

$$\theta_S = \frac{m_e \Delta x}{\hbar^2}\left[\gamma\left[\frac{\pi}{d_{QW}}\right]^2 - S_1\left[2r_{41}r_{FZS} + \frac{1}{2}C_3\right]\right]. \tag{3.31}$$

Again, the spin rotation angle between two fixed locations depends only on distance. Equation 3.31 reveals that a spread of the electron velocities (for example in the case of inefficient carrier transport by the SAW) should not affect Dyakonov-Perel spin precession.

Secondly, the spin orientation is deterministically affected by the structural inversion asymmetry arising from both the piezoelectric and strain fields of the SAW. For the structures studied in this thesis, $\gamma > 0$ [108], $F_z < 0$ (see sec. 2.5.2), $r_{41} < 0$ [110], $S_1 > 0$ (see sec. 2.5.2) and $C_3 < 0$ [118]. Under these conditions, the signs of the Dresselhaus and the strain-induced terms are equal, and opposite to the Bychkov-Rashba term. The magnitudes of the Dresselhaus and strain-induced terms are of the same order, and one-two orders of magnitudes larger than the Bychkov-Rashba term. Therefore, the spin orientation can actively be controlled by acoustic tuning of the strain-induced spin-orbit field. As shown by eq. 3.31, the key parameter determining the spin orientation of different electrons in an electron ensemble is Δx. Since Δx is equal for electrons in a QWR travelling between

two fixed locations on a chip, the QWR can, in principle, act as an acoustic spin transistor: the spin precession frequency, and thereby Ω_S is controlled by the acoustic power.

3.6 Monte Carlo simulations

In the previous section, it is discussed that, for analytical purposes, the assumption $\mathbf{k} = k_{SAW}\hat{\mathbf{x}}$ is made. To assess the viability of this assumption and study the effect of k_y, Monte Carlo simulations of the spin dynamics in a channel with a width of w_{chan} are performed. The simulation is carried out using the Octave software package as described in this section.

- Firstly, a random value for the electron speed v_y along the y axis is generated, taking into account a Maxwell-Boltzmann probability distribution $f(v_y)$ for one dimension:

$$f(v_y) = \frac{1}{v_T\sqrt{\pi}} e^{-\left(\frac{v_y}{v_T}\right)^2}, \tag{3.32}$$

  where $v_T = \sqrt{2k_BT/m_e}$ is the thermal velocity, k_B the Boltzmann constant and $T = 10\,\mathrm{K}$ temperature. Within the boundaries of the channel, the spins are acoustically transported along the x axis with a speed v_{SAW} and freely diffuse along the y axis with speed v_y, until they are scattered. The scattering time τ_p is assumed to be constant, with a value calculated by: $\tau_p = m_e\mu_e/e$. After every scattering event, v_y is randomized using eq. 3.32 (inelastic scattering). Note that this randomization process assumes no information about the scattering dynamics. Furthermore, the channel boundaries are reflective (elastic scattering): when the spin reaches the channel boundaries, the spin is reflected, which means $v_y \to -v_y$.

- Secondly, a three-dimensional vector $\mathbf{\Omega_{SO}}$ is calculated for an experimentally relevant value of $S_1 \propto \sqrt{P_{SAW}}$ using eq. 3.29. The transverse piezoelectric field is calculated using eq. 2.38.

- Finally, the dynamics of a spin in the SO field can then be modelled by a single-spin implementation of the Landau-Lifshitz-Gilbert equation [36]. However, since only the final spin orientation after travelling a distance $\Delta r = \tau\sqrt{v_{\mathrm{SAW}}^2 + v_y^2}$ is of importance (and not the spin dynamics during motion), the spin orientation can be determined by a matrix rotation, which considerably reduces the computation time. The spin rotation angle between two scattering events is calculated by $\theta_S = \Omega_{SO}\tau_p$. Equation 3.29 reveals that the SO field always lies in the (x, y)-plane and makes an angle θ_{SO} with the x axis. The rotation matrix can, therefore, be obtained as follows: (i) translate the spinvector $\mathbf{S}$ to $\mathbf{S_{SO}}$, where $\mathbf{S_{SO}}$ denotes the coordinates of the spin vector in a reference frame where $\mathbf{\Omega_{SO}} \equiv \hat{\mathbf{x}}_{\mathbf{SO}}$, (ii) rotate $\mathbf{S_{SO}}$ an angle θ_S around the $\hat{\mathbf{x}}_{\mathbf{SO}}$-axis, and (iii) translate the new $\mathbf{S_{SO}}$ back to the x, y, z reference frame to finally obtain the new spin vector $\mathbf{S}$. Since θ_{SO} and θ_S are known parameters, the overall rotation matrix is easily obtained by a matrix product of the aforementioned three rotations.

Per particle, this simulation sequence is iterated for a number of steps $n_{steps} = l_{chan}/l_x$, where l_x and l_{chan} are the travel distance along x between two scattering events and the channel length, respectively. After each scattering event (corresponding to one simulation step), the $\mathbf{S}$ is calculated to simulate the spin evolution of a single particle acoustically transported from $x = 0$ to $x = l_{chan}$. By repeating the simulation for multiple particles,

the spin dynamics of a spin ensemble is studied. Results of the simulations are presented in sec. 8.3, where the specific parameters used in the simulation will be reported.

3.7 Dynamic Quantum Dots

The previous discussion is focused on the spin dynamics in two- and one-dimensional systems. A complete description of the spin dynamics in a zero-dimensional system is out of the scope of this thesis. However, in sec. 8.2.3 experimental results of the spin dynamics will be compared with those reported from experiments on dynamic quantum dots (DQDs) in ref. [119]. These DQDs form due to the interference of two SAWs propagating along the [110] and [1$\bar{1}$0] directions in a QW structure.

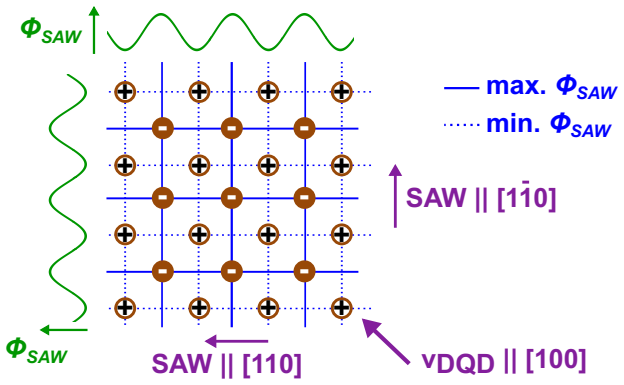

Figure 3.6: Schematic illustration of dynamic quantum dots. The green lines indicate the profiles of ϕ_{SAW} for each SAW separately, while the solid and dashed blue lines indicate the maxima and minima positions of ϕ_{SAW}, respectively. The positions of electrons and holes are depicted by solid and open brown dots, respectively.

Figure 3.6 illustrates the resulting pattern of the piezoelectric potential ϕ_{SAW}. Here, the green lines indicate the separate profiles of ϕ_{SAW} for every SAW, while the solid and dashed blue lines indicate the positions where ϕ_{SAW} takes its maximum and minimum value, respectively. The electrons (holes) reside at the positions where the maxima (minima) of ϕ_{SAW} intersect. As a result, the carriers are transported along the [100] direction with a velocity $v_{DQD} = \sqrt{2} v_{\mathrm{SAW}}$. The microscopic motion of the carriers within each DQD is restricted in three dimensions, where the lateral restriction is determined by the SAW wavelength and the vertical restriction by the QW thickness. Since the SAW wavelength is on the micrometer scale, which is much larger than the carrier deBroglie wavelength, there is no lateral quantum confinement. However, the DQD dimensions are smaller than the spin-orbit length in the QW: this leads to efficient suppression of the DP spin relaxation mechanism. The total SO Larmor vector is given by:

$$\mathbf{\Omega_{SO}^{DQD}} = \sqrt{2}\Omega_D \mathbf{\hat{x}_{DQD}} - 2\left[\Omega_{BR} + \Omega_S\right] \mathbf{\hat{y}_{DQD}}, \tag{3.33}$$

where $\mathbf{\hat{x}_{DQD}}||[100]$ and $\mathbf{\hat{y}_{DQD}}||[010]$ denote the axes parallel and perpendicular to the DQD velocity, respectively. Ω_D, Ω_{BR} and Ω_S denote the amplitudes of the Dresselhaus, Bychkov-Rashba and strain contributions under application of a single SAW beam along [110]. In contrast to the case of the QW and QWR, where all contributions to the SO field are collinear for $\mathbf{k}||[110]$, the precession frequency of the DQD spins is given by:

$$\Omega_{SO}^{DQD} = \sqrt{2\Omega_D^2 + 4\left[\Omega_{BR} + \Omega_S\right]^2} = \frac{m_e v_{SAW}}{\hbar^2} \sqrt{2\gamma^2 \frac{\pi^4}{d_{QW}^4} + 4\left[2r_{41}F_z + \frac{C_3 S_1}{2}\right]^2}. \tag{3.34}$$

chapter 4

Experimental methods

In this thesis, acoustic charge and spin transport in (Al,Ga)As quantum well structures is studied. A simplified illustration of a typical experiment is shown in fig. 4.1. The sample consists of a GaAs quantum well (QW, blue) structure containing planar quantum wires (QWRs, green). The structure is discussed more elaborately in chapter 5. An interdigital transducer (IDT, black) generates a surface acoustic wave (SAW) towards the QWR, where electrons (brown) and holes (not shown) are optically injected and acoustically transported along the QWR axis. Along the transport path, unintended trapping centers lead to carrier recombination and emission of photoluminescence (PL).

The samples are fabricated by photolithography, wet etching and molecular-beam epitaxy (MBE). The first section of this chapter discusses MBE growth and structural analysis of the prepatterned substrates before and after overgrowth. In the second section, the generation of SAWs by IDTs is discussed. The third section introduces the experimental setups used to study photoluminescence and the final section explains the detection of spins by polarization-resolved PL experiments and by Kerr rotation experiments.

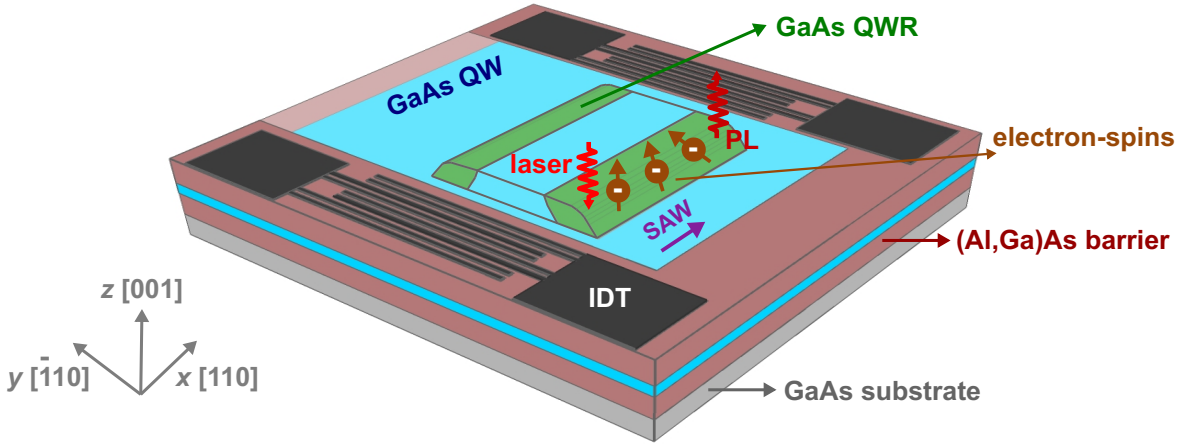

Figure 4.1: Illustration of a typical experiment. (Spin-polarized) charge carriers (brown) are optically injected in the QWR (green) or QW (blue) and transported by a SAW. Along the transport path, the carriers are brought to recombine and emit PL, which is detected using the experimental methods described in this chapter.

4.1 Molecular-beam epitaxy and structural analysis

The samples studied in this thesis are fabricated using molecular-beam epitaxy (MBE) on prepatterned GaAs substrates. A comprehensive discussion of the fabrication method is provided in chap. 5. In this section, the MBE apparatus is introduced. For analysis of the sample quality, atomic-force-microscopy (AFM) and electron microscopy (SEM and STEM) are used. These devices are introduced in this section, after the introduction of the MBE apparatus.

4.1.1 Molecular-beam epitaxy

Quantum well structures consist of multiple thin films with nanoscale thicknesses. These structures require fabrication methods producing high-quality samples. Molecular-beam epitaxy is a crystal growth method employed in an ultra-high vacuum (UHV) environment. In MBE growth, a beam of molecules or atoms impinges on a heated substrate, where the species crystallizes to form thin films with high crystalline quality. The low pressure of the UHV setting suppresses scattering of the beam, which ensures the directionality of the molecular or atomic beam. Moreover, the UHV condition suppresses the presence of impurities which may attach to the sample surface, thereby providing high-quality sample growth. The slow growth rates achievable with MBE provide excellent control of the film thicknesses, even towards subnanometer values [41].

The samples for this thesis are grown in an MBE growth chamber of a VG V80H UHV system. This system consists of a growth chamber, preparation chamber, a chamber with a hydrogen cleaning stage and a load-lock for fast sample transfer. The background pressure of the liquid nitrogen cooled growth chamber is of the order of 10^{-11} mbar. Epitaxial growth is conducted under As fluxes such that the base pressure is of the order of 10^{-7} mbar. The contents of the MBE growth chamber are schematically drawn in fig. 4.2. The sample (grey) is attached to a rotating heated sample holder (dark grey) with accurate control of the sample temperature. The temperature of the sample during MBE growth is a crucial parameter, since it determines the kinetics of the adatoms on the growing surface and thereby the quality of the structure. For overgrowth of thin films on prepatterned substrates, the kinetics also determines the shape of the resulting nanostructures. The molecular beams are generated by heating the source materials in Knudsen evaporation cells, containing for example Ga (bright blue), As (red) and Al (dark blue). Each of the sources is equipped with a mechanical shutter controlling the precise composition of the molecular beam. In the figure, growth of a GaAs layer on a GaAs substrate is illustrated. Here, the shutter in front of the Al source is closed, while opening the shutters in front of the Ga and As sources. Note that the stacking of the Ga and As atoms relative to each other as sketched in the figure does not correspond to a real structure and is for illustrative purposes only. During growth, the substrate is rotated at a speed of typically 12 rpm to achieve a higher degree of the lateral homogeneity. Nevertheless, the layer thickness in the used MBE system decreases from the center to the edge of a 2-inch wafer with roughly 1.5 % to 3.0 %. This becomes mainly important in structures where the optical properties depend critically on layer thicknesses, such as optical microcavities. For this thesis, the growth of the QW structures is conducted in the Frank-van-der-Merwe mode [120]. In this mode, the thin films grow smoothly in a layer-by-layer fashion. This growth mechanism presupposes only a small lattice mismatch between consecutive layers, which is valid for typical GaAs/(Al,Ga)As QW structures as studied in this thesis: the lattice constants of GaAs and AlAs are 5.654 Å and 5.661 Å, respectively [74].

A reflection high-energy electron diffraction (RHEED) system enables real-time in-situ

monitoring of the surface reconstruction [121] and growth rate [122] of the epitaxial layer. In this system, an electron gun (brown) provides a beam of electrons with energies up to 20 keV impinging onto the sample with a shallow angle of only a few degrees. The incident electrons are diffracted by the sample and detected by a phosphor screen (green) placed into the travel path of the diffracted electrons. The wave character of the electrons results in an interference pattern, which is a fingerprint of the surface crystal structure and the surface reconstruction type. The temporal evolution of constructive and destructive interference (which are detected as RHEED intensity oscillations) can be used to determine the growth rate.

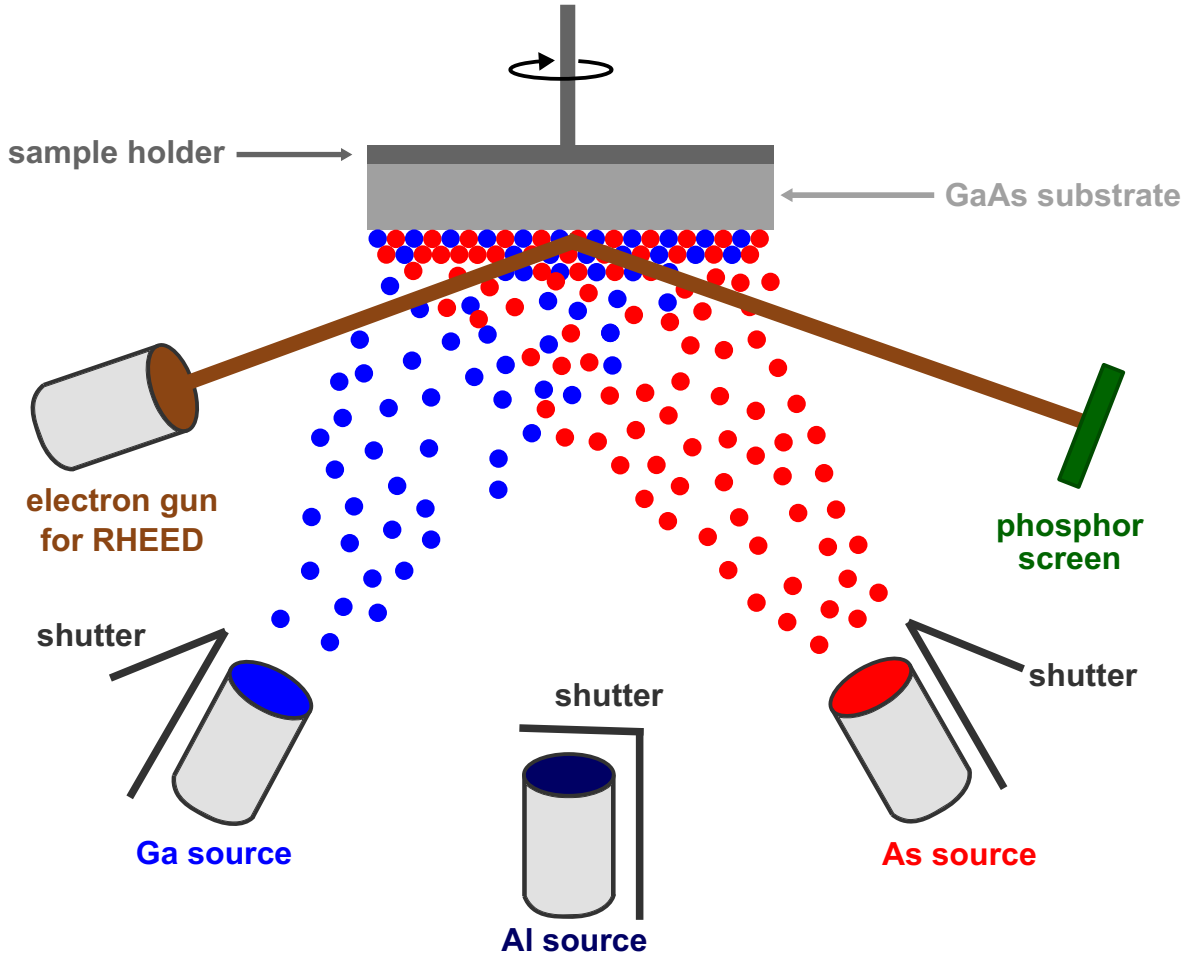

Figure 4.2: Simplified illustration of the MBE apparatus. The sample (grey) is mounted onto a rotating sample holder (dark grey). A GaAs layer is grown by exposing the sample to molecular beams coming from the Ga (bright blue dots) and As (red dots) sources. The shutter (dark grey line) in front of the Al source is closed. A RHEED system (brown and green) is utilized to control epitaxial growth. The sample growth by MBE for this thesis is carried out by Dr. Klaus Biermann.

4.1.2 Atomic force microscopy

The nanostructures studied in this thesis are a result of anisotropic MBE overgrowth on prepatterned substrates. The shape and quality of the prepatterned ridges can be investigated by atomic force microscopy (AFM) [123]. In this technique, an atomically sharp tip attached to a cantilever is brought in close contact with the sample surface. The atomic forces between tip and sample cause a noticeable deflection of the cantilever. AFM

images constructed for this thesis are recorded using a Bruker Dimension Edge device, in which the cantilever deflection is measured using a laser beam.

In fig. 4.3, a patterned GaAs substrate is measured by an AFM. A laser beam (red) is incident on the cantilever (green) and reflected onto a quadrant photodiode (blue). Bending of the cantilever causes a change of the laser reflection. The resulting change of the laser beam position on the quadrant photodiode (black circle) is recorded and directed to a controller. The latter provides a feedback loop between the signal from the quadrant photodiode and the cantilever, that alters the vertical tip position in such a way, to keep the position of the laser beam, and thus cantilever bending, constant. This results in a constant distance between tip and sample. By recording the required cantilever corrections, one can record the surface topography. Since deflections of the cantilever are small, a high sensitivity of the quadrant photodiode is required. By centering the initial position of the laser beam onto the center of the quadrant photodiode, the highest sensitivity is achieved, because this results in the largest intensity variations on the four quadrants of the photodiode. An alternative mode to detect the sample surface topography is to fix the position of the cantilever independently of the sample surface. Here, the changes of the laser reflection resulting from the changing cantilever bending characterize the surface topography. In both modes, the sample surface can be imaged with a subnanometer height resolution and nanoscale lateral resolution, determined by the AFM tip radius.

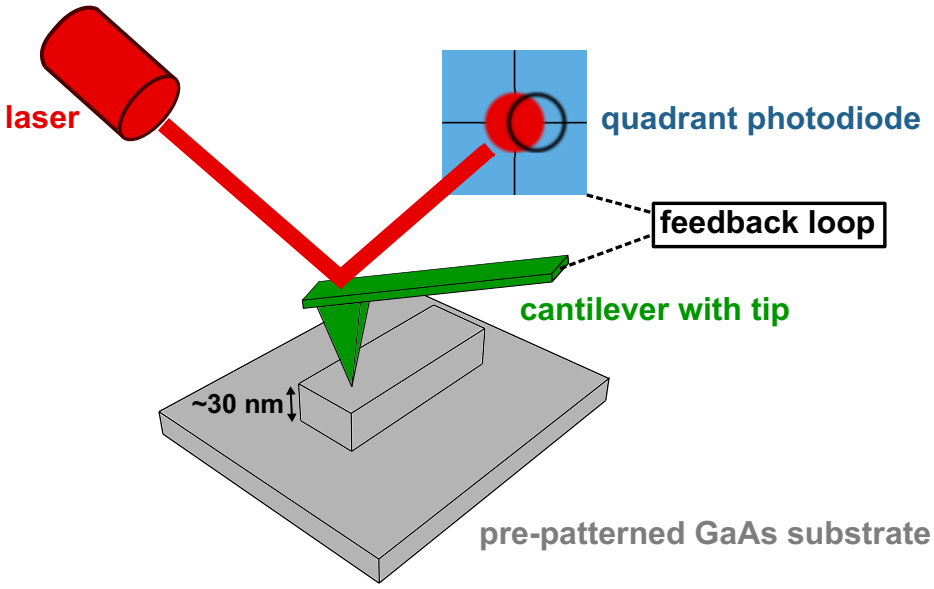

Figure 4.3: Schematic illustration of atomic force microscopy. A tip with cantilever (green) interacts with a sample (grey). The reflection of a laser beam (red) from the cantilever is measured by a quadrant photodiode (blue) and is, via a feedback loop, used to adjust the cantilever position according to the topography of the surface.

Classically, the AFM tip was brought physically in contact with the sample. This method, called contact mode, has a serious drawback in that it may cause modifications of the surface and may even lead to a degradation of the AFM tip. These problems can be avoided using tapping mode [124]. In this mode, the tip is driven to vertically oscillate at its resonance frequency. In contrast to contact mode, the tip only physically contacts the sample surface for a short time once every oscillation period. The oscillation amplitude depends on the distance between sample and tip. The topography of the surface is measured by keeping the root-mean-square (RMS) value of the $10-100\,\mathrm{nm}$ oscillation amplitude constant by adjusting the cantilever vertical position.

A further development is the PeakForce tapping mode. Here, the AFM tip oscillates

below its resonance frequency [125]. In this mode, not the RMS value of the oscillation amplitude, but rather the maximum force during an oscillation period is coupled to the feedback loop. The PeakForce tapping mode combines the direct force information of contact mode with the damage suppression of tapping mode. In the framework of the current thesis, the AFM is operated in PeakForce tapping mode. In addition, the device is equipped with a ScanAsyst function [125], in which the parameters controlling the feedback loop are adjusted automatically. The AFM tip used in the measurements is a pyrex-nitride probe with a typical tip radius of curvature below 10 nm.

While AFM is a powerful method for measuring surface topography, special care has to be taken for the data analysis. Several factors, including sample tilt, cantilever tilt and thermal drift, may result in data artefacts. In order to analyze the acquired data, the Gwyddion software [126] was used to correct the AFM data for these kinds of artefacts.

4.1.3 Electron microscopy

Besides AFM, surface topography can be imaged using electron microscopy. This is particularly useful for features with a height that limits the spatial AFM resolution due to its finite tip radius. In this thesis, scanning electron microscopy (SEM) is used to examine the quality of mesa edges defined in photoresist. The small deBroglie wavelengths of electrons facilitates improved resolution on the nanoscale as compared to conventional optical microscopy. In this section, a brief overview of electron microscopy is given [127].

In the SEM apparatus, an electron gun provides an electron beam, which passes through an electron optical column that accelerates the electrons to 5 keV, positions and focuses the beam on the sample with nanometer-scale spotsize. When the electrons penetrate the sample, they scatter elastically and inelastically. The beam electrons scattered back to the sample surface by elastic scatterings are known as backscattered electrons. Inelastic scatterings of beam electrons release electrons which are loosely bound to the atoms of the sample's material (secondary electrons). The SEM images for this thesis are recorded using the secondary electrons, which are detected by a positively-biased Everhart-Thornley detector. Due to the low energies of secondary electrons, only those generated close to the sample surface are detected. Secondary electron images are, therefore, primarily sensitive to surface features. For grazing angles of incidence, the primary electron beam spends more time close to the sample surface, thereby generating more secondary electrons that can escape from the sample. Thus, for a fixed angle of incidence, the number of detected secondary electrons depends on the local surface orientation. The image contrast by recording secondary electrons is, therefore, mainly a result of surface topography. Before loading the sample into the SEM equipment, a 5 nm thick Ti layer is vapour-deposited onto the entire sample surface to prevent charge accumulation, which disturbs the measurement.

To investigate the formation of QWRs on the prepatterned substrate, cross-sectional images of overgrown ridges are recorded using scanning transmission electron microscopy (STEM). Like the SEM apparatus, the STEM equipment consists of an electron gun which passes an electron beam through an electron optical column, after which the beam hits the sample. However, in contrast to SEM, STEM does not record secondary or backscattered electrons, but rather the primary beam electrons, after they are transmitted through the sample. For this purpose, the sample thickness is reduced to sub-micrometer dimensions. To further enhance electron transmission, the energies of the electrons are typically in the range 10^1 to 10^2 keV. For STEM images, the image contrast relates to the material's local mass density and atomic number. A high mass density or large atomic number increases the scattering rate of primary beam electrons, which decreases the electron transmission through the sample. Thus, areas with high and low mass density (or large and small

atomic number) appear as dark and bright areas, respectively. The cross-sectional STEM image provides, therefore, an overview of the cross-sectional geometry of a multilayer structure.

4.2 Generation and analysis of surface acoustic waves

As discussed in the introduction of this chapter, surface acoustic waves are used to transport carriers along the QW and the QWR axis. The SAWs are generated by interdigital transducers (IDT). The geometry of a delay line, as discussed in sec. 2.2.3, allows for the characterization of the piezoelectric coupling, which is done using a room-temperature probe station to measure the radio-frequency (rf) reflection and rf transmission coefficients (S_{11}, S_{22}, S_{12} and S_{21}). A schematic drawing of the experimental setup is shown in fig. 4.4. Probes (yellow) consisting of two metallic contacts are physically brought into contact with the IDTs and connected with the analysis ports of a vector network analyzer (VNA). The VNA has a separate direct-current output port associated to each probe to which a digital multimeter can be connected to measure the electrical resistance of each IDT. The VNA performs a frequency sweep by applying an rf voltage to the IDTs within a predetermined range of frequencies. For every frequency, S_{11}, S_{22}, S_{12} and S_{21} are recorded. Before executing the frequency sweep, the probes are calibrated using a calibration chip. This chip contains metallic structures to measure the VNA signal while the probes are connected to open gates, short-cutted gates and transmission gates.

The reflection parameters S_{11} and S_{22} measure the rf power, which is reflected by IDT1 and IDT2, respectively. Typical results for a SAW along the [110] direction in a GaAs (001) QW structure are shown in figs. 4.5(a) (S_{11}) and (b) (S_{22}). For both IDTs, a clear dip in the frequency spectrum indicates the conversion of applied rf power into an acoustic mode at the resonance frequency f_{res}. The baseline away from f_{res} provides an estimate of the power losses of the IDT and the experimental setup. The reflection coefficients at the resonant $S_{11,r}$ ($S_{22,r}$) and non-resonant $S_{11,nr}$ ($S_{22,nr}$) conditions can be used to calculate the linear acoustic power density P_{SAW} (in W/m) of the SAW:

$$P_{SAW} = \frac{1}{2w_{SAW}} \left[10^{\frac{S_{11,nr}}{10}} - 10^{\frac{S_{11,r}}{10}} \right] \frac{10^{\frac{P_{rf}}{10}}}{1000}, \tag{4.1}$$

where P_{rf} is the applied rf power to the IDT (in dBm) and w_{SAW} is the width of the SAW beam. The IDTs fabricated for the experiments for this thesis are designed for $w_{SAW} = 120\,\mu\text{m}$. The use of eq. 4.1 assumes that the rf power corresponding to $\Delta S_{11} = S_{11,nr} - S_{11,r}$ is completely converted into two Rayleigh SAW modes propagating in opposite surface directions and that the linear acoustic power density is homogeneously distributed over the SAW beam width. This assumption is justified for the Rayleigh modes used for the experiments in this thesis. For the measurement in figs. 4.5(a) and (b), $S_{11,nr} = S_{22,nr} \approx -2.6\,\text{dB}$, $S_{11,r} \approx -3.9\,\text{dB}$ and $S_{22,r} \approx -4.1\,\text{dB}$. This results in a conversion efficiency of rf into mechanical power of 7 % and 8 % for IDT1 and IDT2, respectively. The graphs show that the resonance frequency at room temperature is 719 MHz, consistent with eq. 2.23 for $v_{\text{SAW}} = 2876\,\text{m/s}$ ($\lambda_{SAW} = 4\,\mu\text{m}$).

The transmission of a SAW can be characterized by applying rf power to either one of the IDTs. The SAW travels along the sample and is converted by the opposite IDT into an rf signal, which is measured by the VNA. The transmission parameters S_{12} and S_{21} of a typical measurement are shown in figs. 4.5(c) and (d), respectively. At the resonance frequency, a large SAW transmission is measured with an amplitude of approximately 40 dB, indicating a good transmission of the SAW.

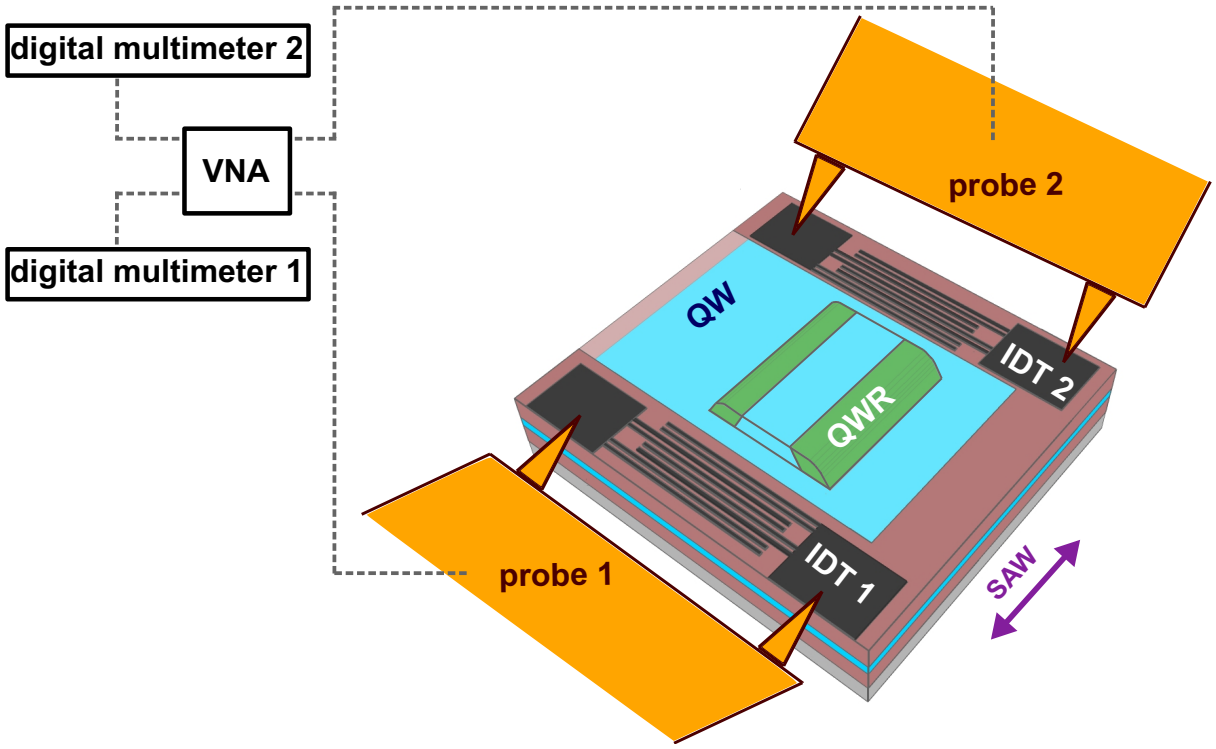

Figure 4.4: Characterization of IDTs (black) using metallic probes (yellow). A vector network analyzer (VNA) is used to sweep a predetermined range of rf frequencies to measure rf reflection and rf transmission coefficients. Both IDTs are associated to a separate output port of the VNA with digital multimeters to measure their electrical resistance.

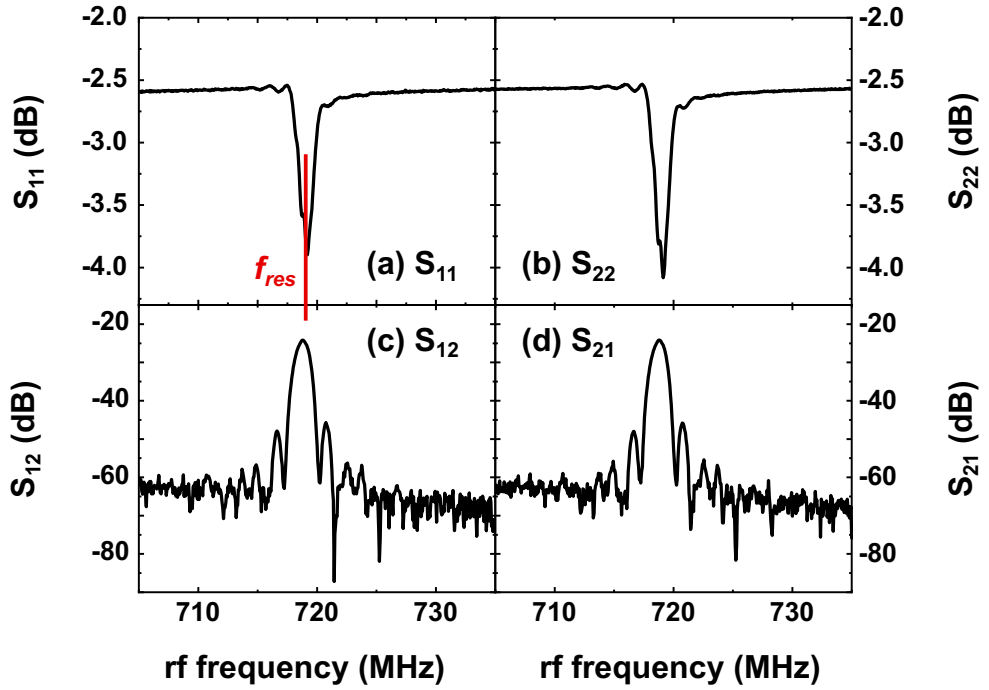

Figure 4.5: IDT characterization results. The rf reflection coefficients are shown in figs. (a) (S_{11}) and (b) (S_{22}), whereas figs. (c) and (d) show rf transmission coefficients S_{12} and S_{21}, respectively. The resonance frequency f_{res} is 719 MHz.

4.3 Photoluminescence methods

Electrical and optical properties of semiconductor samples can be investigated by studying photoluminescence (PL). In this section, the experimental setups used to measure PL are introduced.

4.3.1 Low-temperature probe station

Typical samples consist of an acoustic delay line fabricated on a 5 mm x 5 mm sized semiconductor chip. These samples are cut from 2-inch wafers, containing samples with varying nanostructures. In order to compare the optical properties of multiple samples under equal experimental conditions, one requires a cryostat for 2-inch wafers. A Cascade PLC50 low-temperature probe station provides such a cryostat for optical experiments at low temperatures (approximately 5 K). The sample is clamped by a ring onto a metallic sample holder and introduced into a high-vacuum chamber (of the order of 10^{-7} mbar) containing four probes to apply rf power to the IDTs. The sample holder is positioned on a chuck, connected to a liquid helium cooled system. The chamber vacuum is improved by a liquid helium cooled shield, which acts as a sink for frigid air contaminations. The large sample space brings a disadvantage of long cooling times of approx. three to four hours.

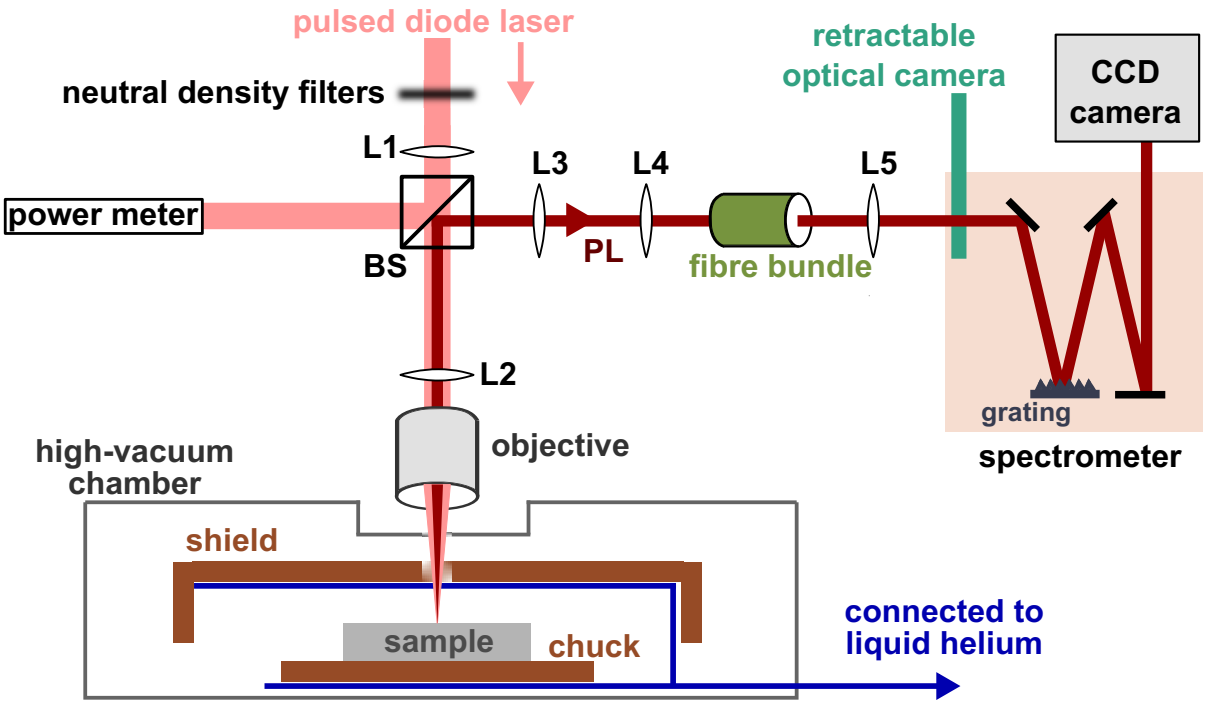

Figure 4.6: Illustration of the low-temperature probe station setup described elaborately in the main text. The high-vacuum chamber is connected to a liquid helium flow system (blue) used to cool the system to low temperatures of approx. 5 K. The high-vacuum chamber is coupled through an optical window to an optical setup containing a pulsed diode laser for excitation and a spectrometer equipped with a CCD camera to detect PL.

An illustration of the optical setup is shown in fig. 4.6. Here, the high-vacuum chamber is shown with grey contours. The optical components, which are positioned outside the high-vacuum chamber, are coupled to the sample via an optical window embedded in the top surface of the high-vacuum chamber. For optical measurements, a PicoQuant LDH-P-635 pulsed diode laser (wavelength 635 nm) is guided through neutral density filters in order to adjust the excitation density. The laser beam then passes through lens

L1, a beam splitter (BS) and lens L2, after which it is focused by a microscope objective onto the sample. At the focal plane of L1, a pinhole may be introduced to adjust the laser spot size on the sample. At the reflection side of the beam splitter, a Thorlabs PM100 powermeter is placed to measure the laser intensity. The laser spot size at the sample has a full-width-at-half-maximum (FWHM) of approx. 4 µm. Lens L2 and the objective are part of a Mitutoyo FS70 microscope, which may alternatively be used for coarse sample positioning (not shown). The laser beam induces PL in the sample, which passes through the same objective, is focused by L2 onto the focal plane of a lens L3 and collimated by the latter lens. A fourth lens L4 focuses the PL image onto a fibre bundle to transmit the image, which constructs the image onto the entrance slit of a Jobin-Yvon SPEX 750M single-grating spectrometer via lens L5. Behind the slit, a retractable optical camera is located for convenient sample positioning. This optical camera is retracted to measure the PL using the spectrometer. Inside the spectrometer, the PL image is collimated by a collimating mirror and hits a diffraction grating. The grating disperses the light due to wavelength-dependent diffraction [128]. The dispersed image is then guided to a set of two mirrors, which focus the image onto the chip of a charge-coupled device (CCD) camera for detection (Princeton Instruments Acton Spec-10). The spectral resolution of the spectrometer using an entrance slit width of 100 µm is 215 µeV (208 µeV) for a wavelength of 800 nm (815 nm). The combination of the spectrometer with a 20x magnification of the objective results in a spatial resolution of approximately 0.5 µm/pixel.

4.3.2 Confocal microscopy

The major part of the experiments are conducted using a confocal microscopy setup. Compared to the low-temperature probe station, the setup has a fast cooling time due to the small size of the corresponding CryoVac Konti cryostat and has the possibility for different types of experiments, connected to the same optical setup. The optical experiments using this setup are conducted at typical temperatures in the range 10-15 K. However, the cryostat can only contain one sample, fabricated on a 5 mm x 5 mm sized chip, cut from a 2-inch wafer. The chip is glued with silver paste onto a metallic chipholder. The IDTs are wire-bonded to the rf contacts of the chipholder using a DelVotec 5430 wire bonder. The chipholder with sample is then mounted on the sample holder of the cryostat, which additionally contains connections to apply an rf power to the IDTs.

A sketch of the experimental setup is shown in fig. 4.7, where the cryostat is omitted for clarity reasons. For basic optical characterization of the energy states in the sample, a one-dimensional PL detection scheme is adapted. For these experiments, a laser beam from a continuous wave (CW), wavelength-tunable, Ti:sapphire laser (Coherent Mira 900) or pulsed diode laser (PicoQuant LDH-P-760, wavelength 760 nm) is focused by lens L1 onto a 50 µm-sized pinhole, which is inserted to reduce the excitation spot size in the sample to a FWHM of approximately 2 µm (using a 20x objective). After the pinhole, the beam passes through a beam splitter and lens L2 to collimate the beam. A combination of neutral density filters is inserted in front of lens L1 to accurately control the excitation density, which is measured by a power meter (Thorlabs PM120D) located in the transmission arm of the beam splitter. The laser beam is reflected from three mirrors (M1, M2, M3) and is focused onto the sample by a microscope objective (Mitutoyo Plan Apo 20x). The objective, mirror M1 and mirror M3 are mounted onto a piezoelectric translation stage, capable of systematically scanning the laser spot over the sample surface with an accuracy of 0.1 µm. The PL from the sample is guided in the same path through the objective towards the beam splitter and focused by L2 on a separate pinhole, which is used to select a narrow area of the PL image and to block scattered laser light. A

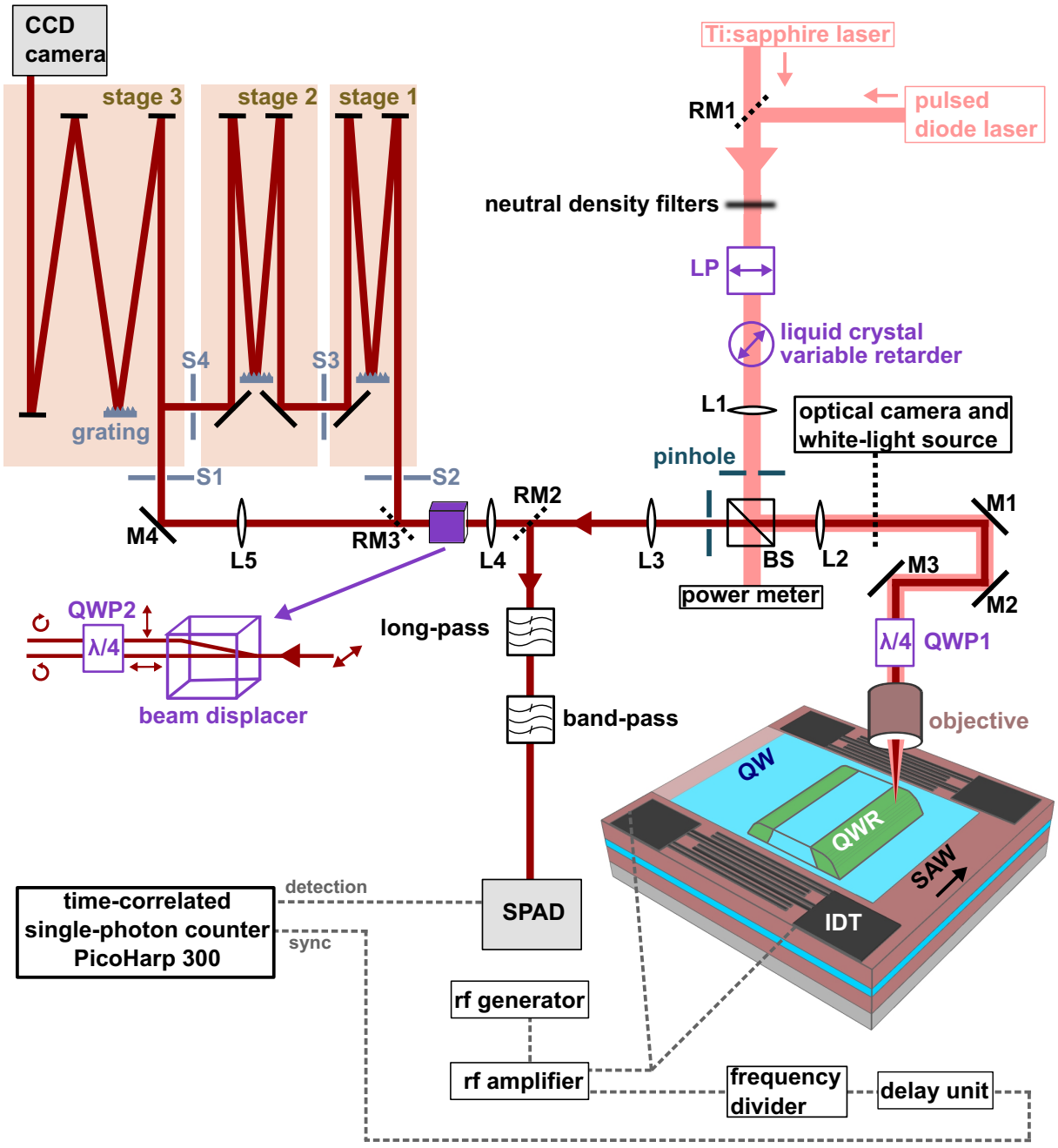

Figure 4.7: Schematic illustration of the confocal microscopy setup, elaborately discussed in the main text. Two lasers can be used to inject (spin-polarized) charge carriers in the sample. The PL (dark red) is directed to the entrance slit of a single- or triple-grating spectrometer equipped with a CCD camera. Alternatively, an experimental scheme for time-resolved PL measurements can be included. The components required to measure polarization-resolved PL are displayed with purple colour.

third lens L3 collimates the PL beam, which is then focused using lenses L4 and L5 onto the entrance slit S1 of a single-grating spectrometer equipped with a Horiba Symphony CCD camera. The working principle of the single-grating spectrometer is discussed in the previous section. In combination with a 20x objective, the setup yields a spatial resolution of approximately 0.5 µm/pixel. Using an entrance slit width of 100 µm, the spectral resolution of the spectrometer at a wavelength of 800 nm (815 nm) is 252 µeV (243 µeV). Furthermore, a beam splitter can be inserted between lens L2 and mirror M1 to couple a white-light source to the optical path, and to guide the image of the sample to an optical camera for coarse positioning of the laser spot on the sample.

The one-dimensional detection scheme discussed above provides knowledge of the energy states in semiconductor samples. For investigation of acoustic charge transport, a two-dimensional PL detection is required. This is achieved by spectral filtering of the PL, which is subsequently recorded as a two-dimensional image. The spectral filtering is carried out by a triple-grating spectrometer (Horiba T64000) by focusing the PL image using lens L4 and retractable mirror RM3 onto its entrance slit S2. The first stage of the triple-grating spectrometer acts as a single-grating spectrometer to spectrally disperse the image, which is focused onto the entrance slit S3 of the second stage. This narrow slit selects a predetermined range of the spectrum by physically blocking the diffracted rays corresponding to the undesired wavelengths. The original image is reconstructed with the filtered light by the second stage and passed to the entrance slit S4 of the third stage. Spatial mapping of the PL is performed by substituting the grating of the third stage by a mirror. The result is a spectrally filtered PL image, spatially resolved in two dimensions.

For acoustic transport measurements, the rf power is applied to the IDTs by a Rohde&Schwarz SMT06 rf signal generator. To amplify the output power of the rf generator, an rf amplifier is inserted between cryostat and rf signal generator. The rf amplifier also splits the applied rf power into two output ports, resulting in an overall amplification of the provided rf power of 20 dB per output port. The first output port is connected to the cryostat to generate a SAW, while the second output port can be connected to the synchronization port ('sync') of a time-correlated single-photon counter (PicoQuant PicoHarp 300). The latter device is part of a time-resolved PL detection scheme, used to investigate the carrier dynamics during acoustic transport. For time-resolved PL detection, the PL image from the sample is guided to a single-photon avalanche diode (PicoQuant τ-SPAD 100) by inserting retractable mirror RM2 (see fig. 4.7). To protect the SPAD against scattered laser light, a long-pass filter is inserted in front of the SPAD, which blocks all light with a wavelength smaller than 800 nm. A band-pass filter is used to filter the PL for either the QW or QWR photoluminescence. The detection signal of the SPAD is then coupled to the 'detection' port of the PicoHarp 300. Time-resolved detection of the PL is carried out by the PicoHarp 300 by recording the time delay between the signals on its 'sync' port (originating from SAW generation) and its 'detection' port (originating from photon detection). This process is then repeated for hundreds of photon counts on the 'detection' port, resulting in the detection of PL as function of time after SAW generation. In order to extend the temporal detection range, a MiniCircuits frequency divider divides the SAW frequency by 16. A delay unit for rf signals furthermore enables to change the temporal synchronization between PL detection and the SAW phase. The time-resolved PL detection scheme can be combined with either the CW Ti:sapphire laser or the pulsed diode laser.

To fix the SAW phase of carrier excitation, the pulsed diode laser can be synchronized to the generation of the SAW (not shown in fig. 4.7). This is achieved by connecting the output of the rf signal delay unit to the 'reference in' port of the diode laser. Since the maximum laser pulsing frequency is much smaller than the SAW frequency, the MiniCircuits

frequency divider is used again to provide a reference signal within the possible laser pulsing frequency range. Temporal detection is now carried out by connecting the 'reference out' port of the diode laser to the 'sync' port of the PicoHarp 300. The result is a PL detection scheme, where laser excitation is correlated to a specific SAW phase, and PL detection is correlated to both the temporal instants of laser excitation and SAW generation. Note that in this case, the rf signal delay unit is only connected to the diode laser and not directly to the PicoHarp 300.

4.4 Spin detection methods

Optical spin detection is performed in two ways. In the first method, one utilizes the magneto-optical Kerr effect. The Kerr signal is a result of reflected laser light and does not require photoluminescence to detect spins. A more detailed discussion of the Kerr effect is provided in sec. 4.4.2, with an overview of the experimental setup used to measure Kerr rotation. Secondly, spin measurements can be carried out by polarization-resolved PL measurements, which is based on the optical selection rules introduced in sec. 3.3. These experiments can be conducted by expanding the confocal microscopy setup discussed in the previous section. This section starts with an overview of the required adjustments of the confocal microscopy setup to conduct polarization-resolved PL measurements.

4.4.1 Polarization-resolved photoluminescence

The additional components inserted in the confocal microscopy setup for polarization-resolved PL measurements are shown with purple colour in fig. 4.7. The polarization of the laser is well-defined by inserting a horizontal oriented linear polarizer (LP) in the laser path before lens L1. Between the polarizer and the lens, a variable phase retarder is placed with its fast axis oriented 45° with respect to the linear polarizer. The phase retarder switches between horizontal and vertical linear polarization of the laser light by applying either a high or low voltage. In this way, the polarization can be switched without significant changes of the laser beam intensity or excitation position in the sample. A spin population is injected in the sample by circularly polarized light. The linear polarized laser light is, therefore, converted into circularly polarized light by quarter wave plate QWP1, located in front of the microscope objective. The circularly polarized laser light injects a spin population in the semiconductor sample, which therefore emits circularly polarized PL (optical selection rules, see sec. 3.3). The circularly polarized PL emitted from the sample is converted into linearly polarized light by QWP1. This is required in order to use a beam displacer, which is sensitive for linearly polarized light. The beam displacer, located in front of the spectrometer, is used to split the PL image in two images, corresponding to opposite polarizations. To eliminate the linear polarization dependency of the diffraction grating of the spectrometer, the linear polarized PL is converted into circularly polarized light by quarter wave plate QWP2. The spin polarization in the sample can be calculated by applying eq. 3.11 using the PL extracted from the two polarization-resolved images.

Dichroism of the optical setup components may, however, affect the polarization of the signal image when it passes through the setup. The method used to correct for dichroism of the optical components will be illustrated using the measurement of reflected laser light, as shown in fig. 4.8. In this experiment, a laser beam with low intensity (of the order of nW) follows the same optical path as described above, reflects from the sample and is guided to the spectrometer. Figure 4.8(a) shows the reflected laser light for an initially left-hand circularly polarized (LHCP) laser beam. The reflection of a circularly polarized laser beam switches its polarization upon near-normal reflection. This accounts for the

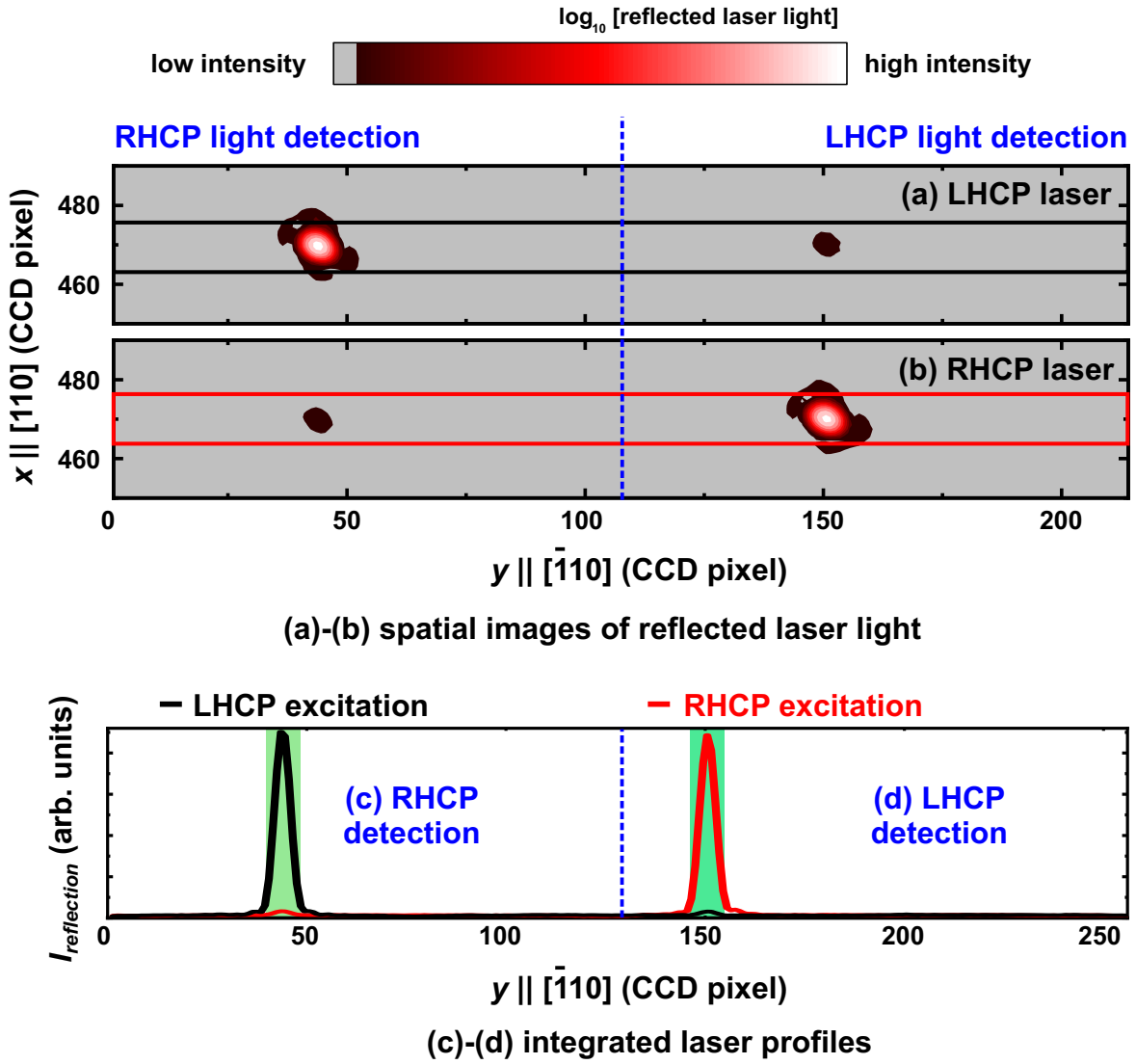

Figure 4.8: Polarization-resolved PL measurement method, illustrated by detection of reflected laser light. Figures (a) and (b) show the reflected laser light for an initially LHCP and RHCP laser beam, respectively. The blue dashed line marks the separation between RHCP and LHCP detection. Figures (c) and (d) show the reflected light intensities integrated within the area highlighted by the black rectangle (for the black plot) in fig. (a) and red rectangle (for the red plot) in fig. (b).

fact that the left-hand side of fig. 4.8(a) corresponds to a right-hand circular polarization (RHCP) of the light when it enters the spectrometer. Thus, the CCD pixels $1 \leq y \leq 107$ correspond to RHCP light detection, while the CCD pixels $108 \leq y \leq 214$ correspond to LHCP light detection. This is indicated by the blue dashed line in the figure. Integration of the detected light within the area highlighted by the black rectangle results in a spatial profile of the intensity of the reflected laser light $I_{reflection}$, shown by the black plot in figs. 4.8(c) and (d). The next step of the correction method is to switch the initial laser polarization to RHCP using the variable phase retarder. Figure 4.8(b) shows the reflected laser light for a RHCP initial laser beam. In this case, the intensity of reflected LHCP light is strong, while the intensity of reflected RHCP light is weak. Integration of the detected light within the area highlighted by the red rectangle results in a spatial profile of the laser reflection, shown by the red plot in figs. 4.8(c) and (d). Further integration of the black plot in figs. 4.8(c) and (d) within the regions highlighted by green rectangles provides the intensities I_{LR} and I_{LL}, respectively. Similarly, integration of the red plot within the same regions provides the intensities I_{RR} and I_{RL}. Here, the first (second) index describes the polarization of the initial (reflected) laser beam. The ratio a_r between LHCP and RHCP reflected laser light is calculated by:

$$a_r^2 = \frac{I_{LL} \cdot I_{RL}}{I_{RR} \cdot I_{LR}} = \left(\frac{r_L}{r_R}\right)^2, \tag{4.2}$$

where r_L and r_R are the transmission coefficients of the optical components in the optical signal path for LHCP and RHCP light, respectively. To correct for a difference between r_L and r_R, the initial laser beam is RHCP polarized and the RHCP detected light is corrected with respect to LHCP detection using a_r:

$$I_{RR} \rightarrow a_r I_{RR}. \tag{4.3}$$

Equation 3.11 is then corrected for polarization-dependent transmission of the optical components in the setup using eqs. 4.2 and 4.3:

$$\rho = \frac{a_r I_{RR} - I_{RL}}{a_r I_{RR} + I_{RL}}. \tag{4.4}$$

The detection of the laser polarization using this method yields a laser polarization of $-95\,\%$. Since one expects the initial laser beam to be fully circularly polarized with a reversal of its polarization upon reflection ($\rho = -100\,\%$), this reveals an error margin of $\Delta\rho = 0.05\rho$. This error margin, which remains after the dichroism correction method, results from (i) a combination of small deviations of the fast axis alignments of the linear polarizer, quarter wave plates, beam displacer or phase retarder and (ii) from the data analysis process. Note that the latter effect contribution should decrease for large intensities of the detected light.

For the experimental detection of spins by polarization-resolved PL, the intensity of the initial laser beam is of the order of 10^1 to $10^2\,\mu W$. Polarization-resolved PL is then detected using the method described above, where the intensities I_{LL}, I_{LR}, I_{RR} and I_{RL} now depict the detected PL (rather than the reflected laser light). The spin polarization $\rho_z \equiv \rho$ is finally calculated by eq. 4.4. In order to avoid division by zero, a small offset is added to the PL intensities in order to always maintain finite and positive intensities. The value of this offset is small compared to the detected PL intensity, so that its effect on the error margin is negligible. In contrast to laser reflection, PL has the same polarization as the excitation laser. Thus, one expects a positive polarization of the PL.

4.4.2 Pump-probe Kerr rotation experiments

Spin dynamics can, alternatively, be measured using the magneto-optical Kerr effect (MOKE), discovered by John Kerr in 1876 [129]. In a spin-polarized material, circular dichroism leads to a rotation of the linear polarization of a laser beam upon reflection. A comparison of the linear polarization of an incident laser beam with its reflection quantifies, therefore, the spin polarization of the sample. For experiments in this thesis, polar MOKE is used, as illustrated in fig. 4.9. Here, a laser beam with a near-normal angle of incidence is reflected off a magnetized sample. The magnetization is indicated by the electrons with spin (brown dots). Before reflection, the laser beam is horizontally polarized. After reflection, the laser beam polarization is rotated by the Kerr angle θ_{Kerr}. The Kerr angle depends linearly on the magnetization of the sample and, typically, has small values. Thus, a large signal sensitivity of the experimental setup is required.

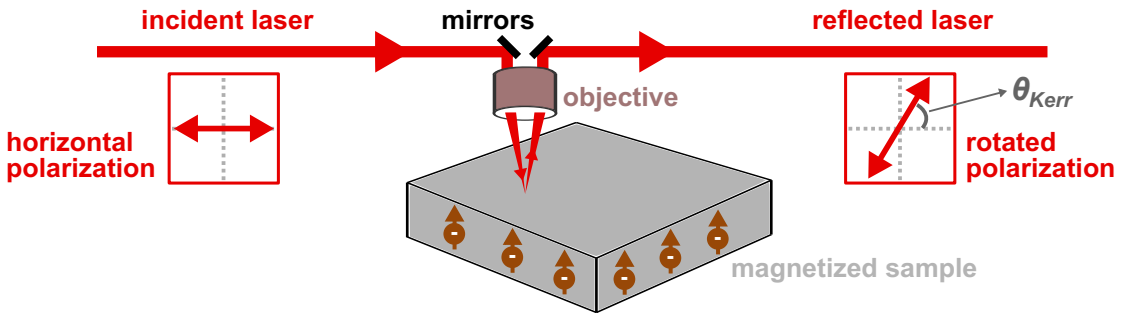

Figure 4.9: Polar MOKE: a horizontally polarized laser beam is reflected off a magnetized sample. The magnetization is represented by the electron-spins (brown dots). The polarization of the reflected laser beam is rotated by the Kerr angle θ_{Kerr}.

In acoustic transport experiments, carriers are transported by a SAW. Remote recombination of carriers can be used for polarization-resolved PL measurements to detect the spin polarization. Kerr rotation experiments have the advantage that one does not require PL to detect the evolution of the spin polarization. Thus, one can use Kerr rotation experiments to probe the spin polarization without requiring carrier recombination. In a time-resolved Kerr rotation (TRKR) experiment, a spin population is optically injected in the sample by a pump beam, after which the Kerr rotation is measured by a separate probe beam. The intensity of the probe beam, of the order of nW, is too small to induce perturbations of the spin population: Kerr rotation detection is, thus, a non-intrusive experimental method. The temporal resolution of TRKR measurements is achieved by pulsing the pump and probe lasers and delaying the arrival of the probe pulse at the sample with respect to the pump pulse. For the studies in this thesis, it is useful to tune the excitation (pump) energy independently from the probe wavelength. Therefore, a two-colour TRKR scheme is used, where the pump and probe beams originate from separate laser sources.

The experimental TRKR setup is shown in fig. 4.10. A wavelength-tunable Ti:sapphire pump laser (Spectra-Physics Tsunami) provides short excitation pulses with a duration of 1.5 ps and is focused by lens L1 onto the sample, with a 45° angle of incidence and a 7 µm FWHM of the spot size. The pump polarization is modulated between LHCP and RHCP light by a photoelastic modulator (PEM) at a frequency of 50 kHz. Before hitting the sample, a beam splitter (BS) directs part of the pump beam into a photodetector (PD), which measures the pump intensity. A connected feedback loop controls a neutral density filter wheel (NDW) to stabilize the excitation density at a preset level. The reflection of the pump off the sample is not required for the experiment and is physically blocked.

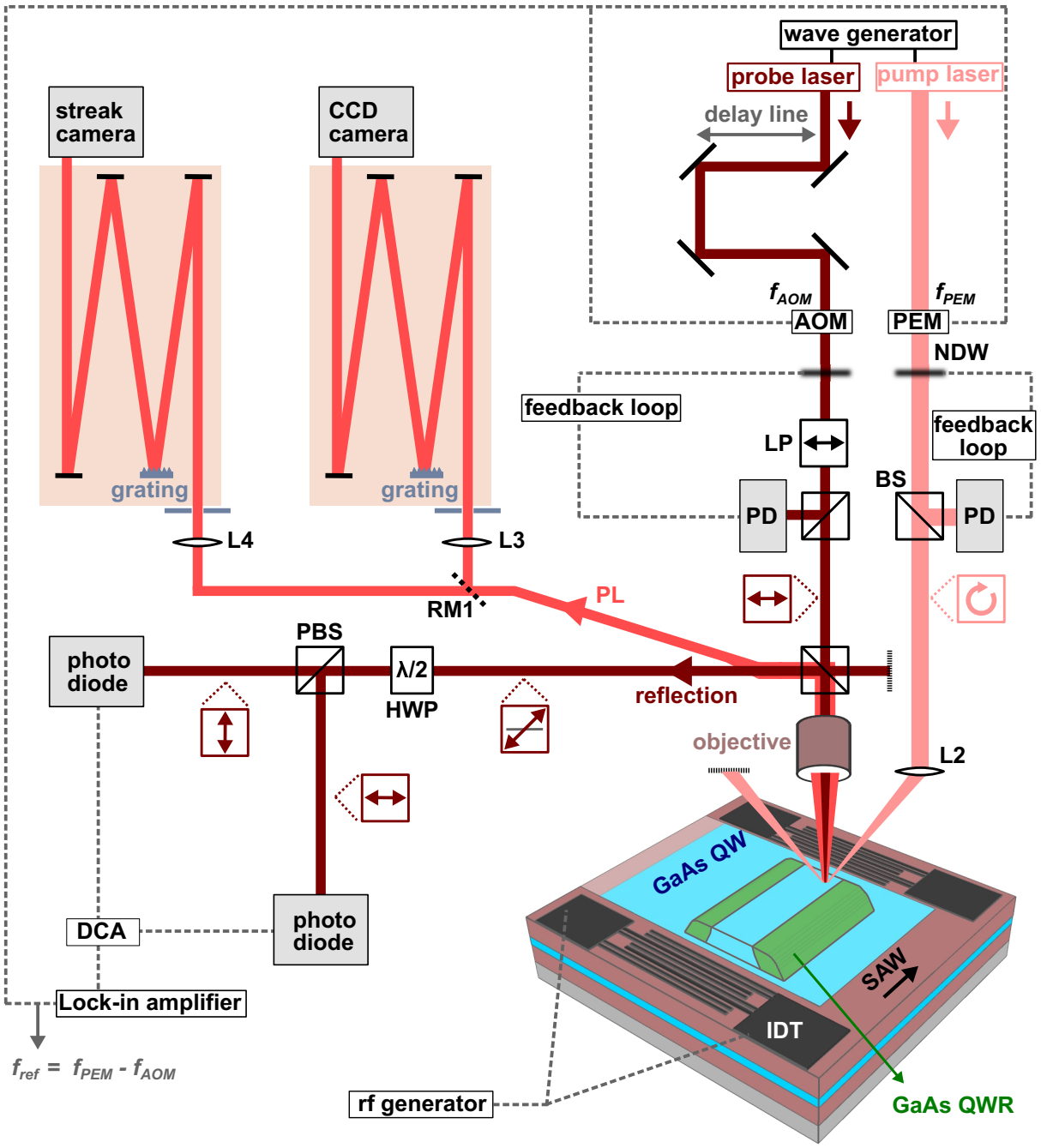

Figure 4.10: Overview of the experimental setup used to perform pump-probe time-resolved Kerr rotation experiments. A pump laser (bright red) is modulated between LHCP and RHCP by a photo-elastic modulator (PEM). A probe beam (dark red) is used to measure the Kerr rotation induced by the pump. Alternatively, the PL can be measured using a single-grating spectrometer equipped with a CCD camera for spectral resolution, or using a separate single-grating spectrometer equipped with a streak camera for additional temporal resolution. An elaborate description of the setup can be found in the main text.

The probe pulse (pulse duration 8 ps) is provided by a separate wavelength-tunable Ti:sapphire laser. The pump and probe pulses are synchronized by an external wave generator. The probe is focused by a microscope objective onto the sample with near-normal incidence and a 3 µm size FWHM of the laser spot. Before hitting the sample, the probe travels through a delay line with a Bragg reflector to systematically vary the delay between the probe and pump pulse arrival times at the sample. After the delay line, the probe intensity is stabilized with a feedback loop consisting of a beam splitter, photodetector and neutral density filter wheel. A linear polarizer (LP) is inserted into the optical path of the probe beam to induce a horizontal polarization. The probe reflection from the sample is guided through the microscope objective onto a polarizing beam splitter (PBS), which separates the reflected probe into horizontally and vertically polarized beams, guided to associated photodiodes. Note that the polarization of the initial and reflected probe beams are linear. The differential signal of the two photodiodes is a measure of the probe polarization and is amplified by a differential current amplifier (DCA). A half-lambda wave plate (HWP) is inserted in front of the PBS to eliminate intrinsic and background polarization rotations by turning its fast axis until the differential signal disappears for zero pump intensity. To improve the detection sensitivity, the initial probe beam is chopped at a frequency of 52 kHz using an acousto-optic modulator (AOM). The DCA signal is supplied to a lock-in amplifier, which is synchronized to the frequency difference of AOM and PEM: $f_{ref} = f_{AOM} - f_{PEM} = 2\,\text{kHz}$. The modulation of the probe and pump beams leads to an improvement of the signal-to-noise ratio, which is an essential part of the experimental method.

The same setup can also be used for basic PL experiments. For these experiments, either the pump or probe laser is used as an excitation source. The PL emitted from the sample follows the same optical path as the reflection of the probe beam in TRKR experiments. The part of the setup used to detect the probe reflection polarization (consisting of the HWP, PBS and photodiodes) is mounted on a removable stage. If this stage is removed, the beam coming from the sample is guided onto the entrance slit of a single-grating spectrometer equipped with a CCD camera. For clarity reasons, the optical paths of the sample reflection in TRKR experiments and the PL in spectroscopic measurements are drawn as different paths in fig. 4.10. The PL can alternatively be guided onto the entrance slit of a separate single-grating spectrometer, equipped with a Hamamatsu streak camera for time-resolved PL measurements. The streak camera converts photons into electrons, which are deflected by a time-varying voltage onto a phosphor screen. By increasing the voltage with time, electrons originating from later photon arrivals are deflected with a larger angle than those originating from earlier photon arrivals. The result is a two-dimensional image, where the horizontal axis represents spectral resolution and the vertical axis represents temporal resolution.

A typical result of time-resolved Kerr and PL experiments, without SAW, is an exponential decay of the signal with time constants τ_K and τ_R, respectively. The Kerr signal contains both the processes of spin decay and carrier recombination. Therefore, τ_K has to be corrected using τ_R to extract the spin lifetime τ_S:

$$\tau_S = \frac{\tau_K \tau_R}{\tau_R - \tau_K}. \tag{4.5}$$

chapter 5

Investigation of the fabrication process

In this chapter, an in-depth study of the fabrication process of sidewall quantum wires on GaAs substrates is presented. The formation of the quantum wires relies on the anisotropic overgrowth by molecular-beam epitaxy (MBE) of a quantum well (QW) structure on mesas prepatterned on the GaAs substrates. The fabrication process involves three main steps, which are outlined in the first section. In the second section, a study by atomic force microscopy (AFM) reveals the structural quality of the mesas on which the quantum wires are formed. The third section provides an analysis of the structural properties of the sidewall quantum wires and the fourth section summarizes the findings of the chapter.

5.1 General outline of the fabrication process

The fabrication of the sidewall quantum wire (QWR) on GaAs substrates is based on previous works as described in refs. [46, 47] and illustrated in fig. 5.1. For the samples studied in this thesis, the starting point of the fabrication is either a GaAs (113)A or GaAs (001) substrate (grey in fig. 5.1(a)). In the first step, a diluted photoresist (brown, AR-P 5800/7) is spin-coated onto the substrate surface using a spinning speed of 4000 rpm, resulting in a photoresist thickness of approx. 100 nm to 200 nm. Subsequently, the photoresist is exposed to UV light with a wavelength of 250 nm. During exposure, the photoresist is partly shielded with an optical chromium mask. This mask contains the mesas to be patterned, as highlighted by the bright brown area in fig. 5.1(b). The photoresist used in this thesis is a positive resist, meaning that it becomes soluble after light exposure. After exposure, the sample is rinsed in a diluted developer (AR 300/35). The light-exposed photoresist is dissolved, so that only those areas, which have not been exposed to light, remain covered by photoresist (fig. 5.1(c)). To remove remaining oxide on the surface, the sample is cleaned by exposure to an ozone plasma for 30 s. The sample is then wet chemically etched by soaking it in a diluted etching solution. Such a solution contains the oxidation agent H_2O_2, which reacts with the substrate surface and creates an oxide layer over it. An acid in the etching solution reacts with this oxide layer, thereby etching the surface. The etching solution is typically diluted by adding H_2O to decrease the etching rate and obtain better control over the etching depth. In this chapter, results of fabrication using various etching solutions are reported. It will be clearly stated which etching solution was used for each result. After etching, rinsing the sample in acetone and isopropanol removes photoresist from those areas, where it was protected by the chromium

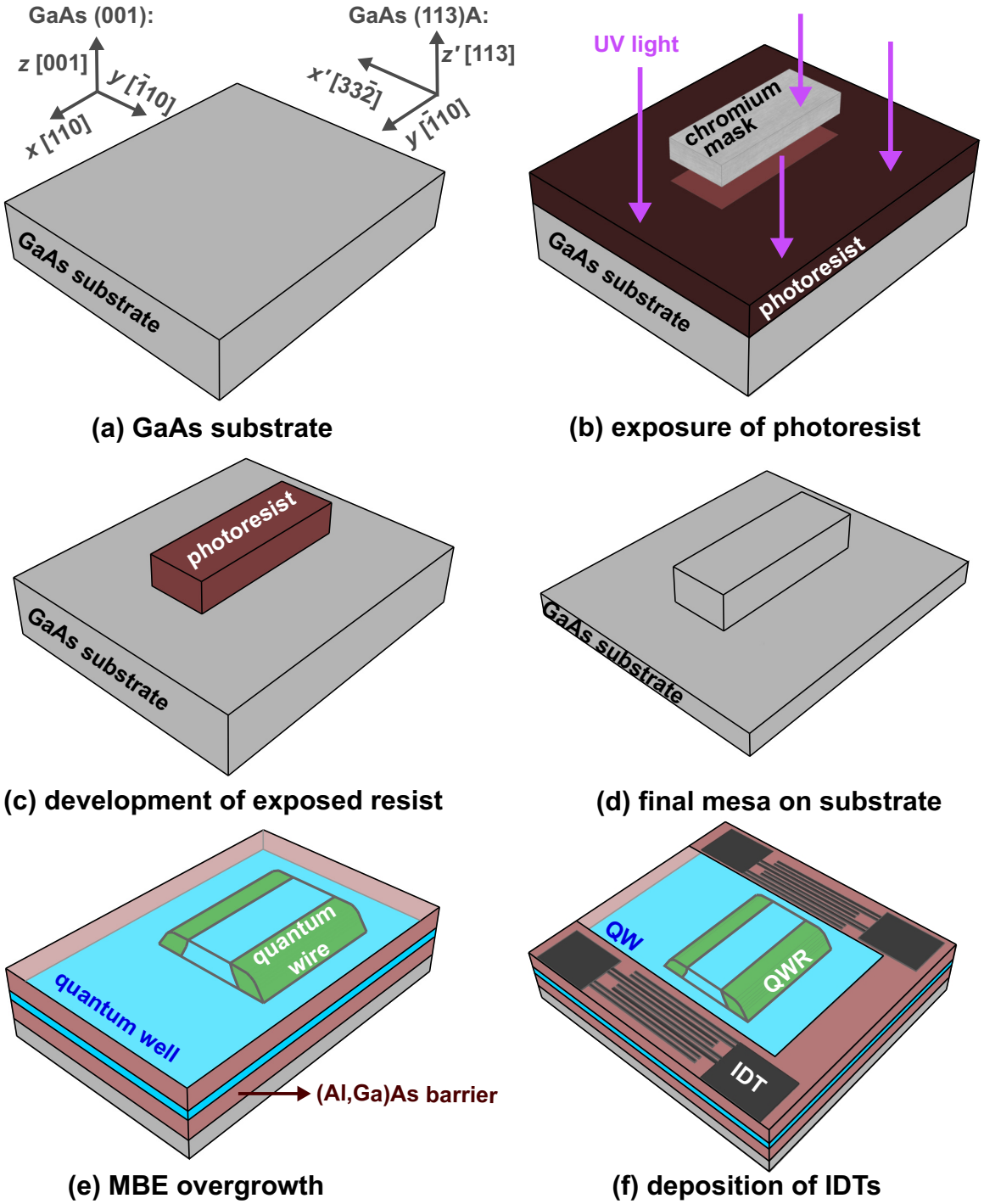

Figure 5.1: Schematical overview of the fabrication process. The starting point is either a GaAs (113)A substrate or a GaAs (001) substrate (grey) (a). (b) A positive photoresist is spin-coated onto the substrate (brown). An optical mask made of chromium shields the ridge area during exposure of the photoresist to UV light. (c) The exposed photoresist becomes soluble in a developer, leaving only those areas covered by photoresist, which were masked during light exposure. (d) Sketch of a typical ridge after wet chemical etching. (e) The prepatterned substrates are overgrown by MBE to form a 10 nm thick GaAs QW layer (blue), sandwiched between two $Al_{0.15}Ga_{0.85}As$ barriers (red). On GaAs (001), the anisotropic overgrowth of the QW layer leads to the formation of planar sidewall quantum wires at both sidewalls of the ridge (green). (f) IDTs (black) are defined for generation of a SAW by deposition of a metallic split-finger structure onto the top surface.

mask. In order to remove any rest of photoresist still sticking to the surface, the sample is exposed to UV light for 60 s without mask and subsequently developed, so that any photoresist is rinsed off the surface. In the final step, the sample is cleaned by soaking it in sulfuric acid for one minute under application of ultrasound. A typical mesa, a rectangular ridge with a height of several tens of nanometers, is illustrated in fig. 5.1(d).

In the next step, the prepatterned substrate is overgrown with a QW structure by MBE. In the cleaning chamber of the MBE apparatus, the sample is exposed to atomic hydrogen to remove remaining carbons and oxides from the sample surface, which takes place in a background H_2 pressure of 5×10^{-5} mbar for 30 minutes, while the substrate is heated to a temperature of 450 °C. After surface cleaning, the sample is transferred inside the UHV system to the MBE growth chamber and heated to the growth temperature of 600 °C. Here, the prepatterned substrate is overgrown with an (Al,Ga)As QW structure (see fig. 5.1(e)). Firstly, a 13 nm thick (Al,Ga)As layer partly smoothens the substrate surface roughness. The sample is then overgrown with a 10 nm thick GaAs QW layer (blue), sandwiched between two $Al_{0.15}Ga_{0.85}As$ barriers (red) with thicknesses of 117 nm (lower barrier) and 200 nm (upper barrier). The (Al,Ga)As barriers are grown in conventional MBE mode, meaning that the substrate is simultaneously exposed to fluxes from the Al, Ga and As sources. The GaAs QW layer, in contrast, is grown by migration-enhanced epitaxy (MEE), where the Ga and As fluxes from the sources are applied in an alternating fashion. The MEE mode increases the surface diffusion length of adatoms during growth, which plays an important role in the formation of QWRs. On GaAs (001) substrates, the anisotropic overgrowth of the QW leads to the formation of QWRs on both sidewalls of ridges oriented along [110], as will be discussed in sec. 5.3.2. On GaAs (113)A substrates, QWR formation occurs only on one sidewall of ridges oriented along $[\bar{1}10]$, as will be discussed in sec. 5.3.1. After the growth of the upper $Al_{0.15}Ga_{0.85}As$ barrier, a 2 nm thick passivating GaAs layer is grown to protect the sample against native oxidation. The growth rates of the GaAs and $Al_{0.15}Ga_{0.85}As$ layers are 0.16 nm/s and 0.14 nm/s, respectively.

The final step of the fabrication process is the deposition of the interdigital transducers (IDT) by a metallization lift-off process. The IDTs are photolithographically predefined in a photoresist, after which a metallic sequence of 10 nm Ti, 30 nm Al and 10 nm Ti is vapour-deposited onto the substrate. The photoresist is then washed away by rinsing the sample in acetone, after which the metallic grating defines the IDTs as sketched in fig. 5.1(f). Unless stated otherwise, the IDTs are designed for a wavelength of $\lambda_{SAW} = 4\,\mu m$, resulting in a SAW frequency of $f_{\mathrm{SAW}} = 726$ MHz at a temperature of 15 K.

5.2 Structural properties of the mesas

In this section, the structural properties of prepatterned mesas are studied by AFM. Since previous works have been carried out on acoustic spin transport in sidewall QWRs on GaAs (113)A substrates, this is the starting point. A typical mesa is rectangular with a width of 10 µm, a variable length and a height of approx. 40 nm. The main etching solution used throughout this thesis is the piranha solution. This is a sulfuric-based solution, consisting of $H_2SO_4 : H_2O_2 : H_2O$. Whenever the text refers to strong acid piranha etching, the ratio of $H_2SO_4 : H_2O_2 : H_2O$ is (8:1:100), whereas weak acid piranha etching is prepared as $H_2SO_4 : H_2O_2 : H_2O$ (1:8:100).

5.2.1 Mesas on GaAs (113)A substrates

Figures 5.2(a)-(d) display AFM profiles across the sidewalls of a 4 µm x 4 µm sized ridge, patterned on a (113)A substrate using weak acid piranha etching. The measurement

directions are depicted by the black lines in the right panel: profiles A and C correspond to the sidewalls along the $[33\bar{2}]$ direction, whereas profiles B and D correspond to the sidewalls along the $[\bar{1}10]$ direction. These line profiles can be fitted by an error function (empirically determined) to characterize the surface height $h(x_m)$ as function of the position coordinate x_m perpendicular to the ridge edge. Such a fit is represented by a red line in fig. 5.2(b) and is mathematically defined by the following equation:

$$h(x_m) = h_0 + \frac{A_{etch}}{2} \operatorname{erf}\left(\frac{x_m - x_{etch}}{w_{etch}}\right), \tag{5.1}$$

where h_0 represents an offset, A_{etch} the etching depth, x_{etch} the center position of the etching step and w_{etch} a parameter defining the width of the etching step. A fit of the sidewall profiles with eq. 5.1 yields a nominal etching depth of 200 nm. The slope of eq. 5.1 at $x_m = x_{etch}$ provides an estimate for the angle $\theta_{sidewall}$ between the ridge and the substrate surface, as marked in fig. 5.2(d):

$$\frac{\partial h}{\partial x_m} = \frac{A_{etch}}{\sqrt{\pi w_{etch}^2}} e^{-\left[\frac{x_m - x_{etch}}{w_{etch}}\right]^2} \rightarrow \theta_{sidewall} = \arctan\left(\frac{A_{etch}}{\sqrt{\pi w_{etch}^2}}\right). \tag{5.2}$$

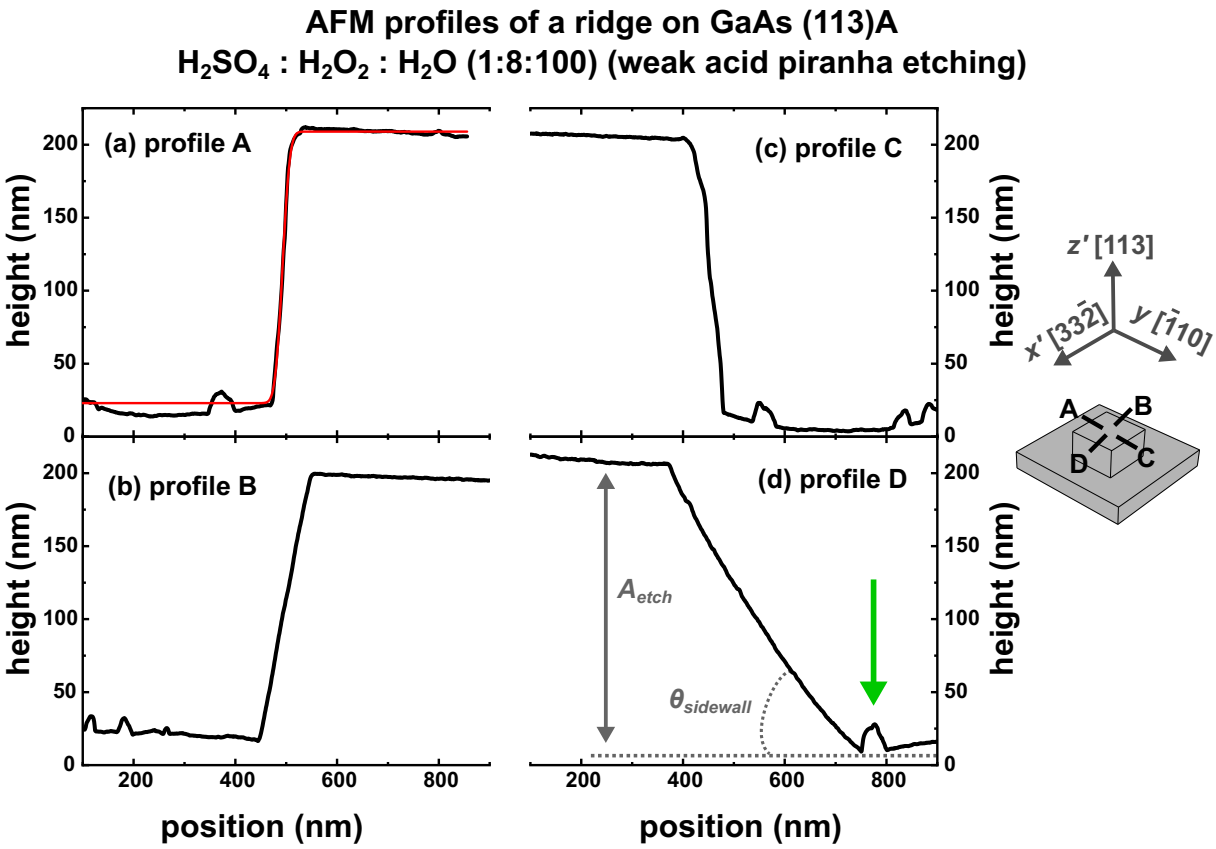

Figure 5.2: AFM profiles of the sidewalls of a 4 µm x 4 µm sized ridge on a (113)A substrate, patterned using weak acid piranha etching. Figures (a)-(d) correspond to the profiles as indicated by black lines in the right panel. The red line in fig. (a) shows a fit of the profile with eq. 5.1, which yield the parameters A_{etch} and $\theta_{sidewall}$ defined in fig. (d). The green arrow in fig. (d) highlights a mound.

Using this procedure, it is found that etching along $[33\bar{2}]$ is steep and symmetric: profiles A and C have inclination angles of approx. 80°. Etching along $[\bar{1}10]$ is asymmetric: profiles B and D have inclination angles of approx. 65° and 33°, respectively. The inclination

angles of profiles B and D imply that these sidewalls correspond to the $(\bar{3}\bar{3}5)$ and the (111) facets, respectively. The findings presented here are similar to those reported in ref. [46]. The profiles of figs. 5.2 also display mounds with a typical height of approx. 10 nm (marked with a green arrow in fig. (d)), which are related to either (i) a local distortion of the etching process or (ii) contaminations on the surface. In some of the cases, these mounds can be removed by an additional cleaning step, hinting that they originate from contaminations as in case (ii), either from the photolithography or from the etching process. A distortion of the etching process as in case (i) would result in a permanent surface feature, which can not be removed by surface cleaning.

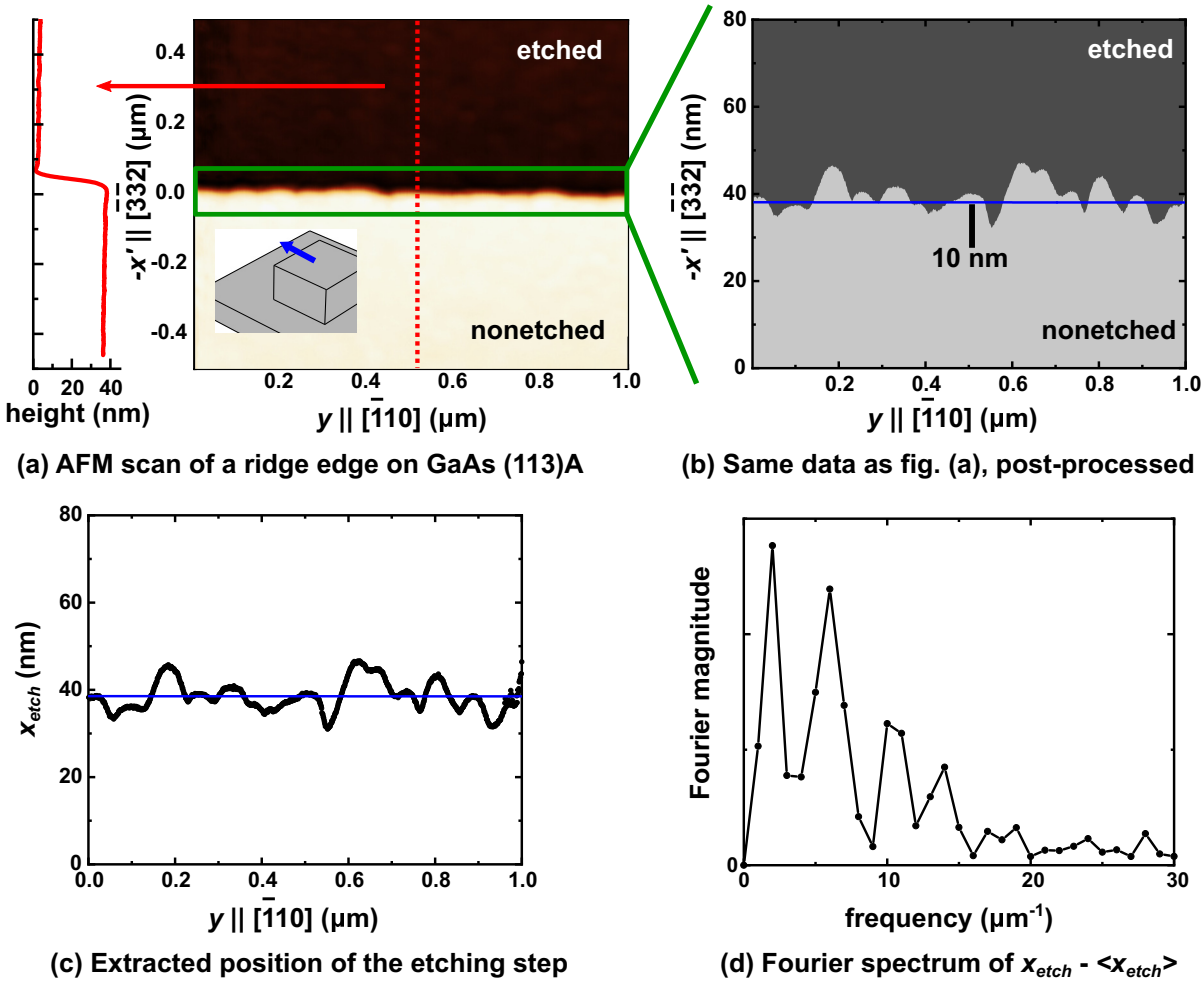

Figure 5.3: (a) AFM scan of the edge of a similar ridge as the one shown in fig. 5.2. The blue arrow in the inset indicates the fast scanning direction of the AFM. The left panel displays the AFM profile along the dashed red line, which is typical for the other profiles. (b) Details of the ridge sidewall in fig. (a), post-processed to show only the etched (dark) and nonetched (bright) surface levels of the area enclosed by a green rectangle in fig. 5.3(a). The blue line represents the nominal position of the ridge edge. (c) Plot of x_{etch} as function of its $y||[\bar{1}10]$ coordinate as extracted from fitting the profiles of fig. (a) with eq. 5.1. The blue line marks the nominal position of x_{etch}. (d) Fourier spectrum of $x_{etch} - \langle x_{etch} \rangle$.

A full AFM scan of a 1 µm x 1 µm sized area around a similar ridge sidewall along $[\bar{1}10]$ is shown in fig. 5.3(a). The fast scanning direction of the AFM is along $[\bar{3}\bar{3}2]$, as indicated in the inset with a blue arrow. The image is constructed with a lateral resolution of approx. 1 nm. The dark and bright areas correspond to etched and nonetched areas,

respectively. A sidewall profile along the vertical dashed red line is displayed in the left panel. The etching depth of this sample is approx. 40 nm. The shallower etching depth of this sample as compared to the sample in fig. 5.2 is attributed to a larger dilution of the etching solution with H_2O (H_2SO_4 : H_2O_2 : H_2O 1:8:400). The image clearly reveals that the ridge edge (the boundary between the etched and the nonetched areas) is not perfectly straight. To study the structural quality of the ridge edge, fig. 5.3(b) displays an enlarged view of the area enclosed by the green rectangle in fig. 5.3(a). For clarity, only the surface levels of the etched (dark) and the nonetched areas (bright) are shown. The boundary between the dark and bright areas clearly illustrates fluctuations of the etching step position x_{etch}. An estimation of the LER value can be obtained by fitting the AFM profiles as in the left panel of fig. 5.3(a) with eq. 5.1, to extract x_{etch} as function of its position along $[\bar{1}10]$. The result is plotted in fig. 5.3(c) by a black line. The resemblance of the black line to the boundary line between the dark and bright areas in fig. 5.3(b) proves that the fitting method works reasonably well. A linear fit of x_{etch} reveals the nominal position of the ridge edge, as indicated by blue lines in figs. 5.3(b) and (c). The standard deviation of x_{etch} is commonly referred to as line-edge roughness (LER) [130] and can be used to quantify the structural quality of the ridge edge. Thus, LER is defined by the following equation:

$$\mathrm{LER} = \sqrt{\frac{\sum \left[x_{etch} - \langle x_{etch} \rangle\right]^2}{N}}. \tag{5.3}$$

Here, $\langle x_{etch} \rangle$ is the nominal position of x_{etch} and N is the total number of AFM profiles. In this way, the LER value for this ridge is determined to be 4 nm. Taking into consideration that the fabrication process involves many parameters, of which some are sensitive to specific environmental conditions, it is worthwhile to repeat the quantification of LER on different samples. From 22 measurements performed on samples originating from two different 2-inch wafers, it is concluded that typical LER values are in the range of 4 nm to 9 nm, with a mean value of 6 nm and a spread of 2 nm. In sec. 5.3.1, this value for LER will be related to the QWR width after MBE overgrowth.

The overgrowth of a QW structure on these ridges leads to the formation of a QWR at the ridge sidewall. If the spatial fluctuations of x_{etch} are smooth, the QWR axis should follow them. In the opposite case, if they are varying with a small spatial period, the fluctuations have negative effects on the formation of the QWR, since this results in QWR width variations, and consequently in potential fluctuations along the QWR axis. The spatial frequency of the deviations can be assessed by the Fourier transform of $x_{etch} - \langle x_{etch} \rangle$ as function of its position along $[\bar{1}10]$, as shown in fig. 5.3(d). The figure demonstrates the presence of some high-frequency components, indicating that potential fluctuations along the QWR axis may be expected. A spatial frequency of 10/µm relates to fluctuations with a spatial period of 100 nm. Such fluctuations can have a negative impact on the optical properties and the transport properties of the QWR. Indeed, potential fluctuations along narrower QWRs with such a small period are reported in ref. [68] to be detrimental for acoustic charge and spin transport. Note that spatial frequencies below 1/µm cannot be measured, since the length of the measurement area is limited to 1 µm.

The surface roughness can be extracted from fig. 5.3(a) as well. The root-mean-square (RMS) surface roughness for the etched and nonetched areas, as extracted from a 0.5 µm^2 region, is approx. 0.5 nm for both cases. The similar surface roughnesses imply that the etching process does not induce a roughening of the surface. Since surface roughness leads to QW layer thickness fluctuations, it can negatively affect the QW properties.

5.2.2 Origin of line-edge roughness

The results presented in this section are obtained in collaboration with the Cavendish Laboratory located at the University of Cambridge (UCAM). There are two possible contributions from the fabrication process to LER: contributions from either photolithography and/or wet chemical etching. The etching process is investigated at first. The study of the etching process is conducted at UCAM, whereas the samples discussed in sec. 5.2.1 are fabricated at Paul-Drude-Institut Berlin. Therefore, a separate control sample is fabricated using weak acid piranha etching and with a different mask design available at UCAM. This sample has a LER value of 7 nm, which is similar to the results reported in the previous section. Firstly, the ratio of the piranha solution is changed from H_2SO_4 : H_2O_2 : H_2O (1:8:400) to (8:1:100) (changed from weak acid to strong acid), which results in a LER of 9 nm. This indicates no significant change.

Secondly, instead of a sulfuric based solution, a HCl-based solution HCl : H_2O_2 : H_2O (1:5:100) is tested for ridge fabrication. A post-processed AFM image of this sample is displayed in fig. 5.4(a), where the dark and bright areas represent the etched and nonetched areas, respectively. The LER value for this measurement is approx. 4 nm, which is on the lower bound of the previously measured 4 nm-9 nm range. However, subsequent measurements on a different sample revealed LER values of 9 nm and 10 nm, not confirming the small LER value. Furthermore, the inset shows a typical sidewall profile of a ridge fabricated by the HCl-based solution. As highlighted by a brown circle, a valley with a depth of approx. 10 nm between the ridge bottom (etched surface) and the ridge sidewall is observed. Although the valley does not appear if the sample is rinsed in a solution of HCl : H_2O (1:4) prior to etching, it suggests that the degree of control over the etching process is smaller for a HCl-based solution than for a H_2SO_4-based solution and, therefore, does not result in an improvement of the fabrication process.

Thirdly, a sample is also fabricated using a phosphoric-based solution, H_3PO_4 : H_2O_2 : H_2O (1:5:100). A post-processed AFM image of a ridge fabricated on this sample is shown in fig. 5.4(b). As the figure shows, the ridge edge has very large deviations from a straight line, resulting in a LER value of 17 nm, thus implying that the piranha solution is to be preferred over this phosphoric-based solution.

The AFM images of figs. 5.4(a) and (b) can be used to study surface roughness. A comparison of the RMS surface roughness of the etched and nonetched areas depicts that the surface roughness, which is approx. 1.0 ± 0.2 nm for both cases, is not significantly affected by the etching process for both solutions.

Finally, better control of the GaAs etching process is reported in previous works by using wet chemical digital etching [131]. In this method, treatment of the sample with the oxidation agent (H_2O_2) and the acid (H_2SO_4) is separated in two subsequent steps. Since oxidation is a self-limiting process, a well-defined thickness of the oxidation layer forms on the substrate surface. This limited oxide layer thickness should result in a limited etching depth per etching cycle. Therefore, better control over the etching rate can be expected, possibly resulting in an improvement of the ridge edge quality. To test whether this process reduces LER, a ridge is fabricated using the following sequence: (i) rinse the sample in a diluted H_2O_2 solution (31.5 %) for 15 s; (ii) rinse the sample for 15 s in a flowing DI cascade bath; (iii) etching the sample in a diluted H_2SO_4 solution (9 %) for 15 s; and (iv) rinse the sample for 15 s in a flowing DI cascade bath. Between every step, the sample is dry blown with a nitrogen pistol for 5 s. This sequence is repeated seven times. A 1 µm x 1 µm sized AFM scan of the ridge edge is shown in fig. 5.4(c). The figure displays that instead of a well-defined ridge edge, wet chemical digital etching results in a staircase of several etching steps, where each successive etching cycle creates an additional step. The step width is not constant, indicating that the etching rate varies over the course

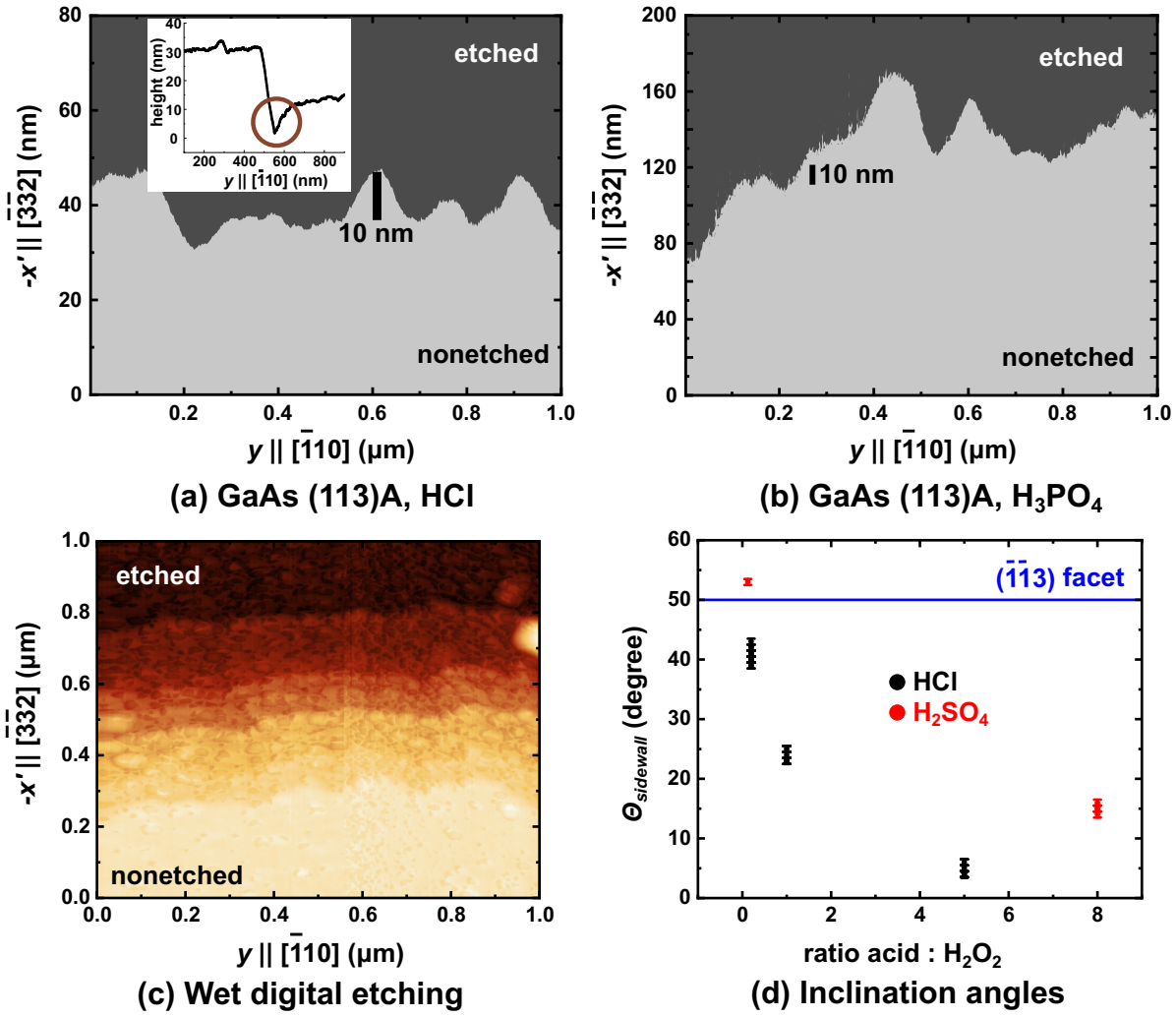

Figure 5.4: Investigation of the etching process. The figures show (post-processed) AFM images of ridge edges fabricated by a HCl-based solution (a), by a H_3PO_4-based solution (b), and by wet chemical digital etching using weak acid piranha etching (c). The inset in fig. (a) shows that HCl-based fabrication without pretreatment results in a valley between ridge bottom and sidewall. (d) Sidewall inclination angle for different ratios between the amount of acid and oxidation agent in the etching solution for HCl-based fabrication (black) and H_2SO_4-based etching (red). The blue line marks the angle of the $(\bar{1}\bar{1}3)$ facet, previously utilized for QWR fabrication [46].

of the different etching cycles, which may be explained as follows. The sidewall facet after the first etching cycle differs from the initial substrate orientation. Therefore, the sidewall etching of the second cycle starts with a different surface orientation than in the first cycle, which may result in different etching characteristics. This mechanism repeats itself after every etching cycle, since each etching cycle may change the orientation of the sidewall surface. However, a detailed study is out of the scope of this thesis. The step-wise sidewall after wet digital etching is not reported in ref. [131]. The results reported here exclude improvement and better control over the etching process.

Summarizing, both the H_2SO_4-based and HCl-based solutions produce similar results, whereas the H_3PO_4-based solution and the wet chemical digital etching show poor results. The MBE growth rate of the sidewall depends on the inclination angle of the sidewall and is fast for a steep sidewall, resulting in a sidewall facet close to (001) [132, 49]. The sidewall angle can be engineered by changing the ratio of the acid and the oxidation agent in the etching solution, as is shown in fig. 5.4(d). Here, the inclination angle of the sidewall resulting from ridge fabrication using a HCl-based solution (black) and a H_2SO_4-based solution (red) is shown for different ratios. A small ratio corresponds to a weak acid concentration. The blue line marks the inclination angle required for a $(\bar{1}\bar{1}3)$ facet, which is the one used for the QWR formation reported in ref. [46]. A weak acid concentration results in a steep sidewall and is, therefore, preferable for the fabrication of planar sidewall quantum wires on (113)A substrates.

The results presented above suggest that the origin of LER lies in the photolithography process. A quantification of photoresist LER could not be obtained using AFM, since the large height of the photoresist limits the resolution of the AFM tip, which has a finite radius. To study LER in the photoresist, fig. 5.5(a) presents a side-view scanning electron microscopy (SEM) image of the photoresist, after development and before etching. The photoresist is displayed as a dark layer on top of the (113)A substrate, which is represented by a bright layer. The lower panel shows an enlarged view of the photoresist edge. The edge between the covered and uncovered substrate areas is not a perfect straight line, as is clear from the surface roughness on the photoresist mesa sidewall, i.e. the sidewall is not flat.

A top-view SEM image of a triangular mesa on a (113)A substrate is shown in fig. 5.5(b). Here, an equilateral triangle with an arm length of 5.5 µm is imaged before etching the substrate. As in fig. 5.5(a), the covered and uncovered substrate areas are represented by the dark and bright areas, respectively. The inset illustrates how the mesa looks like on the optical mask and how it should be transferred to the substrate. The corners of the triangle are intended to be sharp. However, for small features such as these triangle corners, the resolution of the photolithography limits the fabrication process, resulting in a misformation of the triangular corners on the substrate. Furthermore, the edges of the triangle are not perfectly straight lines, which demonstrates that LER is also present in the photoresist before wet chemical etching. An estimation of the LER value can be provided by enlarging the triangular edge, as shown in fig. 5.5(c). The upper and lower areas of the image represent the (113)A substrate and the photoresist, respectively. The image clearly reveals fluctuations of the mesa edge in the photoresist. The 10 nm bar indicates that the scale of the fluctuations is similar to those observed in fig. 5.3(b). The SEM image confirms, therefore, that the main origin of LER lies in the photolithography process. Some of the parameters influencing LER are fluctuations of the mesa shape in the optical mask, photon shot noise from the light source, acid diffusion and photoresist sticking. For a detailed discussion the reader is referred to ref. [130].

The fact that photolithography is the main source of line-edge roughness implies that electron beam lithography (EBL) can be exploited to improve the quality of the mesa.

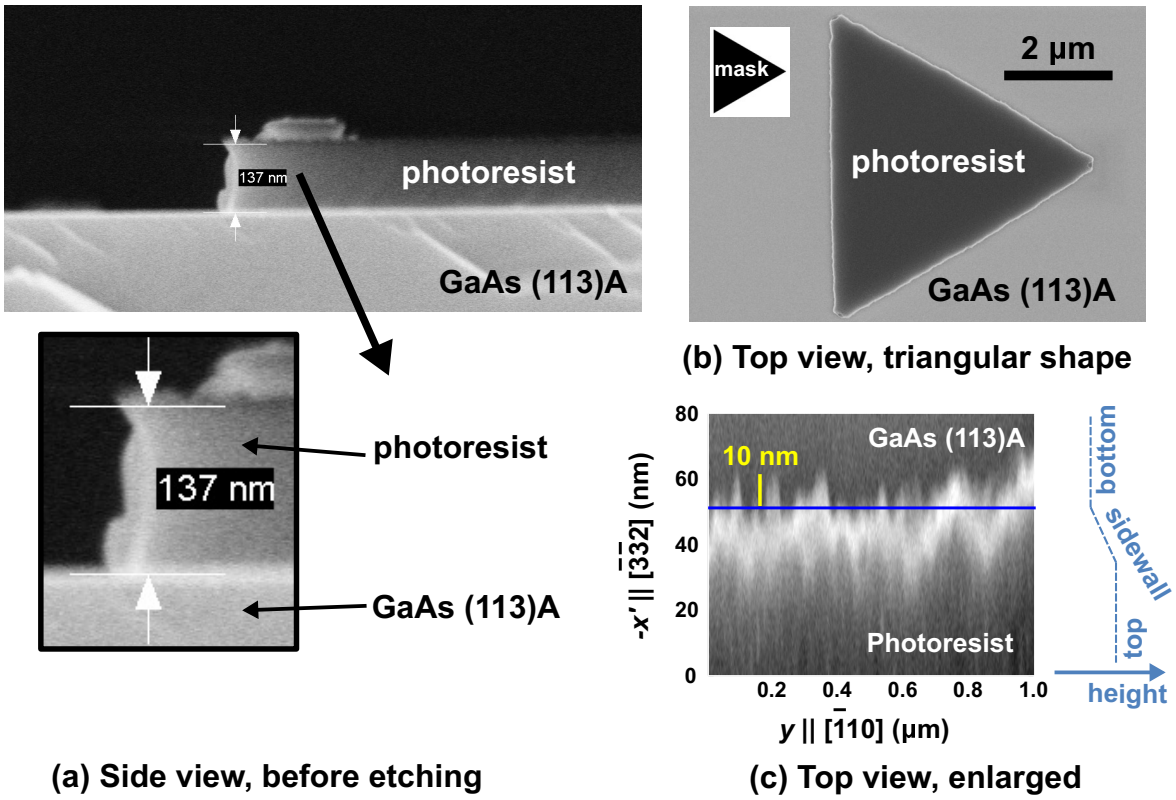

Figure 5.5: Line-edge roughness resulting from photolithography. (a) SEM side-view image of the photoresist edge. The photoresist and (113)A substrate appear as dark and bright areas, respectively. The lower panel shows an enlarged view of the photoresist edge. (b) Top-view SEM image of a typical triangular mesa as defined in the photoresist, before etching. The colours and contrast are conform fig. (a). The inset is a sketch of the design as defined on the optical mask. (c) Enlarged top-view of the photoresist edge. The blue line indicates the nominal position of the ridge edge. The right panel schematically illustrates a typical sidewall profile. The SEM images of figs. (a), (b) and (c) are recorded by Anne-Kathrin Bluhm.

In this method, an electron-sensitive resist is exposed to an electron beam. Since the wavelength of electrons is much smaller than the UV light wavelength, this leads to a better resolution. Although a detailed study of quantum wire formation on EBL-patterned substrates is not conducted in this thesis, some remarks about the structural quality of the EBL-defined mesas can be given from preliminary studies using test structures defined by EBL. For this purpose, an electron-sensitive resist (AR-P 6200) is spin-coated onto a (113)A substrate. The structures are defined by exposure of the resist to an electron beam, using a dose of 22 µC/cm^2, writing field of 100 µm and a step size of 20 nm. A post-processed AFM image of a mesa edge oriented along the [$\bar{1}$10] direction, after etching, is shown in fig. 5.6(a). The mesa is fabricated using weak acid piranha etching. The spatial fluctuations of the mesa edge have a similar scale as the ones observed for the photolithographically defined mesas. The LER value for this specific measurement is 6 nm, which is within the previous observed range.

In a second sample, the step size of the EBL is reduced to 2 nm. Due to the Gaussian shape of the electron beam, a smaller EBL step size should result in a better homogeneity of the resist exposure, which may improve the quality of the mesa edge. The mesa is, again, oriented along the [$\bar{1}$10] direction and etched using weak acid piranha etching. A post-processed AFM image of the result is shown in fig. 5.6(b). The reduction of the EBL step size results in an improvement of the mesa edge quality, since the amplitude of the spatial fluctuations is clearly reduced. For this specific measurement, the LER value is approx. 3 nm, which indicates the EBL step size as a way to improve the structural edge quality. Considering the low cost, ease of use, scalability and the low LER value (as compared to the QWR width, see sec. 5.3) for photolithography, it is justified to prepattern the GaAs substrates by photolithographically defined mesas. The reported results in the remainder of this thesis involve, therefore, only samples in which the mesas have been defined by photolithography.

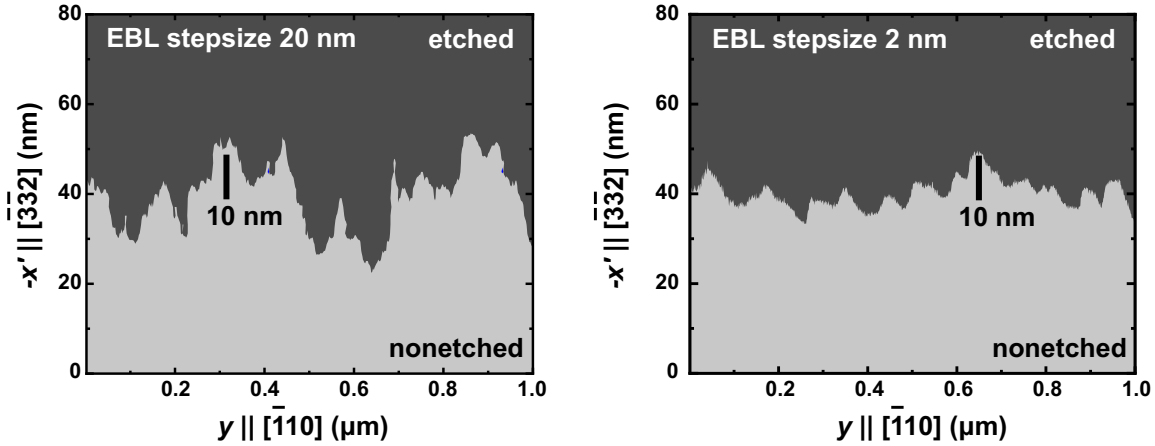

(a) Processed AFM image, GaAs (113)A (b) Processed AFM image, reduced stepsize

Figure 5.6: Line-edge roughness resulting from electron beam lithography. (a) Post-processed AFM image of a ridge edge defined by EBL after etching. The etched and nonetched areas appear as dark and bright, respectively. The step size of the EBL is 20 nm and the ridge is fabricated by weak acid piranha etching. (b) Post-processed AFM image of a similar ridge edge after etching, defined by EBL with a reduced step size of 2 nm. Again, the etched and nonetched areas appear as dark and bright, respectively.

5.2.3 Mesas on GaAs (001) substrates

In the following discussion, mesas fabricated on (001) substrates are investigated. The mesas are fabricated using (i) weak acid piranha etching and (ii) strong acid piranha etching. The AFM profiles of a 4 µm x 4 µm sized mesa fabricated using weak acid piranha etching are shown in figs. 5.7(a)-(d). Here, profiles A and C plot the AFM profiles of the sidewalls along [110] and profiles B and D display AFM profiles of the sidewalls along [$\bar{1}$10]. The profiles plotted in figs. 5.7(a)-(d) can be fitted with eq. 5.1, as displayed by the red lines. The fits depict a nominal etching depth of approx. 30 nm and indicate that etching the (001) substrate with weak acid piranha etching is symmetric, leading to profiles inclined at an angle of $30 \pm 3°$.

Figures 5.7(e)-(h) present AFM profiles across the sidewalls of a similar mesa, but fabricated using strong acid piranha etching. Profiles E and G correspond to edges oriented along [110], whereas profiles F and G correspond to the edges oriented along [$\bar{1}$10], as indicated in the right panel. As is the case for weak acid piranha etching, strong acid piranha etching is symmetric: the inclination angle of the sidewalls is $10 \pm 1°$ for all directions. The etching depth is of the same order of magnitude as observed in fig. 5.7(a)-(d).

Figure 5.8(a) illustrates a full AFM scan of a 1 µm x 1 µm sized area of a different mesa edge fabricated using strong acid piranha etching. The mesa is oriented along [110], which is the direction along which the QWRs form [47]. The dark and bright areas represent the etched and nonetched areas, respectively. The fast scanning direction of the AFM is along [$\bar{1}$10], as indicated in the inset by the blue arrow. A typical sidewall profile extracted from this image is displayed in the right panel. The profile is similar to those shown in figs. 5.7(e)-(h), demonstrating that the fabrication method is a reproducible process. A post-processed image of the same data is shown in fig. 5.8(b). For clarity reasons, only the surface heights of the etched area (dark) and nonetched area (bright) are displayed. A similar procedure as in sec. 5.2.1 depicts a LER value of 9 nm for this measurement, which is similar to the one for (113)A substrates. This implies that mesa fabrication on (113)A and (001) substrates result in a comparable edge quality.

Figure 5.8(c) shows a SEM image of the photoresist on a (001) substrate before etching. As observed for (113)A substrates, line-edge roughness is observed directly in the photoresist (i.e. before etching). A comparison of figs. 5.8(c) and (b) reveals that the scale of the line-edge roughness in the photoresist before etching is similar to the scale of LER after etching. This result confirms the conclusion that the main origin of LER is to be found in the photolithography process as well for (001) substrates.

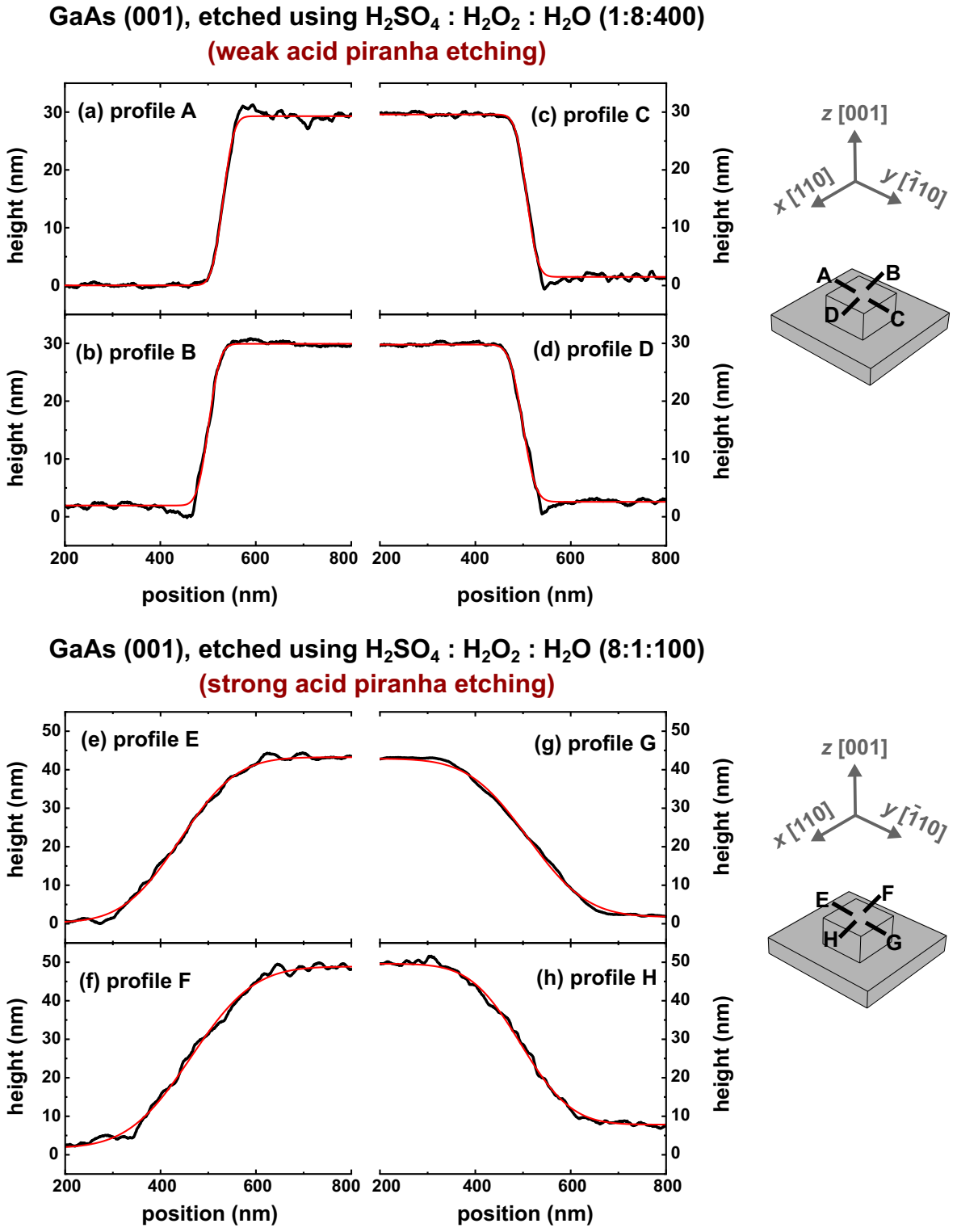

Figure 5.7: AFM profiles of mesa sidewalls across the edges of a 4 µm x 4 µm sized mesa on a GaAs (001) substrate. The red lines correspond to fits of the profiles with eq. 5.1. The black lines in the right insets indicate the directions along which the profiles are measured. Figures (a)-(d) show the line profiles measured on a mesa fabricated using weak acid piranha etching. Figures (e)-(h) show the AFM profiles measured on a different mesa fabricated using strong acid piranha etching.

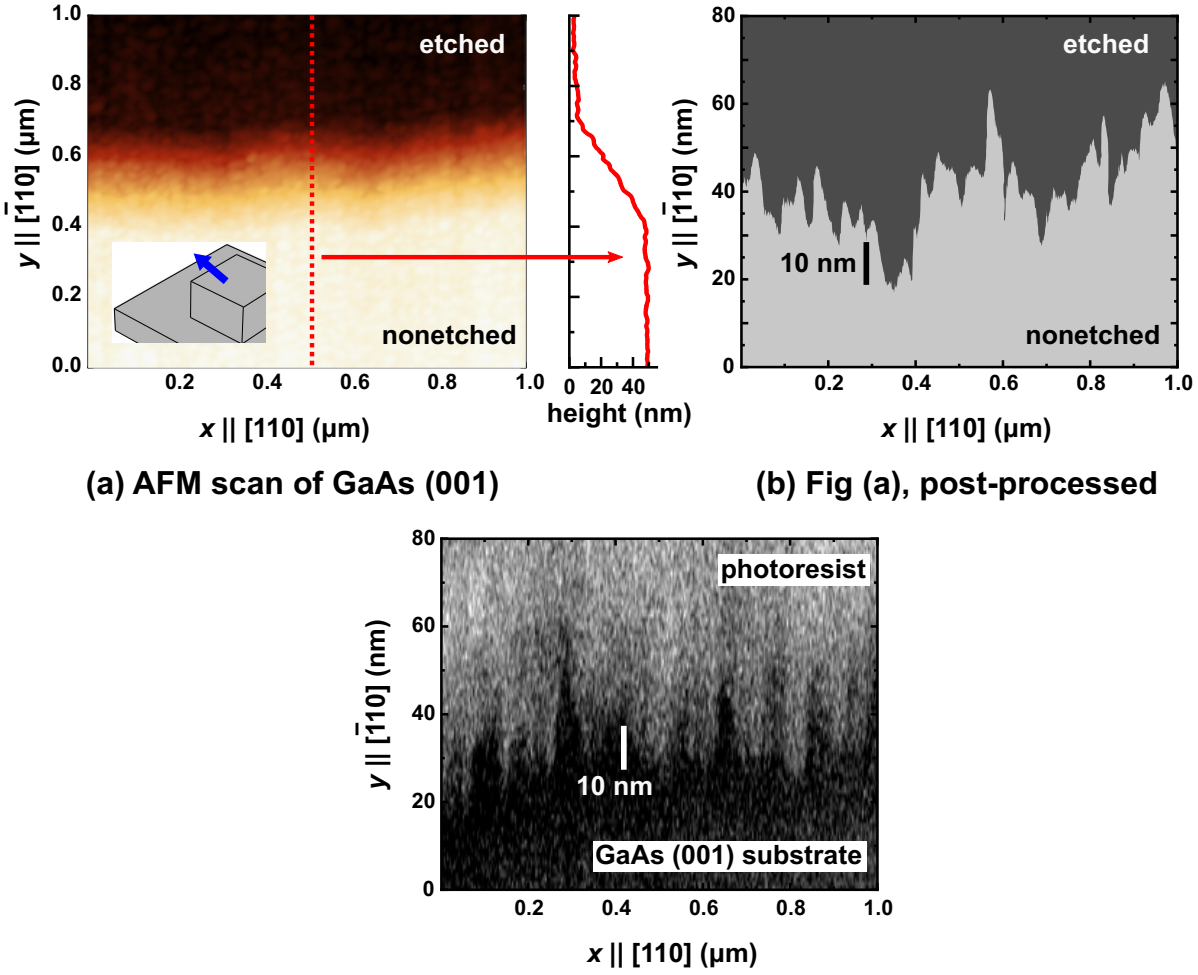

Figure 5.8: (a) AFM scan of a mesa edge of a similar mesa as the one shown in figs. 5.7(e)-(h). The blue arrow in the inset indicates the fast scanning direction of the AFM. The right panel characterizes the AFM profile along the dashed red line, which is typical for the other profiles. The etched area appears as a dark area and the nonetched area appears as a bright area. (b) Same data as fig. (a), but post-processed to show only the surface heights of the etched area (dark) and the nonetched area (bright). (c) Top-view SEM image of the photoresist at a (001) substrate before etching. The photoresist and substrate appear as bright and dark areas, respectively. The SEM image of fig. (c) is recorded by Anne-Kathrin Bluhm.

5.3 Planar sidewall quantum wire formation

In the previous section, it is demonstrated that the ridges prepatterned on the (113)A and (001) substrates are subjected to line-edge roughness, which has comparable values for both substrates. The final step of the fabrication process is studied in this section: the overgrowth of a GaAs QW structure by MBE. As will be discussed, this growth process is anisotropic on the prepatterned substrate, leading to the formation of QWRs at the ridge sidewalls.

5.3.1 Quantum wire formation on GaAs (113)A substrates

Figure 5.9(a) displays cross-sectional AFM profiles of a ridge on a prepatterned (113)A substrate, oriented along the [33$\bar{2}$] direction and fabricated using weak acid piranha etching (leading to steep sidewalls, see sec. 5.2.1). The red and black lines correspond to the profiles before and after MBE overgrowth, respectively. Note that the profile measurements before and after MBE overgrowth must be carried out separately. For this reason, the AFM data needs to be post-processed to align the black and red profiles in figs. 5.9(a) and (b). Comparing the ridge profiles before and after MBE overgrowth is, therefore, only possible for qualitative purposes. The black line reveals that the ridge shape after MBE overgrowth follows the shape of the fabricated ridge along [33$\bar{2}$] reasonably well. This expected behaviour arises from the conformal nature of the MBE growth, when the diffusion length of adatoms is small. Small modifications are observed on both sides of the ridge top: mounds with a height of approx. 10 nm. The appearance of these mounds is most likely related to adatom diffusion from the slow-growing sidewall facets towards the fast-growing ridge top. A similar feature is reported in ref. [46].

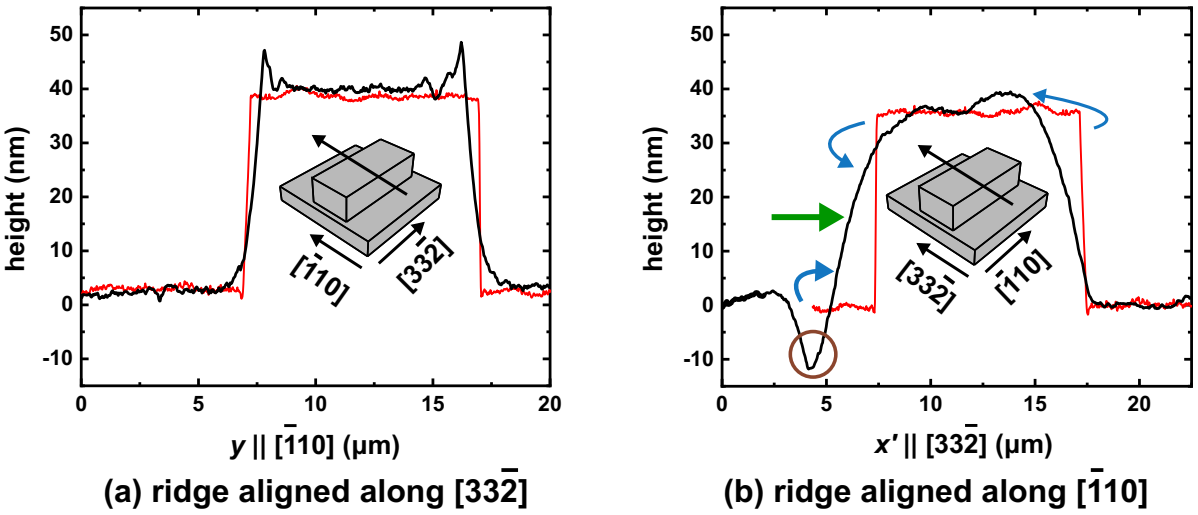

Figure 5.9: AFM profiles of differently oriented ridges before (red) and after (black) MBE overgrowth of a prepatterned GaAs (113)A substrate. The black arrows of the insets show the fast scanning direction of the AFM. The ridges are fabricated by weak acid piranha etching. (a) Profiles of a ridge oriented along [33$\bar{2}$]. (b) Profiles of a ridge oriented along [$\bar{1}$10]. The blue arrows indicate the diffusion of Ga adatoms during MBE overgrowth, whereas the green arrow highlights the location of the sidewall QWR.

Figure 5.9(b) shows AFM profiles before (red) and after (black) MBE overgrowth of a different ridge, oriented along [$\bar{1}$10]. Clearly, in this case the shape of the fabricated ridge is modified by the MBE overgrowth as a result of anisotropic growth of the QW structure. This can be explained by the fact that the Ga adatom diffusion length (or equivalently,

its incorporation rate) depends on the surface orientation on which it impinges during overgrowth. Reference [133] reports that the Ga adatom diffusion length is minimum at the (001) facet, is much larger at the (111) facet and has a value in between the latter two for the (113) facet. As a reminder, a small diffusion length normally corresponds to a facet with a fast growth [134, 133]. The shape of the sidewall profiles indicate that the preferential Ga diffusion (as highlighted with blue arrows) is from the flat areas towards the sidewall on the left side, while on the right side preferential diffusion is from the sidewall towards the flat areas. Correspondingly, the left and right sidewalls regions contain a QW thickness which is larger and smaller as compared to the flat areas, respectively. Note that the local QW layer thicknesses at the corners between sidewall and flat areas change accordingly: at the left side, the corner QW thickness is decreased, while on the right side, the corner QW thickness is increased. The lateral scale of the induced modifications indicates that the preferential adatom diffusion takes place over micrometer-scaled distances. Indeed, previous works found typical Ga adatom diffusion lengths to be on this scale [134]. The characteristics of the ridges after MBE overgrowth are consistent with previous works by Notzel *et al.* [46, 132, 49].

The increase of the QW thickness on the left sidewall gives rise to a local decrease of the QW confinement energy. As will be shown in sec. 6.1, this results in a lateral confinement of charge carriers at the left sidewall by the QW on the flat areas. The left sidewall region (highlighted by a green arrow in fig. 5.9(b)) may, therefore, be regarded as a planar sidewall quantum wire. In contrast, on the right sidewall, the material diffusion away from the sidewall causes the QW confinement energy to increase. Thus, charge carriers at the right sidewall are not laterally confined by the surrounding QW. Additionally, no corner QWR is expected at the right sidewall, because the material diffused towards the corners from the right sidewall is smeared out over several micrometers at the flat areas.

The AFM profile in fig. 5.9(b) shows a valley with a depth of approx. 10 nm on the ridge bottom, as highlighted by a brown circle. The observed valley is the result of a decrease of the total sample thickness, including the thickness of the $Al_{0.15}Ga_{0.85}As$ barriers. References [135, 136] used high-resolution spectroscopy to study the evolution of the QW energy of similar structures. They found that the thickness variation of the corner QW is much smaller than the nominal QW thickness at the flat areas. The amplitude of the valley observed in fig. 5.9(b), which is much larger than the QW layer thickness variations, reveals therefore that the $Al_{0.15}Ga_{0.85}As$ barriers grow in an anisotropic fashion as well. This results from the high Ga content of the (Al,Ga)As layers.

A cross-sectional scanning transmission electron microscopy (STEM) image of a similar ridge as in fig. 5.9(b) is shown in fig. 5.10(a). The etching step on the GaAs substrate (bottom dark layer) is visible at the right-hand side of the image. The lower and upper $Al_{0.15}Ga_{0.85}As$ barriers are represented by bright layers, whereas the dark layer between them corresponds to the QW layer. The thickness of the QW layer locally increases at the ridge sidewall, which confirms to the formation of a sidewall QWR. The QWR is laterally shifted with approx. 850 nm as compared to the etching step at the substrate. Since the lower (Al,Ga)As layer has a thickness of 130 nm, this implies that the lateral growth rate of the (Al,Ga)As barrier is approx. 6.5 times as fast as its vertical growth rate, thereby confirming anisotropic growth of the (Al,Ga)As layers. However, since the diffusion length of Ga is much larger than Al [134], one also expects to observe a gradual evolution of the Ga content in the (Al,Ga)As layer around the ridge sidewall. This may explain the darkish feature between the etching step on the substrate and the QWR position. Figure 5.10(b) shows an enlarged view of the QWR region. The increased QW thickness at the sidewall is clearly visible by comparing the QW thickness at the bottom of the ridge (position (i)) with the QW thickness at the sidewall (position (ii)). From this image, it is estimated that

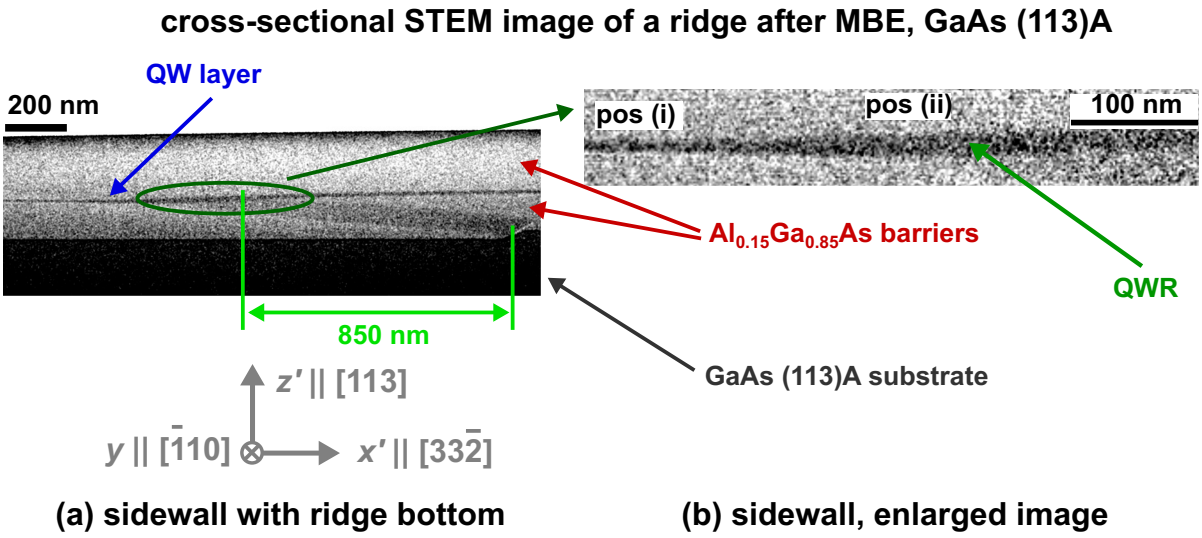

Figure 5.10: (a) Cross-sectional STEM image of the ridge sidewall after MBE overgrowth of a ridge, oriented along $[\bar{1}10]$ on a GaAs (113)A substrate. The GaAs substrate and GaAs QW layers appear dark, whereas the $Al_{0.15}Ga_{0.85}As$ barriers appear as bright layers. (b) Enlarged view of the ridge sidewall in fig. (a). Positions (i) and (ii) correspond to the ridge bottom and sidewall, respectively. The STEM image is recorded by technicians of NTT-BRL (contacted via Dr. Yoji Kunihashi).

the QWR thickness and width are 20 ± 5 nm and 210 ± 5 nm, respectively. This reveals a ratio of lateral-to-vertical growth of approx. 10 times. The larger anisotropy ratio of the QW layer as compared to the (Al,Ga)As layer can be understood by considering the 15 % Al content in the latter. The QWR dimensions are larger than those reported in previous works [132, 68], which is attributed to the larger nominal QW layer thickness of 10 nm, in contrast to the 6 nm thick QW layer used in refs. [132] and [68].

5.3.2 Quantum wire formation on GaAs (001) substrates

In this section, QWR formation on GaAs (001) substrates is studied. The substrate is prepatterned using strong acid piranha etching and overgrown with a structure containing a 10 nm thick QW layer. Since the (001) surface of the ridge top and bottom exhibit the largest incorporation rates, one would expect wire formation to occur on these areas. However, the growth mechanism for QWRs on (001) substrates differs qualitatively from the mechanism on (113)A substrates and relies on the (2x4) surface reconstruction [137, 50]. At the flat surfaces, this surface reconstruction leads to the appearance of As-dimers oriented along the $[\bar{1}10]$ direction. However, at step edges, the As atoms can not take part in the formation of these dimers and provide free dangling bonds. Diffusing Ga adatoms easily react with these bonds, which are therefore efficiently incorporated at the steps of a staircase along $[\bar{1}10]$ (i.e. for a ridge oriented along [110]). This leads to a much faster growth rate of the ridge sidewall as compared to the flat surfaces, due to the high step density at the sidewall [137, 50].

Figure 5.11(a) shows AFM profiles of a ridge oriented along $[\bar{1}10]$, before (red) and after (black) MBE overgrowth. The AFM profiles are similar, which reveals the absence of QWR formation on the sidewalls of ridges along $[\bar{1}10]$. This is consistent with the findings of ref. [47]. The absence of QWR growth on these ridges can be understood by considering that As dimer formation occurs along the step edges for sidewalls of this ridge. For these steps, the free dangling bonds are provided by other Ga adatoms. The

diffusing Ga adatoms only react weakly with this type of free bond [50]. Thus, there is no preferential attachment of adatoms on the sidewalls of ridges oriented along the [$\bar{1}$10] direction.

In contrast, the shape of a different ridge oriented along the [110] direction is modified after MBE overgrowth, as shown in fig. 5.11(b). Here, the red and black lines display AFM profiles of the ridge before and after MBE overgrowth, respectively. The formation of QWRs is witnessed by a local increase of the thickness of both sidewalls, as highlighted by the green arrows. The QWR properties on both sidewalls should be equal: the symmetric etching process leads to equal inclination angles of the sidewalls. This means that they have a similar density of step edges, which in turn leads to a similar degree of anisotropic MBE overgrowth. The material accumulated on the sidewalls originates from Ga adatoms which diffuse from the mesa top and bottom towards the sidewall, as highlighted by the blue arrows. The As-induced free dangling bonds at the sidewalls lead to the preferential attachment of Ga adatoms, which results in a planar sidewall QWR region. At the mesa bottom adjacent to the QWR, a valley with a depth of approx. 10 nm is observed on both sides of the mesa. The appearance of these valleys indicates an anisotropic growth mechanism for the $Al_{0.15}Ga_{0.85}As$ barriers. Note that the thicknesses of the barriers are much larger than the QW thickness. As a consequence, a similar degree of anisotropy in QW and barriers should result in a larger contribution to the valley depth from the barriers.

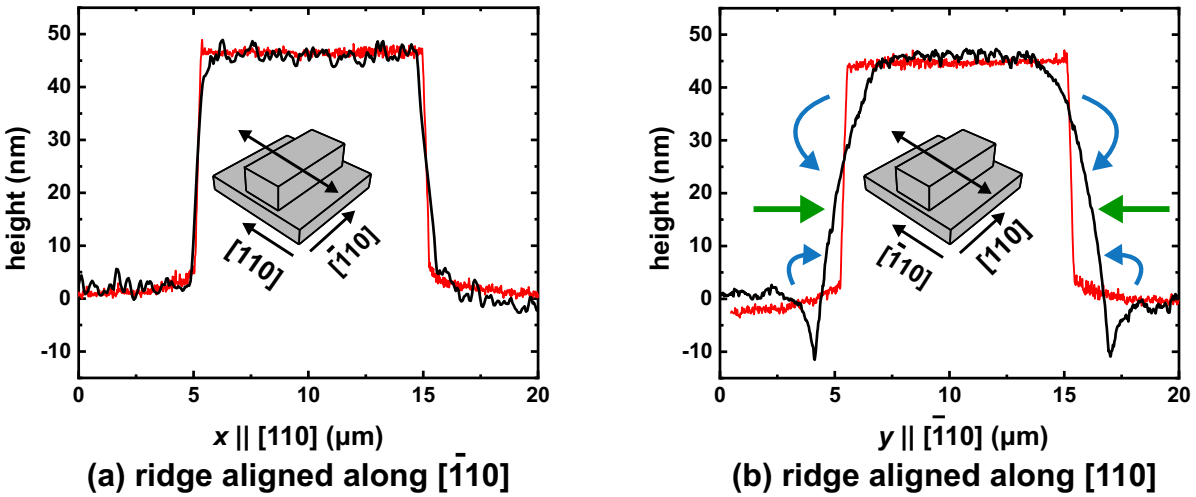

Figure 5.11: AFM profiles of differently oriented ridges before (red) and after (black) MBE overgrowth of a prepatterned GaAs (001) substrate. The black arrows of the insets indicate the fast scanning direction of the AFM. The ridges are fabricated by strong acid piranha etching. (a) Profiles of a ridge oriented along [$\bar{1}$10]. (b) Profiles of a ridge oriented along [110]. The blue arrows schematically depict diffusion of Ga adatoms from the ridge top and bottom towards the sidewall. The sidewall QWRs are indicated by green arrows.

Figure 5.12(a) shows a cross-sectional STEM image of the region around a sidewall of an overgrown ridge, patterned on a (001) substrate and oriented along [110], fabricated using strong acid piranha etching. The dark layer at the bottom of the image represents the substrate, with the etching step on the left-hand side of the image. The 45 nm etching depth is similar to the one observed in previous samples discussed in figs. 5.7(e)-(h) and fig. 5.11(b). The nominally 10 nm thick QW layer is clearly visible as a dark layer, sandwiched between two $Al_{0.15}Ga_{0.85}As$ barriers (bright). The sidewall QWR is horizontally shifted from the substrate sidewall by approx. 600 nm after the growth of the lower barrier. Since the thickness of the lower barrier is 130 nm, the lateral growth of the lower barrier is

approx. $600/130 \approx 5$ times faster than the vertical growth. This anisotropy ratio between lateral and vertical growth is smaller than the one observed for (113)A substrates.

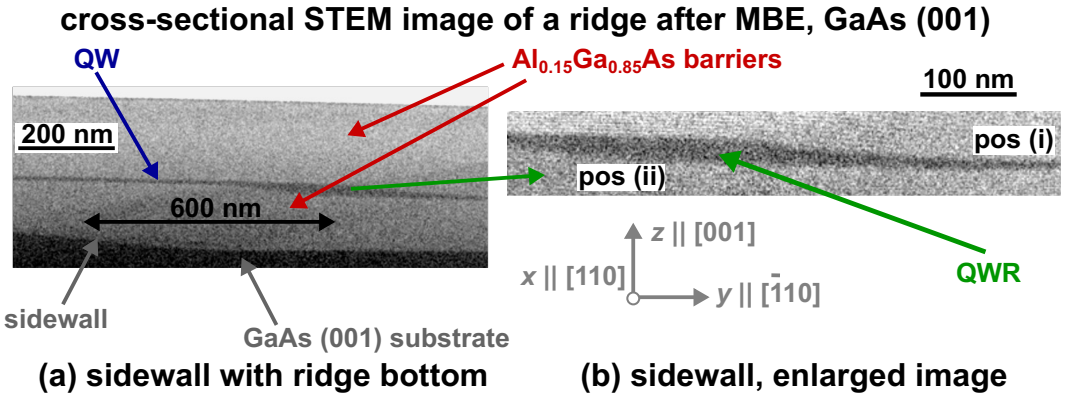

Figure 5.12: (a) Cross-sectional STEM image of a ridge sidewall after MBE overgrowth of a ridge oriented along [110] on a GaAs (001) substrate, fabricated by strong acid piranha etching. The GaAs substrate and GaAs QW layers appear as dark areas. The $Al_{0.15}Ga_{0.85}As$ barrier layers appear as bright areas. (b) Enlarged view of the ridge sidewall in fig. (a). Positions (i) and (ii) correspond to the ridge bottom and sidewall, respectively. The STEM image is recorded by technicians of NTT-BRL (contacted via Dr. Yoji Kunihashi).

Figure 5.12(b) shows an enlarged view of the sidewall region. The QW layer thickness clearly increases at the sidewall, as is evident from a comparison of its thicknesses at the ridge bottom (position (i)) and ridge sidewall (position (ii)). The thickness and the width of the QWR can be estimated from this figure to be 25 ± 5 nm and 200 ± 5 nm, respectively. The ratio of the lateral and vertical growth rates is thus approx. 8 times. As is the case for (113)A substrates, the anisotropic growth of the QW layer is larger as compared to the growth of the (Al,Ga)As layers due to the Al content of the latter. Note that in contrast to the QW at the flat areas, the QWR region is also laterally confined by the (Al,Ga)As barriers. The contrast between the QW layer and the $Al_{0.15}Ga_{0.85}As$ barriers in the image can be used to estimate the evolution of the QW thickness as a function of its corresponding position along $[\bar{1}10]$ (i.e. perpendicular to the QWR axis), as illustrated in fig. 5.13. The QWR shape appears to be asymmetric: a steeper increase of the QW layer thickness is observed adjacent to the ridge top, whereas it evolves in a more gradual way adjacent to the ridge bottom.

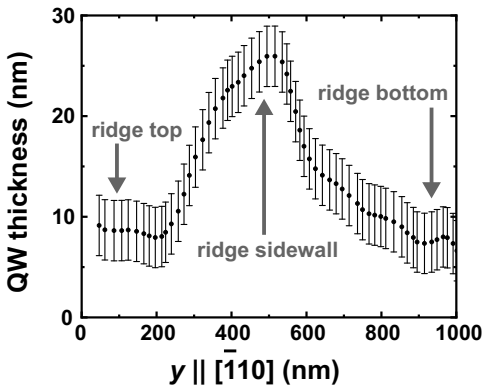

Figure 5.13: Evolution of the QW layer thickness at the ridge sidewall as function of its corresponding position along $[\bar{1}10]$.

The plot of fig. 5.13 reveals a spatial QWR width (at half its thickness) of approx. 400 nm. Although the physically relevant QWR width is not well-defined from figs. 5.12 and 5.13, it is evident that its order of magnitude is much larger than the reported LER value of the underlying ridges (which is in the range of 4 nm-9 nm, see sec. 5.2). As a result, it is expected that potential fluctuations resulting from LER are small and do not play a role in determining the transport properties of the QWR.

5.4 Summary of the chapter's findings

This chapter provides a detailed overview of the fabrication process for planar sidewall quantum wires on prepatterned GaAs substrates. AFM studies have demonstrated a similar (high) quality of ridges on (113)A and (001) substrates. This high structural quality is quantified by a small value of line-edge roughness, which mainly results from the photolithography process. Since the QWR width is much larger, it is expected that LER does not have a significant impact on the transport properties of the QWRs.

The overgrowth of a QW structure by MBE is anisotropic on both substrates. However, the growth mechanisms responsible for the anisotropy is different for each substrate. On one hand, the QWR formation on (113)A substrates relies on the dependency of the adatom diffusion length on the surface orientation. As a result, the ridge shape is modified for both ridges oriented along the $[\bar{1}10]$ and $[33\bar{2}]$ directions. On the other hand, for (001) substrates, the (2x4) surface reconstruction is responsible for free dangling bonds on step edges at the sidewall. The type of free bonds on which Ga atoms preferentially attach (those provided by As atoms) only form for step staircases along the $[\bar{1}10]$ direction. The ridge shape is, therefore, only modified if the ridge is oriented along the [110] direction.

Figure 5.14 shows a top-view optical microscopy image of a typical final sample. As shown in the figure, the ridges are enclosed by two IDTs. In the final sample for the transport experiments, the ridges are fabricated on (001) substrates using strong acid piranha etching and oriented along the [110] direction. In this sample, five rectangular ridges are fabricated, each with a width of 10 µm and a length of 190 µm. The five ridges contain ten QWRs, of which one is highlighted by a green line. At the end of the QWRs, a metal stripe is deposited for experimental purposes explained in chaps. 7 and 8.

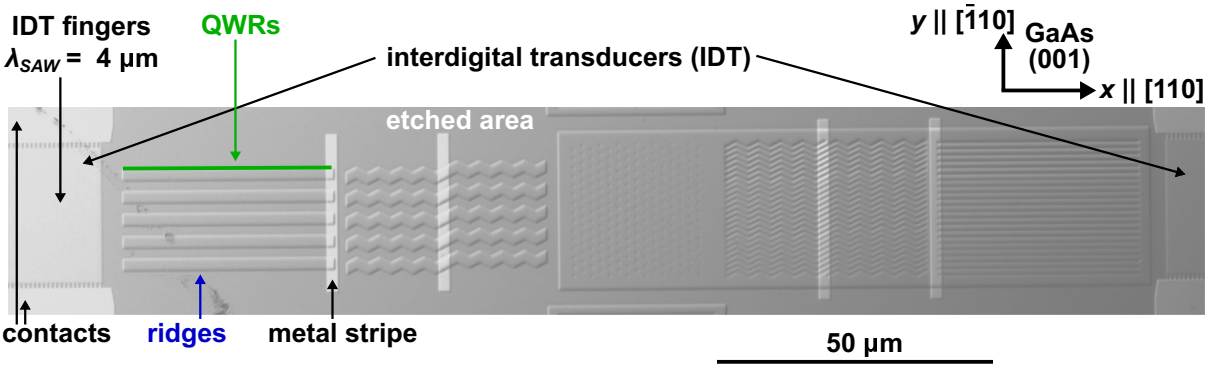

Figure 5.14: Optical microscopy image of a typical sample with nanostructures between two interdigital transducers (IDT). At the left-hand side of the figure, five ridges with ten planar sidewall QWRs are fabricated, of which one is highlighted by a green line. The IDTs consist of a center area containing its fingers and two contact pads. A metal stripe is deposited onto the end of the QWRs for experimental purposes, which will be discussed in chaps. 7 and 8.

chapter 6

Optical properties

The previous chapter provides an elaborate analysis of the fabrication process of planar sidewall quantum wires (QWR). The small line-edge roughness of the ridges on which the quantum well (QW) layer is overgrown is important to guarantee good QWR transport properties, as potential fluctuations induced by it should be small. In this chapter, the optical properties of the QW structures are investigated by means of photoluminescence (PL) and cathodoluminescence (CL). The optical properties spectroscopically access the quality of the QWRs. In sec. 6.1, the optical properties of QWRs on (113)A substrates are studied, while those of QWRs on (001) substrates are investigated in sec. 6.2. The carrier dynamics in the QW structures is investigated by time-resolved photoluminescence in sec. 6.3. In the fourth section, some interesting properties of the (Al,Ga)As barrier emission are shown. The final section gives a summary of the chapter's findings. The studies presented in this chapter are all conducted on GaAs QW structures.

6.1 Quantum wires on (113)A substrates

The optical properties of sidewall QWRs fabricated on a (113)A substrate are shown in fig. 6.1(a). The figure depicts a map of the photoluminescence intensity (I_{PL}), collected by scanning the laser spot along the $[33\bar{2}]$ direction of the (113)A sample in steps of 0.5 µm over a distance of 40 µm. The scanning line includes two ridges oriented along $[\bar{1}10]$. For every step, the PL from a 1.5 µm x 2 µm sized detection area is collected and spatially integrated to yield the result in the figure. The excitation energy is 1.954 eV (above the QW transition) and the excitation density 3.6 W/cm^2. As a reference, the central panel displays the positions of the two ridges. The PL map clearly shows three optical transitions in the QW structure. At the flat surfaces on the ridge top and bottom, the transition energy is 1.543 eV, which is attributed to the emission from the nominally 10 nm thick QW. At sidewall A, the increased QW thickness leads to a red-shift of its transition energy to 1.525 eV. Accordingly with finite-potential-well calculations, this transition energy corresponds to a QW thickness of 18 nm, which is consistent with the STEM images discussed in sec. 5.3.1. At sidewall B, the thickness of the QW decreases, resulting in a transition energy of 1.551 eV. A finite-potential-well calculation reveals that this energy corresponds to a QW thickness of 8.5 nm.

Detailed PL spectra extracted from fig. 6.1(a) are shown in fig. 6.1(b) for the ridge bottom (red), sidewall A (green) and sidewall B (blue). The spectrum of the ridge top resembles the one of the ridge bottom and is omitted for clarity reasons. At the ridge bottom, the nominally 10 nm thick QW is the only optical transition within the spectral

detection window. The QW transition has a spectral linewidth, defined as the full-width-at-half-maximum (FWHM), of approx. 9.5 meV. The broad linewidth is attributed to inhomogeneous broadening due to thickness fluctuations of the QW, mainly induced by roughness of the surface on which the QW layer is grown. The spectrum at the ridge top has a similar linewidth, indicating that the etching process does not induce significant surface roughening. This is consistent with AFM studies discussed in sec. 5.2.1.

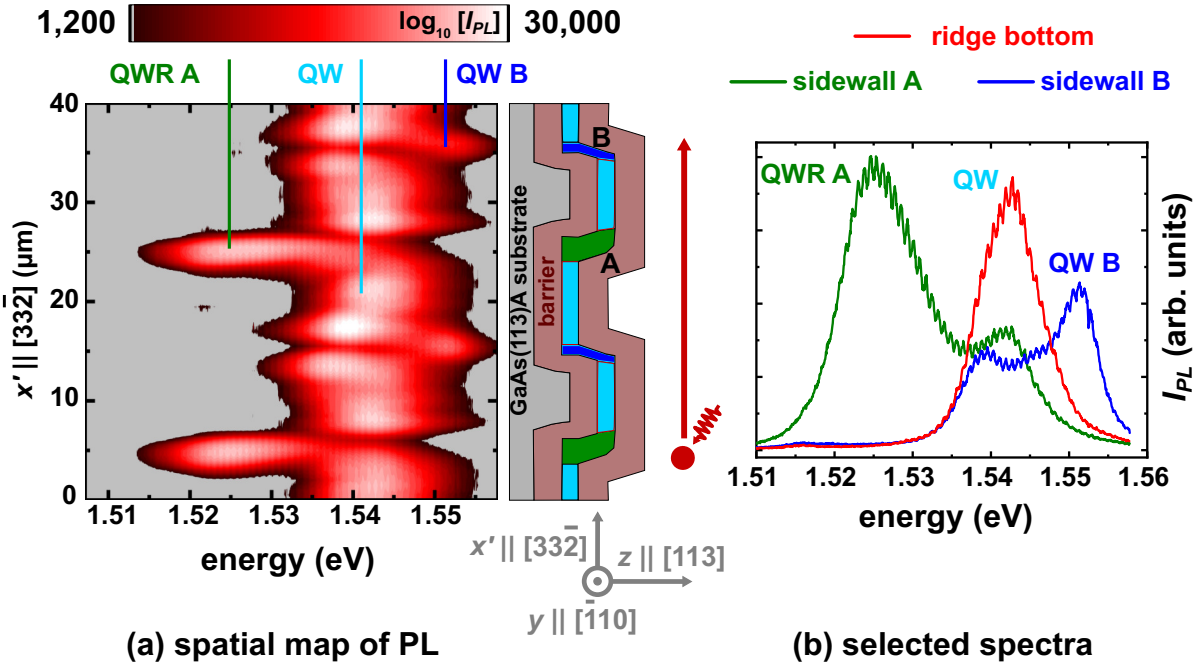

Figure 6.1: Optical properties of sidewall QWRs on (113)A substrates. (a) Spatial map of the PL, collected by scanning a laser spot over a 40 µm-long line along [33$\bar{2}$], containing two ridges oriented along [$\bar{1}$10]. The geometry of the experiment is illustrated in the central panel. Here, the grey layer represents the substrate, the red layers represent the (Al,Ga)As barriers, the blue layer the QW and the green area the QWR. (b) Selected spectra extracted from fig. (a). Green: spectrum at sidewall A, red: spectrum at the ridge bottom and blue: spectrum at sidewall B.

The spectrum of sidewall A (green) clearly includes the QWR transition, which is red-shifted with respect to the surrounding QW by 18 meV. Taking into account a smaller exciton binding energy in the QWR with respect to the QW due to its larger thickness, the QW induces a lateral potential barrier of 17 meV (3 meV) for electrons (holes). This lateral potential barrier prevents motion of QWR carriers into the surrounding QW, whereas the $Al_{0.15}Ga_{0.85}As$ barrier layers restrict motion of the QWR carriers along the growth direction. This two-dimensional confinement effectively results in quantum wire - like behaviour of carriers at the ridge sidewall. The large QWR width (200 nm, see sec. 5.3.1) leads, however, to a dominance of its thickness (18 nm) in the determination of the optical properties. The linewidth of the QWR is approx. 12 meV. The additional inhomogeneous broadening of the QWR transition with respect to the QW transition may be attributed to two effects. Firstly, fluctuations of the QWR thickness lead to fluctuations of its transition energy. Fluctuations of the QWR width have a similar result, but are expected to be small due to the small LER value as compared to the QWR width (see sec. 5.2.1). The second source of inhomogeneous broadening comes from alloy fluctuations in the $Al_{0.15}Ga_{0.85}As$ barriers, which will be discussed in more detail in sec. 6.4. Since the increased thickness of the QWR as compared to the QW should reduce the impact of thickness fluctuations, the broadening of the QWR spectral line indicates (i) an increased surface roughness at

the sidewall as compared to the flat surfaces and (ii) the presence of alloy fluctuations of the (Al,Ga)As layers.

The number of recombination events detected at sidewall A is clearly larger than detected at the ridge bottom, as indicated by the larger integrated PL intensity shown by the green plot with respect to the red plot in fig. 6.1(b). This confirms the lateral confinement of QWR carriers. Carriers excited at the flat surfaces diffuse along $[33\bar{2}]$ and leave the detection window, which has a finite width of 1.5 µm along $[33\bar{2}]$. Thus, not all optically induced recombination events of the flat QW area are detected. In contrast, carriers which are confined in the quantum wire do not diffuse along $[33\bar{2}]$. The QWR width of approx. 210 nm is much smaller than the detection window width. As a result, QWR carriers do not diffuse out of the detection window, thus leading to an increase of the detection efficiency for recombination events in the QWR region as compared to the flat QW regions.

The spectrum at sidewall B is shown in fig. 6.1(b) by a blue plot and reveals a 8 meV blue-shift of the QW transition. Due to this blue-shift, carriers excited in this region are not laterally confined and easily escape into the surrounding QW. This manifests itself as a reduced intensity of QW B with respect to the other transitions in the structure. Furthermore, the blue plot shows that the QW adjacent to sidewall B is slightly red-shifted with respect to the flat areas, which is attributed to diffusion of Ga adatoms during MBE overgrowth from sidewall B to the flat areas.

Similar experiments involving ridges oriented along $[33\bar{2}]$ only revealed the transition of the nominally 10 nm thick QW. It is therefore concluded that the QWRs only form on the sidewalls of ridges oriented along the $[\bar{1}10]$ direction, which is consistent with the findings of sec. 5.3.1 and refs. [46, 49, 132].

6.2 Quantum wires on (001) substrates

In this section, the optical properties of QWRs on (001) substrates are studied. Figure 6.2(a) shows a map of the PL from a 40 µm-long line scan along $y||[\bar{1}10]$. This line contains two ridges on a (001) substrate oriented along the $x||[110]$ direction and fabricated by strong acid piranha etching. The PL is collected by exciting the QW structure at an excitation energy of 1.954 eV (above the QW energy) and excitation density of 9 W/cm^2. A sketch of the ridges showing the positions of the sidewalls (green) is illustrated in the right panel. In contrast to similar experiments on a (113)A substrate (see fig. 6.1(a)), only two transitions are now detected. The transition energy at 1.546 eV is attributed to the electron-to-heavy-hole transition of the QW (QW_{hh}) on the ridge bottom and top. This is consistent with finite-potential-well calculations (see sec. 3.1). The optical properties of sidewall A are identical to those of sidewall B, with a transition energy of the QWR electron-to-heavy-hole resonance (QWR_{hh}) of 1.520 eV. This transition energy corresponds to a QWR thickness of approx. 25 nm, consistent with STEM images shown in sec. 5.3.2. Taking into account a smaller binding energy for the QWR with respect to the QW, the lateral potential barriers between QW and QWR on (001) substrates amount to 22 meV and 4 meV for electrons and holes, respectively. The fact that the optical properties for the QWRs on sidewalls A and B are identical is expected, since an analysis of the etching process in sec. 5.2.3 depicts a symmetric ridge for (001) substrates. A closer inspection of the figure reveals that the transition energy of the QW directly adjacent to the sidewall (the corner QW) is blue-shift by approx. 3 meV with respect to the QW transition at the flat surfaces. The blue-shift is attributed to the diffusion of Ga adatoms during MBE overgrowth from the ridge top and bottom towards the sidewalls of the ridge, leading to a local decrease of the QW thickness. The evolution of the QW transition energy is

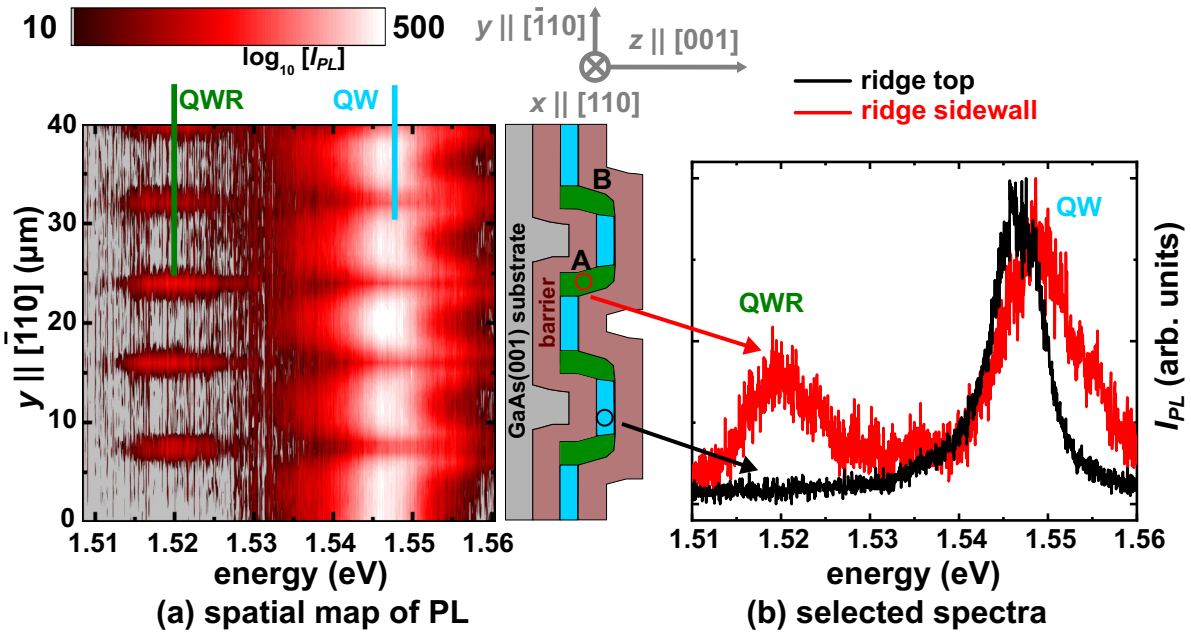

Figure 6.2: Optical properties of sidewall QWRs on (001) substrates. (a) Spatial map of the PL, collected by scanning the laser spot over a 40 µm-long line along [$\bar{1}$10], containing two ridges oriented along [110]. The geometry of the experiment is illustrated in the central panel, where the grey layer represents the substrate, the red layers represent the (Al,Ga)As barriers, the blue layer the QW and the green area the QWRs. (b) Selected spectra extracted from fig. (a). Black: spectrum at the ridge top, red: spectrum at the ridge sidewall.

symmetric on both sides of the QWR, indicating that the adatom diffusion towards the sidewall proceeds in a similar fashion from ridge bottom to the sidewall and ridge top to the sidewall.

Some extracted spectra, shown in fig. 6.2(b), reveal more information about the QW structure. The black plot shows a spectrum as observed on the ridge top and displays a QW_{hh} transition energy of 1.546 eV with a linewidth of 7.4 meV. The linewidth is attributed to inhomogeneous broadening due to QW thickness fluctuations. A spectrum of the sidewall is shown by the red plot. The QWR transition is clearly observed at the low-energy side of the QW, with a QWR_{hh} energy of 1.520 eV and a linewidth of approx. 10 meV. As is also visible in fig. 6.2(a), the transition of the corner QW is blue-shifted and broadened. The broadening of the corner QW transition can be explained by the local decreased QW thickness, which makes the QW energy more susceptible to thickness fluctuations. As was the case for QWRs on (113)A substrates, the difference in linewidths between the QW and the QWR transitions indicates that the QWR linewidth is broadened due to an increased surface roughness at the sidewall and local alloy fluctuations of the $Al_{0.15}Ga_{0.85}As$ barriers. The smaller linewidth of the (001) QWRs as compared to (113)A can be explained by the smaller linewidth of the surrounding QW, indicating better growth conditions as compared to the previous sample discussed in sec. 6.1.

A similar experiment is conducted on similar ridges on a (001) substrate, fabricated using weak acid piranha etching. In this case, the QWR transition energy is 1.522 eV with a linewidth of approx. 11 meV. The MBE overgrowth for this sample is performed under exactly the same growth conditions as for the one discussed above (both samples were inserted into the MBE growth chamber simultaneously). Thus, for equal growth conditions, these results indicate that strong piranha etching is preferable, since it leads to a larger potential barrier between QW and QWR, and additionally to a slight improvement of

the linewidth. The remainder of this thesis considers, therefore, only QWRs fabricated by strong acid piranha etching. This procedure results in shallow sidewalls (i.e. small inclination angle), as discussed in sec. 5.2.3.

The QW structure measured in this experiment is fabricated by migration-enhanced-epitaxy growth (see sec. 5.1), which enhances Ga adatom diffusion during overgrowth. This leads to a larger anisotropy of the QW growth and, as a result, to thicker QWRs. Indeed, the transition energy of QWRs fabricated on prepatterned (001) substrates using conventional MBE mode (not shown here) is blue-shifted by approx. 5 meV with respect to those fabricated in MEE mode. The smaller transition energy of the MEE-grown QWRs implies that their thickness is larger, resulting from the enhanced diffusion of Ga adatoms. Additionally, a map of the PL of ridges oriented along $[\bar{1}10]$ does not show any other transition as the QW for both structures fabricated using MEE and MBE growth. Thus, conform the findings of sec. 5.3.2, the QWRs only form at sidewalls of ridges oriented along the [110] direction.

The carrier dynamics of the QW structure can be further investigated by photoluminescence excitation spectra (PLE). Here, the emission from the QW_{hh} and QWR_{hh} transitions are detected while the excitation energy E_{exc} is varied. In such an experiment, the PL intensity is strongly enhanced when the excitation energy is resonant with an electronic state in the structure, leading to efficient absorption of the laser light. The PLE spectra of the QW and the QWR at the sidewall of a ridge fabricated on a typical sample are shown in figs. 6.3(a) and (b), respectively. The excitation density is $5.1\,W/cm^2$, while the detection energy of the QW_{hh} and QWR_{hh} transitions are 1.546 eV and 1.521 eV, respectively. The PLE spectrum of the QW clearly depicts two absorption peaks at excitation energies of 1.548 eV and 1.558 eV. The first absorption peak is attributed to the QW_{hh} transition, while the second peak corresponds to the QW electron-to-light-hole transition (QW_{lh}). The spectral shift of 2 meV between the QW_{hh} absorption and QW_{hh} emission peaks is related to a Stokes shift due to exciton localization [138]. The small value of the Stokes shift indicates a good quality of the QW structure [26, 139].

Figure 6.3(b) shows the PLE spectrum of the QWR_{hh} transition. The onset of its emission is observed at 1.521 eV. Interestingly, no clear absorption peaks corresponding to the heavy-hole and light-hole excitations are observed. This may be caused by the small PL signal for these excitation energies. Alternatively, it may indicate that the excitonic states in the QWR can not be accessed directly. The data presented here does, however, not provide a clear explanation for the absence of excitonic features. The small PL signal for low excitation energies is attributed to the narrow QWR width of approx. 200 nm, which is much smaller than the laser spot size. The QWR absorption area covers only approx. 2 % of the laser spot. Therefore, direct optical injection of carriers in the QWR is very small for these experimental conditions. For increasing excitation energy above 1.542 eV, the QWR signal is strongly enhanced, indicating that the majority of the QWR carriers originate from diffusion of QW carriers into the QWR.

Two clear absorption peaks are observed in the PLE spectrum of the QWR. The first absorption peak (1.552 eV) is blue-shifted by 4 meV with respect to the QW_{hh} absorption peak in fig. 6.3(a). This peak is attributed to excitation of carriers in the QW, which then diffuse from the QW into the QWR. Figure 6.3(c) schematically depicts the energy diagram of the QW layer along the $[\bar{1}10]$ direction (perpendicular to the QWR axis), in the vicinity of the sidewall. The upper inset schematically indicates the position of the QWR (green). The lowest energy state at the sidewall and flat areas correspond to the QWR_{hh} and QW_{hh} transitions, respectively. At the corners between the sidewall and flat areas, a local decrease of the QW thickness results in a blue-shift of its energy. The complete potential barrier is, therefore, 25.4 meV and 4.8 meV for electrons in the

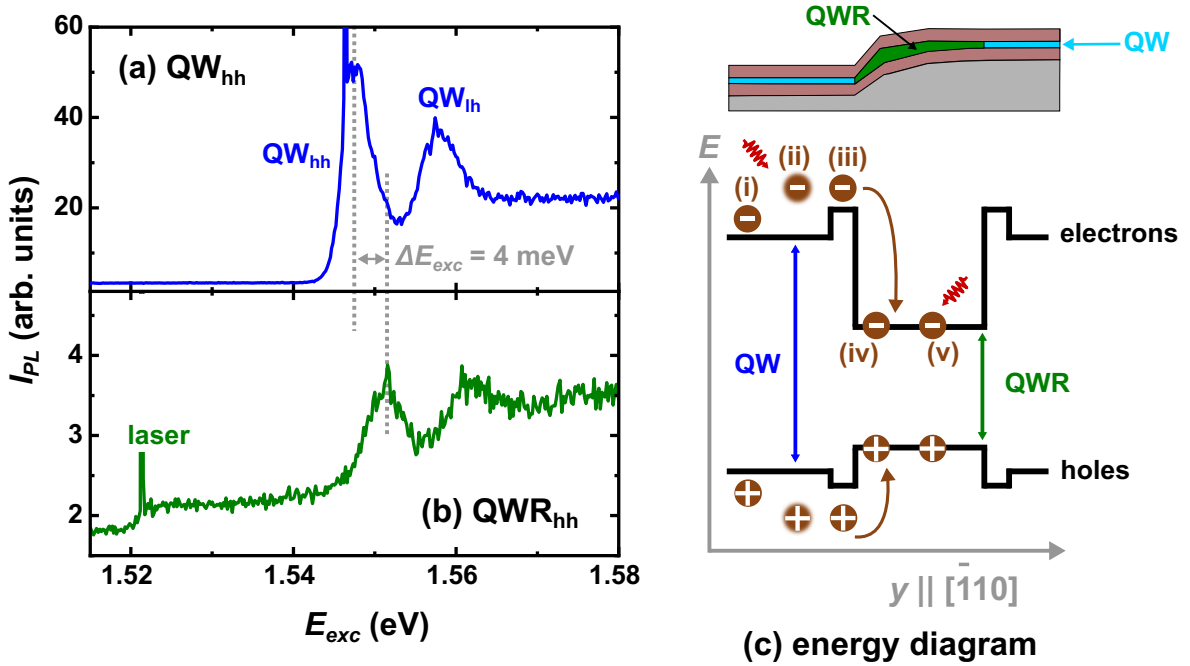

Figure 6.3: PL excitation spectra at the ridge sidewall. (a) Detection at the electron-to-heavy-hole resonance for the QW (QW_{hh}) (b) Detection at the electron-to-heavy-hole resonance for the QWR (QWR_{hh}). (c) Schematic energy diagram along the QW layer in the direction of $y||[\bar{1}10]$. The dynamics of the electrons (holes) is depicted by brown circles with a minus (plus) sign. The upper panel indicates the position of the QWR.

conduction band and holes in the valence band, respectively. Excitation in resonance with the QW_{hh} transition (denoted by (i) in fig. 6.3(c)) can not lead to diffusion of QW carriers into the QWR, since this is prevented by the local blue-shift of the corner QW energy. If the excitation energy is raised by approx. 4 meV, carriers are resonantly excited in the corner QW (denoted by (iii)). These carriers may either diffuse into the QWR (denoted by (iv)) or into the QW at the flat area. In the former case, they contribute to the QWR emission, while energy relaxation prevents diffusion of the carriers in the latter case. Additionally, carriers with an excess energy are excited in the flat QW area (denoted by (ii)). Since the energy relaxation of these carriers usually is faster than their diffusion towards the sidewall, these carriers are not expected to contribute significantly to the QWR population. The absorption peak at 1.552 eV observed in the QWR PLE spectrum is, therefore, attributed to diffusion of carriers excited in the corner QW. The absorption peak corresponding to 1.563 eV is, likewise, attributed to excitation of carriers associated with the QW_{lh} transition at the corner, which diffuse into the QWR.

The optical properties are influenced by the experimental conditions, such as the temperature and excitation density. All optical experiments in this thesis are conducted at low temperatures in a range of 5 K to 15 K. In this range of temperatures, the optical properties studied here are not expected to change significantly. However, the excitation densities used throughout this thesis may alter the optical properties considerably. Figures 6.4(a) and (b) show results of optical experiments on both the QWR and QW as function of excitation density P_{exc}. The experiment is conducted using an excitation energy of 1.633 eV (above the QW transition). For every excitation density, the optical properties of both the QW and the QWR are extracted from a PL spectrum. The peak intensities of the QW_{hh} (black) and QWR_{hh} transitions (red) are plotted as function of excitation density in fig. 6.4(a). Two conclusions can be drawn from this figure. Firstly, both the QW_{hh} and the QWR_{hh} transitions are in the linear excitation regime, meaning that their carrier

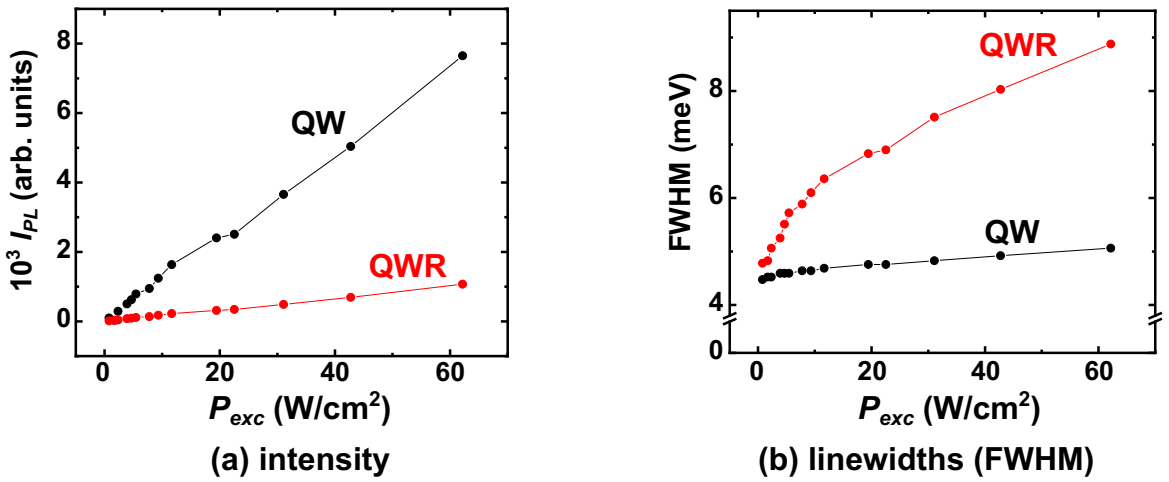

Figure 6.4: (a) Excitation density dependency of the PL intensities of the QW_{hh} (black) and the QWR_{hh} transitions (red). (b) Excitation density dependency of the spectral full-width-at-half-maximum (FWHM) of the QW_{hh} transition (black) and the QWR_{hh} transition (red).

densities are linearly dependent on the excitation density. Since the excitation energy is above the QW_{hh} transition, the majority of the QWR carriers results from diffusion of QW carriers into the QWR. However, the number of QW carriers diffusing into the QWR is much smaller than the number of QW carriers which recombine in the QW. Realizing that direct excitation into the QWR is weak, this explains why the slope of the QWR plot is smaller than the one for the QW. Secondly, the PL intensity is not limited, meaning that the electronic states are not saturated for these excitation densities. The linewidth, previously defined as the FWHM of the spectral line, is plotted as function of excitation density in fig. 6.4(b). Whereas the broadening of the QW transition with excitation density is small, the QWR transition broadens strongly with excitation density. Note however, that for high excitation densities, the PL signal of the substrate exceeds the one of the QWR, indicating that the carrier density in the substrate becomes substantially larger than in the QWR. Due to the proximity of the substrate and QWR transitions, the QWR transition becomes, therefore, less well-resolved for large excitation densities.

Information about the quality of the QWRs manifests itself also in a study of the QWR_{hh} transition energy as function of position along the QWR axis, as shown in fig. 6.5(a). Here, a PL map of the QWR_{hh} emission is constructed, obtained by scanning the laser spot along the QWR axis and spatially integrating the PL from a 1.5 µm x 2 µm sized detection area. The experiment is conducted using an excitation energy of 1.601 eV and an excitation density of 125 W/cm^2. Two typical spectra at positions of 58 µm (blue) and 10 µm (black) are displayed in the upper panel. The similar shapes of the spectra, which are typical for all positions, depict a high degree of homogeneity of the QWR transition energy. The difference between the spectral linewidths at the positions with narrowest and broadest transitions is approx. 1 meV, which is only a fraction of the average linewidth of approx. 7.5 meV.

The intensity of the QWR_{hh} transition, spectrally integrated, is plotted in fig. 6.5(c) as function of position along the QWR axis. Clearly, the total emission fluctuates along the QWR axis, where the intensity of the weakest position is only approx. 42 % of the strongest intensity. The intensity fluctuations indicate the presence of randomly distributed PL hotspot centers. The presence of these centers is also evident from a comparison of the carrier diffusion profiles at different positions along the QWR axis. Figure 6.5(b) shows the spatial diffusion profile of the QWR carriers at four different positions along the QWR.

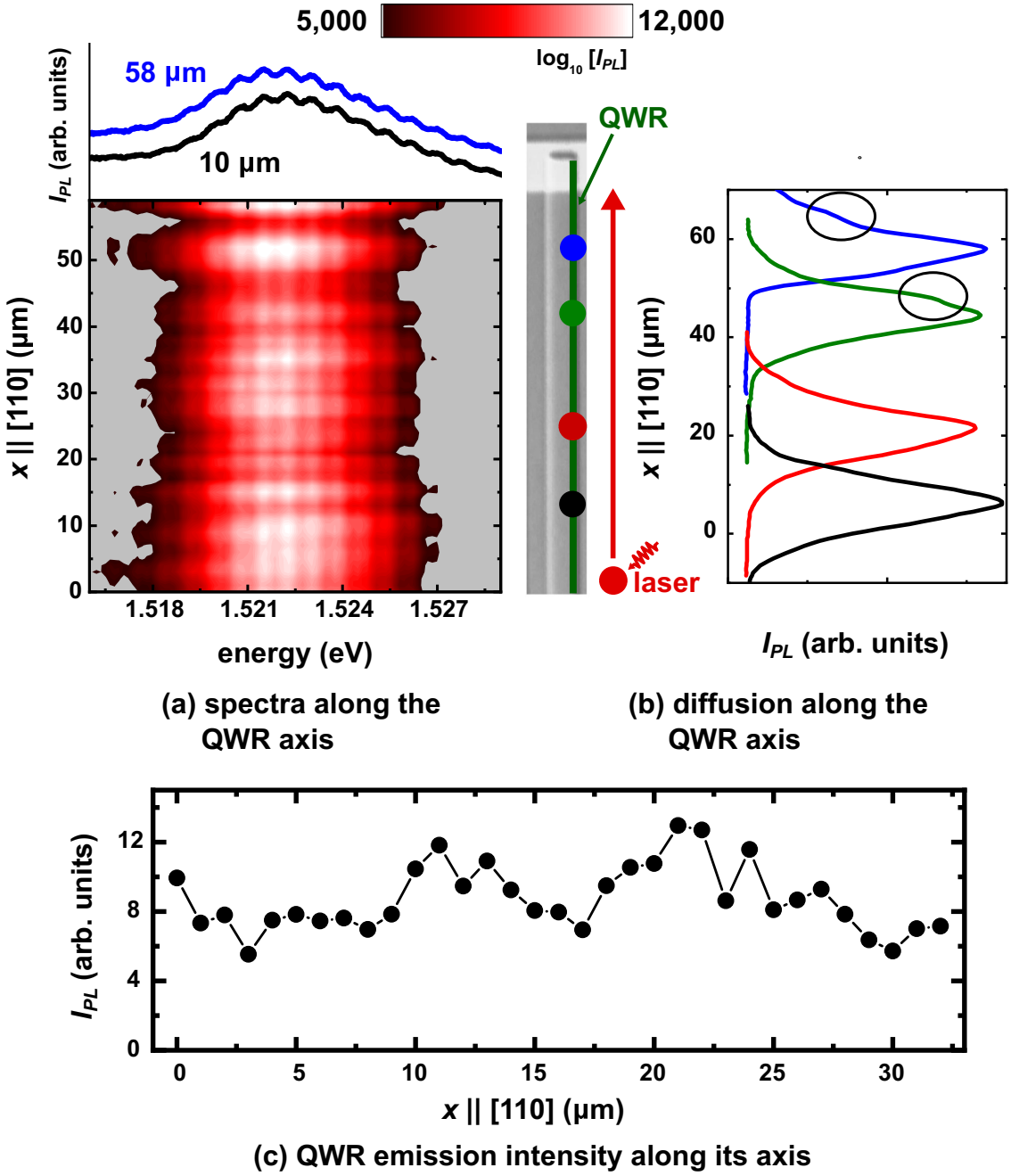

Figure 6.5: (a) Map of the PL, collected by scanning the laser spot over a 60 µm-long line along the QWR axis, as depicted by the central panel. The upper panel shows spectra extracted at positions $x = 10\,\mu\text{m}$ (black) and $x = 58\,\mu\text{m}$ (blue). The small amplitude oscillation is an artefact resulting from pixel interference at the CCD camera. (b) Diffusion profiles of the QWR carriers excited at four different positions along the QWR axis, as depicted in the central panel. (c) Intensity of the QWR emission along the QWR axis.

A closer inspection of the figure reveals that the shape of the diffusion profiles at the four positions are different, as highlighted by black circles. These particular features are ascribed to potential fluctuations along the QWR axis resulting from either thickness fluctuations or alloy fluctuations in the $Al_{0.15}Ga_{0.85}As$ barriers. Note that the density of defects and impurities is small, as is evidenced by the small Stokes shift in the previously discussed PLE spectrum.

6.3 Time-resolved photoluminescence

More insights into the carrier dynamics are obtained from time-resolved PL measurements. Figure 6.6 displays the PL intensity of a ridge sidewall as function of time (vertical axis) and detection energy (horizontal axis). The experiment is conducted using a pulsed Ti:sapphire laser (excitation energy 1.571 eV, excitation density 2.3 W/cm^2, pulse duration 1.5 ps). The figure clearly shows the signals of the substrate (1.514 eV), the QWR_{hh} (1.520 eV) and the QW_{hh} transitions (1.546 eV), which all decay exponentially in time. The right panel depicts the spectral integrated temporal traces extracted for the substrate (orange), the QWR_{hh} (green) and the QW_{hh} (blue) transitions. While the substrate signal decays with a short recombination lifetime of approx. 70 ps, the QWR_{hh} and the QW_{hh} transitions are substantially long lived. The enhanced recombination lifetimes detected in the QWR and QW result from their carrier confinement. The dynamics of exciton formation at short timescales is described by the following process [26]. First, light absorption leads to the excitation of electron-hole pairs, which form free excitons at high-energy states with large in-plane momenta within a typical timescale below 20 ps. The fast rise time of the temporal PL plots is a signature of the energy relaxation of these excitons into states within the optical cone around zero momentum. A minor part of the high-energy states recombine before relaxation, which is detected as a small red-shift of the initial emission as time progresses up to approx. 100 ps. The excitons within the optical cone (with small in-plane momenta) recombine efficiently and emit a photon with the corresponding energy. A fit of the QW_{hh} signal with a single exponentially decaying function results in a recombination lifetime of approx. 0.5 ns. Note that the QW signal mainly represents carriers injected in the flat QW areas, since the spatial extent of the corner QW is expected to be small as compared to the excitation and detection areas.

The temporal trace of the QWR exhibits an additional plateau for intermediate timescales $200\,\text{ps} < t < 500\,\text{ps}$. Note that according to the results presented in the previous section, direct excitation of QWR carriers is negligible for the excitation conditions used in this experiment. The major part of the QWR PL signal results from carrier diffusion from the corner QW into the QWR. The rise time of the QWR signal corresponds, therefore, to carriers which are excited into the corner QW and directly diffuse into the QWR. At intermediate timescales, these QWR carriers start to decay, while diffusion of the corner QW carriers into the QWR may still take place. A balance of QWR carrier decay and QW carrier diffusion leads to the observed plateau, since the former process reduces the QWR signal, while the latter process increases the QWR signal. After approx. 500 ps, diffusion of the corner QW carriers becomes negligible. Therefore, at longer timescales the signal contains only a contribution of the decaying QWR carriers, with a typical recombination lifetime of approx. 0.9 ns. The longer recombination lifetime of the QWR with respect to the QW is attributed to its larger thickness. The larger dimensions decrease the degree of exciton localization and the magnitude of the exchange interaction [140].

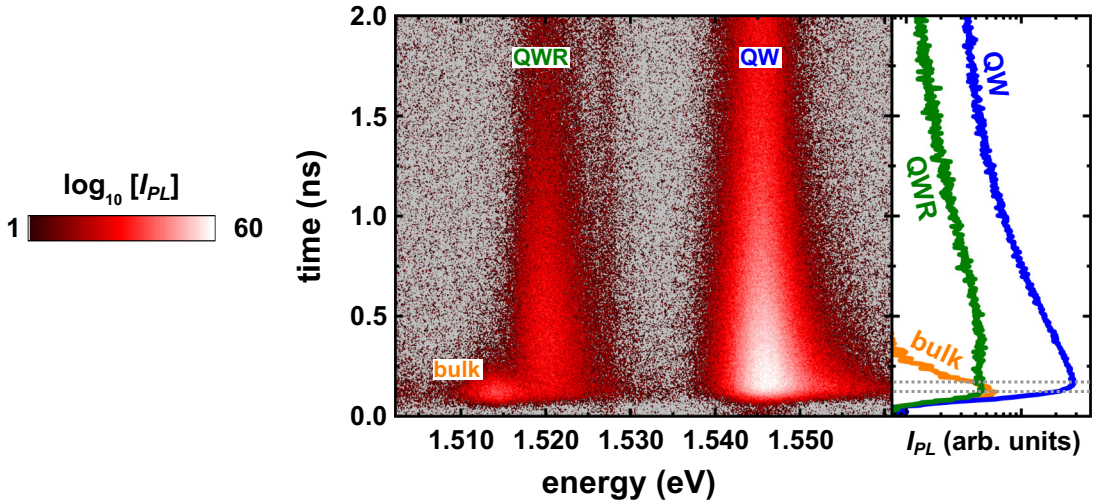

Figure 6.6: Time-resolved PL traces recorded on a ridge sidewall as a function of emission energy. The substrate has an optical transition energy of 1.514 eV, the QWR of 1.520 eV and the QW of 1.546 eV. The right panel shows the extracted temporal traces for the substrate (orange), the QW_{hh} (blue) and the QWR_{hh} (green) transitions. The dashed grey lines indicate the maximum PL for the QW and the QWR.

6.4 (Al,Ga)As barrier emission

The anisotropic overgrowth of Ga-rich layers also affects the growth and composition of the (Al,Ga)As layers. Figure 6.7(a) shows a map of the barrier PL, while exciting the QW structure with an excitation energy of 2.332 eV and excitation density of 10 kW/cm^2. Two clear resonances are observed in the figure. Away from the sidewall, the barrier PL contains two transition lines at approx. 1.700 eV and 1.710 eV, respectively, indicating a nominal Al content of 13 % - 14 %. When the laser spot approaches the ridge sidewall, the transition line at 1.700 eV vanishes and a second transition appears at 1.646 eV. A clear intensity reduction of the transition at 1.700 eV close to the ridge sidewall supports the assignment of the 1.646 eV transition line to the barrier. The 1.646 eV transition energy corresponds to an Al content of 9 %. The modification of the Al content at the ridge sidewall clearly demonstrates that the (Al,Ga)As barriers grow anisotropically as well. The Al content at the sidewall is reduced because of the larger diffusion length of Ga adatoms as compared to Al adatoms [134]. STEM images (see sec. 5.3.2) showed that the lateral growth of the barriers is approx. five time faster than its vertical growth. In fig. 6.7(a), the spatial separation between two consecutive y-positions of the 1.646 eV transition line at the ridge top (bottom) is denoted by Δy_{top} (Δy_{bottom}). Clearly, $\Delta y_{top} > \Delta y_{bottom}$, which confirms the conclusions drawn from the afore mentioned STEM images.

A similar conclusion can be drawn from cathodoluminescence (CL) measurements. In these experiments, the electron-hole pairs are excited by bombardment of the sample by a nanometer sized electron beam, while integrating the emission of the full sample area. The spatial resolution is determined by the electron-beam size and the diffusion lengths of the carriers in the sample. The electron acceleration voltage is 7 kV and the beam current 1.4 nA. Diffusion of the electrons into the lower barrier layer is prevented by the QWR, so that emission of that barrier can not be observed. A SEM image of a 17 µm x 17 µm sized area containing the end of a ridge is shown in fig. 6.8(a). Figure 6.8(b) displays the CL map of the same area for a detection energy of 1.633 eV. Here, CL is observed only at the ridge sidewall and is attributed to the upper (Al,Ga)As layer. Note that the emission pattern depicts several hot spots along the x direction. Similar emission patterns are

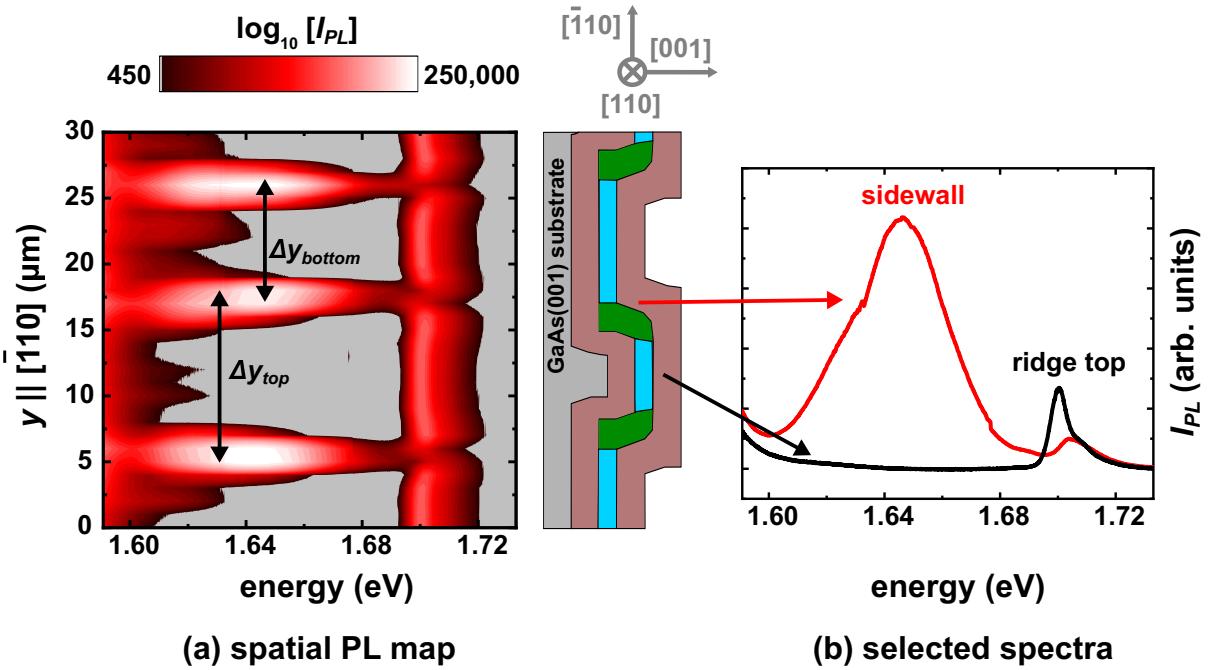

Figure 6.7: Emission of the (Al,Ga)As barrier. (a) Spatial map of the PL, collected by scanning the laser spot over a 30 µm-long line along [$\bar{1}$10]. The geometry of the experiment is illustrated in the central panel, where the grey layer represents the substrate, the red layers the (Al,Ga)As barriers, the blue layer the QW and the green area the QWR. (b) Selected spectra extracted from fig. (a) at the ridge top (black) and at the sidewall (red).

observed for detection energies of 1.654 eV and 1.622 eV (not shown here), with different x positions of the emission hotspots. The positions of these hotspots seem to be randomly distributed. These emission hotspots are, therefore, ascribed to random fluctuations of the Al content in the upper (Al,Ga)As barrier.

Figure 6.8(c) depicts the CL map, recorded while detecting at the QW_{hh} energy. At the position of the QWRs, the QW CL intensity is reduced due to QW carrier diffusion into the QWR. The stronger CL intensity at the ridge top as compared to the ridge bottom is most likely related to a better sensitivity of the optical setup at the center of the image. The emission energy at ridge top and bottom are found to be similar. A complementary CL map of the QWR_{hh} transition is shown in fig. 6.8(d). As expected, the emission of the QWR_{hh} transition is only observed at the ridge sidewalls. The right panel depicts the spatial profile of the QWR_{hh} transition (black) and the barrier emission (red). The dashed grey lines indicate the peak positions of the QWR emission, which coincide with their physical $y||[\bar{1}10]$ coordinates. The black plot indicates that the carrier diffusion length is larger at the ridge top as compared to the ridge bottom. Comparing the spatial profiles of the QWR emission and the sidewall barrier emission, a lateral shift of approx. 500 nm is observed, which is consistent with STEM images shown in sec. 5.3.2.

In previous literature, a change of the QWR transition energy was observed for ridges on (113)A substrates oriented at a finite angle with the [$\bar{1}$10] direction (which is the primary QWR axis direction for (113)A substrates). This is explained by a gradual transition of the fast-growing facet towards a slow growing-facet [141, 49]. A SEM image of a similar pattern on a (001) substrate is shown in fig. 6.9(a). In this case, the width of the fabricated ridges, before MBE overgrowth, is 10 µm. The distance between two adjacent sidewalls of two different ridges is 5 µm (i.e. the distance between two ridge centers is 15 µm). The ridges are oriented with an inclination angle of 27° with respect to the [110] direction. This direction corresponds to the [130] direction. PL measurements (not shown here) do

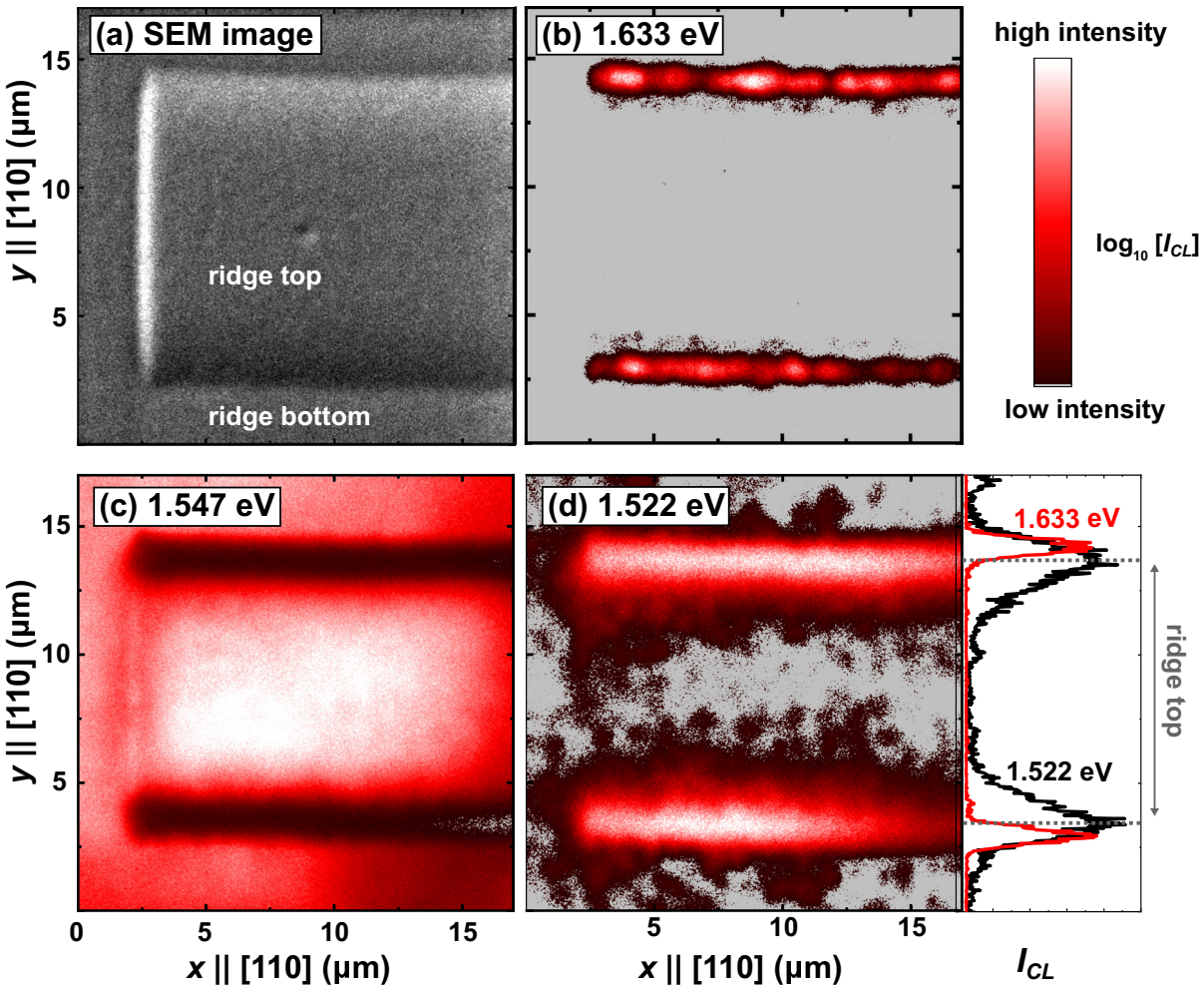

Figure 6.8: Cathodoluminescence of the (Al,Ga)As barrier. (a) SEM image of the inspected area, showing the end of a 10 µm-wide ridge. (b) Map of the CL of the 1.633 eV transition, indicating the position of diluted Al content in the upper $Al_{0.15}Ga_{0.85}As$ barrier. (c) Map of the QW_{hh} CL (detection energy: 1.547 eV). (d) Map of the QWR_{hh} CL (detection energy: 1.522 eV). The right panel shows spatial profiles of the 1.633 eV transition (red) and QWR_{hh} transition (black). The dashed grey lines depict the maxima of the QWR intensities, which coincide with their y positions. The SEM image of fig. (a) and the CL data of figs. (b)-(d) are recorded by Dr. Jonas Lähnemann.

not demonstrate significant energy shifts of the sidewall QWRs of these structures with respect to the sidewall QWRs formed at rectangular mesas. A map of the CL yields a similar conclusion. The barrier CL shows a behaviour similar to the rectangular ridges, e.g. a red-shift of the transition energy close to the ridge sidewall, associated to a dilution of Al at this position. Figure 6.9(c) shows the emission pattern of such a barrier transition (detection energy 1.633 eV) of the same area as fig. 6.9(a). The vertical distance Δy between two consecutive emissions in fig. 6.9(c) is approx. 11.5 µm at the ridge top, while it is 3.5 µm at the ridge bottom. This corresponds again to the difference in growth rates of the (Al,Ga)As growth along the lateral and the vertical directions and is clearly observed as well in the SEM image of fig. 6.9(a).

The QW emission at the ridge top is 1.547 eV, similar to the previously studied rectangular ridges. The QW emission pattern is shown in fig. 6.9(b). As can be seen in the figure, the intensity is much stronger at the ridge top than at the bottom. Note that in this case, the effect is observed on both ridges within the detection area and is, therefore, not related to artefacts from the stronger sensitivity of the setup to the image center. From a closer inspection of the spectra at the ridge top (blue) and ridge bottom (black) in the upper panel, it is inferred that the QW energy at the ridge bottom is blue-shifted by approx. 3 meV with respect to the ridge top. Due to the small width of the QW area at the ridge bottom (5 µm instead of the 10 µm in the samples discussed before), diffusion of Ga adatoms during MBE overgrowth can take place even from the center of the ridge bottom, towards both sidewalls (see white arrows in fig. 6.9(a)). One can, therefore, expect a decrease of the QW thickness even in the center of the narrow ridge bottom. As a result, the QW transition peak of the ridge bottom lies outside the detection window for fig. 6.9(b). The QW emission at the ridge bottom is, thus, not detected, which explains the smaller intensity as compared to the ridge top.

Finally, fig. 6.9(d) displays the emission pattern of the QWR emission (detection energy 1.522 eV). Similar to the rectangular ridges, the position of the QWR is complementary with fig. 6.9(b), since the QWR_{hh} CL is strong at the position where the QW_{hh} CL is weak. The homogeneous intensity indicates a good uniformity of the QWR energy along its axes, since fluctuations of the transition energy should lead to recombinations outside the spectral detection window. The fact that the QWR energy for the zig-zag structures is similar to the one on straight structures can be understood by considering the QWR formation mechanism. For (113)A substrates, the QWR formation depends on the differences of the diffusion lengths on the ridge facets. Since the surface orientation of the ridge sidewall may change with varying ridge orientation, the dimensions of the QWR depend on the ridge orientation on the substrate surface. In contrast, for (001) substrates, QWR formation relies on the step density along the $[\bar{1}10]$ direction, which should only depend on the sidewall inclination angle and be independent of the ridge orientation.

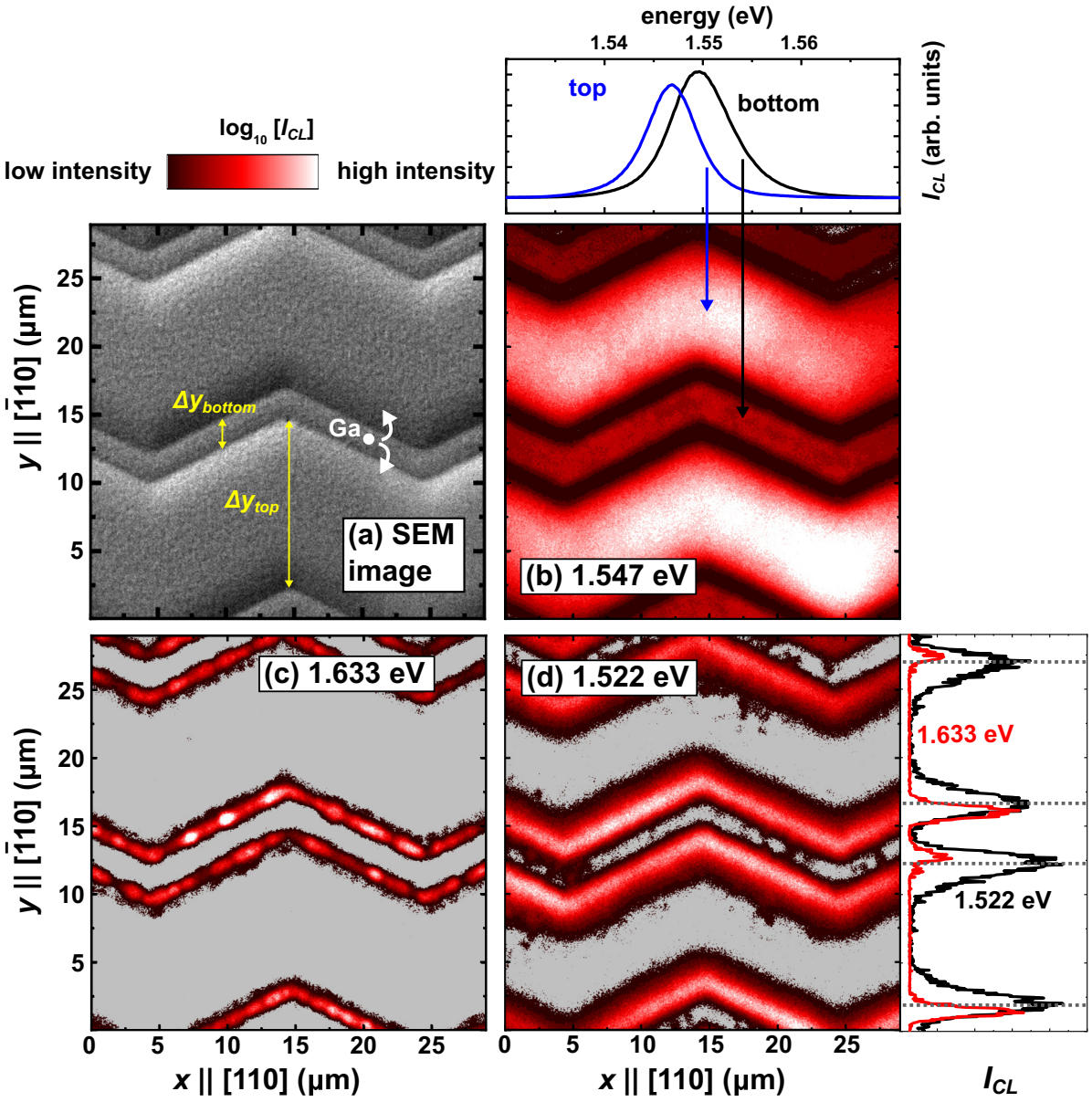

Figure 6.9: Cathodoluminescence maps. (a) SEM image of the inspected area with zig-zag structures, defined by substrate mesas with a width of 10 µm and interdistance (between two adjacent sidewalls of two different ridges) of 5 µm. (b) Map of the QW_{hh} CL (detection energy: 1.547 eV). The upper panel shows the spectrum at the ridge top (blue) and at the ridge bottom (black). (c) Map of the CL of the 1.633 eV transition, indicating the positions of reduced Al content in the upper $Al_{0.15}Ga_{0.85}As$ barrier. (d) Map of the QWR_{hh} emission (detection energy: 1.522 eV). The right panel shows spatial profiles of the 1.633 eV transition (red) and QWR_{hh} transition (black). The dashed grey lines depict the maxima of the QWR intensities, which coincide with their y positions. The SEM image of fig. (a) and the CL data of figs. (b)-(d) are recorded by Dr. Jonas Lähnemann.

6.5 Summary of the chapter's findings

The experiments conducted in this chapter show that planar sidewall quantum wires form on prepatterned ridges fabricated on both (113)A and (001) substrates. Their spectral lines are inhomogeneously broadened with respect to the surrounding QW transition, which is attributed to surface roughness at the sidewall and to alloy fluctuations of the $Al_{0.15}Ga_{0.85}As$ barrier at the ridge sidewall. The latter manifests itself also by local, randomly distributed, red-shifts of the barrier transition at the ridge sidewall. The spectral linewidth of the QWRs fabricated on (113)A substrates is larger than those fabricated on (001) substrates. This is attributed to the favourable growth mode on (001) substrates. Furthermore, the red-shift of the QWR transition with respect to the QW transition is larger on (001) substrates, so that the QWR carriers are better protected against escaping into the surrounding QW for this orientation. For the QWRs on (001) substrates, the lateral potential barrier for electrons in the conduction band and holes in the valence band imposed by the surrounding QW is approx. 25.4 meV and 4.8 meV, respectively.

A summary of the main properties of sidewall QWRs on different substrates and fabricated with different lithography methods is presented in table 6.1. The results presented in this chapter are promising for the transport characteristics of planar sidewall quantum wires on (001) substrates. The remainder of this thesis investigates, therefore, acoustic charge and spin transport along planar sidewall QWRs on (001) substrates.

	photolithography		**e-beam lithography**
	(001)	(113)A	(113)A
QW thickness (nm)	10	10	8
QW_{hh} transition (eV)	1.546	1.543	1.558
QWR_{hh} transition (eV)	1.521	1.526	1.546
ΔE_e (meV)	25.4	17	10
ΔE_{hh} (meV)	4.8	3	2
linewidth (FWHM, meV)	5-10	12	9

Table 6.1: Summary of the optical properties of QWRs fabricated on (001) and (113)A substrates, fabricated using photolithography and e-beam lithography.

chapter 7

Acoustic charge transport

The previous chapter demonstrates the superior optical properties of QWRs fabricated on (001) substrates over those fabricated on (113)A substrates. In this chapter, the transport properties of QWRs on GaAs (001) substrates are investigated utilizing a surface acoustic wave. Section 7.1 discusses ambipolar transport while exciting the QW structure using an excitation energy above the QW transition. Next, excitation below the QW energy (above the QWR energy) is discussed in sec. 7.2. Some of the transport characteristics are studied in sec. 7.3, while an investigation of the transport efficiency is provided in sec. 7.4 by means of time-resolved photoluminescence (PL) measurements. Section 7.5 discusses SAW-assisted extraction of QWRs carriers into the surrounding QW. Finally, sec. 7.6 provides a summary of the chapter's findings. As in the previous chapters, the reference frame used throughout this chapter is constructed by $x||[110]$, $y||[\bar{1}10]$ and $z||[001]$. The orientation of the ridges is along the x axis (i.e. along [110]*).*

7.1 Excitation above the quantum well energy

Figures 7.1(a)-(c) show a typical acoustic charge transport experiment, conducted using the confocal microscopy setup (see sec. 4.3.2). The sample consists of a 5 mm x 5 mm chip, cut from a processed 2-Inch GaAs (001) substrate wafer, and contains five ridges with ten sidewall QWRs. As illustrated by the right panel, carriers are optically injected at the ridge sidewall at a position of $x = 0\,\mu m$ by a laser with an energy of 1.591 eV, excitation density of $60\,W/cm^2$ and spotsize (FWHM) of approx. 2.5 µm. The sample temperature is approx. 15 K. Under these conditions, carriers are excited above the QW transition, so that the majority of the QWR carriers originates from diffusion of QW carriers (cf. fig. 6.3). Figure 7.1(a) displays an image of the PL intensity I_{PL} without a SAW. Clearly, emission from both the QW and QWR transitions is observed only within the vicinity of the excitation location. The small tilt of the image (the x positions of the excitation locations in the QW and QWR appear to differ slightly) is an artefact resulting from the alignment of the optical setup. Spatial integration of the PL at the excitation location results in a typical spectrum (upper panel) containing spectral lines from the substrate (1.516 eV), the QWR (1.521 eV) and the QW (1.546 eV) transitions. Spatial profiles of the PL depict similar diffusion lengths (defined as the half-width-at-half-maximum) in the QW and the QWR below 5 µm.

The application of a SAW (wavelength $\lambda_{SAW} = 4\,\mu m$, frequency $f_{SAW} = 726\,MHz$) with an acoustic power of $P_{SAW} = 14\,dBm$ ionizes the photo-excited excitons at the excitation location, resulting in free electrons and holes. These free carriers are spatially separated by

the SAW potential. The separation reduces the wavefunctions overlap between electrons and holes and, hence, prevents their recombination. The free electrons and holes are stored in the conduction band minimum and valence band maximum, respectively (see sec. 2.3.1). The carriers in the band extrema travel along the SAW propagation path. This results in a strong quenching of the PL at the excitation location [142, 59, 143], as shown by fig. 7.1(b). Under ideal transport conditions, the charge carriers are acoustically transported by the SAW potential towards a metal stripe between $x = 65\,\mu m$ and $x = 75\,\mu m$. The metal stripe screens the SAW potential and forces recombination of the transported carriers. One expects, therefore, to observe PL only at the excitation location and at the position of the metal stripe. However, only a small part of the recombination events taking place below the metal stripe can be detected due to the low optical transmission of the metal stripe, which is smaller than 1 %. Nonetheless, the screening effect is also partly effective around the edges of the metal stripe, leading to weak PL at the edges of the metal stripe. Consistent with these expectations, fig. 7.1(b) clearly shows the remote PL at the metal stripe edges for both the QWR and the QW. The absence of QWR PL between the excitation location and the metal stripe, in combination with the large PL quenching at the excitation location, indicates that for this SAW power, charge transport along the QWR axis is very efficient. In contrast, the QW PL clearly shows distinctive PL hotspots along the transport path between excitation location and metal stripe. At the positions of these hotspots, trapping centers lead to carrier trapping and subsequent recombination, as will be discussed in more detail in the next paragraph. For the QW, PL is also observed directly below and even beyond the metal stripe. The former demonstrates that a large fraction of the QW carriers injected at the excitation location is transported towards the metal stripe, while the latter indicates that for this SAW power, the metal stripe only partly screens the SAW potential.

Figure 7.1(c) displays the PL map for a lower SAW power, $P_{SAW} = 8\,dBm$. In this case, no PL is observed around the edge of the metal stripe. Instead, PL hotspots are observed at $x \approx 33\,\mu m$ and $x \approx 37\,\mu m$. Here, a trapping potential captures transported carriers of one polarity (negative electrons or positive holes). Recombination events are detected with the passage of carriers stored by the SAW potential, carrying the opposite polarity. The trapping center may originate from three different trapping mechanisms, which are discussed in sec. 2.4: inhomogeneities of the channel dimensions, presence of interface states and defects or impurity sites. Since trapping at defects or impurities should lead to large spectral shifts [84], which are not observed in fig. 7.1(c), these can be ruled out. The narrow thickness of the QW layer means that thickness inhomogeneities should result in spectral shifts of the order of meV. The absence of such spectral shifts indicates that the main cause of the carrier trapping centers are interface states. The disappearance of the trapping center for high acoustic powers as in fig. 7.1(b) reveals that the trapping dynamics depends on the SAW fields.

The degree of PL quenching at the excitation location is plotted in fig. 7.1(d) as function of acoustic power for the QW (black) and the QWR (red). Here, the PL quenching is defined by the following formula:

$$\text{degree of PL quenching} = \frac{I_{PL,NoSAW} - I_{PL,SAW}}{I_{PL,NoSAW}} \times 100\%, \tag{7.1}$$

where $I_{PL,NoSAW}$ and $I_{PL,SAW}$ denote the integrated PL intensities without a SAW and with a SAW, respectively. The inset displays the spectra at the excitation location without a SAW (black), and with SAW powers of 8 dBm (red) and 14 dBm (blue). The plots in this inset clearly show the strong degree of PL quenching of both the QWR and the QW. Interestingly, even for high acoustic powers, no clear spectral shift of the QWR transition

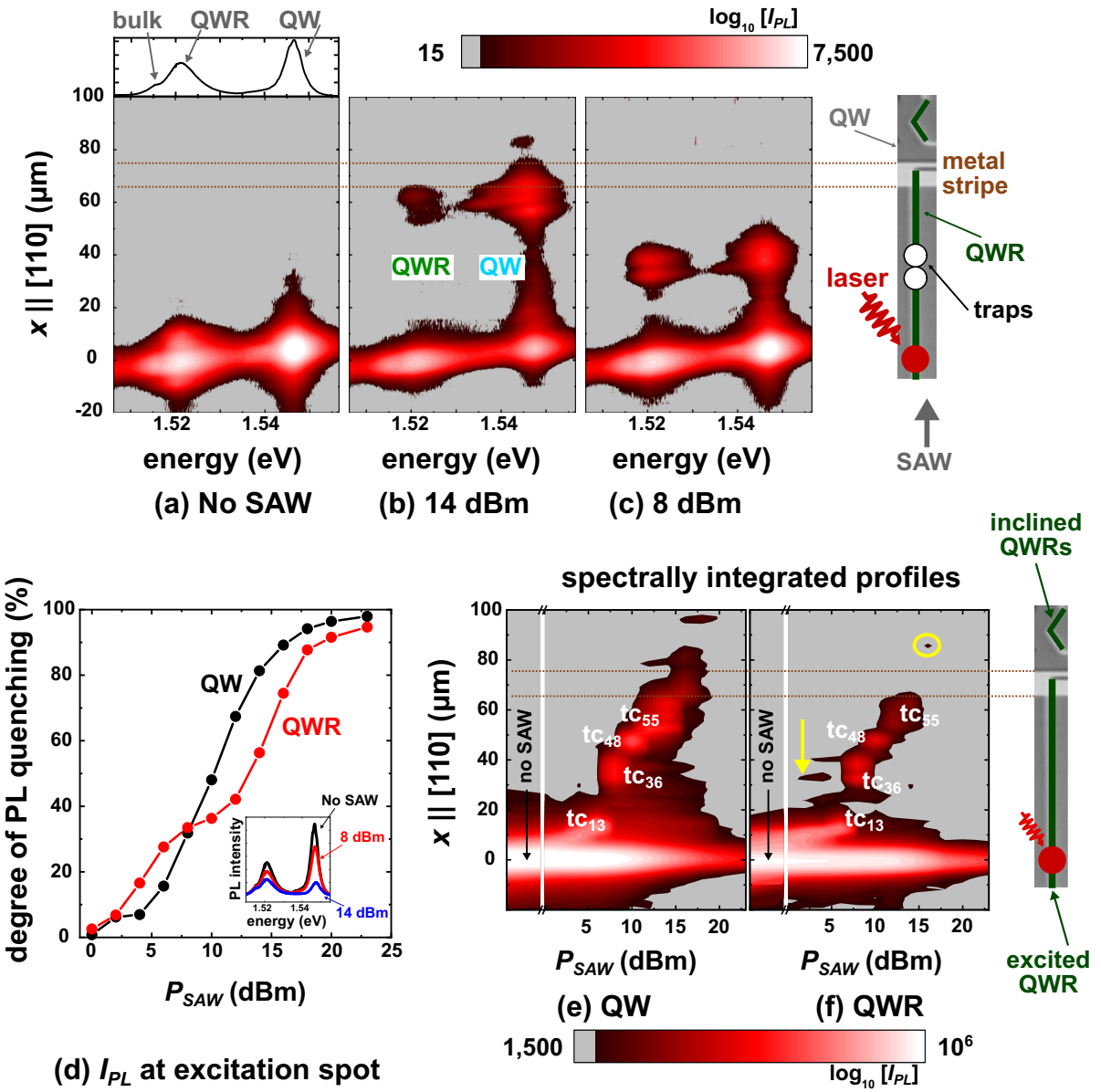

Figure 7.1: Acoustic charge transport at the ridge sidewall. Spatial PL map without application of a SAW (a), with a SAW of 14 dBm (b) and 8 dBm (c). The upper panel in fig. (a) depicts the spatially integrated spectrum at the excitation location, showing the substrate, QWR and QW transitions. The right panel illustrates the geometry of the experiment: carriers are optically injected at the excitation location (red dot), transported by the SAW (grey arrow) along the QWR (green line) and QW up to a metal stripe deposited onto the end of the QWR. Along the path, trapping centers (open dots) may be present, leading to recombination. (d) PL quenching at the excitation location as function of SAW power for the QW (black) and QWR (red). The inset depicts the spectra at the excitation location without SAW (black) and with SAW powers of 8 dBm (red) and 14 dBm (blue). Spectrally integrated vertical profiles of the PL are shown in figs. (e) (QW) and (f) (QWR) as function of acoustic power. The numbers correspond to trapping centers along the transport path.

energy is observed. The absence of such a shift, which is expected because of the bandgap modulation by the strain fields (see sec. 2.3.2), is attributed to the large QWR linewidth with respect to the expected spectral shift. In contrast, the QW transition is blue-shifted by approx. 0.5 meV, indicating that recombination of QW carriers at the excitation location takes place where the SAW strain fields lead to a maximum bandgap. It was shown in sec. 2.3.2 that this corresponds to the SAW phase where holes are stored. The small PL quenching for small acoustic powers displayed by the main graph of fig. 7.1(d) reveals that for small acoustic powers, the SAW potential is too weak to ionize excitons. In this case, the optically injected charge carriers are able to easily escape from the SAW potential. Increasing the acoustic power increases the amplitude of the SAW potential, leading to a higher degree of PL quenching. At high acoustic powers, PL quenching is nearly complete, indicating that the separation of the electrons and holes is very efficient. Thus, under this condition, the carriers are transported in their respective SAW-phases away from the excitation location in both the QWR and the QW (no carrier spread).

Figures 7.1(e) and (f) show the spectrally integrated PL along the transport path for the QW and the QWR, respectively, as function of position along the SAW propagation path $x||[110]$ (vertical) and SAW power (horizontal). Without application of a SAW, emission is only observed within the vicinity of the excitation location. For small SAW powers, the SAW potential is too weak to induce carrier transport, as is indicated by the absence of PL quenching at the excitation location and the absence of remote PL. For intermediate acoustic powers, remote PL can be observed from various positions along the transport path, due to the capture of acoustically transported carriers by several trapping centers. These will be denoted by tc_i, where i represents their x position. Closer inspection of the figures reveals that the majority of the recombination events in the QWR appear at equal x positions as those observed in the QW. The QWR carriers at these trapping centers can originate from either (i) QWR carriers directly transported from excitation location towards the trapping center or (ii) QW carriers which remotely diffuse into the QWR. The latter is, however, prevented by the the lateral potential barrier between the QWR and the QW at the flat areas imposed by the corner QW (see sec. 6.2). Additionally, the carriers transported along the QW diffuse along the y direction away from the ridge sidewall. Note that remote PL can only appear if a trapping center is present, which means that the trapping centers which appear in both the QW and the QWR indicate a large trapping center extending over several hundreds of nanometers. This could result from, for example, a local cluster of interface states. For the highest acoustic powers (e.g. 20 dBm), no remote PL is observed from both the QW and the QWR. For these acoustic powers, the trapping potentials along the transport path are overcome by the strong SAW potential, which explains the absence of remote PL from the trapping centers. As discussed in this paragraph and in sec. 7.3.1, the screening effect of the metal stripe is strongly reduced at high acoustic power, so that QW carriers can be transported beyond the metal stripe. QWR carriers, in contrast, can not be transported beyond the metal stripe, since the end of the QWR is positioned directly below it. However, the PL signal of the QWR directly below the metal stripe is expected to be weak due to the smaller number of carriers in the QWR and the very low optical transmission of the metal stripe.

The lateral potential barrier imposed by the corner QW can be overcome if the QWR is oriented at some angle with respect to the SAW propagation path, resulting in a piezoelectric field component across the ridge sidewall cross-section. Such a QWR is located beyond the metal stripe, as illustrated by the green triangle in the right panel of fig. 7.1(f). Indeed, at a position of $x = 85\,\mu m$, remote PL at the QWR energy is observed (highlighted by a yellow circle in fig. 7.1(f)). This signal can only originate from QW carriers transported beyond the metal stripe, which remotely diffuse into the QWR,

assisted by the lateral piezoelectric SAW field.

Direct transport of QWR carriers is evidenced by the appearance of remote QWR PL at a position, where no QW PL is observed. Such a position at $x = 30\,\mu m$ is highlighted by the yellow arrow in fig. 7.1(f). A comparison with fig. 7.1(e) shows that at this position and for the same SAW power, no recombination events are detected in the QW. The QWR emission must, therefore, originate from carriers, which are directly transported from the excitation location towards the trapping center along the QWR axis.

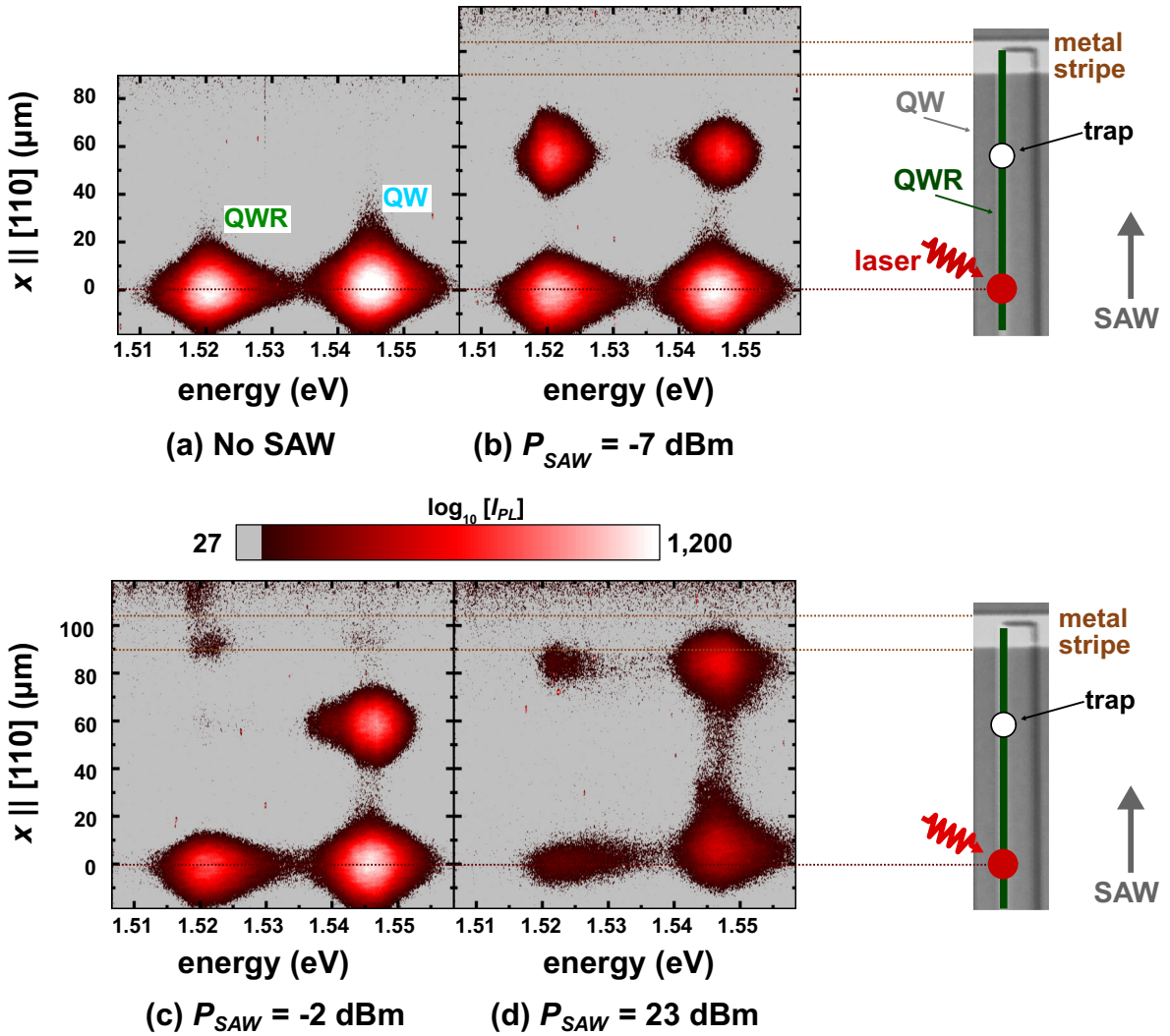

Figure 7.2: Acoustic charge transport at the ridge sidewall. (a)-(b) Spatial PL map without application of a SAW (a) and with application of a SAW of $-7\,dBm$ (b). The right panel illustrates the geometry of the experiment: carriers are optically injected at the excitation location (red dot), transported by the SAW (grey arrow) along the QWR (green line) and along the QW up to a metal stripe deposited onto the end of the QWR. (c)-(d) Spatial PL maps with application of a SAW of $-2\,dBm$ (c) and $23\,dBm$ (d).

The results presented above correspond to a typical case. Another experiment, conducted using a different experimental setup (the low-temperature probe station, see sec. 4.3.1) is presented in the following paragraphs. The experiment has been carried out on a different 5 mm x 5 mm chip, cut from the same 2-Inch GaAs wafer as the sample used in the experiments presented above. In this case, the excitation of electrons and holes is carried out by a pulsed diode laser with an excitation energy and density of 1.954 eV and $4\,W/cm^2$, respectively. The sample temperature during the experiment is approx. 5 K. The sample contains a split-finger type IDT designed for a SAW wavelength of $\lambda_{SAW} =$

5.6 µm (f_{SAW} = 519 MHz). Although the outcomes of this experiment are not typical, the results are presented because they provide additional information for carrier transport directly along the QWR axis.

Without a SAW (fig. 7.2(a)), QW PL and QWR PL is, as expected, only observed around the excitation location. The PL from the substrate is suppressed due to the low excitation density. When a SAW with an acoustic power of $P_{SAW} = -7$ dBm is applied (fig. 7.2(b)), PL quenching is observed for both the QWR and the QW transitions. For both transitions, remote PL is observed at a position of approx. $x = 60$ µm. Extracted spectra at the excitation location for increasing acoustic power (not shown here) depict that the degree of PL quenching is stronger in the QWR as compared to the QW for all acoustic powers. Since PL quenching is strong when carrier transport is efficient, one expects a high degree of PL quenching for high carrier mobilities [55, 87]. Thus, the stronger PL quenching of the QWR as compared to the QW indicates that the carrier mobility in the QWR is larger than in the QW. This is consistent with the findings of ref. [144]. Note that this result is initially consistent with the findings presented in fig. 7.1(d) for small acoustic powers. From the data presented here, it can not be inferred what is the reason of the weaker degree of PL quenching in the QWR as compared to the QW for higher acoustic powers in fig. 7.1(d). A further increase of the acoustic power to P_{SAW} = −2 dBm (fig. 7.2(c)) results in a stronger PL quenching at the excitation location for both the QWR and QW transitions. Contrarily to the excitation location, the QW PL at the trapping center increases, while the QWR PL at the trapping center is suppressed. Remote QW carrier diffusion into the QWR at the position of the trapping center should, in contrast, lead to a stronger QWR PL. The findings of figs. 7.2(b) and (c) are, therefore, a proof of acoustic charge transport directly along the QWR axis. For a high acoustic power of $P_{SAW} = 23$ dBm (fig. 7.2(d)), the emission from the trapping center is completely suppressed for both the QW and the QWR, leading to the transport of charge carriers up to the metal stripe at $x = 90$ µm along both the QW and QWR.

There are two clear differences between the results presented in figs. 7.1 and 7.2. Firstly, acoustic charge transport in both the QW and the QWR is observed for much smaller acoustic powers in the latter case. This indicates that the radio-frequency (rf) power losses from rf signal generator to IDT were smaller during the experiment of figs. 7.2. Secondly, whereas figs. 7.2 depict one major trapping center with a large PL intensity, the results of figs. 7.1(e) and (f) show the presence of multiple trapping centers with similar PL intensities. There are four experimental conditions which were different and may affect the behaviour of the trapping dynamics: (i) sample temperature, (ii) SAW wavelength, (iii) acoustic power (due to the differences in power losses) and (iv) excitation density. The results presented in figs. 7.2 could not be reproduced in experiments on different samples, when using the conditions for the experiment of figs. 7.1. More studies are, therefore, required to clarify the reason for the two differences. Such a study should include a systematic examination of the effect of the four afore mentioned experimental conditions on the trapping dynamics.

7.2 Selective excitation of the quantum wire

Unambiguous proof of acoustic charge transport directly along the QWR axis will be provided in this section, by exciting the ridge sidewall below the QW transition (above the QWR energy). Under this condition, the QWR is selectively excited: carriers are optically injected directly into the QWR and not via diffusion of QW carriers. The results of such an experiment are presented in figs. 7.3(a)-(e). The experimental geometry is illustrated in the right panel. In the remainder of this chapter, all acoustic experiments are conducted

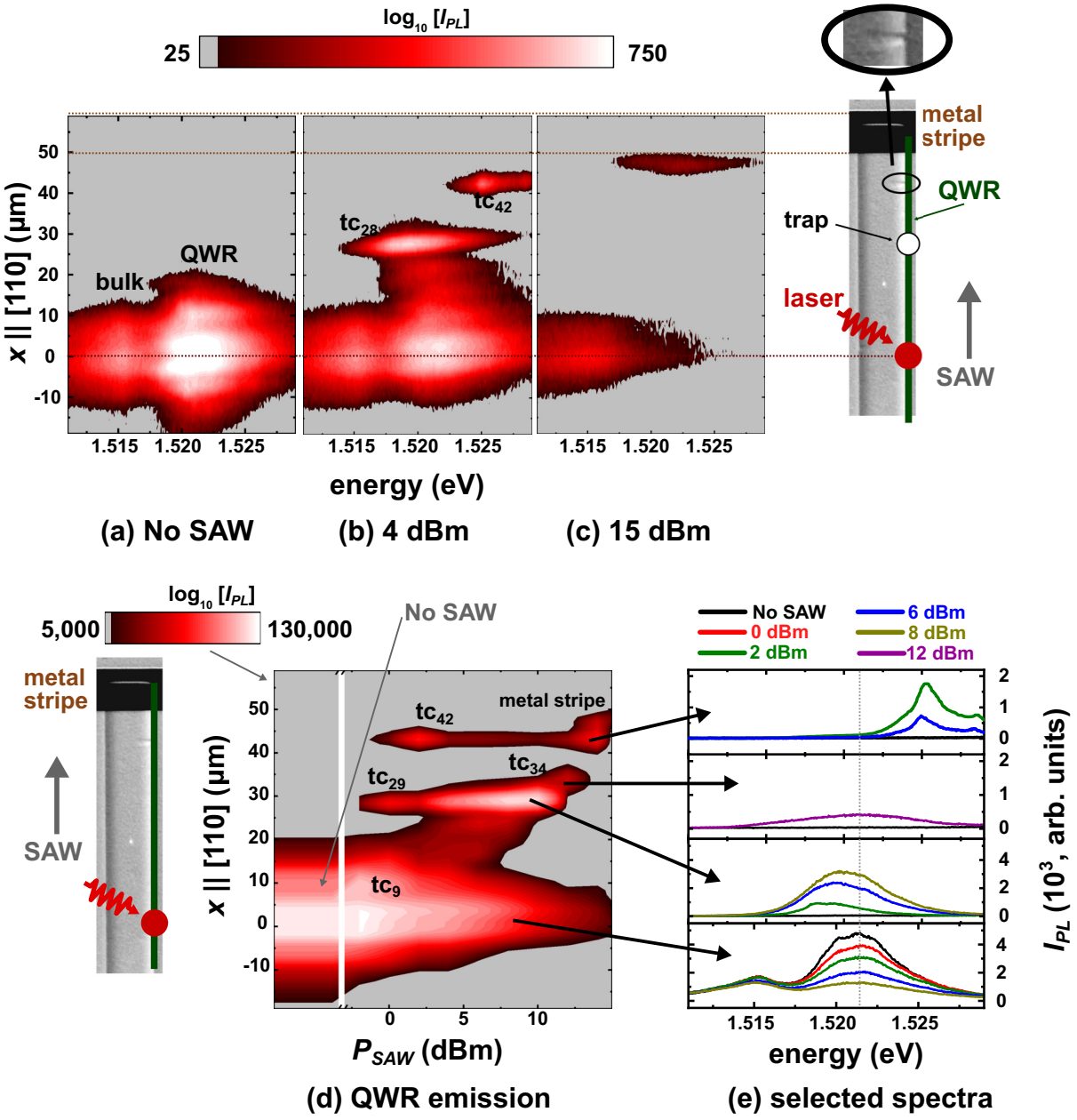

Figure 7.3: Acoustic charge transport at the ridge sidewall with selective excitation of the QWRs. Spatial PL map without application of a SAW (a) and SAW powers 4 dBm (b) and 15 dBm (c). The right panel illustrates the geometry of the experiment: carriers are optically injected at the excitation location (red dot), transported by the SAW (grey arrow) along the QWR (green line) up to a metal stripe deposited onto the end of the QWR. The black circle highlights a scratch-like feature on the ridge sidewall. (d) Spectrally integrated profiles of the QWR transition as function of SAW power, with denoted numberings of different trapping centers along the transport path. (e) Spectra extracted for different trapping centers (first, second and third panel) and at the excitation location (fourth panel) for SAW powers of 0 dBm (red), 2 dBm (green), 6 dBm (blue), 8 dBm (yellow), 12 dBm (purple) and without SAW (black).

using SAWs with $\lambda_{SAW} = 4\,\mu m$ ($f_{SAW} = 726\,MHz$) and a laser spot FWHM of approx. $2.5\,\mu m$. The ridge sidewall is excited at $x = 0\,\mu m$ by a laser with an excitation energy of $1.537\,eV$ and excitation density of $350\,W/cm^2$. The high excitation density as compared to the experiments in the previous section is required due to the small absorption area of the QWR. Without a SAW (fig. 7.3(a)), emission is observed only within the vicinity of the excitation location. The QWR carriers diffuse along x over a distance of approx. $8\,\mu m$ (as extracted from the spatial half-width-at-half-maximum). In this experiment, the metal stripe is located between $x = 50\,\mu m$ and $x = 60\,\mu m$. Application of a SAW with an acoustic power of $P_{SAW} = 4\,dBm$ (fig. 7.3(b)) results in the quenching of the QWR PL at the excitation location, while transport of carriers, their capture along the transport path and subsequent recombination is clearly evidenced by the remote PL of trapping centers tc_{29} and tc_{42}. While the remote spectrum of trapping center tc_{29} is red-shifted by less than 1 meV, the emission of trapping center tc_{42} is blue-shifted by approx. 4 meV. Closer inspection of the specific QWR studied during this experiment by an optical microscopy image (right panel) reveals that at the position of tc_{42}, a local scratch-like feature disrupts the ridge structure, as highlighted by a black circle. This feature may locally decrease the QWR dimensions, leading to a blue-shift of the local QWR transition. Raising the SAW power to $P_{SAW} = 15\,dBm$ (fig. 7.3(c)) overcomes the trapping potentials of all trapping centers along the transport path and, consequently, leads to the transport of QWR carriers towards the metal stripe. Recombination events directly below the metal stripe are not detected due to the limited optical transmission of the metal stripe.

Figure 7.3(d) shows the spectrally integrated QWR emission as function of x position along the QWR axis (vertical) and acoustic power (horizontal). The spatial separation of electrons and holes and subsequent transport of QWR carriers is clearly evidenced by a gradual quenching of the PL at the excitation location. For small acoustic powers, carriers stored at the extrema of the SAW potential are transported over a small distance up to trapping center tc_9. Increasing the acoustic power overcomes the trapping potential of trapping center tc_9 and carriers are transported towards trapping centers tc_{29} and tc_{42}. The figure confirms, furthermore, that for the highest acoustic powers, trapping along the full transport path is overcome by the strong SAW potential. Under this condition, carriers are transported up to the metal stripe.

Figure 7.3(e) displays the spectra of trapping centers tc_{42} (upper panel), tc_{34} (second panel), tc_{29} (third panel) and at the excitation location (lower panel). The latter clearly demonstrates the effect of the SAW by the increasing degree of PL quenching with SAW power. Since the nominal shapes of the spectra at the excitation location for all acoustic powers are similar, no clear sign of the strain-induced band-edge modulation is observed at the excitation location. This results from the broad linewidth of the QWR transition. The spectrum of trapping center tc_{34} is similar to the spectrum at the excitation location, which implies that this trapping center can be assigned to the presence of interface states. In contrast, the red-shift of approx. 1 meV observed for trapping center tc_{29} indicates that this trapping center can be attributed to a local increase of the QWR thickness. As was concluded in secs. 5.2.3 and 5.3.2, line-edge roughness is small and not expected to lead to carrier trapping. In addition to thickness inhomogeneities, the emission from trapping center tc_{29} can as well result from carriers trapped into interface states, which are subsequently released into a location with increased QWR dimensions [82].

7.3 Acoustic charge transport characteristics

In the previous sections, acoustic charge transport is demonstrated in both the QW and the QWR, for excitation energies above the QW transition, as well as below the QW

transition. In this section, some characteristics of the acoustic charge transport are studied.

7.3.1 PL quenching at the excitation location

A large carrier density leads to unintentional (partly) screening of the piezoelectric potential [145, 146], thus preventing efficient carrier transport. A schematic sketch to understand this effect is illustrated in the lower inset of fig. 7.4(a). The electron (brown dot, −) and hole (brown dot, +) are separated with a distance of half a SAW wavelength by the lateral piezoelectric SAW field ($F_{x,SAW}$, green arrow). The separated electron and hole form an electric dipole, generating an electric field $F_{x,e-h}$ anti-parallel to $F_{x,SAW}$. For large excitation densities, this dipole field becomes significantly strong and partly screens the piezoelectric SAW field, resulting in a weakening of the PL quenching. Figure 7.4(a) displays the degree of PL quenching (defined by eq. 7.1) at the excitation location as function of excitation density for the QW (black solid dots) and QWR (red solid dots). The SAW power is $P_{SAW} = 11\,\text{dBm}$. For low excitation densities, PL quenching is strong. For increasing excitation densities, the decreasing degree of PL quenching indicates that $F_{x,SAW}$ indeed becomes partly screened by the high carrier density. The degree of PL quenching is, however, still considerably large for high excitation densities. Moreover, a similar experiment for high acoustic power ($P_{SAW} = 21\,\text{dBm}$, open triangles in fig. 7.4(a)) shows that for such high powers, PL quenching is strong even for very high excitation densities. This indicates a high efficiency of carrier transport.

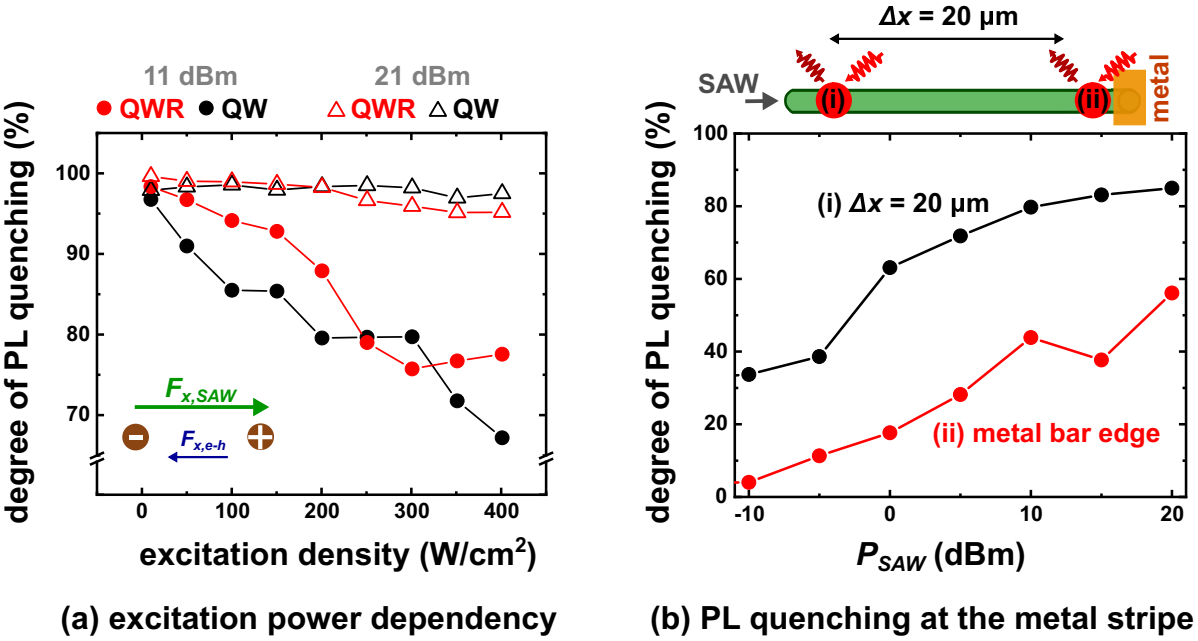

Figure 7.4: (a) PL quenching at the excitation location as function of excitation density in the QW (black) and QWR (red), for SAW powers of 11 dBm (solid dots) and 21 dBm (open triangles). The inset illustrates the screening process of the SAW potential by the separated electrons and holes. (b) QWR PL quenching at the excitation location as function of SAW power at a position 20 µm away from the metal stripe (black) and at the edge of the metal stripe (red).

Screening of the SAW potential can intentionally be achieved by a metal stripe deposited onto the sample surface (see sec. 2.2.2). To induce the screening effect in the QW layer, its depth should be close enough to the sample surface. In a typical sample, the depth of the QW layer is approx. 200 nm from the metallized sample surface. As revealed from

simulations of the SAW fields (not shown here), this should lead to strong screening of the SAW potential in the QW layer. For high acoustic powers the screening effect may, nonetheless, rapidly vanish as function of depth. Figure 7.4(b) shows the degree of QWR PL quenching as function of SAW power, at a lateral position 20 µm away from the metal stripe (black) and in the vicinity of the metal stripe (red). The QWR is selectively excited using an excitation energy of 1.536 eV and excitation density 30 W/cm^2. As expected, away from the metal stripe, the PL quenching is strong and becomes stronger with increasing acoustic powers. In contrast, the PL quenching is extremely suppressed in the vicinity of the metal stripe, demonstrating the screening effect of the metal stripe. However, for strong acoustic powers (e.g. 20 dBm), the degree of PL quenching still reaches up to 56 % in the vicinity of the metal stripe. Thus, for high acoustic powers, the screening effect by the metal stripe is only partly effective. As a result, charge carriers can be transported even beyond the metal stripe for the right conditions. This is observed in fig. 7.1(e), where the QW transport path extents beyond the metal stripe. Note that the QWR ends directly below the metal stripe, so that QWR carriers can not be transported beyond the metal stripe.

7.3.2 Trapping dynamics dependency on local carrier density

To study the effect of the carrier density on the trapping dynamics, the excitation location is fixed at $x = 0\,\mu m$. A metal stripe is deposited at a distance of 35 µm away from the excitation location. A QWR is selectively excited using an excitation energy of 1.538 eV and systematically varying excitation density. The PL is spectrally filtered by the triple-grating spectrometer to detect only the QWR PL. The results of the experiment are presented in figs. 7.5. For a low excitation density of 51 W/cm^2 (fig. 7.5(a)), PL is observed from trapping centers tc_{21}, tc_{24} and tc_{27}. As shown by the figure, carrier capture by trapping center tc_{21} prevents the majority of carriers to reach trapping centers tc_{24} and tc_{27} for SAW powers $11\,dBm < P_{SAW} < 16\,dBm$. Increasing the excitation density to 102 W/cm^2 leads to a change of the trapping dynamics (fig. 7.5(b)). In this case, another trapping center tc_{18} appears for $11\,dBm < P_{SAW} < 15\,dBm$. Acoustic transport beyond this trapping center for low acoustic powers $P_{SAW} < 11\,dBm$ manifests itself as the PL from tc_{21} and tc_{24} for $P_{SAW} < 11\,dBm$. The fact that carriers are trapped by tc_{18} for intermediate SAW powers also affects the number of carriers trapped by tc_{21}, as can be deduced from the disappearance of tc_{21} for the corresponding SAW powers (e.g. 13 dBm). All experimental conditions, except for the excitation density, are the same for figs. 7.5(a) and (b). However, the excitation density can not directly affect the trapping dynamics due to the large distance between excitation location and trapping center. The results imply, therefore, that the carrier density stored by the SAW affects the trapping dynamics.

For an even higher excitation density of 306 W/cm^2 (fig. 7.5(c)), the trapping dynamics are changed again. Here, a strong PL intensity of tc_{21} is observed for $P_{SAW} = 6\,dBm$, which reveals, again, the acoustic transport of carriers beyond tc_{18}. However, the onset of carrier trapping by tc_{18} is now for lower acoustic powers, starting from $P_{SAW} = 8\,dBm$. As compared to fig. 7.5(b), the carrier density stored by the SAW for a fixed acoustic power should be much larger for the experiment reported in fig. 7.5(c). This means that the local carrier density in the vicinity of the trapping center corresponding to $P_{SAW} = 11\,dBm$ in fig. 7.5(b) is now reached for lower acoustic powers, which may be $P_{SAW} = 8\,dBm$. The appearance of PL from tc_{18} for such lower acoustic powers indicates, therefore, that the carrier trapping dynamics depends on the local carrier density in the vicinity of the trapping center. The acoustic power for which the PL of the trapping center disappears, is equal in figs. 7.5(b) and (c), indicating that the screening of the trapping potential is,

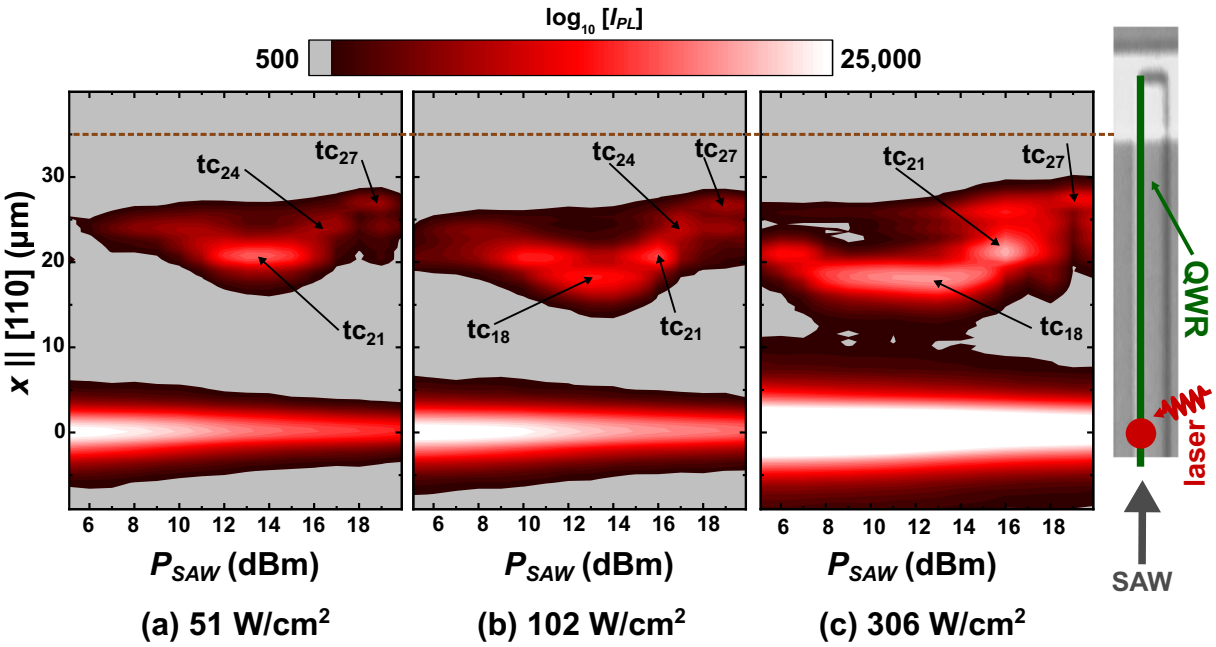

Figure 7.5: Map of the QWR PL along the transport path as function of SAW power for excitation 35 µm away from the metal stripe. The excitation densities are 51 W/cm^2 (a), 102 W/cm^2 (b) and 306 W/cm^2 (c). The right panel illustrates the geometry of the experiment: the carriers are injected by excitation below the QW energy (red dot), while a SAW (grey arrow) transports them along the QWR axis (green line). The numberings correspond to trapping centers along the transport path.

in this case, only affected by the strength of the SAW potential.

It is shown by fig. 6.5(c), that the carrier density, which is optically injected at the excitation location, may fluctuate along the QWR axis even for a constant excitation density. While the screening of the SAW potential by a higher carrier density affects the PL quenching at the excitation location, it can not directly account for a change of the trapping dynamics of a remote trapping center. However, the fluctuating optically injected carrier density also affects the number of carriers stored by the SAW and thereby the local carrier density in the vicinity of the trapping center. As a result, the trapping dynamics observed during a typical experiment may also vary with the excitation position along the QWR axis. In another systematic study (not shown here), it is, indeed, observed that the appearance and disappearance of the trapping centers also depends on the position of the excitation location.

7.4 Time-resolved photoluminescence

Information about the transport efficiency can be gathered from time-resolved PL (TRPL) experiments. The results of such an experiment are summarized in figs. 7.6(a) and (b). Here, a QWR is selectively excited using a continuous-wave (CW) laser at an excitation energy of 1.538 eV, excitation density of 66 W/cm^2 and laser FWHM of 2.5 µm. A PL map with a SAW of 18 dBm is shown in fig. 7.6(a). While excitation takes place at $x = 0$ µm, the remote emission from a trapping center at $x = 28$ µm demonstrates acoustic charge transport as discussed in the previous sections.

To acquire more insights about the trapping dynamics, fig. 7.6(b) shows the time-resolved emission of the trapping center, where detection of the PL is synchronized with the rf generator used to generate the SAW. The isolation of the trapping center emission

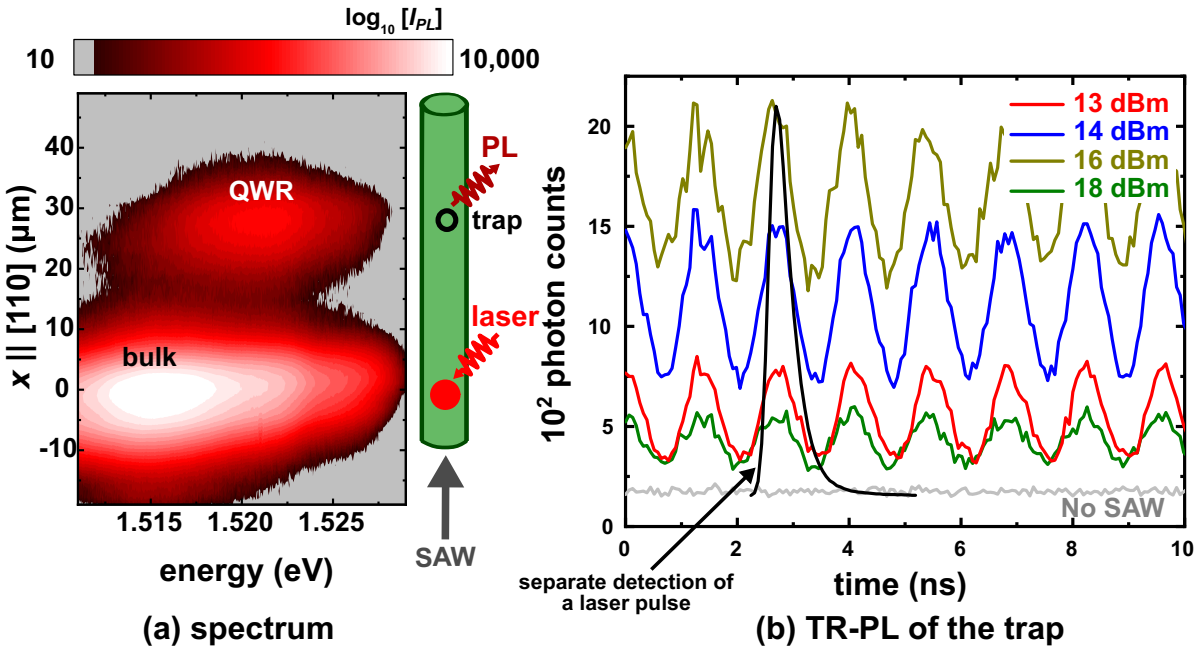

Figure 7.6: Time-resolved photoluminescence (TR-PL). (a) A spatial image of the PL with application of a SAW with a power of 18 dBm. The right panel illustrates the experimental geometry. (b) TR-PL measured from the trapping center observed in fig. (a) for SAW powers of 13 dBm (red), 14 dBm (blue), 16 dBm (yellow), 18 dBm (green) and without SAW (grey). The black plot shows the separate detection of a laser pulse.

is achieved by inserting a 100 µm sized pinhole in the optical signal path. This results in the spectral and spatial integration of the QWR PL over an area with dimensions along x and y of approx. 10 µm and 1.5 µm, respectively. The small number of photon counts without a SAW (grey) is attributed to background detection. The emission of the trapping center while a SAW is applied is shown for acoustic powers of 13 dBm (red), 14 dBm (blue), 16 dBm (yellow) and 18 dBm (green). The fact that for all SAW powers the PL intensity is above the level without a SAW proves that the PL results from acoustically transported carriers. The temporal traces are characterized by a single-frequency sine function. The fact that the peaks are broader than the detection of a separate laser pulse (shown with a black plot) reveals that the width of the peaks is not resolution-limited. The signal frequency corresponds to the SAW frequency, which implies that the majority of the recombination events from the trapping center take place during a well-defined SAW phase, where carriers of one polarity are stored. This means that (i) the SAW potential is efficient in storing the carriers and (ii) the trapping center preferentially captures one type of carriers (either electrons or holes)[1][2]. For low acoustic power (red), the PL intensity is small, indicating that only a few carriers are transported and captured by the trapping center. Increasing the acoustic power to 14 dBm and 16 dBm increases the number of carriers stored by the SAW and subsequently captured by the trapping center, thereby enhancing the trapping center PL.

For all acoustic powers, the peaks have a finite width (rather than being sharp lines), which may result either from (i) a spread of carriers during the SAW period or (ii) the presence of a dense distribution of trapping centers with different carrier trapping

[1]The data can not discriminate between electrons or holes. Such a distinction can be made, when the spectral shift between a minimum and maximum transition energy induced by the strain SAW fields can be resolved, which is not the case for the experiments reported here.

[2]The preference for either electrons or holes is not necessarily the same for all acoustic powers.

probabilities. When the acoustic power is increased from 13 dBm to 14 dBm and from 14 dBm to 16 dBm, the baseline level increases relatively stronger than the amplitude of the peaks, which indicates a broadening of the peak. For increasing acoustic power, the SAW potential becomes more effective in the separation of carriers, which should lead, in contrast to the observations, to a temporal narrowing of the peaks. Thus, a spread of carriers in the SAW period can not explain the observed baseline level. It is, therefore, concluded, that the PL originates from a cluster of trapping centers within the detection area. This is further supported by the fact that within a typical length of the detection area, multiple trapping centers are observed during a typical experiment (see for example fig. 7.3(b)). The peaks observed in fig. 7.6(b) indicate the presence of one trapping center (or a cluster of very closely located trapping centers), which is much more effective in trapping acoustically transported carriers than the dense distributed background trapping centers. The changing ratio between baseline and peak amplitudes hints on a relative change of the trapping efficiency of this strong trapping center with respect to the dense distributed background trapping centers.

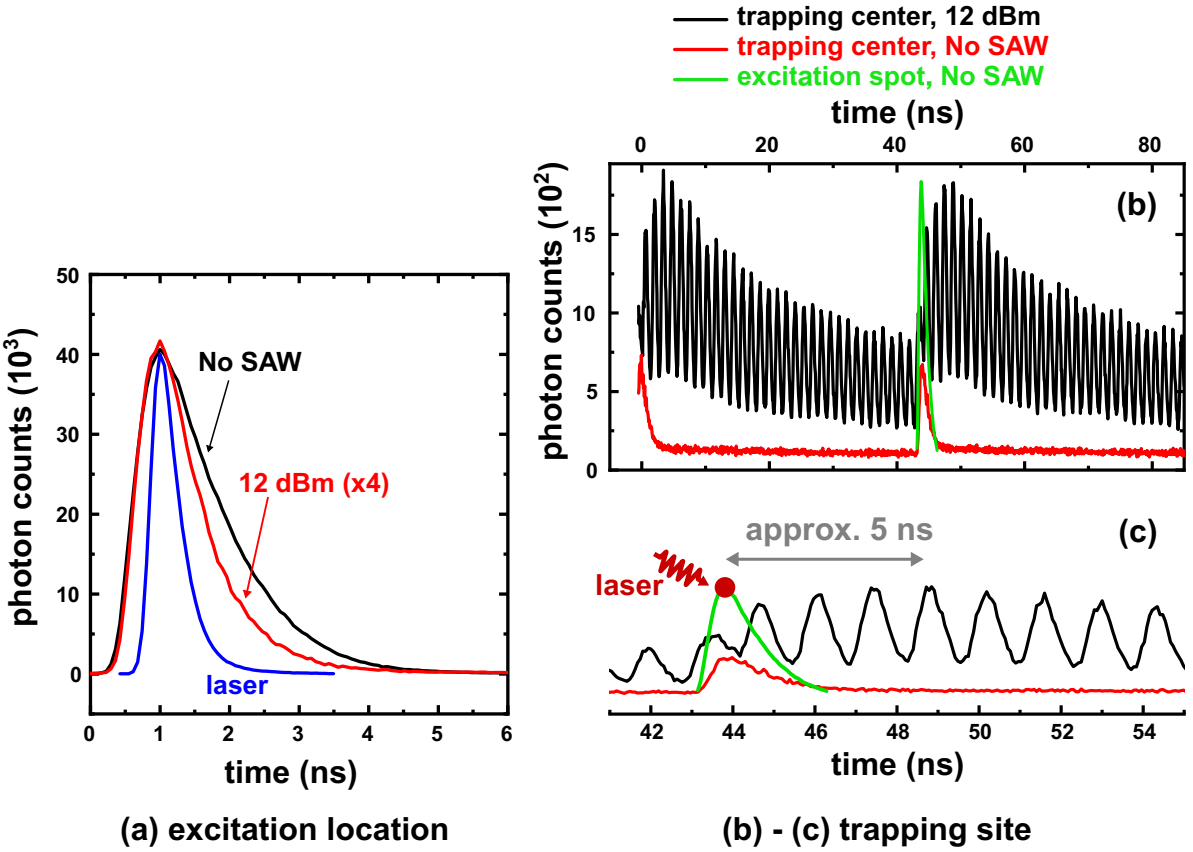

Figure 7.7: (a) TR-PL at the excitation location while exciting a ridge sidewall with a pulsed diode laser. Black: without a SAW, red: acoustic power of 12 dBm (multiplied by four for clarity reasons) and blue: separate detection of a laser pulse (horizontally shifted). (b) Black: TR-PL of a trapping center under a SAW with an acoustic power of 12 dBm. Green: TR-PL at the excitation location without a SAW, normalized to the intensity of the PL at the trapping center. Red: TR-PL of the trapping center without a SAW (real intensity). (c) Same data as in fig. (b), but enlarged to determine the transport time between excitation location and trapping center.

More knowledge about the transport efficiency can be acquired using pulsed excitation. Figure 7.7(a) shows the time-resolved QWR PL at the excitation location, while exciting a QWR using a pulsed laser diode with an excitation energy of 1.633 eV and excitation

density of 26 W/cm^2. In this experiment, the laser pulse is synchronized with the SAW using a divide-by-16 frequency divider, i.e. carrier excitation takes place during a well-defined SAW phase every 16th SAW period. Note that in this case, the excitation energy is above the QW transition. Thus, the majority of the QWR carriers at the excitation location originates from diffusion of QW carriers into the QWR. Without a SAW (black) the temporal trace corresponds to a recombination lifetime of the QWR carriers of approx. 1 ns, which is comparable to the one reported in sec. 6.3. With the application of a SAW (red, multiplied by four for clarity), the decay time of the PL signal is clearly reduced. In both cases, the temporal traces are clearly broader than the temporal width of the laser (blue, horizontally shifted for clarity), meaning that the estimated time constants of the PL are not resolution-limited. The transport of carriers away from the excitation location by the SAW effectively leads to an additional channel of carrier loss, which explains the reduced decay time of the PL signal with the application of a SAW. Note that the carrier transport by the SAW implies also spatial separation of the electrons and holes, and therefore an enhancement of their recombination lifetimes. Furthermore, the fact that the PL intensity with a SAW is much weaker than without a SAW demonstrates the fact that the SAW-induced carrier separation is much faster than the typical recombination lifetime.

The time-resolved QWR PL of a trapping center, located at approx. $x = 15\,\mu$m, is shown by the black plot in fig. 7.7(b), without a SAW (red) and with $P_{SAW} = 12$ dBm (black). As a reference, the QWR PL at the excitation location without a SAW is shown with a green plot, normalized to the black plot. As in the previous case, the length of the detection window along x is approx. 10 µm. Thus, the spectrally integrated PL is spatially integrated over an area of 10 µm x 1.5 µm around the trapping center. The red plot (trapping center, without SAW) shows the appearance of a small carrier population at the instant of excitation without a SAW. Since the corresponding time coordinate of the maximum PL is equal to the one at the excitation location (green plot), these carriers originate from a small laser light intensity incident on the detection window, thereby exciting carriers directly into the detection area. The trapping dynamics due to acoustic transport is similar to the one observed in the CW experiments: an oscillating function with the SAW frequency, on top of a background function. The much larger PL intensity shown by the black plot as compared to the red plot demonstrates that in the former case, the majority of the detected recombination events originates from QWR carriers acoustically transported from the excitation location. This process clearly takes place during the full period between two laser pulses. This is attributed to the formation of a pool of long-lived carriers at the excitation location, which are transported by successive SAW periods towards the trapping center. The background function can be fitted with an exponential decaying function with a time constant of approx. 44 ns. This implies a strong enhancement of the recombination lifetime of QWR carriers, which clearly illustrates the separation of the electrons and holes by the SAW potential. Charge transport of QWR carriers by the SAW is, thus, very efficient.

Figure 7.7(c) displays an enlarged view of the plots in fig. 7.7(b) with corresponding colours. The time delay between the PL peak corresponding to laser excitation (red and green plots) and the one corresponding to acoustic transport (black plot) is approx. 5 ns. This corresponds to the required acoustic transport time for the carriers from excitation location towards the trapping center at 15 µm. This indicates a good transport efficiency without carrier spread, since such a spread would lead to slower transport velocities. Note that the black plot increases immediately after laser excitation: this is attributed to a small carrier density excited directly within the detection window, as witnessed by the red plot. Additionally, the PL oscillations caused by acoustic transport do not vanish before a new laser pulse excites new carriers: the PL intensity with application of a SAW

is always above the one without a SAW. This means that the enhancement of the QWR recombination lifetime at the excitation location is so strong, that a part of the carriers excited by one laser pulse survives even until the new laser pulse arrives.

The transport dynamics of the QW is studied in a CW laser experiment, carried out by exciting the QW at the ridge top (excitation energy of 1.633 eV) and detecting the time-resolved PL synchronized with the application of a SAW. In fig. 7.8(a) a map of the QW PL is shown, revealing a trapping center tc_{30} approx. 30 µm away from the excitation location. In fig. 7.8(b), the trapping center PL is shown without SAW (grey) and with acoustic powers of 12 dBm (black) and 14 dBm (blue). Without a SAW, the number of detected photon counts is small, confirming that the remote PL originates from carriers transported by the SAW. The application of a SAW with an acoustic power of 12 dBm leads to similar trapping dynamics as observed for the QWR: a single-frequency sine function with a non-zero minimum. The clear peaks demonstrate, as was the case for the QWR, the presence of a dominant trapping center which preferentially captures carriers of one polarity. Increasing the SAW power to 14 dBm strongly reduces the remote PL. The nominally constant emission under this condition could result from a distribution of trapping centers spread over several micrometers. Because of the large length of the detection window of approx. 10 µm, such a distribution could explain why time-resolved PL takes place continuously within the SAW period. The absence of peaks indicates that the trapping efficiency by these trapping centers is similar, in contrast to the dominating trapping center observed for an acoustic power of 12 dBm.

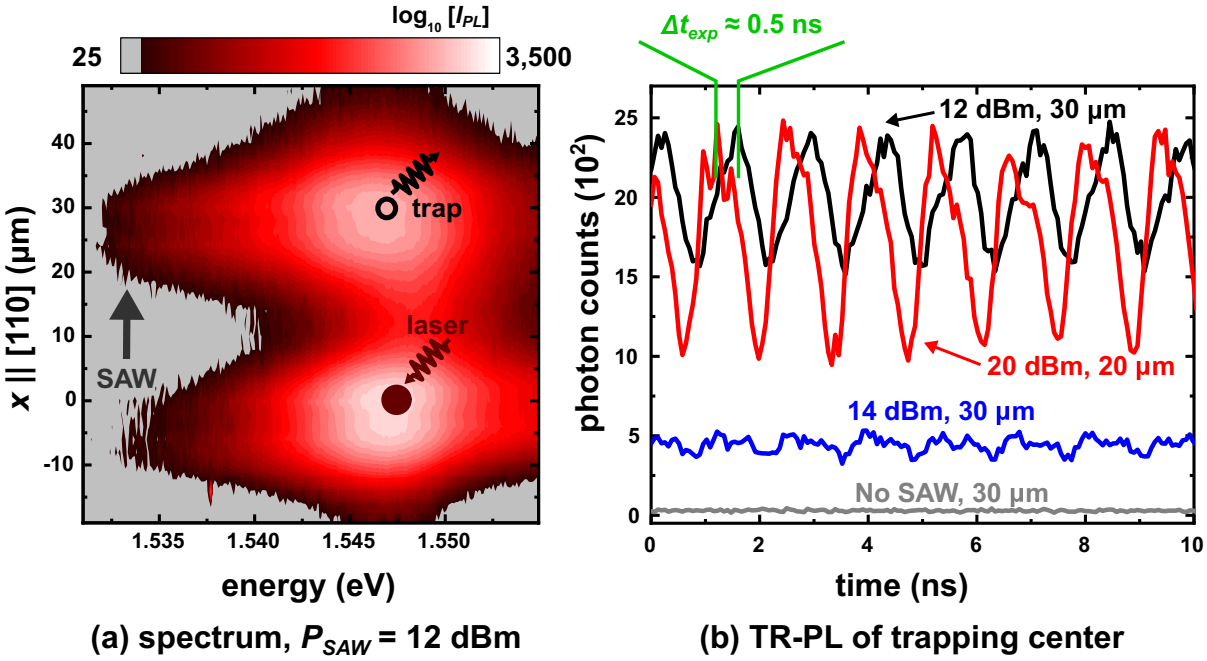

Figure 7.8: Time-resolved PL of the QW on a ridge top. (a) Spatial image of the PL while a SAW of 12 dBm is applied. (b) TR-PL of two trapping centers, located at distances of 20 µm (red, 20 dBm) and 30 µm (grey: no SAW, black: 12 dBm, blue: 14 dBm away from the excitation location).

For a high acoustic power of 20 dBm, a new trapping center tc_{20} at $x = 20$ µm appears in the spatial map of the PL (not shown here). This confirms the presence of multiple trapping centers along the transport path. The trapping efficiency depends on the acoustic potential. Possibly, this trapping center contributes to the PL minimum observed in the previous case. For $P_{SAW} = 20$ dBm tc_{20} becomes, however, much more efficient as is deduced from its clear PL hotspot in the PL map. The time-resolved PL from the same

area, as detected for the black and blue plots, is shown in fig. 7.8(b) with a red plot for $P_{SAW} = 20\,\mathrm{dBm}$. The carriers which are otherwise captured by tc_{30} require approx. $\Delta t_{20\to30} = 3.3\,\mathrm{ns}$ more time to reach the trapping center than those which are captured by tc_{20}. Considering the CW excitation scheme, there is no reference time coordinate and thus, the exact transport time from excitation location towards the trapping center can not be determined. The different positions of the trapping center manifest itself, however, by a temporal phase shift of their corresponding plots by $\Delta t_{exp} = \Delta t_{20\to30} - n_S T_S \approx 0.5\,\mathrm{ns}$, where $n_S = 2$ is the largest number of complete SAW periods which fit into $\Delta t_{20\to30}$. This is consistent with the results presented in fig. 7.8(b).

7.5 Carrier extraction from the QWR

In sec. 6.2 it is discussed that a potential barrier prevents lateral diffusion of QWR carriers into the surrounding QW. However, it will be shown in this section that QWR carriers can still be extracted into the surrounding QWR during acoustic transport. Fur this purpose, figs. 7.9(a) and (b) show the two-dimensional PL maps without a SAW of the QWR and QW emission, respectively. The detection area contains three ridge sidewalls, with QWRs 1 to 3 (numbering starting from the left-hand side of the figure). The position of the QWRs is marked by green lines. During the experiment, QWR 2 is selectively excited using an excitation energy of 1.532 eV and density of $200\,\mathrm{W/cm^2}$. Under these conditions, the excitation of QW carriers should be suppressed. Without the SAW, the QWR emission is only observed within the vicinity of the excitation location, consistent with the results of secs. 7.1 and 7.2. Detection at the QW energy reveals a much smaller light intensity, attributed to scattered laser light.

Figure 7.9(c) shows a QWR PL map of the same area with a SAW of $P_{SAW} = 12\,\mathrm{dBm}$. Conform the findings of the previous sections, acoustic charge transport in QWR 2 is witnessed by the remote PL from two trapping centers tc_{10} and tc_{29}. As is clear from the absence of QWR 1 PL at the excitation location in fig. 7.9(a), no carriers are optically injected in QWR 1. Nevertheless, a remote PL hotspot tc_{21} is also observed in QWR 1. Thus, carriers must be extracted from QWR 2 into the surrounding QW, which then diffuse into QWR 1. Figure 7.9(d) shows a map of the PL recorded at the QW energy under the same experimental conditions. Around the trapping center tc_{10}, the QW emission is largely enhanced as compared to the condition without a SAW. This indicates that the carriers transported in QWR 2 can be extracted into the surrounding QW at the position of tc_{10}. These carriers may undergo three processes. In the first place, they are transported in the QW, until they reach a second trapping center. This process may cause the remote PL of trapping center tc_{24} in fig. 7.9(d). Secondly, the QW carriers may laterally diffuse into another QWR, after which they are acoustically transported along that QWR's axis and recombine when they encounter a trapping center. This is demonstrated by the remote PL hotspot of tc_{21} in fig. 7.9(c) (highlighted by a yellow circle). Finally, the QW carriers which diffuse into a QWR and transported in that QWR may also be extracted back into the surrounding QW. This could be an alternative explanation for the PL hotspot tc_{24} in fig. 7.9(d). Note that no remote PL is observed from QWR 3, which may result from a number of reasons: (i) the absence of trapping potentials in QWR 3 for this acoustic power, (ii) a strong trapping potential in the right QW, which captures the major part of the carriers before they are able to diffuse or (iii) prevention of carrier diffusion into QWR 3 for other reasons. The data shown in figs. 7.9(c) and (d) can, however, not discriminate between these three reasons.

A further increase of the acoustic power to $P_{SAW} = 20\,\mathrm{dBm}$ (see figs. 7.9(e) (QWR emission) and (f) (QW emission)) leads to an increase of the number of carriers extracted

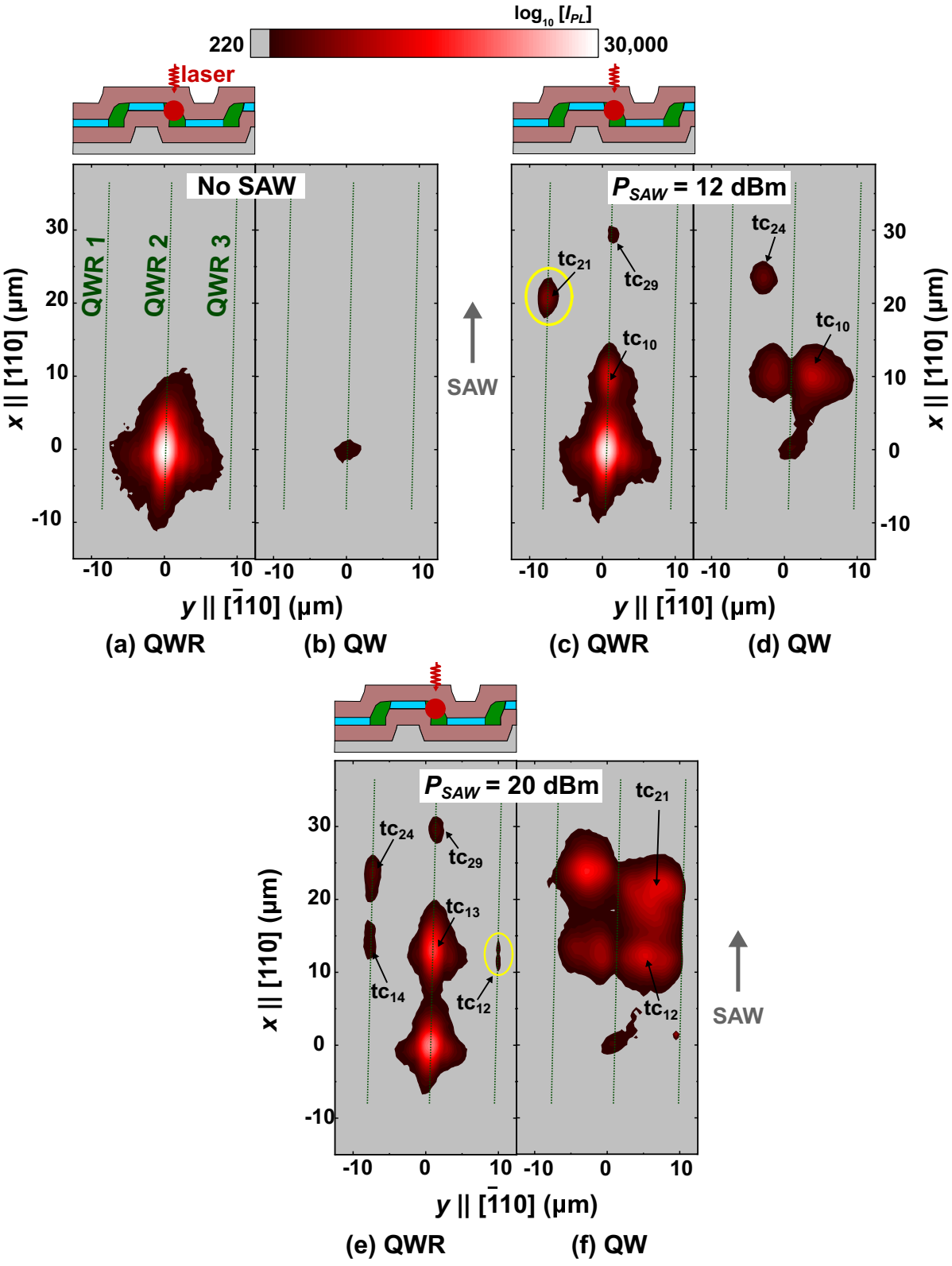

Figure 7.9: Spatial PL images of the QWR (a) and QW (b) without SAW. Spatial PL images of the same area while a SAW of 12 dBm is applied are shown in fig. (c) (QWR) and in fig. (d) (QW). Figures (e) and (f) depict the spatial PL images for a SAW of 20 dBm for the QWR and the QW, respectively. The upper panels of figs. (a), (c) and (e) illustrate the geometry of the experiment. The green dashed lines mark the positions of the QWRs within the detection window. The numberings correspond to trapping centers along the transport path.

from the QWR into the QW, as evidenced by a further enhancement of the QW emission. Under this condition, carrier diffusion from the right QW into QWR 3 is clearly observed by a PL hotspot tc_{12} in fig. 7.9(e) (highlighted by a yellow circle). The emission pattern in fig. 7.9(f) reveals that the carriers extracted into the QW are also acoustically transported along the QW, as indicated by a continuous emission between tc_{12} and tc_{21} and the absence of remote PL from QWR 2 for the corresponding positions. Since the QW PL intensities on both sides of QWR 2 are similar, the efficiency of the carrier extraction seems to be similar for carriers from QWR 2 into the left QW (located at the ridge top) and into the right QW (located at the ridge bottom). This is consistent with the findings of fig. 6.2, where it was shown that the lateral potential barriers between QWR and surrounding QW have a similar magnitude on both sides of the QWR.

The extraction process is observed at locations where a trapping center induces the recombination of charge carriers transported by the SAW. The findings indicate, therefore, that the extraction process is mediated by such a trapping center. However, PL of recombining carriers can only be detected at locations where trapping centers induce carrier recombination. Carriers extracted from the QWR into the surrounding QW at other locations are only detected when they reach a nearby trapping center. Therefore, further studies are required to reveal the exact origin of the extraction process.

7.6 Summary of the chapter's findings

The results presented in this chapter demonstrate the feasibility of acoustic charge transport along the QWR axis and the surrounding QW up to at least 90 µm. The ambipolar nature of the transport is proven by the observation of remote PL from various positions along the transport path, which can only take place if both the electrons and holes are transported. The emission originates from carriers randomly trapped either in interface states at the QW layer - $Al_{0.15}Ga_{0.85}As$ barrier interface or by inhomogeneities of the transport channel dimensions. The capture of the carriers by trapping centers is assisted by the SAW fields and depends, therefore, on the acoustic power. For high acoustic powers, the trapping potentials are overcome by the piezoelectric SAW fields and the carriers are transported towards a metal stripe. Here, the carriers are forced to recombine. The carriers in the QW may be transported even beyond the metal stripe, since its screening effect is only partly effective for high acoustic powers. It is demonstrated that the potential barrier between QWR and its surrounding QW is not large enough to prevent SAW-assisted carrier escape from the QWR into the QW. The carrier escape process results in a loss of QWR carriers and can become a significant source of carrier leakage as evidenced by the strong QW emission.

The transport efficiency is assessed by time-resolved PL measurements of the remote emission. For both the QWR and the QW, the time-resolved PL of a typical trapping center shows clear peaks appearing with the SAW frequency. This indicates that the majority of the recombination events from the trapping center take place at a well-defined SAW phase. This means that the SAW potential is efficient in storing carriers, since it implies that the carriers are stored at a well-defined SAW phase. This conclusion is, furthermore, confirmed by the carrier travel time from the excitation location towards the trapping center, which corresponds to the one expected from the acoustic velocity. Note that the overall transport efficiency is expected to be better in the QWR, since its larger dimensions should result in larger carrier mobilities [144] and smaller potential fluctuations which may trap carriers. Moreover, the distinctive peaks of the time-resolved PL illustrate that a typical trapping center preferentially captures one type of carrier (either electrons or holes).

chapter 8

Acoustic spin transport

The results presented in the previous chapters point towards long acoustic spin transport distances in sidewall QWRs. In this chapter, the spin dynamics of the QWRs and the surrounding QW is studied. All studies presented in this chapter are carried out on QW structures on GaAs (001) substrates. The chapter starts with a study of the spin lifetimes as revealed from Kerr rotation experiments (sec. 8.1) and then discusses acoustic spin transport measured by polarization-resolved photoluminescence (PL) (sec. 8.2). The third section considers the results of Monte Carlo simulations of spin dynamics for a Dyakonov-Perel spin relaxation dominated case. The final section summarizes the findings of the chapter.

8.1 Spin lifetimes

In this section, the spin dynamics is studied by magneto-optical Kerr experiments using both CW- and pulsed excitation schemes. Firstly, sec. 8.1.1 discusses the intrinsic spin dynamics in absence of a SAW, after which the effect of the SAW is studied in sec. 8.1.2. As discussed in sec. 4.4.2, the spot sizes (full-width-at-half-maximum) of the pump and probe beams are 7 µm and 3 µm, respectively.

8.1.1 Spin lifetimes without SAW

Figure 8.1(a) shows the results of a typical Kerr measurement of an unstructured QW area, obtained by operating both pump and probe lasers in the CW mode. During the experiment, the excitation energy is 1.571 eV (excitation density 188 W/cm^2), while the detection energy is varied. A Kerr signal is clearly observed from two transitions: one transition corresponding to the substrate (1.515 eV) and the second transition corresponding to the QW (1.549 eV). The energies are consistent with the PL studies presented in sec. 6.2. For both transitions, starting from low detection energy the Kerr signal is positive, vanishes when approaching the resonance energy and increases in strength, but with a negative sign for a further raise of the detection energy. The particular shape of the curve can be explained by the characteristics of the material's circular dichroism: the inset of fig. 8.1(a) illustrates a toy model for the refractive indices for right-hand circularly polarized (RHCP) light n_R (red) and left-hand circularly polarized (LHCP) light n_L (black), as well as the difference $\Delta n = n_R - n_L$ (green), as function of the detection energy ΔE (the resonant energy corresponds to $\Delta E = 0$). The model illustrates that the Kerr signal, which is proportional to Δn, changes its sign when the detection energy crosses $\Delta E = 0$.

If n_R and n_L are asymmetric, the amplitudes for the negative and positive signals may be different.

Figure 8.1(b) displays typical temporal Kerr traces of the substrate (red, detection energy 1.514 eV) and the QW (blue, detection energy 1.546 eV), recorded at the unstructured area. In this experiment, the pump and probe lasers are both operated in pulsed mode. At time $t = 0$, the pump beam optically injects spin-polarized carriers (excitation energy 1.571 eV, excitation density 63 W/cm^2). The Kerr signal is subsequently measured by a probe beam arriving at the detection spot with a variable time delay with respect to the pump beam (see sec. 4.4.2). The black lines depict fits with a single-exponential decaying function, which in both cases reveals a time constant of the Kerr signal τ_K of approx. 0.25 ns. The decay of the Kerr signal results from a combination of carrier recombination and spin decay. Due to the fast hole-spin relaxation, the Kerr signal can be assumed to reflect the dynamics of the electron-spin relaxation. To extract the spin lifetime τ_S, τ_K has to be corrected by the recombination lifetime using eq. 4.5. However, time-resolved PL experiments (see sec. 6.3) revealed very fast carrier recombination in the substrate. The relatively long-lived Kerr signal indicates, therefore, a long spin lifetime for the substrate. Since the QW recombination lifetime is nearly twice as large as τ_K, τ_S can be estimated to be approx. 0.5 ns. The main source for spin relaxation of the exciton-bound electron-spin is the electron-hole exchange interaction. This interaction results in an effective magnetic field $\mathbf{B_{ex}}$, leading to spin relaxation due to frequent excitonic momentum scattering [27]. The strength of the exchange interaction increases due to the confinement of the carriers within the QW layer [147, 27]. The spin lifetime of the substrate should, therefore, be larger than 0.5 ns as measured in the QW.

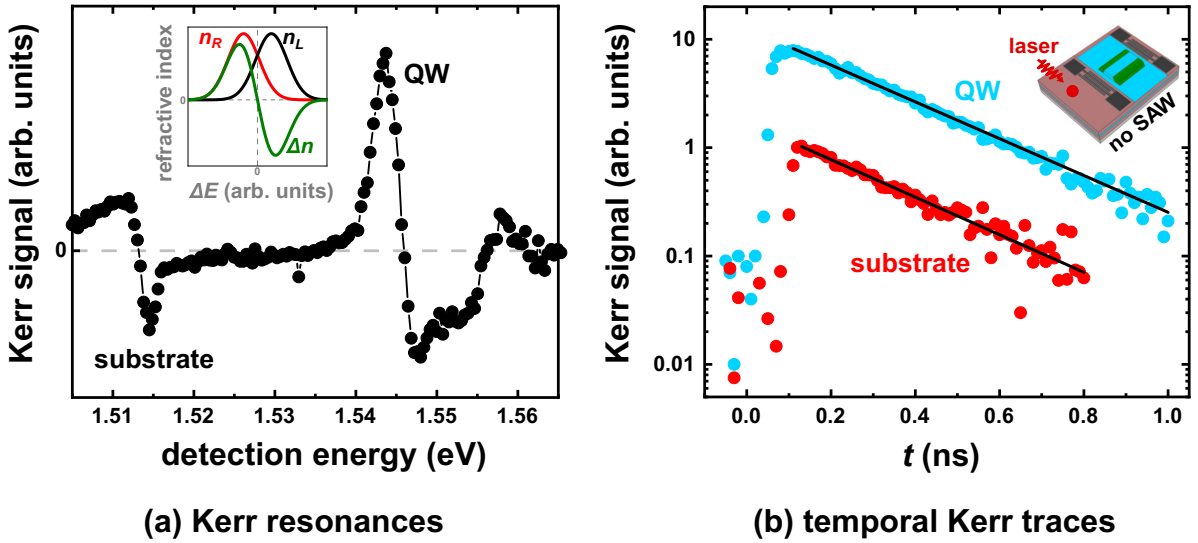

Figure 8.1: (a) Kerr signal as function of detection energy at an unstructured QW area. The inset illustrates a toy model to explain the Kerr effect: circular dichroism leads to different refractive indices for RHCP (red) and LHCP (black) light. The green curve depicts this difference $\Delta n = n_R - n_L$. (b) Temporal Kerr traces of the QW (blue) and the substrate (red). The black lines are fits to a single-exponentially decaying function.

Next, the spin lifetimes at the ridge sidewall are investigated. Figure 8.2(a) displays an optical microscopy image of the sample: five ridges with ten QWRs (green). The width of the QW between two QWRs is approx. 8.5 µm and 11.5 µm at the ridge bottom and top, respectively. The difference of these widths comes from the anisotropic overgrowth of the (Al,Ga)As layers. Figure 8.2(b) displays the Kerr signal, recorded while nonselectively exciting a ridge sidewall using a CW excitation scheme (excitation energy 1.551 eV and

excitation density 188 W/cm^2). Comparing figs. 8.1(a) and 8.2(b), it is clear that the sidewall QWR adds an additional peak to the Kerr signal. The detection energy corresponding to the QWR is close to the substrate detection energy, which is consistent with their spectral proximity observed in PL experiments (see sec. 6.2). The spectral proximity of the substrate and QWR complicates the analysis of the Kerr signal, since it leads to mixing of the QWR and substrate signals. It was found that throughout the complete spectral range of the QWR transition, such a mixing of the substrate and QWR takes place. This effect is expected to be strong at high excitation densities, when the carrier density in the substrate exceeds the one in the QWR.

Figure 8.2(c) shows temporal Kerr traces of the ridge sidewall, detected at the QW energy (blue, detection energy 1.546 eV) and the QWR energy (green, detection energy 1.520 eV). This experiment is performed while operating both pump and beam in pulsed mode. Excitation is above the QW energy: the excitation energy is 1.551 eV and excitation density 16 W/cm^2. For the (structured) QW, τ_K is similar to the one observed at the QW of the unstructured area. A correction of τ_K for carrier recombination reveals that for the QWR, the spin lifetime is approx. 2 ns to 3 ns. Thus, the QWR spin lifetime is 4- to 6- fold enhanced as compared to the QW. An enhancement of the QWR spin lifetime is expected due to a reduction of the exchange interaction by its larger thickness [148, 149, 150]. However, as will be discussed in detail in sec. 8.2.3, the QWR spin lifetime is mainly limited by Elliott-Yafet spin relaxation.

In order to inspect the effect of the substrate Kerr signal on the QWR Kerr signal, fig. 8.2(d) displays temporal Kerr traces at the ridge sidewall, probed using a detection energy of 1.522 eV (corresponding to the QWR transition) and excitation energy of 1.551 eV. For higher excitation densities, the carrier density of the substrate becomes substantially larger than the one of the QWR. As a consequence, the effect of the substrate Kerr signal on the QWR Kerr signal may depend on the excitation density. The latter is, therefore, varied to be 16 W/cm^2 (black), 94 W/cm^2 (red), 188 W/cm^2 (blue) and 282 W/cm^2 (green). The green curve shows a strong negative feature for short timescales, attributed to substrate carriers, while a weaker positive contribution is observed for longer timescales, corresponding to the QWR Kerr signal. The data can not simply be fitted with a double-exponential decay, since the rise time of the spin population in the QWR may be much longer than for the substrate due to the complex dynamics of the QW/QWR system. The mixing of the substrate and QWR Kerr signals prevents the correct determination of the rise times for the substrate and QWR signals. As the substrate carrier density becomes smaller than the QWR carrier density for a small excitation density, the amplitude of the negative (substrate) signal decreases (blue and red curves) and eventually vanishes for the smallest excitation density (black curve). Even in the latter case, the rise time of the QWR spin population is considerably larger than the one of the QW and the substrate. The apparent rise time of the spin population in the QWR is on a similar timescale as the diffusion of QW carriers into the QWR (see sec. 6.3). Thus, the majority of the spins in the QWR originates from spin diffusion of carriers in the QW into the QWR. The large Kerr signal of the QWR resonance demonstrates, therefore, the conservation of spin during the diffusion process. Furthermore, although the spin lifetime in the QW is considerably shorter, it is long enough to sustain a spin population transfer from the QW into the QWR.

The mixing of the substrate and QWR signals puts an experimental constraint on the resonant pumping of the QWR, where a high excitation density is required due to the small absorption area of the QWR: under the condition of resonant pumping, QWR spins can not be injected from diffusion of QW carriers. Such a high excitation density results in a very strong negative substrate signal, which may disturb the detection of the QWR spins as discussed above. The remainder of the Kerr experiments discussed in this

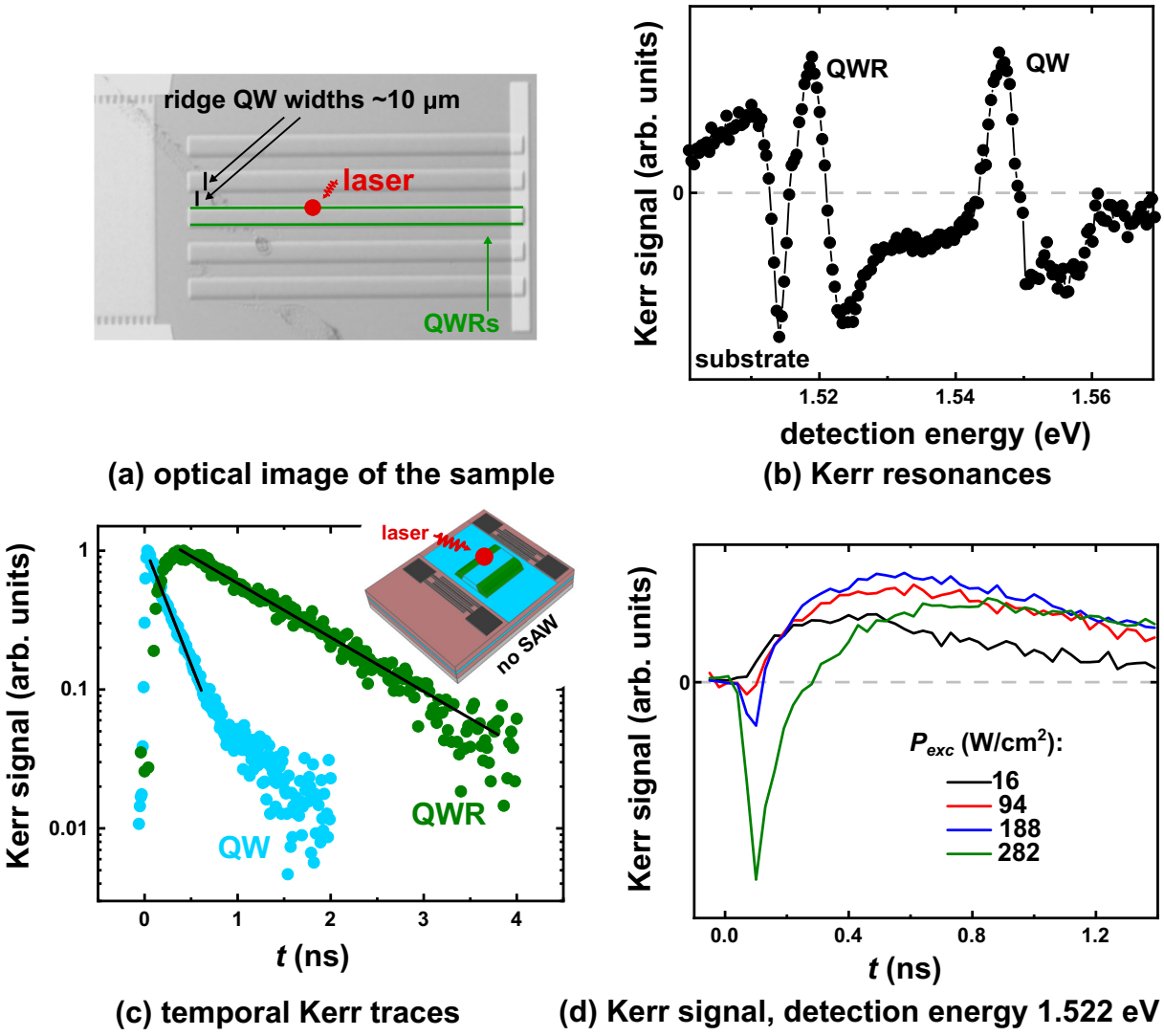

Figure 8.2: (a) Optical image of the sample with QWRs (green lines). (b) Kerr signal as function of detection energy at a ridge sidewall. (c) Temporal Kerr traces measured at the ridge sidewall, blue: QW and green: QWR. The black lines are fits with a single-exponentially decaying function. (d) Temporal Kerr traces measured while tuning the probe beam to the QWR transition and varying the excitation density to 16 W/cm^2 (black), 94 W/cm^2 (red), 188 W/cm^2 (blue), 282 W/cm^2 (green).

chapter are, therefore, conducted using off-resonant excitation of the QWR (above the QW energy). Under this condition, the density of substrate carriers is reduced.

8.1.2 Kerr experiments with a SAW

When a SAW is applied to the QWR, suppression of exchange interaction should lead to a considerable increase of the spin lifetime (see sec. 3.5). Figure 8.3 compares the QWR Kerr signal at the excitation location without SAW (black) and while applying a SAW with acoustic powers of $P_{SAW} = 0\,\mathrm{dBm}$ (green), 10 dBm (blue) and 15 dBm (red). The excitation energy is 1.555 eV (above the QW energy) and the excitation density $20\,\mathrm{W/cm^2}$. The SAW is generated by a split-finger IDT designed for a SAW wavelength of 4 µm (frequency of 726 MHz). Clearly, the Kerr signal decay time increases when a SAW of power 0 dBm is applied. Note that a correct estimation of τ_S requires the knowledge of the recombination lifetime. The detection of the time-resolved QWR PL while a SAW is applied is not possible due to the strong degree of PL quenching at the excitation location under this condition. However, the increased decay time of the Kerr rotation implies the separation of the carriers by the SAW potential. This should, in principle, also increase the spin lifetime since it should be limited by exchange interaction. A further increase of the SAW power leads to a decrease of the Kerr signal decay time. This can be understood by acoustic transport of spins away from the excitation location, which effectively leads to an additional channel of spin removal from the excitation location. Surprisingly, the amplitude of the Kerr signal strongly reduces with the application of a high acoustic power. This may possibly result from a shift of the detection energy for which the Kerr signal becomes optimal (i.e. a horizontal shift of the curve in fig. 8.2(b)). A systematic correspondence between the acoustic power and the optimal detection energy is, however, not found. Note that acoustically transported spins require a finite time to traverse the detection spot. Assuming an ideal overlap of the (Gaussian-shaped) pump and probe beams, the majority of the spins are excited in the center of the detection spot. The half-width-at-half-maximum of the probe beam is approx. 1.5 µm. Thus, the majority of the spins require a time of at least $1.5\,\mu\mathrm{m}/v_{\mathrm{SAW}} = 0.5\,\mathrm{ns}$ to travel outside the detection spot, where v_{SAW} is the acoustic velocity. Consequently, a transport-induced reduction of the Kerr signal can only be expected for $t > 0.5\,\mathrm{ns}$. The decreased Kerr amplitude at the shorter timescale can, therefore, not be explained by spin transport.

Figures 8.4(a)-(b) display the spatially resolved Kerr rotation along the QWR axis without a SAW (fig. (a)) and with a SAW power of 15 dBm (fig. (b)). In this experiment, the position of the pump beam is fixed, while the probe beam is systematically scanning the detection area. The time at which the spins stored by the SAW arrive at a certain position varies with position. If the delay time between pump and probe is not tuned to the time arrival of the spin package, the Kerr signal will not be detected. Tuning the correct pump-probe delay time for the complete detection area is, anyhow, not easily done due to the afore mentioned position-dependency of the spin arrival time. To that end, the experiment is conducted using a CW excitation and detection scheme, in which one temporally integrates the Kerr signal. On the other hand, the temporal integration for the CW scheme strongly reduces the Kerr signal, since a Kerr rotation is only induced during the short time when the spins pass through the detection spot. In the pulsed scheme the detection is 'synchronized' with the arrival time of the spins (assuming the correct time delay), meaning that a Kerr rotation is constantly induced during the measurement time. While this should not be a problem at the excitation location (spins are steadily injected), it leads to a large reduction of the Kerr signal at remote locations, where the time coordinate of the spin passage is dictated by the carrier velocity. To achieve a strong

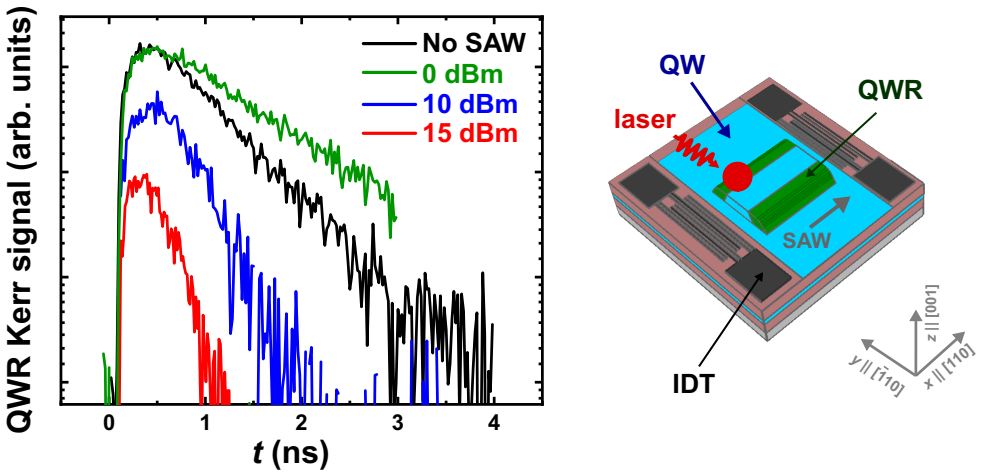

Figure 8.3: Temporal Kerr traces of the QWR without SAW (black) and with P_{SAW} = 0 dBm (green), 10 dBm (blue) and 15 dBm (red). The split-finger IDTs are designed for a SAW wavelength λ_{SAW} = 4 µm and frequency f_{SAW} = 726 MHz. The right panel illustrates the sample geometry: the QWRs (green) are enclosed by two IDTs (black).

Kerr signal, a high excitation density is, therefore, required. To minimize the contribution of the substrate to the Kerr signal, the ridge sidewall is excited above the QW energy (excitation energy 1.5492 eV, excitation density 78 W/cm^2). Under this condition, the majority of the QWR carriers originates from diffusion of QW carriers, while the excitation of substrate carriers is minimized.

During acoustic transport, the spins rotate around an effective magnetic field, which originates from spin-orbit (SO) coupling and is characterized by the Larmor vector $\mathbf{\Omega_{SO}}||y$ (see eq. 3.30). As shown by eq. 3.31, the acquired spin phase at a certain position only depends on its position along the QWR axis (assuming a linear, quasi-1D approximation). The independency of the spin phase on time means that the temporal integration by a CW excitation and detection scheme does not lead to a precession-induced reduction of the Kerr signal at a well-defined position. The QWR Kerr signal without a SAW is displayed in fig. 8.4(a). Here, the vertical $y|||[\bar{1}10]$ and horizontal $x|||[110]$ axes are perpendicular and parallel to the QWR axis, respectively. A red (blue) area corresponds to a positive (negative) spin orientation. The area highlighted by the dashed black circle indicates the position and size of the pump beam. As expected, the elongated shape of the red area around the excitation location demonstrates the confinement of the spins within the boundaries of the QWR width. The much larger extent of the Kerr signal along y (approx. 2.5 µm) as compared to the QWR width is a result of the limited spatial resolution. The extent of the Kerr signal along the QWR axis (approx. 5 µm) mainly results from the large excitation spot of 7 µm (full-width-at-half-maximum, FWHM) and indicates that the spin diffusion length under this condition is rather small.

Figure 8.4(b) displays a spatial map of the QWR Kerr signal when applying an acoustic power of 15 dBm using a split-finger IDT. From eq. 3.31, one expects the spins to acquire a phase of 180° at approx. x = 8 µm[1]. Thus, in fig. 8.4(b), one expects a strong negative Kerr signal (blue) at $x \approx 8$ µm. As can be seen in the figure, similar to fig. 8.4(a), the signal vanishes quickly beyond the excitation location. To increase the Kerr signal, fig. 8.4(c) shows the QWR Kerr signal, while the carriers are injected at the same position with twice the excitation density (156 W/cm^2) and the same acoustic power (15 dBm). As shown in the figure, no clear sign of acoustic spin transport is detected for these conditions

[1]Here, it is assumed that $C_3 = -2.6$ eV nm, as determined from polarization-resolved PL studies presented in sec. 8.2.3.

either. The QWR spin lifetime without SAW is approx. 2 ns to 3 ns, which corresponds to 6 µm to 9 µm, assuming that the spins are transported with the acoustic velocity. However, a profile of the Kerr signal along the green line in fig. 8.4(c) reveals a quick reduction of the Kerr signal outside the excitation spot. This is much faster than what one expects for an exponential transport length of at least 6 µm and is attributed to the size of the excitation location. The Kerr signal vanishes quickly beyond the excitation location due to a combination of spin precession, spin decay and the escape of QWR carriers into the surrounding QW. It is, therefore, likely that the Kerr rotation induced by the transported QWR spins is smaller than the one required as dictated by the experimental sensitivity.

Figure 8.5(a) shows the spatially resolved Kerr signal of the unstructured QW without a SAW, as function of position along $y||[\bar{1}10]$ (vertical axis) and $x||[110]$ (horizontal axis). The position of the excitation spot is highlighted by the black dashed circle. As in figs. 8.4, the red and blue areas correspond to a positive and negative Kerr signal, respectively. The scale of the Kerr signal is equal to figs. 8.4. The position of the excitation location on the sample is illustrated by the right panel. As can be seen in the figure, the spin diffusion length is rather small without a SAW, as it approximately coincides with the size of the laser spot.

Figure 8.5(b) displays the Kerr signal, recorded with $P_{SAW} = 10$ dBm. In this case, the SAW is generated using a single-finger type IDT designed for a SAW wavelength $\lambda_{SAW} = 2.8$ µm (frequency 1049 MHz). Comparing figs. 8.5(a) and (b), spin transport is revealed by the emergence of a clear negative Kerr signal as characterized by the blue area at the position denoted by (ii). The mean trajectory of the spins, as extracted from the direction with the strongest Kerr signal, is indicated by the blue dashed line. The particular shape of this trajectory results from acoustic transport along the $[\bar{1}\bar{1}0]$ direction and diffusion along the $[1\bar{1}0]$ direction. Due to the large laser spot, the start position of spin precession is not well-defined, since the CW scheme leads to a continuous alignment of the spins within the boundaries of the laser spot. An estimation of the spin precession length L_{SO} can, however, be made by taking the distance between positions (i) (corresponding to $\rho_z = 0$) and (ii) (corresponding to the minimum of ρ_z), as denoted in fig. 8.4(b). This distance of approx. 3 µm corresponds to $L_{SO}/4$, revealing that $L_{SO} \approx 12$ µm. A systematic study of spin precession in both the QWR and the QW is provided in sec. 8.2.3.

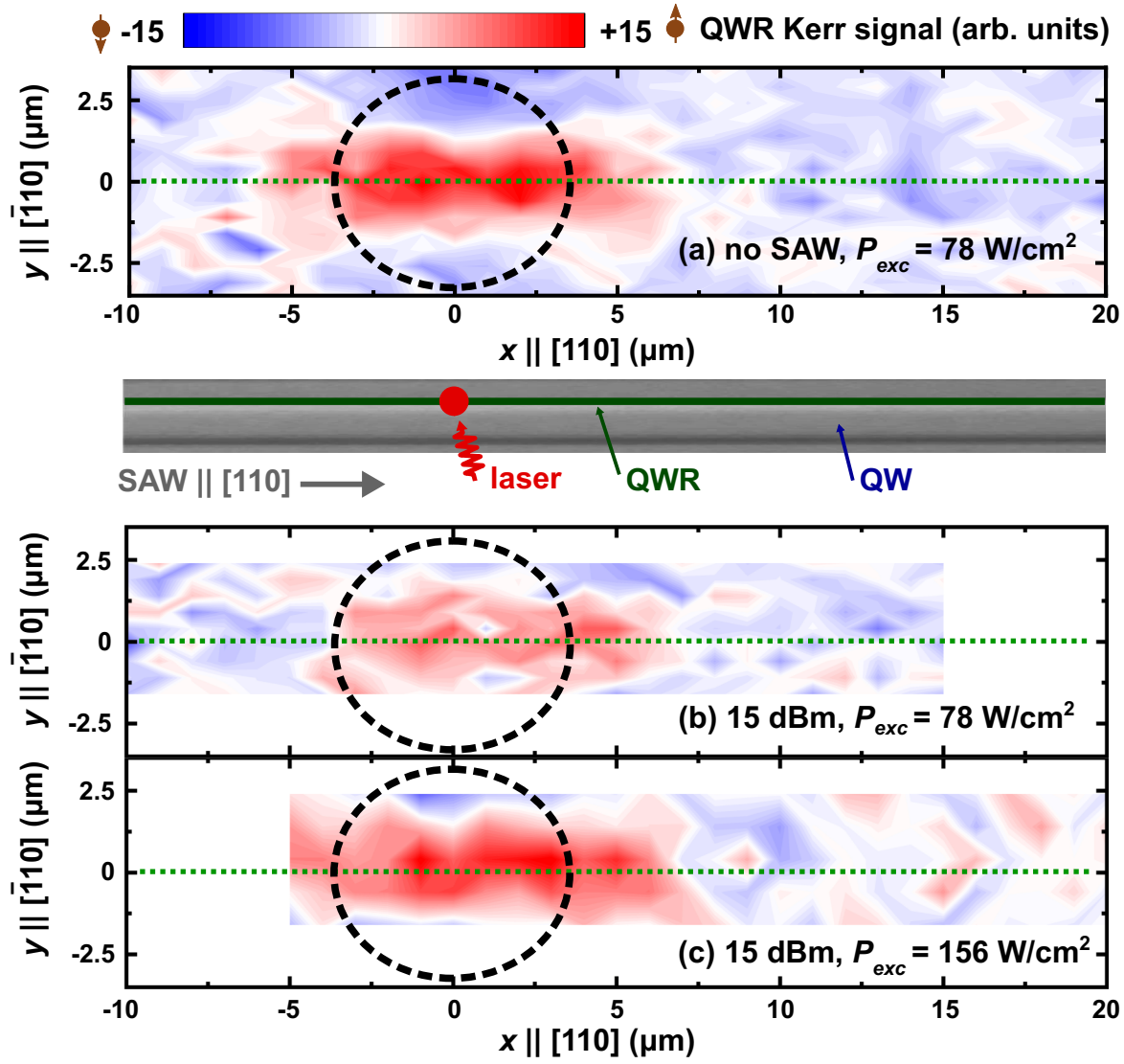

Figure 8.4: Spatial map of the QWR Kerr signal without a SAW (a), with $P_{SAW} = 15\,\mathrm{dBm}$ (b), and with double excitation density and $P_{SAW} = 15\,\mathrm{dBm}$ (c). The upper panel of fig. (b) illustrates the geometry: the SAW travels from left to right, while carriers are optically injected at the excitation location denoted by the red dot. For every figure, the green dashed line marks the position of the QWR and the black dashed circle the approximate size of the excitation spot. As shown by the legend, the red and blue areas correspond to $\rho_z > 0$ and $\rho_z < 0$, respectively.

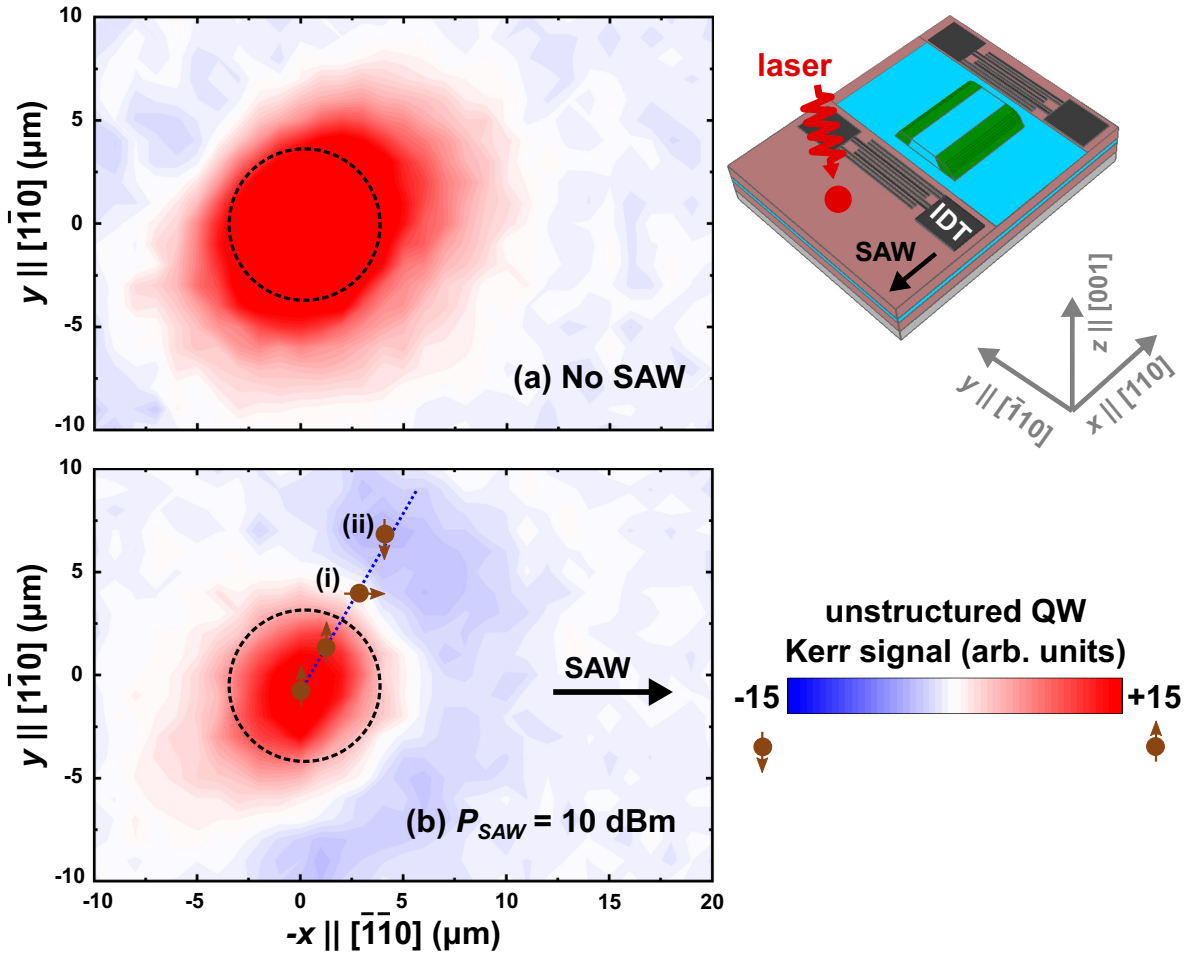

Figure 8.5: Spatial map of the Kerr rotation at an unstructured QW area, without SAW (a) and with a SAW of power $P_{SAW} = 10\,\mathrm{dBm}$ (b). As shown by the legend, the red and blue areas correspond to $\rho_z > 0$ and $\rho_z < 0$, respectively. The size of the excitation spot is indicated by the dashed black circle. The right panel illustrates the sample geometry: spins are optically injected (red arrow) into the QW layer (blue). A SAW travelling along the negative x-axis transports the injected spins. In fig. (b), the blue dashed line depicts the transport path of the majority of the carriers. The brown dots represent the spins, which rotate in the spin-orbit field.

8.2 Polarization-resolved photoluminescence studies

In this section, spin dynamics is studied by means of polarization-resolved photoluminescence experiments. This method is discussed in detail in sec. 4.4.1. Its application to detect spin transport is addressed in sec. 8.2.2. Firstly, the spin polarization will be investigated as function of excitation energy in sec. 8.2.1. The results of acoustic spin transport studies are presented in sec. 8.2.3. The experiments reported in this section are performed while operating the excitation laser in CW mode. The split-finger IDTs used for SAW generation are designed for a SAW wavelength of $\lambda_{SAW} = 4\,\mu\text{m}$ (frequency 726 MHz at a temperature of approx. 12 K).

8.2.1 Spin polarization as function of excitation energy

Figure 8.6(a) shows the PL polarization ρ_z of the QW (defined by eq. 4.4) at the excitation location as function of excitation energy. Here, a QW area at the ridge top is excited using an excitation density of $123\,\text{W/cm}^2$, while the PL of the QW electron-to-heavy-hole transition is detected, using spectral filtering by a triple grating spectrometer as described in sec. 4.3.2. For excitation energies above 1.565 eV, the heavy-hole and light-hole transitions are both excited off-resonantly. In this case, one expects a spin polarization of the conduction band electrons of 50 %. If only the electron-to-heavy-hole transition is measured, ρ_z should be a direct reflection of the spin polarization of the conduction band electrons, meaning $\rho_z = 50\,\%$. However, even when spin relaxation is absent, the detected ρ_z will be smaller due to the broad PL linewidths, which may lead to a small contribution to the signal from electron-to-light-hole recombinations.

As can be seen in fig. 8.6(a), for off-resonant excitation, ρ_z is approx. 13 %. The much smaller PL polarization than expected can be understood by considering spin relaxation. In secs. 6.3 and 8.1.1 it was shown that the QW recombination and spin lifetimes are of the same order of magnitude. Due to spin relaxation, the degree of spin polarization decays during the recombination process. Thus, electrons involved in recombination events at later times carry a smaller degree of spin polarization than those recombining early in the process. The temporal integration of the PL results, therefore, in a decrease of the overall detected PL polarization. For resonant excitation of the light-hole (QW_{lh} in the figure), the transition probability of the light-hole dominates over the one of the heavy-hole. Under that condition, the spin polarization in the conduction band will be negative (see sec. 3.3). This explains the negative sign of ρ_z for an excitation energy of 1.556 eV. Note that the resonant excitation of the heavy-hole (QW_{hh}) should lead to a 100 % spin polarization, as the transitions from the light-hole become completely suppressed under that condition. However, due to the proximity of the laser energy to the detection energy for resonant excitation, this can not be measured during the experiment.

Figure 8.6(b) presents ρ_z for the QWR as function of excitation energy, detected by measuring the electron-to-heavy-hole PL. Here, a ridge sidewall is excited using an excitation density of $123\,\text{W/cm}^2$. For excitation energies below 1.542 eV, the polarization can be explained by considering the direct excitation of carriers into the QWR. As is the case for the QW, detection for resonant excitation of the heavy-hole (QWR_{hh}) is not possible, because the laser energy is close to the detection energy under that condition. From finite-potential-well calculations, the QWR light-hole transition (QWR_{lh}) should have a transition energy of 1.525 eV. May that as it be, detection of the QWR PL polarization around this excitation energy does not lead to a negative ρ_z, indicating that the light-hole can not be accessed. For excitation energies above 1.542 eV, the majority of the QWR carriers originates from diffusion of carriers excited into the corner QW (CQW) into the

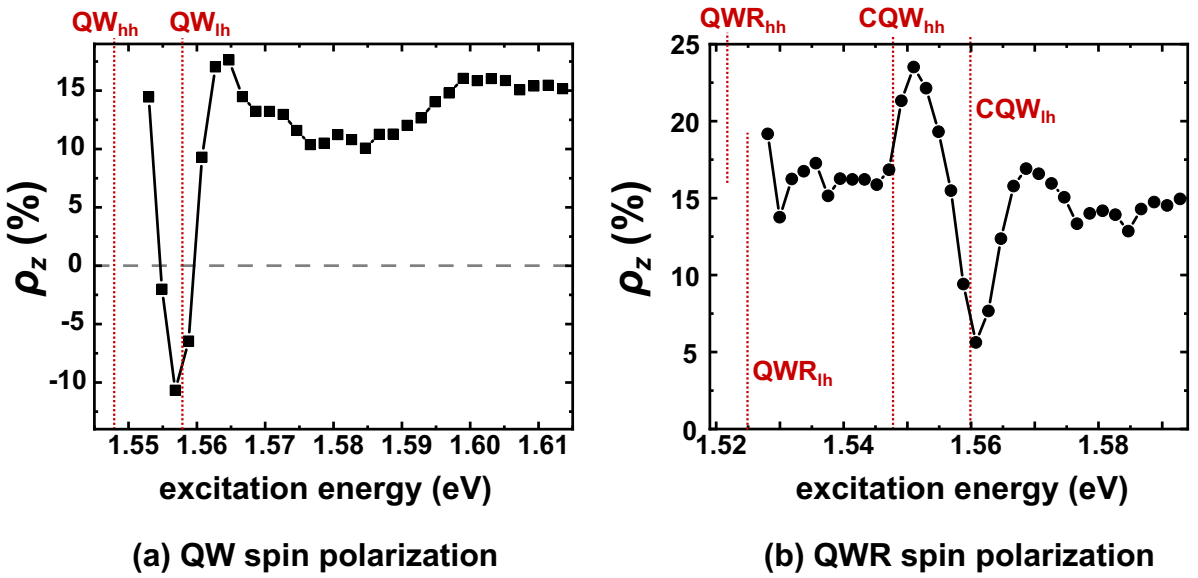

Figure 8.6: Spin polarization of the QW (a) and QWR (b) as function of excitation energy. In the figures, QW_{hh} and QW_{lh} mark the QW heavy- and light-hole transition energies, respectively. CQW_{hh} and CQW_{lh} denote the corresponding energies for the corner QW, while QWR_{hh} and QWR_{lh} indicate those of the QWR.

QWR. The maximum of ρ_z for an excitation energy of 1.551 eV corresponds to resonant excitation of the heavy-hole in the corner QW (CQW_{hh}). The particular magnitude of ρ_z is a results of the balance between the spin relaxation in the corner QW, the spin conservation during carrier diffusion from CQW into the QWR and the spin relaxation in the QWR. The minimum ρ_z at approx. 1.560 eV corresponds to resonant excitation of the light-hole of the corner QW (CQW_{lh}). The positive sign of ρ_z observed for the QWR indicates, however, that the majority of the spins in the QWR does not come from carriers associated to the CQW_{lh} excitation. Thus, even for this excitation energy, the majority of the QWR spins originates from diffusion of carriers excited into the CQW_{hh} transition. A small contribution can also be expected from direct injection of carriers into the QWR (which should lead to a positive ρ_z for this excitation energy).

8.2.2 Acoustic spin transport: method

Figures 8.7(a)-(e) illustrate the method of a typical experiment of acoustic spin transport as studied by polarization-resolved PL. In fig. 8.7(a), the experimental geometry is sketched: a spin-polarized carrier population (brown) is optically injected in the QWR (green) by a right-hand circularly polarized (RHCP) CW laser (bright red, (i)), while the sample is continuously subjected to a SAW along the $x||[110]$ direction. The piezoelectric potential accompanying the SAW transports the spins along the QWR axis towards a position, where recombination is enforced (dark red, (ii)), either unintended due to a trapping center or intentionally due to a metal stripe. Along the transport path, the spins precess around the effective SO field characterized by the Larmor vector $\mathbf{\Omega_{SO}}||y$ (see eq 3.30, black arrow). At the instant of carrier recombination, the local spin polarization at the detection spot is converted to circularly polarized PL via the optical selection rules (see sec. 3.3). The degree of PL polarization ρ_z is detected utilizing a combination of beam displacer and quarter-wave-plate to map the spectrally integrated PL into two polarization-dependent images onto a CCD camera (see sec. 4.4.1). Furthermore, a considerable fraction of the excited carriers recombines at the excitation location before they could be transported

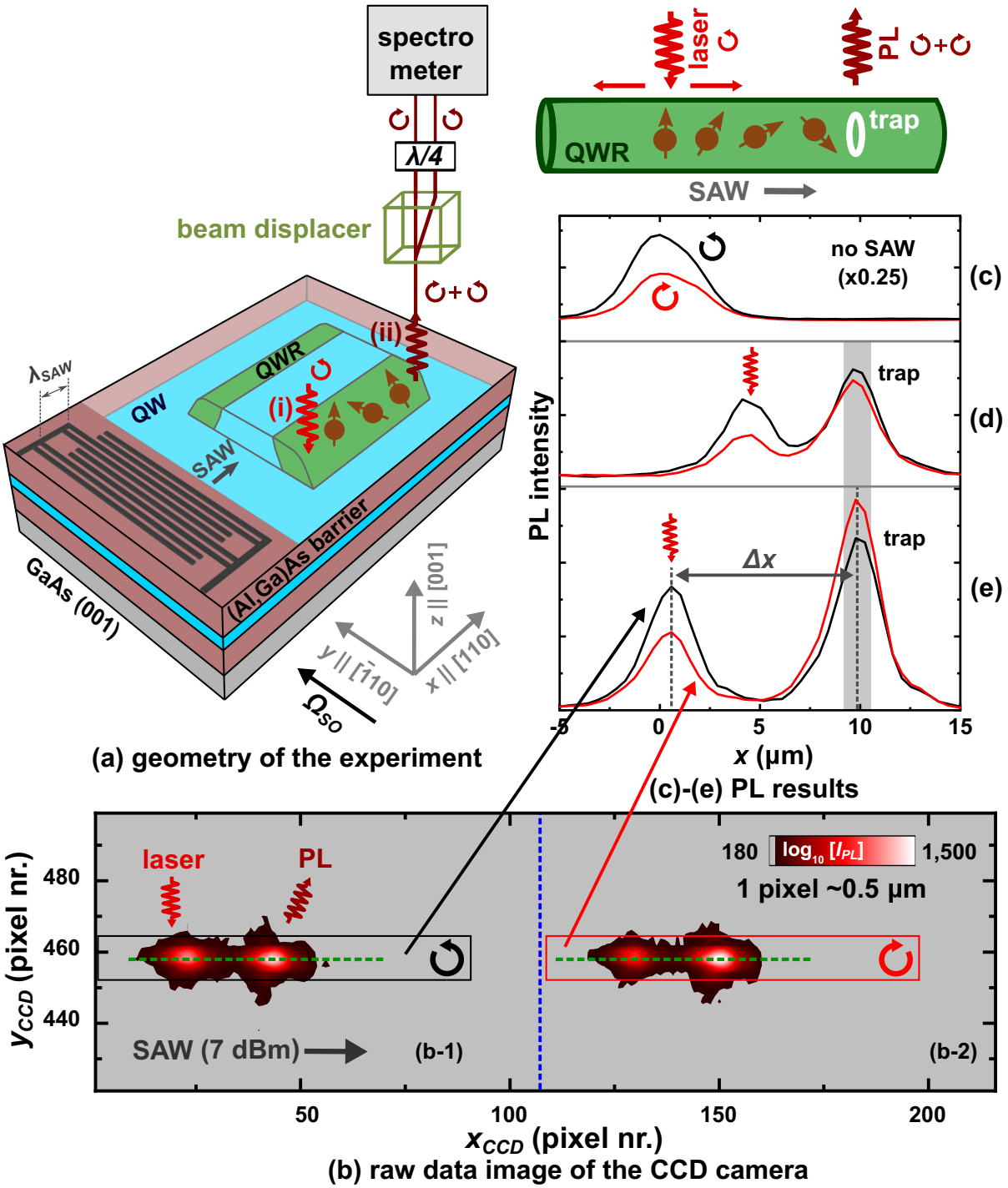

Figure 8.7: Illustration of the experimental method to detect acoustic spin transport. (a) Sketch of the sample geometry: the red, blue and green colours represent the (Al,Ga)As barriers, QW and QWRs, respectively. A spin population is excited by a RHCP laser (i). The carriers are transported by a SAW towards a trapping center, where they recombine (ii). The PL polarization is detected by a beam displacer, quarter wave plate and spectrometer. The SO field (black arrow) is oriented along y. (b) A typical raw image detected by the CCD camera. The dashed blue line marks the start of the second image, while the dashed green lines indicate the QWR positions. (c)-(e) Profiles of RHCP (black) and LHCP (red) PL without SAW (c, multiplied by 0.25) and with $P_{SAW} = 7\,\mathrm{dBm}$ (d) and (e). The upper panel of fig. (c) indicates the positions of the trapping center (white), laser beam (bright red) and the evolution of the spins (brown) during acoustic spin transport.

by the SAW. This allows the detection of the initial spin polarization at the excitation location. Similar experiments are performed in the surrounding QW by moving the excitation location to either the ridge top or ridge bottom, and detecting the QW PL along the x-axis.

Figure 8.7(b) shows a typical image as detected by the CCD camera, where x_{CCD} and y_{CCD} correspond to the dimensions parallel and perpendicular to the QWR axis, respectively. The blue dashed line marks the boundary between the polarization images, such that the range $0 < x_{CCD} < 107$ corresponds to RHCP PL (fig. 8.7(b-1)) and the range $108 < x_{CCD} < 216$ corresponds to LHCP PL (fig. 8.7(b-2)). In both images, the position of the QWR is indicated by a dashed green line. Two clear PL hotspots are detected, where in each image the left one corresponds to the excitation location and the right one corresponds to a trapping center. The spatial resolution is approx. 0.5 µm/pixel, meaning that the distance between excitation location and trapping center is approx. 10 µm. In the next step, the PL is spatially integrated along the y direction within the boundaries marked by the black and red rectangles, resulting in line profiles of the PL along x, corresponding to RHCP and LHCP, respectively. These profiles are shown in fig. 8.7(e). The profiles are shifted along the x-axis, such that the excitation location corresponds to $x_{exc} = 0$ µm, while the trapping center leads to remote PL at $x_{tc} = 10$ µm. The transport distance is defined by $\Delta x = x_{tc} - x_{exc}$.

Figure 8.7(c) shows the corresponding PL profiles without a SAW. The PL polarization is approx. +25 % at the excitation location. The vanishing difference between the black and red curves in fig. 8.7(c) for $x > 5$ µm indicates that the intrinsic spin diffusion length is limited to approx. 5 µm. As illustrated by the upper panel, the PL polarization is measured as function of Δx by spatially moving the laser beam (bright red arrow) along the QWR axis. Figure 8.7(d) displays the PL profiles for $\Delta x = 6$ µm ($x_{exc} = 4$ µm). A positive (negative) PL polarization at the remote location means that the spins are parallel (opposite) to the spin orientation at the excitation location. As figs. 8.7(d) and (e) show, the remote PL from the trapping center is polarized to a certain degree, demonstrating acoustic spin transport over distances larger than the intrinsic spin diffusion length. Furthermore, the difference between the black and red curves reveals that the remote ρ_z has opposite signs, when the transport distance increases from $\Delta x = 6$ µm (fig. 8.7(d)) to $\Delta x = 10$ µm (fig. 8.7(e)). This is a result of spin precession, and as will be shown in the next section, can potentially be used in a spin transistor.

A typical experiment of acoustic spin transport includes measurements at approx. thirty intermediate positions. Each of these measurements results in profiles as shown by figs. 8.7(d) and (e), corresponding to a specific Δx. For each of these profiles, the remote PL is further spatially integrated along x within a narrow window highlighted by the grey rectangles in figs. 8.7(d) and (e). In this way, the spatial integration of the black and red profiles yields the intensities I_{RR} and I_{RL}, respectively: the first and second index represent the circular polarizations of the excitation light and photoluminescence, respectively. In order to obtain an appropriate number of datapoints along the spin precession length, it is important to keep the integration windows small along both the x and y dimensions. The integration area is, therefore, chosen to be approx. 1.5 µm x 1.5 µm, which is below 15 % of L_{SO} for both the QW and the QWR for all acoustic powers used throughout the experiment. In the final step, this procedure is repeated for LHCP excitation, providing numbers for the intensities I_{LL} and I_{LR}. The results for I_{LL}, I_{LR}, I_{RL} and I_{RR} are then combined to correct for the circular dichroism of the components of the experimental setup and calculate ρ_z as function of Δx using eq. 4.4.

In an ideal experiment, the remote PL originates from the same recombination source for all intermediate measurements. However, as discussed in sec. 7.3.2, the trapping center

leading to remote PL may change when the excitation location is varied along the QWR axis. The detection of $\rho_z(\Delta x)$ is, in principle, susceptible to the spin dynamics of the trapping centers. For simplicity, the analysis of the experiments discussed here assumes that typical trapping centers exhibit similar spin dynamics, so that the Δx dependency of ρ_z should not depend on the detected trapping center. For high acoustic powers, the trapping potentials along the QWR axis are overcome by the large piezoelectric potential. As a result, the carriers are transported up to the metal stripe. In that case, the source of recombination events is equal for all intermediate measurements and does not influence the measurement of the spin dynamics.

8.2.3 Acoustic spin transport: results

Typical profiles of the QW ρ_z along the transport path, extracted using the method described above, are shown in figs. 8.8(a) and (b) for low and high acoustic power, respectively. The QWR ρ_z along the QWR axis is displayed in figs. 8.8(c) (low acoustic power) and (d) (high acoustic power). The upper panels of figs. 8.8(a) and (c) illustrate the experimental geometries, which are similar to the one sketched in fig. 8.7(a). The spin dynamics is governed by (i) spin precession in the effective SO field and (ii) spin relaxation. The profiles can, therefore, be fitted by the following function:

$$\rho_z(\Delta x) = \rho_z(0) e^{-\Delta x/\ell_\rho} \cos\left(\frac{\Omega_{SO}}{v_{SAW}}\Delta x\right), \tag{8.1}$$

where ℓ_ρ characterizes the spin transport length, Ω_{SO} the angular frequency corresponding to the SO field, $v_{SAW} \approx 2904\,\mathrm{m/s}$ the acoustic velocity and $\rho_z(0)$ the initial spin polarization. As is clear from a comparison of figs. 8.8(c) and (d), Ω_{SO} strongly depends on the acoustic power for the QWR, whereas figs. 8.8(a) and (b) reveal a much weaker dependency for the QW. This implies that the QWR is a promising candidate to be used as an active element in a spin transistor, since the orientation of the spin can be acoustically controlled over a fixed transport distance. This is illustrated by the brown line in figs. 8.8(c) and (d): for a fixed $\Delta x \approx 13\,\mu\mathrm{m}$, a low acoustic power results in $\rho_z < 0$, while a high acoustic power results in $\rho_z > 0$.

Figure 8.9(a) displays the dependency of Ω_{SO} on the uniaxial component of the SAW strain S_1, for the QW (black squares) and the QWR (red dots). Here, S_1 is calculated from P_{SAW} using eq. 2.32. The much stronger dependency of Ω_{SO} on S_1 in the QWR as compared to the QW is, again, clearly demonstrated by the figure. Since the QWR thickness is much smaller than its width, the spin behaviour for the QWR can be approximated by the one of a QW with a thickness equal to the QWR thickness. Therefore, both the QWR and the QW plots shown in fig. 8.9(a) can be fitted with the following equation (assuming that the electron wave vector is $\mathbf{k} = m_e v_{\mathrm{SAW}}/\hbar\hat{x}$, see sec. 3.5):

$$\Omega_{SO} = \Omega_D + \Omega_{BR} + \Omega_S = \frac{m_e v_{SAW}}{\hbar^2}\left[\gamma\left[\frac{\pi}{d_{eff}}\right]^2 - S_1\left[2r_{41}r_{SF} + \frac{C_3}{2}\right]\right]. \tag{8.2}$$

Here, the piezoelectric field F_z is substituted by $F_z = r_{SF}S_1$ to simplify the fitting procedure, where $r_{SF} = \text{-}1.2 \times 10^9\,\mathrm{V/m}$ (cf. eq. 2.38). Note that $r_{SF} < 0$ because of the orientation of F_z: the electrons are subjected to $F_z || -z$. The fixed parameters are the effective electron mass $m_e = 0.067{\times}9.109 \times 10^{-31}\,\mathrm{kg}$, the Dresselhaus spin-splitting parameter $\gamma = 17 \pm 2\,\mathrm{eV\,m^3}$ [108] and the Rashba spin-splitting parameter $r_{41} = -6 \pm 1 \times 10^{-20}\,e\,\mathrm{m^2}$ [109, 110]. Since $r_{41} \times r_{SF} > 0$, the Dresselhaus and Bychkov-Rashba terms have opposite signs for $S_1 > 0$ (which is the case for electron storage by the SAW potential, see sec. 2.5.2). The free fitting parameters are the parameter C_3 quantifying the strain-induced

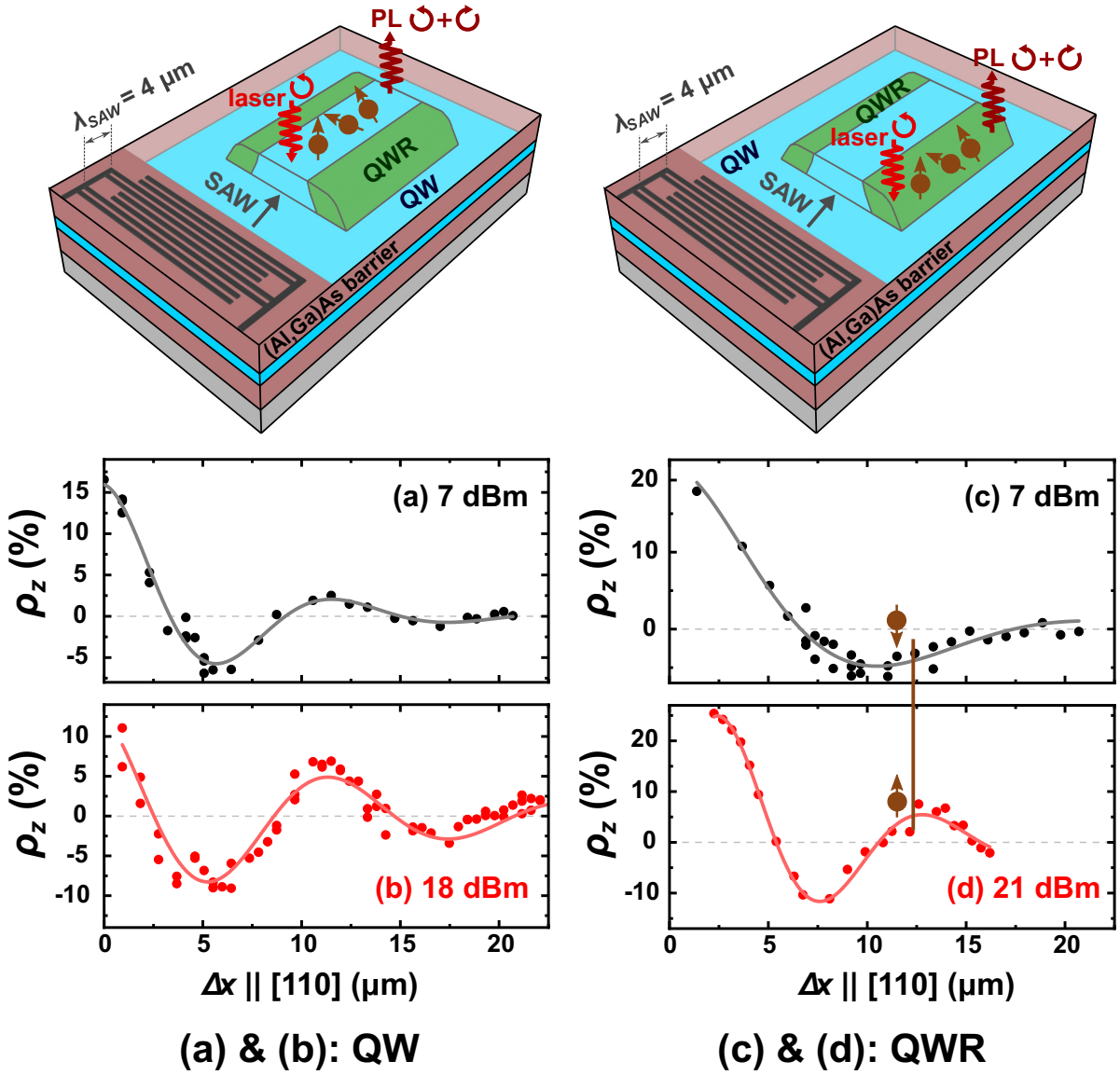

Figure 8.8: (a)-(b) Spin polarization along the transport path of QW carriers for $P_{SAW} = 7\,\mathrm{dBm}$ (a) and $P_{SAW} = 18\,\mathrm{dBm}$ (b). (c)-(d) Spin polarization along the transport path of QWR carriers for $P_{SAW} = 7\,\mathrm{dBm}$ (c) and $P_{SAW} = 21\,\mathrm{dBm}$ (d). The upper panels illustrate the position of laser excitation at the sample. In each panel, the red, blue, grey and green colours represent the (Al,Ga)As barriers, QW, substrate and QWR, respectively. The evolution of the spins (brown) along the acoustic transport path is schematically sketched in the illustrations.

field and the effective QW thickness $d_{eff} = d_{QW} + 2\alpha_{QW}$, where α_{QW} is the penetration depth of the electronic wavefunctions through the (Al,Ga)As barriers.

The grey line in fig. 8.9(a) depicts a fit of the QW data with eq. 8.2, while fixing $C_3 = -0.31\,\text{eV nm}$. The value and sign of C_3 are taken from refs. [117] and [118], respectively. In this case, the dependency of Ω_{SO} on the SAW strain is very weak. The QW thickness is the only free fitting parameter, resulting in $d_{eff} = 16.2 \pm 0.3\,\text{nm}$. This value is larger than $d_{eff} = 14.5\,\text{nm}$ as estimated from finite-potential-well calculations for the 10 nm thick QW. The larger thickness as estimated by the fit indicates that the Dresselhaus field in the QW is approx. 20 % weaker than expected. This may indicate that the penetration depth of the electron wavefunction through the (Al,Ga)As barriers is underestimated by the finite-potential-well calculations, which can be a result of a slightly smaller QW thickness or a smaller Al content in the (Al,Ga)As barrier layers. Taking into account such a larger penetration depth, the effective thickness of the QW layer is larger than the assumed value of 14.5 nm.

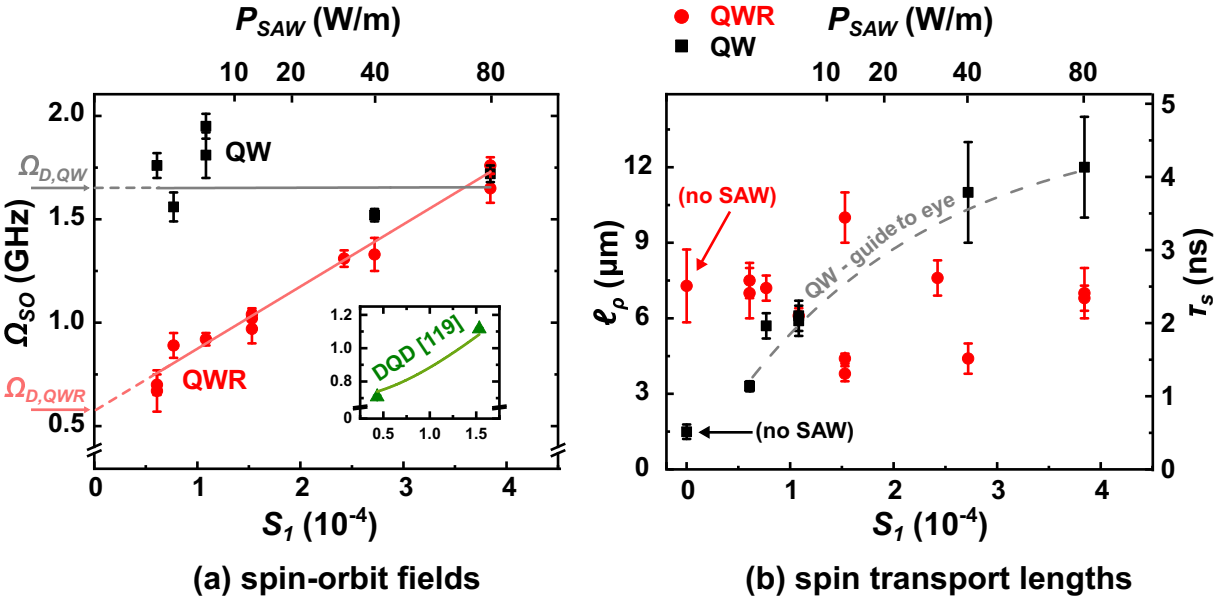

Figure 8.9: (a) Plot of Ω_{SO} as measured in the QW (black squares) and the QWR (red dots). The data points for DQDs from ref. [119] are shown in the inset by green triangles. The red and grey lines display a fit with eq. 8.2 of the QWR and QW data, respectively. The green line in the inset displays a fit of the DQD data with eq. 3.34. (b) Spin transport lengths ℓ_ρ as function of strain in the QWR (red) and QW (black). The grey dashed line provides a guide to the eye for the QW data.

For the QWR, the dependency of Ω_{SO} on S_1 is much stronger. A fit leaving both C_3 and d_{eff} as free fitting parameters reveals that $d_{eff} = 27.4 \pm 0.6\,\text{nm}$ and $C_3 = -2.6 \pm 0.1\,\text{eV nm}$. The value for the QWR thickness is consistent with the findings of secs. 5.3.2 and 6.2. The negative sign of the C_3 parameter complies with the findings of ref. [118]. Its value is, however, substantially larger than previously reported values in bulk [116] and in QWs [117]. Furthermore, the experimental conditions to obtain the data for the QW and the QWR presented in fig. 8.9(a) are similar. Note that since the QWR is embedded within the QW layer, and its thickness is much smaller than λ_{SAW}, the strain S_1 associated to a certain value of P_{SAW} is equal for the QW and the QWR. The much larger value of C_3 indicates, therefore, that the additional lateral confinement of the spins in the QWR affects the spin dynamics.

The influence of the spin confinement on the SO field is further supported by data

reported in ref. [119]. Here, dynamic quantum dots (DQD) are induced as a result of the interference between two perpendicular SAWs (see sec. 3.7). The inset of fig. 8.9(a) shows the two datapoints taken from ref. [119][2]. The green line displays a fit of the data with eq. 3.34. To obtain this fit, the same parameters as assumed for the QWR fit are used, additionally fixing $C_3 = -2.6\,\mathrm{eV\,nm}$ as determined for the QWR, and leaving the effective DQD thickness as the only free fitting parameter. As shown by the green line, this procedure provides a reasonable fit of the DQD data with $d_{eff} = 29.5 \pm 0.9\,\mathrm{nm}$. This finding is consistent with the sample design, since the QW layer thickness is 30 nm in this case. Using $C_3 = -0.3\,\mathrm{eV\,nm}$ results in a poor fit, which confirms the effect of the lateral confinement on the strain-induced spin dynamics.

Figure 8.9(b) displays a plot of the fitted spin transport lengths ℓ_ρ along the SAW path in the QW (black) and the QWR (red). The right axis provides the corresponding spin lifetime τ_S calculated by $\tau_S = \ell_\rho / v_{\mathrm{SAW}}$, assuming that the carriers are transported with the acoustic velocity. It was shown in sec. 7.4 that this assumption is justified. As explained in sec. 3.5, the lateral separation of electrons and holes by the SAW piezoelectric potential leads to suppression of the electron-hole exchange interaction and, consequently, to a strong enhancement of the spin lifetimes [65]. In the QW, such a large increase of the spin lifetime is indeed observed: at high acoustic powers, the spin lifetime is 8x as large as under the condition without a SAW. For high acoustic powers, the strong suppression of exchange interaction means that the spin lifetimes are limited by the Dyakonov-Perel (DP) mechanism. In contrast to the QW, the spin lifetimes in the QWR are essentially similar as those observed without SAW and do not suggest a systematic dependency on the acoustic power. In the QWR, DP spin dephasing is suppressed and the additional suppression of the electron-hole exchange interaction by the SAW should lead to very large spin lifetimes. Note that although the exchange interaction plays a role at the trapping center and at the excitation location, this should not result in a spatial decay of ρ_z, but merely in a decrease of the overall ρ_z. As compared to the QW, the QWR has additional boundaries defined by the lateral interfaces with the (Al,Ga)As barriers and the surrounding QW. These interfaces induce Elliott-Yafet spin relaxation. Such a process was suggested previously to explain a decrease of the spin lifetime for narrow QWRs [37, 68]. This process is independent of the acoustic power, which explains why there is no systematic dependency of the QWR spin lifetime on acoustic power. Thus, the QWR spin lifetimes, even without application of a SAW, are dominated by Elliott-Yafet spin relaxation.

8.3 Monte Carlo simulations of acoustic spin transport

The previous section presents the results of acoustic spin transport experiments. For the analysis of these results, it was assumed that the precession length can be calculated taking into account that the electron wavevector is given by $\mathbf{k} = m_e v_{\mathrm{SAW}} / \hbar \hat{x}$. In order to justify this assumption, and to examine the effect of SAW power and channel width on the spin dynamics, this section presents the findings of Monte Carlo simulations of the spin dynamics under a DP dominated condition. The simulation algorithm is described in sec. 3.6.

In the simulations, $d_{eff} = 15\,\mathrm{nm}$ is used, which roughly corresponds to the effective thickness of the experimental QW layer, as calculated from a finite-potential-well model.

[2]The strain values reported for the DQDs as shown by the inset of fig. 8.9(a) are calculated by the SAW powers reported in ref. [119], using a conversion factor communicated by Prof. Dr. James Stotz.

The parameter $C_3 = -2.6\,\text{eV nm}$ used in the simulation corresponds to the one extracted from the QWR data. Figure 8.10(a) shows the simulated spin polarization as function of position along x (horizontal axis) and y (vertical axis), for a channel width $w_{ch} = 1\,\mu\text{m}$. This width can be used to simulate the QWR (note that the QWR width is of the order of $10^{-1}\,\mu\text{m}$ and that the real QWR thickness is larger than the simulated d_{eff}). The simulated acoustic power density for this figure is $P_{SAW} = 0.5\,\text{W/m}$. As shown by the figure, the spins rotate around the effective DP field with a precession length $L_{SO} \approx 10\,\mu\text{m}$. The much smaller width of the channel as compared to L_{SO} results in the well-known motional narrowing effect [36], suggesting that the spin lifetime is essentially infinite. If the channel width is increased to $15\,\mu\text{m}$ (fig. 8.10(b)), L_{SO} is again approx. $10\,\mu\text{m}$, while it is clear that spin relaxation is much stronger as in fig. 8.10(a). For the wide channel of fig. 8.10(b), the channel width is larger than L_{SO}, so that the spin lifetime is not affected by motional narrowing due to the channel width.

Figure 8.10(c) displays the spin polarization simulated for a channel width of $15\,\mu\text{m}$ and acoustic power density $P_{SAW} = 80\,\text{W/m}$. As expected from eq. 3.30 for these simulation conditions, in this case the precession length decreases to $L_{SO} \approx 6\,\mu\text{m}$. A comparison with fig. 8.10(b) reveals that the application of a high acoustic power strongly reduces DP spin relaxation with respect to a weak acoustic power for the same channel width. The SO field for $P_{SAW} = 80\,\text{W/m}$ is approx. twice as large as the SO field for $P_{SAW} = 0.5\,\text{W/m}$ and, in contrast to what the figure shows, should lead to a strong reduction of the spin lifetime [36]. The suppression of spin relaxation can be understood as follows. For a weak SAW, the SAW induced SO fields, characterized by α in eq. 3.29, and the intrinsic Dresselhaus contribution, characterized by β in eq. 3.29, are related as $0 > \alpha > -\beta$. Under this condition, the SO field has components along both the x- and y-axes, which leads to the usual DP spin relaxation. If the SAW power is increased, the relation between α and β approaches the one for a persistent spin helix: $\alpha = -\beta$. As a result, the x component of $\mathbf{\Omega_{SO}}$ (given by $\beta + \alpha$) strongly reduces, thereby weakening DP spin relaxation. In fact, if the acoustic power density is increased to $P_{SAW} = 225\,\text{W/m}$ (fig. 8.10(d)), the PSH condition $\alpha = -\beta$ is exactly met for the simulation parameters. In this case, the SO field only has a component along the y-axis and the spin lifetime is essentially infinite. As expected, the spin precession length, which is determined by the y component of Ω_{SO}, is further reduced. Finally, for a high acoustic power density of $P_{SAW} = 550\,\text{W/m}$ (fig. 8.10(e)), α and β are related by $\alpha < -\beta$. In this case, the x component of Ω_{SO} increases again, thereby inducing DP spin relaxation again. Note that the exact direction of Ω_{SO} depends on both α and β, which differs for the three cases described in this paragraph. Consequently, the direction of spin precession is different in the three cases.

For the experiments reported in sec. 8.2.3, the conditions $P_{SAW} = 225\,\text{W/m}$ and $P_{SAW} = 550\,\text{W/m}$ are out of the range of accessible SAW powers. To reach such high SAW powers, one should either use a high-power rf generator, or reduce the power losses between rf generator and IDT. Moreover, the results for the QW presented by fig. 8.9 (black squares) indicate that the strain dependency of the spin precession frequency in the QW is much smaller than the one characterized by $C_3 = -2.6\,\text{eV nm}$. As a result, the condition for the PSH requires a much larger SAW power than $P_{SAW} = 225\,\text{W/m}$. The enhancement of the QW spin lifetime shown in fig. 8.9(b) is, therefore, attributed to the suppression of electron-hole exchange interaction by the SAW piezoelectric potential. However, the simulation results presented in fig. 8.10(d) and (e) are useful for illustrative purposes.

Figure 8.11(a) shows the simulated spin lifetimes (for Dyakonov-Perel spin relaxation) as function of the channel width w_{ch} for the conditions $P_{SAW} = 0.5\,\text{W/m}$ (black), $P_{SAW} = 40\,\text{W/m}$ (red) and $P_{SAW} = 80\,\text{W/m}$ (blue). The spin lifetimes depend on w_{ch} as $\tau_S \propto w_{ch}^{-2}$

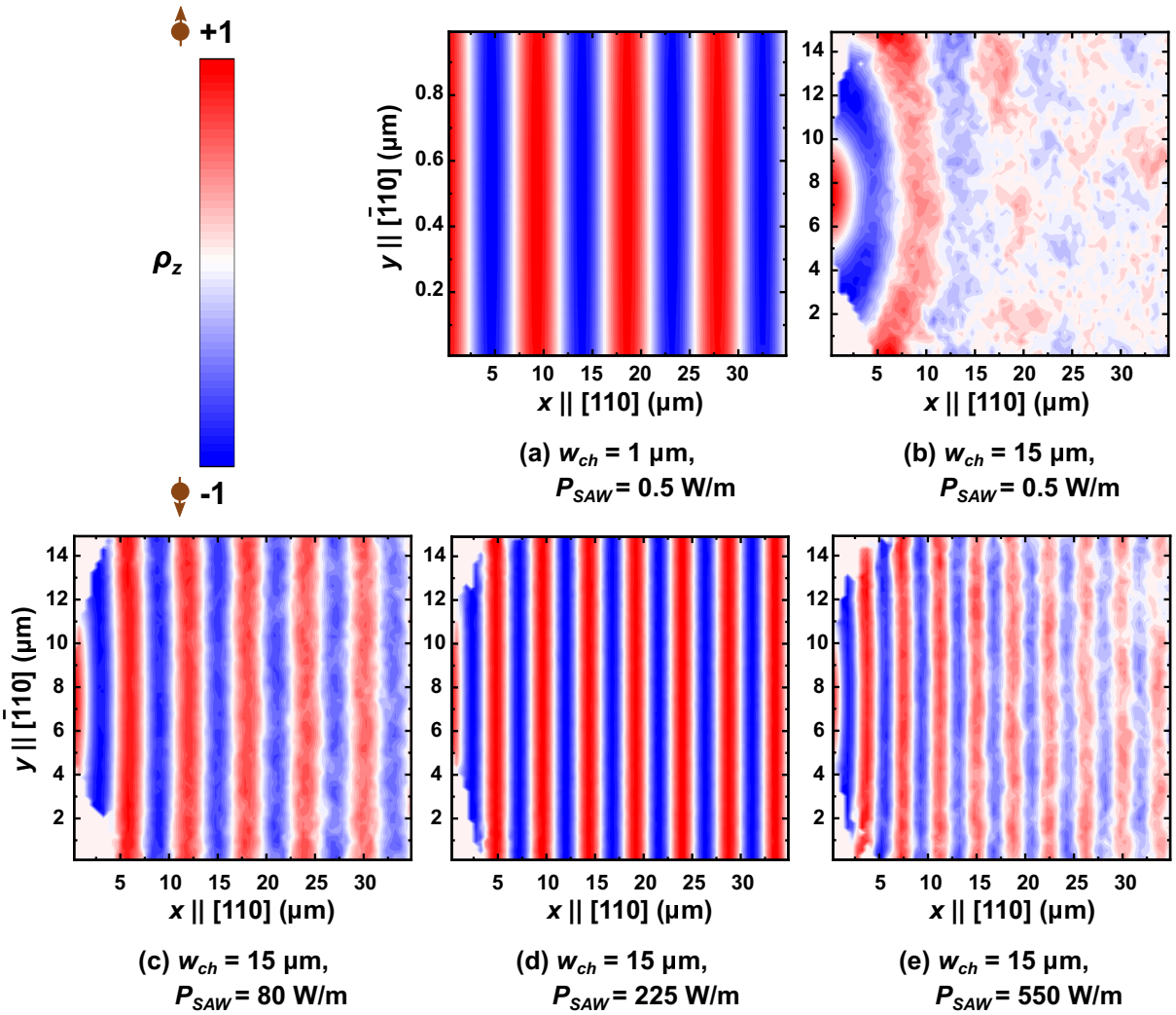

Figure 8.10: Map of the spin polarization simulated for $d_{eff} = 15\,\text{nm}$ for a channel width of (a) $w_{ch} = 1\,\mu\text{m}$ and $P_{SAW} = 0.5\,\text{W/m}$, (b) $w_{ch} = 15\,\mu\text{m}$ and $P_{SAW} = 0.5\,\text{W/m}$, (c) $w_{ch} = 15\,\mu\text{m}$ and $P_{SAW} = 80\,\text{W/m}$, (d) $w_{ch} = 15\,\mu\text{m}$ and $P_{SAW} = 225\,\text{W/m}$ and (e) $w_{ch} = 15\,\mu\text{m}$ and $P_{SAW} = 550\,\text{W/m}$. Note that the scale of the y-axis in fig. (a) is smaller with respect to figs. (b)-(e).

and are essentially infinite for narrow width, as expected from ref. [36]. The figure shows clearly that the 2D spin lifetime (approximated by the one for $w_{ch} = 15\,\mu m$) becomes enhanced with increasing acoustic power, because the SO field approaches the persistent spin helix for large acoustic powers. Furthermore, since the SO field becomes larger for increasing acoustic power, the spin precession length decreases. As a result, the spin lifetime corresponding to the 2D case appears at a smaller channel width. This is because the ratio of the spin precession length to the channel width, which determines the motional narrowing regime, is unity for a smaller channel width.

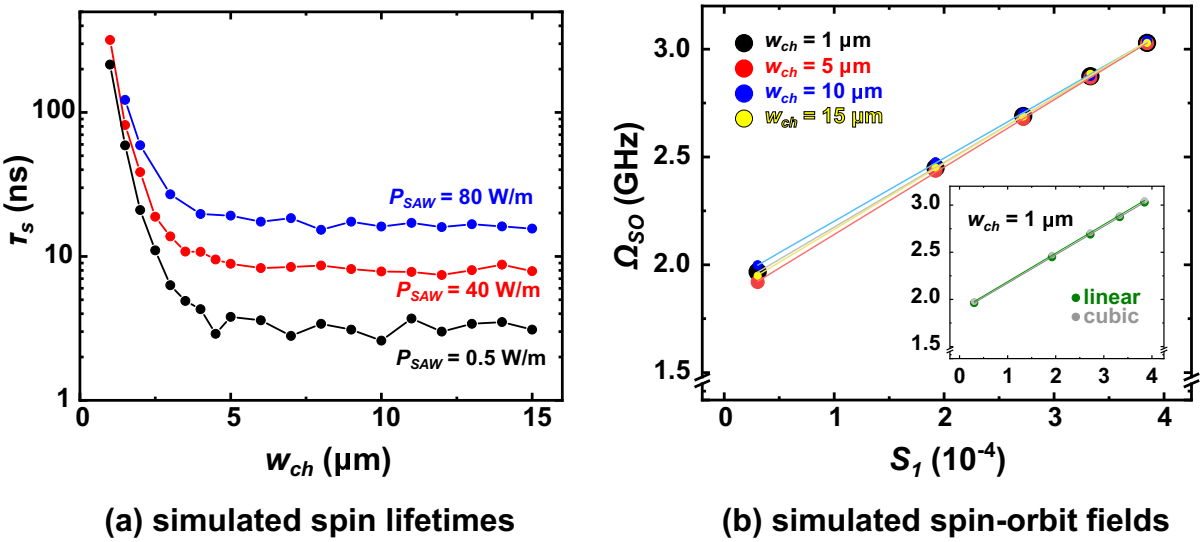

Figure 8.11: (a) Simulated spin lifetimes as function of channel width for $P_{SAW} = 0.5\,W/m$ (black), $P_{SAW} = 40\,W/m$ (red) and $P_{SAW} = 80\,W/m$ (blue). (b) Simulated spin-orbit fields for $w_{ch} = 1\,\mu m$ (black), $w_{ch} = 5\,\mu m$ (red), $w_{ch} = 10\,\mu m$ (blue), $w_{ch} = 15\,\mu m$ (yellow). The inset shows the spin-orbit field for $w_{ch} = 1\,\mu m$ taking into account only the linear terms (green) and also taking into account the cubic terms (grey).

Figure 8.11(b) shows the simulated spin precession frequency as function of uniaxial strain component S_1 for a channel width of $w_{ch} = 1\,\mu m$ (black), $w_{ch} = 5\,\mu m$ (red), $w_{ch} = 10\,\mu m$ (blue) and $w_{ch} = 15\,\mu m$ (yellow). As revealed by the figure, the dependency of the SO field on S_1 is rougly the same for all channel widths. This indicates that there is no effect of the channel width on the magnitude of the SO field like there is on the spin lifetime. Thus, the experimental weaker dependency of the SO field on S_1 in the QW as compared to the QWR revealed by fig. 8.9(a) can not be explained by a motional effect. Furthermore, the inset of fig. 8.11(b) shows that the SO field is essentially equal when for the Dresselhaus field only linear-in-k terms are considered, as compared to the full expression taking into account the cubic-in-k terms (the terms which are linear to k_x^2 and k_y^2 in eq. 3.21). The results of fig. 8.11(b) demonstrate that it is justified to analyse the experimental data assuming that $\mathbf{k} = m_e v_{\mathrm{SAW}}/\hbar\hat{x}$ and taking only those terms into account, which are linear in $\langle k_z^2 \rangle$.

8.4 Summary of the chapter's findings

In this chapter, the spin dynamics in the QWR and in the surrounding QW is investigated. For the QW, the intrinsic spin lifetime is approx. 0.5 ns and is enhanced by 8x by the application of a high acoustic power. The spin lifetimes in the QWR are enhanced by 4 to 6 times with respect to the QW. The suppression of Dyakonov-Perel spin relaxation by

the narrow QWR width and the suppression of exchange interaction by a SAW should lead to a further enhancement of the QWR spin lifetime during acoustic spin transport. In contrast, the QWR spin lifetime does not depend systematically on the acoustic power. This reveals that the QWR spin lifetime is limited by interface scattering, which induces the Elliott-Yafet type of spin relaxation. Acoustically transported spins in the QWR reach, nevertheless, distances of up to at least 15 µm.

The results presented in this chapter show a strong dependency of the SO field on uniaxial strain in the QWR, whereas it is much weaker in the QW. This indicates an effect of the lateral confinement of the spins within the narrow boundaries of the QWR on the strain-induced spin-orbit field. This is characterized by a parameter $C_3 = -2.6 \pm 0.1\,\mathrm{eV\,nm}$ for the QWR, which is much larger than reported in earlier works [116, 117]. The lateral confinement effect on the SAW-induced spin dynamics is further supported by the analysis of the data reported in ref. [119]. The strong strain dependency of the SO field in the QWRs makes these QWRs a promising candidate to be used in a spin transistor. Here, the strain fields of a SAW act as a strain gate on the spins: the orientation of acoustically transported QWR spins over a fixed transport length can be actively controlled by the acoustic power.

chapter 9

Conclusions and outlook

The functionality of current, classical, computation devices can be improved by complementing them with quantum mechanical spin. One such example is the Datta-Das spin transistor. The combination of a narrow semiconductor spin channel with surface acoustic waves facilitates long-range spin transport, while actively controlling the spin orientation. In this thesis, acoustic charge and spin transport in growth-defined quantum wires (QWR), fabricated on prepatterned GaAs (113)A and GaAs (001) substrates, is studied. In the first section of this chapter, the main conclusions are summarized. The second section provides some future research prospects based on the results of this thesis.

9.1 Conclusions

The quantum wires (QWR) investigated here form as a result of the anisotropic overgrowth of a quantum well (QW) structure by molecular-beam epitaxy (MBE) on ridges prepatterned on GaAs substrates. These QWRs are embedded in a 10 nm thick QW layer. On both the (113)A and (001) substrates, the edges of the ridges before MBE overgrowth contain deviations from a straight line. These deviations are characterized by line-edge roughness (LER) in the range from 4 nm to 9 nm. The main source of LER is the photolithography process. Since the LER value is much smaller than the approx. 200 nm QWR width for both substrate orientations, it does not play a significant role for transport properties in the QWR. This is a positive finding for acoustic charge transport.

On (113)A substrates, the QWR forms on a steep sidewall of ridges oriented along the $[\bar{1}10]$ direction. In this case, the QWR formation results from the larger incorporation rate of Ga adatoms during MBE overgrowth at the ridge sidewall as compared to the one at the ridge top and bottom. The thickness and width of the QWR are 20 ± 5 nm and 210 ± 5 nm, respectively. Since the QWR width is much larger than its thickness, the electronic and optical behaviour are mainly determined by the QWR thickness. Therefore, to a good approximation, the properties of the QWR can be described by those of a QW layer with a thickness equal to the one of the QWR. The electron-to-heavy-hole transition energy of the QWR is 1.525 eV, which is consistent with the QWR thickness.

On (001) substrates, QWRs form on both sidewalls of ridges oriented along the [110] direction. The QWR formation mechanism relies, in this case, on the availability of free dangling bonds at step edges due to the (2x4) surface reconstruction. STEM images of the QWR reveal a QWR thickness and width of 25 ± 5 nm and 200 ± 5 nm, respectively. The electron-to-heavy-hole transition energy of the QWR is approx. 1.521 eV, which is consistent with the QWR thickness. For off-resonant optical excitation of the QWR

(excitation energy above 1.542 eV), the majority of the QWR carriers originates from carriers optically injected in the surrounding QW, which diffuse into the QWR. This process takes place over a timescale of approx. 0.5 ns and is attributed to the narrow QWR width, meaning that its light absorption area is much smaller than a typical laser spot size. The recombination lifetimes of the optically excited QWR carriers (approx. 0.9 ns) are roughly twice as large as those of the QW carriers (approx. 0.5 ns). This is attributed to a decreased exciton localization. The escape of electrons and holes from the QWR into the surrounding QW is prevented by a lateral potential barrier of 25.4 meV and 4.8 meV, respectively. These potential barriers are larger than the corresponding ones on (113)A substrates, which is beneficial for acoustic transport studies. Therefore, the remainder of this chapter addresses the acoustic transport properties for QWRs on GaAs (001) substrates only.

Spatially-resolved photoluminescence (PL) experiments demonstrate the transport of electrons and holes in both the QW and the QWR by a surface acoustic wave (SAW). For high acoustic powers, the majority of the optically injected carriers at the excitation location is transported along the QWR axis. This is evidenced by a strong degree of PL quenching. Under this condition, charge transport takes place over a distance of up to 90 µm, where a metal stripe is deposited to screen the SAW potential and to induce carrier recombination. The observed travel time for carriers transported over a fixed distance corresponds to the one expected from the acoustic velocity, which indicates a high transport efficiency by the SAW.

Along the transport path, several unintentional trapping centers, randomly distributed, can lead to recombination of the transported carriers. These trapping centers originate from interface states and from fluctuations of the QW and QWR thicknesses. They display a preference for one type of carrier (i.e. electrons or holes). The trapping dynamics depends on the local carrier density in the vicinity of the trapping center. For high acoustic power, the strong SAW potential counteracts the trapping potential and transports the carriers beyond the trapping centers. Furthermore, it is shown that during acoustic transport, carriers can be extracted from the QWR into the surrounding QW, even though this is prevented in the absence of a SAW by lateral potential barriers.

The intrinsic spin lifetime in the QWR of approx. 2 ns to 3 ns is enhanced with respect to the one in the QW (approx. 0.5 ns) and is limited by Elliott-Yafet spin relaxation due to the QWR interfaces. In the QWR, acoustic transport of optically injected spins is observed over a distance of approx. 15 µm. The SAW strain induces a spin-orbit (SO) field, which acts on the carrier spins. During acoustic transport, the QWR spins rotate around this SO field, which is strongly dependent on the acoustic power. For the highest available acoustic power, the QWR spin precession frequency is enhanced by approx. 3.5 times with respect to the intrinsic SO field. A systematic study of the spin precession frequency reveals the C_3 parameter, describing the strain-induced SO field, to be $C_3 = -2.6 \pm 0.1\,\mathrm{eV\,nm}$.

The results of the acoustic spin transport studies show that the combination of the QWR with a SAW is a promising concept to be used in a spin transistor. Here, the strain field of the SAW acts as a strain gate for the QWR spins: the orientation of optically injected QWR spins, acoustically transported over a fixed distance, can actively be controlled by appropriate tuning of the acoustic power.

9.2 Outlook

The strain gate of the QWR-based spin transistor can be used for the development of devices processing optical information. Here, one exploits the optical selection rules, through which the optical information, encoded in the photon polarization, can be converted into spin information. The strain gate operates on the spin information during the transport of the flying spins over a fixed distance. At the end of the transport path, the optical selection rules convert the spin information back into optical information.

An acoustically driven single-photon source could play an important role in optical information processing. For this purpose, all injected spins start with equal orientation. This can be achieved, for example, by excitation by circular polarized laser light. The state of the flying spins is then controlled by the strain gate, thereby controlling the polarization of the photon emitted when the spin carriers recombine. Single-photon emission with a well-defined polarization can, hence, be achieved by implementing a single-photon emitter at a fixed distance from the spin injection location.

The quantum wire can as well be used as a quantum processor of optical information. In this case, the state of the injected spins is not a-priori known, but determined by the optical information entailed in the polarization of an incoming photon. As in the previous case, the output of the device is a single-photon, with a polarization determined by the state of a flying spin at the instant before carrier recombination. Since the strain gate acts on the flying spins, it also operates as a polarization switch for photons: for low acoustic powers, the circular polarizations of the incoming and emitted photons will be opposite, while for high acoustic powers their circular polarizations will be equal.

The switching device differs fundamentally from the acoustically driven single-photon source. For the single-photon source, the optically injected spins are initially aligned: they start with the same orientation. In this case, the precise outgoing photon polarization (i.e. left- or right-hand circular polarization) is determined by the intensity of the SAW. In contrast, the switching device only determines the relation between the polarizations of the incoming and outgoing photons. For the switching device, the consecutive injected spins are not aligned, but their initial orientations depend on the polarization of the incoming photon. It is evident that the development of both devices requires (i) sustainability of the spin over the transport distance and (ii) the implementation of a single-photon emitter at the end of the transport channel. The emission properties of the devices may, furthermore, be improved by embedding the quantum wire in a microcavity.

The studies conducted in this thesis imply that there should be an optimal QWR width for the spin lifetime, at which Dyakonov-Perel spin relaxation is suppressed, while Elliott-Yafet spin-flip scattering is minimized. One obvious future topic of investigation is, therefore, to systematically vary the QWR width for acoustic spin transport studies. Under the right MBE growth conditions (e.g. temperature), the QWR width is mainly determined by the thickness of the QW layer, which is, consequently, the controlling parameter for the QWR dimensions. Changing the QWR dimensions also changes its transition energy, which affects the intrinsic SO field. This effect should be considered when studying the dependency of the spin dynamics on the QWR width. Another issue to take into account is the height of the lateral potential barrier between QWR and surrounding QW, which is expected to vary with the thickness of the QW layer.

The integration of single-photon emitters connected with the QWR provides a promising application of the QWR system as an acoustically driven single-photon source [64]. Ideally, the position and emission properties of the emitter should be well-defined by a suitable sample design. This can be achieved by embedding quantum dots (QD) within a QWR, since their emission properties can, in principle, be very well-defined. However, their

positions are, generally, determined by a random distribution. The QD density can be controlled by choosing the appropriate MBE growth conditions. Thus, by choosing the right growth conditions, one can manipulate the number of QDs which are connected to the QWR, as well as the average distance between the QDs. Previous works have, furthermore, shown the ordering of QDs on GaAs substrates. QD positioning can be achieved by prepatterning the underlying surface using, for example, focussed ion beam [151], atomic force microscope lithography [152] and oxide-based masks [153]. Once integrated, single-photon emission by the QD can be detected by means of photon-antibunching [64].

An improvement of the single-photon source properties can be achieved by embedding the QW-QWR-QD system in a microcavity. Such a structure consists of a cavity spacer layer sandwiched between two Bragg mirrors. The mirrors confine the photon along the vertical direction if its wavelength corresponds to the cavity resonance wavelength. The interaction between the QD and the cavity field increases the photon emission frequency and redirects emitted photons into a narrow extraction cone, thereby increasing the detection yield. The quality factor of the microcavity is defined by the ratio between its resonance energy and linewidth: the smaller the cavity resonance linewidth, the higher the quality. The interaction between QD and cavity field is strongest for an exact match (tuning) between the QD transition and the cavity resonance, as well as for high quality factors. Some preliminary studies on microcavities have been carried out for this thesis. It is found that the QWR transition energy of those embedded in the microcavity is similar to the one without a cavity. Furthermore, using in-situ continuous spectral reflectivity measurements during MBE growth, one can precisely control the cavity resonance to tune it with the embedded emitter resonance [154]. Indeed, the preliminary studies (using a low quality microcavity) revealed the feasibility of matching the QWR energy with the cavity resonance.

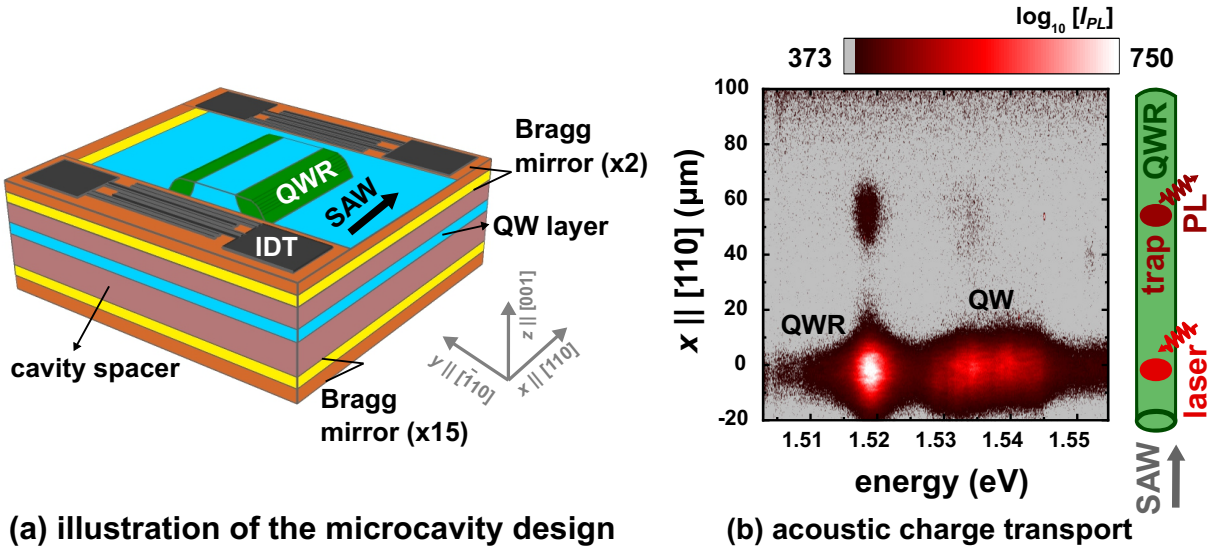

Figure 9.1: (a) Illustration of the microcavity design. The QW layer (blue) is embedded in a cavity spacer (red). The cavity spacer is sandwiched by a lower Bragg mirror (orange-yellow) and an upper Bragg mirror (yellow-orange). The SAW (black arrow) is generated by interdigital transducers (IDT, black) deposited onto the sample surface. (b) Spatial PL map of an area around a ridge sidewall in the microcavity sample as sketched in fig. (a). The right panel schematically illustrates the experimental geometry: the QWR is excited using an excitation energy of 1.633 eV (bright red). The carriers are transported by a SAW (grey arrow) along the QWR axis (green) and recombine due to a trapping center (dark red).

Preliminary experiments of acoustic charge transport in a QWR, embedded in a low quality microcavity, have been performed to demonstrate acoustic carrier transport. Figure 9.1(a) illustrates the sample design: a GaAs QW layer (blue) is embedded in an $Al_{0.15}Ga_{0.85}As$ cavity spacer (red). The lower Bragg mirror is constructed by 15 pairs of alternating low/high refractive index layers (yellow and orange). The upper Bragg mirror has only two of these pairs. For the sample studied here, the Bragg mirrors consist of alternating $Al_{0.95}Ga_{0.05}As$ and $Al_{0.10}Ga_{0.90}As$ layers, which act as the low and high refractive index layers, respectively. As discussed in chap. 5, the QWRs (green) form at ridges prepatterned on the substrate surface. However, for the experiment discussed here, the ridges are patterned in the cavity spacer layer. At the top surface of the sample, interdigital transducers are deposited, which generate a SAW along the QWR axis. Figure 9.1(b) displays the spectrally resolved PL detected along the QWR axis, which aligns with the acoustic transport path and is directed along [110]. During the experiment, a ridge sidewall is optically excited with an excitation energy of 1.633 eV. A SAW (acoustic power 13 dBm) is applied along the [110] direction (vertical axis in fig. 9.1(b)). As can be seen in the figure, the QWR emission is detected with a transition energy similar to the one observed in fig. 6.2. Emission from the QW is strongly reduced, because its transition energy is not tuned with the cavity resonance energy. Charge transport of QWR carriers by the surface acoustic wave is clearly demonstrated by a QWR PL hotspot at $x \approx 60\,\mu m$. In future studies, analysis of the photoluminescence should reveal the characteristics of the spin dynamics, as well as photon-antibunching, in microcavity samples.

Bibliography

[1] D. Reinsel, J. Gantz, and J. Rydning. "The digitization of the world from edge to core". In: *Framingham: International Data Corporation* (2018).

[2] T. Ytterdal, Y. Cheng, and T. A. Fjeldly. *Device modeling for analog and RF CMOS circuit design*. John Wiley & Sons, 2003.

[3] G. E. Moore. "Progress in digital integrated electronics". In: *Electron devices meeting*. Vol. 21. 1975, pp. 11–13.

[4] T. Cross. "After Moore's law". In: *The Economist* (2016-03-12).

[5] R. P. Feynman. "Simulating physics with computers". In: *Int. J. Theor. Phys* 21 (1982).

[6] C. H. Bennet and G. Brassard. "Quantum cryptography: Public key distribution and coin tossing". In: *Proc. IEEE Intl. Conf. on Computers, Systems, and Signal Processing*. 1984, p. 175.

[7] P. Kok, W. J. Munro, K. Nemoto, T. C. Ralph, J. P. Dowling, and G. J. Milburn. "Linear optical quantum computing with photonic qubits". In: *Reviews of Modern Physics* 79.1 (2007), p. 135.

[8] R. Hanson, L. P. Kouwenhoven, J. R. Petta, S. Tarucha, and L. M. K. Vandersypen. "Spins in few-electron quantum dots". In: *Reviews of modern physics* 79.4 (2007), p. 1217.

[9] C. G. Almudever, L. Lao, X. Fu, N. Khammassi, I. Ashraf, D. Iorga, S. Varsamopoulos, C. Eichler, A. Wallraff, L. Geck, A. Kruth, J. Knoch, H. Bluhm, and K. Bertels. "The engineering challenges in quantum computing". In: *Design, Automation & Test in Europe Conference & Exhibition*. IEEE. 2017, pp. 836–845.

[10] G. E. Uhlenbeck and S. Goudsmit. "Spinning electrons and the structure of spectra". In: *Nature* 117.2938 (1926), pp. 264–265.

[11] A. Hirohata, K. Yamada, Y. Nakatani, L. Prejbeanu, B. Diény, P. Pirro, and B. Hillebrands. "Review on spintronics: Principles and device applications". In: *Journal of Magnetism and Magnetic Materials* (2020), p. 166711.

[12] M. N. Baibich, J. M. Broto, A. Fert, F. N. Van Dau, F. Petroff, P. Etienne, G. Creuzet, A. Friederich, and J. Chazelas. "Giant magnetoresistance of (001) Fe/(001) Cr magnetic superlattices". In: *Physical review letters* 61.21 (1988), p. 2472.

[13] G. Binasch, P. Grünberg, F. Saurenbach, and W. Zinn. "Enhanced magnetoresistance in layered magnetic structures with antiferromagnetic interlayer exchange". In: *Physical review B* 39.7 (1989), p. 4828.

[14] IDEMA (International Disk Drive Equipment and Materials Association). *2016 ASTC Technology Roadmap*. 2016.

[15] S. Bhatti, R. Sbiaa, A. Hirohata, H. Ohno, S. Fukami, and S. N. Piramanayagam. "Spintronics based random access memory: a review". In: *Materials Today* 20.9 (2017), pp. 530–548.

[16] S. Datta and B. Das. "Electronic analog of the electro-optic modulator". In: *Applied Physics Letters* 56.7 (1990), pp. 665–667.

[17] S. Sugahara, Y. Takamura, Y. Shuto, and S. Yamamoto. "Devices and Applications: Spin Transistors and Spin Logic Devices". In: *Handbook of spintronics* (2014), 1243â–1279.

[18] G. Dresselhaus. "Spin-orbit coupling effects in zinc blende structures". In: *Physical Review* 100.2 (1955), p. 580.

[19] E. I. Rashba. "Properties of semiconductors with an extremum loop. I. Cyclotron and combinational resonance in a magnetic field perpendicular to the plane of the loop". In: *Soviet Physics, Solid State* 2 (1960), pp. 1109–1122.

[20] J. Nitta, T. Akazaki, H. Takayanagi, and T. Enoki. "Gate Control of Spin-Orbit Interaction in an Inverted $In_{0.53}Ga_{0.47}As/In_{0.52}Al_{0.48}As$ Heterostructure". In: *Physical Review Letters* 78.7 (1997), p. 1335.

[21] H. C. Koo, J. Eom, J. Chang, and S.-H. Han. "A spin field effect transistor using stray magnetic fields". In: *Solid-state electronics* 53.9 (2009), pp. 1016–1019.

[22] X. Cartoixà, D. Z.-Y. Ting, and Y.-C. Chang. "A resonant spin lifetime transistor". In: *Applied physics letters* 83.7 (2003), pp. 1462–1464.

[23] J. Wunderlich, B.-G. Park, A. C. Irvine, L. P. Zârbo, E. Rozkotová, P. Nemec, V. Novák, J. Sinova, and T. Jungwirth. "Spin Hall effect transistor". In: *Science* 330.6012 (2010), pp. 1801–1804.

[24] F. Li, C. Song, B. Cui, J. Peng, Y. Gu, G. Wang, and F. Pan. "Photon-Gated Spin Transistor". In: *Advanced Materials* 29.2 (2017), p. 1604052.

[25] Y. Kato, R. C. Myers, A. C. Gossard, and D. D. Awschalom. "Coherent spin manipulation without magnetic fields in strained semiconductors". In: *Nature* 427.6969 (2004), pp. 50–53.

[26] T. C. Damen, J. Shah, D. Y. Oberli, D. S. Chemla, J. E. Cunningham, and J. M. Kuo. "Dynamics of exciton formation and relaxation in GaAs quantum wells". In: *Physical Review B* 42.12 (1990), p. 7434.

[27] M. Z. Maialle, E. A. de Andrada e Silva, and L. J. Sham. "Exciton spin dynamics in quantum wells". In: *Physical Review B* 47.23 (1993), p. 15776.

[28] G. L. Bir, A. G. Aronov, and G. E. Pikus. "Spin relaxation of electrons due to scattering by holes". In: *JETP* 42 (1976), p. 705.

[29] M. I. Dyakonov and V. I. Perel. "Spin orientation of electrons associated with the interband absorption of light in semiconductors". In: *JETP* 33 (1971), p. 1053.

[30] M. A. Brand, A. Malinowski, O. Z. Karimov, P. A. Marsden, R. T. Harley, A. J. Shields, D. Sanvitto, D. A. Ritchie, and M. Y. Simmons. “Precession and motional slowing of spin evolution in a high mobility two-dimensional electron gas”. In: *Physical review letters* 89.23 (2002), p. 236601.

[31] Y. Ohno, R. Terauchi, T. Adachi, F. Matsukura, and H. Ohno. “Spin relaxation in GaAs (110) quantum wells”. In: *Physical Review Letters* 83.20 (1999), p. 4196.

[32] K. Biermann, O. D. D. Couto, E. Cerda, H. B. De Carvalho, R. Hey, and P. V. Santos. “Spin transport in (110) GaAs-based cavity structures”. In: *Journal of superconductivity and novel magnetism* 23.1 (2010), p. 27.

[33] X. Cartoixà, D. Z.-Y. Ting, and Y.-C. Chang. “Suppression of the D’yakonov-Perel’spin-relaxation mechanism for all spin components in [111] zincblende quantum wells”. In: *Physical Review B* 71.4 (2005), p. 045313.

[34] A. Balocchi, Q. H. Duong, P. Renucci, B. L. Liu, C. Fontaine, T. Amand, D. Lagarde, and X. Marie. “Full electrical control of the electron spin relaxation in GaAs quantum wells”. In: *Physical review letters* 107.13 (2011), p. 136604.

[35] J. D. Koralek, C. P. Weber, J. Orenstein, B. A. Bernevig, S.-C. Zhang, S. Mack, and D. D. Awschalom. “Emergence of the persistent spin helix in semiconductor quantum wells”. In: *Nature* 458.7238 (2009), pp. 610–613.

[36] A. A. Kiselev and K. W. Kim. “Progressive suppression of spin relaxation in two-dimensional channels of finite width”. In: *Physical Review B* 61.19 (2000), p. 13115.

[37] A. W. Holleitner, V. Sih, R. C. Myers, A. C. Gossard, and D. D. Awschalom. “Suppression of spin relaxation in submicron InGaAs wires”. In: *Physical review letters* 97.3 (2006), p. 036805.

[38] Y. Kunihashi, M. Kohda, and J. Nitta. “Enhancement of spin lifetime in gate-fitted InGaAs narrow wires”. In: *Physical review letters* 102.22 (2009), p. 226601.

[39] F. Dirnberger, M. Kammermeier, J. König, M. Forsch, Faria P. E., T. Campos, J. Fabian, J. Schliemann, C. Schüller, T. Korn, P Wenk, and D. Bougeard. “Ultralong spin lifetimes in one-dimensional semiconductor nanowires”. In: *Applied Physics Letters* 114.20 (2019), p. 202101.

[40] J. A. H. Stotz, R. Hey, P. V. Santos, and K. H. Ploog. “Coherent spin transport through dynamic quantum dots”. In: *Nature materials* 4.8 (2005), pp. 585–588.

[41] K. Ploog. “Molecular beam epitaxy of III-V compounds: Technology and growth process”. In: *Annual Review of Materials Science* 11.1 (1981), pp. 171–210.

[42] X. Q. Shen, M. Tanaka, and T. Nishinaga. “Resharpening effect of AlAs and fabrication of quantum-wires on V-grooved substrates by molecular beam epitaxy”. In: *Journal of crystal growth* 127.1-4 (1993), pp. 932–936.

[43] Y. Nakamura, S. Koshiba, M. Tsuchiya, H. Kano, and H. Sakaki. “Enhanced crystallographic selectivity in molecular beam epitaxial growth of GaAs on mesas and formation of (001)-(111)B facet structures for edge quantum wires”. In: *Applied physics letters* 59.6 (1991), pp. 700–702.

[44] M. López, T. Ishikawa, and Y. Nomura. “Molecular beam epitaxy of GaAs/AlAs on mesa stripes along the [001] direction for quantum-wire fabrication”. In: *Japanese journal of applied physics* 32.8A (1993), p. L1051.

[45] S. Koshiba, S. Watanabe, Y. Nakamura, M. Yamauchi, M. Yoshita, M. Baba, H. Akiyama, and H. Sakaki. "Selective molecular beam epitaxy (MBE) growth of GaAs/AlAs ridge structures containing 10 nm scale wires and side quantum wells (QWs) and their stimulated emission characteristics". In: *Journal of crystal growth* 201 (1999), pp. 810–813.

[46] R. Nötzel, J. Menniger, M. Ramsteiner, A. Ruiz, H.-P. Schönherr, and K. H. Ploog. "Selectivity of growth on patterned GaAs (311)A substrates". In: *Applied physics letters* 68.8 (1996), pp. 1132–1134.

[47] J. Lee, Z. Wang, B. Liang, W. Black, V. P. Kunets, Y. Mazur, and G. J. Salamo. "Formation of self-assembled sidewall nanowires on shallow patterned GaAs (100)". In: *IEEE transactions on nanotechnology* 6.1 (2007), pp. 70–74.

[48] J. Fricke, R. Nötzel, U. Jahn, H.-P. Schönherr, L. Däweritz, and K. H. Ploog. "Patterned growth on GaAs (311)A substrates: Dependence on mesa misalignment and sidewall slope and its application to coupled wire-dot arrays". In: *Journal of applied physics* 85.7 (1999), pp. 3576–3581.

[49] R. Nötzel and K. H. Ploog. "Patterned growth on high-index GaAs (311)A substrates". In: *Applied surface science* 166.1-4 (2000), pp. 406–412.

[50] Y. Horikoshi, M. Kawashima, H. Yamaguchi, and M. Sato. "Surface atomic processes during epitaxial growth". In: *Semiconductor Interfaces at the Sub-Nanometer Scale*. Springer, 1993, pp. 1–10.

[51] Lord Rayleigh. "On waves propagated along the plane surface of an elastic solid". In: *Proceedings of the London mathematical Society* 1.1 (1885), pp. 4–11.

[52] R. M. White and F. W. Voltmer. "Direct piezoelectric coupling to surface elastic waves". In: *Applied physics letters* 7.12 (1965), pp. 314–316.

[53] R. M. White. "Surface elastic waves". In: vol. 58. 8. IEEE, 1970, pp. 1238–1276.

[54] M. M. de Lima, M. van der Poel, R. Hey, P. V. Santos, and J. M. Hvam. "Modulation of cavity-polaritons by surface acoustic waves". In: *Quantum Electronics and Laser Science Conference*. Optical Society of America. 2006, QFA6.

[55] T. Sogawa, P. V. Santos, S. K. Zhang, S. Eshlaghi, A. D. Wieck, and K. H. Ploog. "Dynamic band-structure modulation of quantum wells by surface acoustic waves". In: *Physical Review B* 63.12 (2001), p. 121307.

[56] L. Thevenard, I. S. Camara, S. Majrab, M. Bernard, P. Rovillain, A. Lemaître, C. Gourdon, and J.-Y. Duquesne. "Precessional magnetization switching by a surface acoustic wave". In: *Physical Review B* 93.13 (2016), p. 134430.

[57] G. Andersson, B. Suri, L. Guo, T. Aref, and P. Delsing. "Non-exponential decay of a giant artificial atom". In: *Nature Physics* 15.11 (2019), pp. 1123–1127.

[58] M. J. Hoskins, H. Morkoç, and B. J. Hunsinger. "Charge transport by surface acoustic waves in GaAs". In: *Applied Physics Letters* 41.4 (1982), pp. 332–334.

[59] C. Rocke, S. Zimmermann, A. Wixforth, J. P. Kotthaus, G. Böhm, and G. Weimann. "Acoustically driven storage of light in a quantum well". In: *Physical Review Letters* 78.21 (1997), p. 4099.

[60] F. Alsina, J. A. H. Stotz, R. Hey, and P. V. Santos. "Radiative recombination during acoustically induced transport in GaAs quantum wells". In: *Journal of Vacuum Science & Technology B: Microelectronics and Nanometer Structures Processing, Measurement, and Phenomena* 24.4 (2006), pp. 2029–2035.

[61] F. Alsina, P. V. Santos, H.-P. Schönherr, W. Seidel, K. H. Ploog, and R. Nötzel. "Surface-acoustic-wave-induced carrier transport in quantum wires". In: *Physical Review B* 66.16 (2002), p. 165330.

[62] F. Alsina, J. A. H. Stotz, R. Hey, and P. V. Santos. "Acoustically induced potential dots in GaAs quantum wells". In: *Solid state communications* 129.7 (2004), pp. 453–457.

[63] P. D. Batista, R. Hey, and P. V. Santos. "Efficient electrical detection of ambipolar acoustic transport in GaAs". In: *Applied Physics Letters* 92.26 (2008), p. 262108.

[64] O. D. D. Couto, S. Lazić, F. Iikawa, J. A. H. Stotz, U. Jahn, R. Hey, and P. V. Santos. "Photon anti-bunching in acoustically pumped quantum dots". In: *Nature Photonics* 3.11 (2009), pp. 645–648.

[65] T. Sogawa, P. V. Santos, S. K. Zhang, S. Eshlaghi, A. D. Wieck, and K. H. Ploog. "Transport and lifetime enhancement of photoexcited spins in GaAs by surface acoustic waves". In: *Physical review letters* 87.27 (2001), p. 276601.

[66] O. D. D. Couto, R. Hey, and P. V. Santos. "Spin dynamics in (110) GaAs quantum wells under surface acoustic waves". In: *Physical Review B* 78.15 (2008), p. 153305.

[67] B. Bertrand, S. Hermelin, S. Takada, M. Yamamoto, S. Tarucha, A. Ludwig, A. D. Wieck, C. Bäuerle, and T. Meunier. "Fast spin information transfer between distant quantum dots using individual electrons". In: *Nature nanotechnology* 11.8 (2016), pp. 672–676.

[68] F. Alsina, J. A. H. Stotz, R. Hey, U. Jahn, and P. V. Santos. "Acoustic charge and spin transport in GaAs quantum wires". In: *physica status solidi c* 5.9 (2008), pp. 2907–2910.

[69] R. J. Elliott. "Theory of the effect of spin-orbit coupling on magnetic resonance in some semiconductors". In: *Physical Review* 96.2 (1954), p. 266.

[70] H. Sanada, T. Sogawa, H. Gotoh, K. Onomitsu, M. Kohda, J. Nitta, and P. V. Santos. "Acoustically induced spin-orbit interactions revealed by two-dimensional imaging of spin transport in GaAs". In: *Physical Review Letters* 106.21 (2011), p. 216602.

[71] J. Curie and P. Curie. "Développement par compression de l'électricité polaire dans les cristaux hémièdres à faces inclinées". In: *Bulletin de minéralogie* 3.4 (1880), pp. 90–93.

[72] A. Arnau and D. Soares. "Fundamentals of piezoelectricity". In: *Piezoelectric transducers and applications*. Springer, 2009, pp. 1–38.

[73] B. A. Auld. *Acoustic fields and waves in solids*. Krieger Publishing Company, 1973.

[74] O. Madelung. *Semiconductors: group IV elements and III-V compounds*. Springer Science & Business Media, 2012.

[75] M. J. A. Schuetz, E. M. Kessler, G. Giedke, L. M. K. Vandersypen, M. D. Lukin, and J. I. Cirac. "Universal Quantum Transducers Based on Surface Acoustic Waves". In: *Phys. Rev. X* 5 (3 2015), p. 031031.

[76] S. H. Simon. "Coupling of surface acoustic waves to a two-dimensional electron gas". In: *Physical Review B* 54.19 (1996), p. 13878.

[77] A. A. Oliner. *Acoustic Surface Waves*. Berlin: Springer, 1994.

[78] K.-Y. Hashimoto. *Surface acoustic wave devices in telecommunications*. Vol. 116. Springer, 2000.

[79] R. L. Greene, K. K. Bajaj, and D. E. Phelps. "Energy levels of Wannier excitons in GaAs-$Ga_{1-x}Al_xAs$ quantum-well structures". In: *Physical Review B* 29.4 (1984), p. 1807.

[80] G. Bastard, E. E. Mendez, L. L. Chang, and L. Esaki. "Variational calculations on a quantum well in an electric field". In: *Physical Review B* 28.6 (1983), p. 3241.

[81] M. M. de Lima and P. V. Santos. "Modulation of photonic structures by surface acoustic waves". In: *Reports on progress in physics* 68.7 (2005), p. 1639.

[82] S. Lazić, R. Hey, and P. V. Santos. "Mechanism of non-classical light emission from acoustically populated (311)A GaAs quantum wires". In: *New Journal of Physics* 14.1 (2012), p. 013005.

[83] P. Krispin, R. Hey, H. Kostial, and K. H. Ploog. "Growth mode-related generation of electron traps at the inverted AlAs/GaAs interface". In: *Journal of applied physics* 83.3 (1998), pp. 1496–1498.

[84] L. Pavesi and M. Guzzi. "Photoluminescence of $Al_xGa_{1-x}As$ alloys". In: *Journal of Applied Physics* 75.10 (1994), pp. 4779–4842.

[85] D. Royer and E. Dieulesaint. *Elastic Waves in Solids I*. Berlin: Springer, 2000.

[86] Y. Takagaki, E. Wiebicke, P. V. Santos, R. Hey, and K. H. Ploog. "Propagation of surface acoustic waves in a GaAs/AlAs/GaAs heterostructure and micro-beams". In: *Semiconductor science and technology* 17.9 (2002), p. 1008.

[87] P. V. Santos, F. Alsina, J. A. H. Stotz, R. Hey, S. Eshlaghi, and A. D. Wieck. "Band mixing and ambipolar transport by surface acoustic waves in GaAs quantum wells". In: *Physical Review B* 69.15 (2004), p. 155318.

[88] A. Fert. "Origin, development, and future of spintronics (Nobel lecture)". In: *Angewandte Chemie International Edition* 47.32 (2008), pp. 5956–5967.

[89] C. Kittel and P. McEuen. *Introduction to solid state physics*. Vol. 8. Wiley New York, 1996.

[90] J. H. Davies. *The physics of low-dimensional semiconductors: an introduction*. Cambridge university press, 1998.

[91] D. J. Griffiths and D. F. Schroeter. *Introduction to quantum mechanics*. Cambridge University Press, 2018.

[92] J. Daintith. *A dictionary of chemistry*. OUP Oxford, 2008, p. 308.

[93] M. I. Dyakonov and A. V. Khaetskii. *Spin physics in semiconductors*. Vol. 1. Springer, 2008.

[94] R. Winkler. "Spin-orbit coupling effects in two-dimensional electron and hole systems". In: *Springer Tracts in Modern Physics* 191 (2003), pp. 1–8.

[95] Y. A. Bychkov and E. I. Rashba. "Oscillatory effects and the magnetic susceptibility of carriers in inversion layers". In: *Journal of physics C: Solid state physics* 17.33 (1984), p. 6039.

[96] O. Krebs and P. Voisin. "Giant optical anisotropy of semiconductor heterostructures with no common atom and the quantum-confined Pockels effect". In: *Physical review letters* 77.9 (1996), p. 1829.

[97] F. Meier and B. P. Zakharchenya. *Optical orientation*. Elsevier, 2012.

[98] V. I. Perel and B. P. Zakhharchenya. "Major physical phenomena in the optical orientation and alignment in semiconductors". In: *Optical Orientation*. Vol. 8. Amsterdam: North Holland, Amsterdam, 1984.

[99] A. W. Overhauser. "Polarization of nuclei in metals". In: *Physical Review* 92.2 (1953), p. 411.

[100] A. Hernández-Mínguez, K. Biermann, R. Hey, and P. V. Santos. "Spin transport and spin manipulation in GaAs (110) and (111) quantum wells". In: *physica status solidi (b)* 251.9 (2014), pp. 1736–1752.

[101] Y. V. Pershin and V. Privman. "Spin relaxation of conduction electrons in semiconductors due to interaction with nuclear spins". In: *Nano Letters* 3.6 (2003), pp. 695–700.

[102] G. Fishman and G. Lampel. "Spin relaxation of photoelectrons in p-type gallium arsenide". In: *Physical Review B* 16.2 (1977), p. 820.

[103] T. Uenoyama and L. J. Sham. "Hole relaxation and luminescence polarization in doped and undoped quantum wells". In: *Physical review letters* 64.25 (1990), p. 3070.

[104] B. Baylac, X. Marie, T. Amand, M. Brousseau, J. Barrau, and Y. Shekun. "Hole spin relaxation in intrinsic quantum wells". In: *Surface science* 326.1-2 (1995), pp. 161–166.

[105] E. Fermi. *Nuclear physics: a course given by Enrico Fermi at the University of Chicago*. University of Chicago Press, 1950.

[106] Y. Yafet. "g Factors and spin-lattice relaxation of conduction electrons". In: *Solid state physics*. Vol. 14. Elsevier, 1963, pp. 1–98.

[107] I. Žutić, J. Fabian, and S. Das Sarma. "Spintronics: Fundamentals and applications". In: *Reviews of modern physics* 76.2 (2004), p. 323.

[108] J. A. H. Stotz, R. Hey, P. V. Santos, and K. H. Ploog. "Spin transport and manipulation by mobile potential dots in GaAs quantum wells". In: *Physica E: Low-dimensional Systems and Nanostructures* 32.1-2 (2006), pp. 446–449.

[109] A. Hernández-Mínguez, K. Biermann, R. Hey, and P. V. Santos. "Electrical suppression of spin relaxation in GaAs (111)B quantum wells". In: *Physical review letters* 109.26 (2012), p. 266602.

[110] A. Violante, R. Hey, and P. V. Santos. "Coherent transport and manipulation of spins in indirect-exciton nanostructures". In: *Physical Review B* 91.12 (2015), p. 125302.

[111] M. I. Dyakonov and V. Y. Kachorovskii. "Spin relaxation of two-dimensional electrons in noncentrosymmetric semiconductors". In: *Sov. Phys. Semicond.* 20 (1986), p. 110.

[112] A. Bournel, P. Dollfus, P. Bruno, and P. Hesto. "Gate-induced spin precession in an $In_{0.53}Ga_{0.47}As$ two dimensional electron gas". In: *The European Physical Journal Applied Physics* 4.1 (1998), pp. 1–4.

[113] A. G. Mal'Shukov and K. A. Chao. "Waveguide diffusion modes and slowdown of D'yakonov-Perel'spin relaxation in narrow two-dimensional semiconductor channels". In: *Physical Review B* 61.4 (2000), R2413.

[114] J. Ishihara, M. Ono, Y. Ohno, and H. Ohno. "A strong anisotropy of spin dephasing time of quasi-one dimensional electron gas in modulation-doped GaAs/AlGaAs wires". In: *Applied Physics Letters* 102.21 (2013), p. 212402.

[115] P. Altmann. "Spin precession in spin-orbit fields under wire confinement and drift". PhD thesis. University of Basel, 2016.

[116] M. Beck, C. Metzner, S. Malzer, and G. H. Döhler. "Spin lifetimes and strain-controlled spin precession of drifting electrons in GaAs". In: *EPL (Europhysics Letters)* 75.4 (2006), p. 597.

[117] D. J. English, P. G. Lagoudakis, R. T. Harley, P. S. Eldridge, J. Hübner, and M. Oestreich. "Strain-induced spin relaxation anisotropy in symmetric (001)-oriented GaAs quantum wells". In: *Physical Review B* 84.15 (2011), p. 155323.

[118] S. A. Crooker and D. L. Smith. "Imaging spin flows in semiconductors subject to electric, magnetic, and strain fields". In: *Physical review letters* 94.23 (2005), p. 236601.

[119] J. A. H. Stotz, R. Hey, P. V. Santos, and K. H. Ploog. "Enhanced spin coherence via mesoscopic confinement during acoustically induced transport". In: *New Journal of Physics* 10.9 (2008), p. 093013.

[120] S. Lindsay. *Introduction to nanoscience*. Oxford University Press, 2010.

[121] W. Braun, H. Möller, and Y.-H. Zhang. "Reflection high-energy electron diffraction during substrate rotation: A new dimension for in situ characterization". In: *Journal of Vacuum Science & Technology B: Microelectronics and Nanometer Structures Processing, Measurement, and Phenomena* 16.3 (1998), pp. 1507–1510.

[122] P. J. Dobson, B. A. Joyce, J. H. Neave, and J. Zhang. "Current understanding and applications of the RHEED intensity oscillation technique". In: *Journal of Crystal Growth* 81.1-4 (1987), pp. 1–8.

[123] G. Binnig, C. F. Quate, and C. Gerber. "Atomic force microscope". In: *Physical review letters* 56.9 (1986), p. 930.

[124] Q. Zhong, D. Inniss, K. Kjoller, and V. B. Elings. "Fractured polymer/silica fiber surface studied by tapping mode atomic force microscopy". In: *Surface science* 290.1-2 (1993), pp. L688–L692.

[125] S. B. Kaemmer. "Introduction to bruker's scanasyst and peakforce tapping afm technology". In: *Bruker application note. Bruker Nano Inc., Santa Barbara, CA* (2011).

[126] D. Nečas and P. Klapetek. "Gwyddion: an open-source software for SPM data analysis". In: *Open Physics* 10.1 (2012), pp. 181–188.

[127] R. F. Egerton. *Physical principles of electron microscopy*. Springer, 2005.

[128] F. L. Pedrotti, L. M. Pedrotti, and L. S. Pedrotti. *Introduction to optics*. Cambridge University Press, 2017.

[129] M. Freiser. "A survey of magnetooptic effects". In: *IEEE Transactions on magnetics* 4.2 (1968), pp. 152–161.

[130] C. A. Mack. "Line-edge roughness and the ultimate limits of lithography". In: *Advances in Resist Materials and Processing Technology XXVII*. Vol. 7639. International Society for Optics and Photonics. 2010, p. 763931.

[131] G. C. DeSalvo, C. A. Bozada, J. L. Ebel, D. C. Look, J. P. Barrette, C. L. A. Cerny, R. W. Dettmer, J. K. Gillespie, C. K. Havasy, and T. J. and Jenkins. "Wet chemical digital etching of GaAs at room temperature". In: *Journal of The Electrochemical Society* 143.11 (1996), p. 3652.

[132] R. Nötzel, M. Ramsteiner, J. Menniger, A. Trampert, H.-P. Schönherr, L. Däweritz, and K. H. Ploog. "Patterned growth on high-index GaAs (n11) substrates: Application to sidewall quantum wires". In: *Journal of applied physics* 80.7 (1996), pp. 4108–4111.

[133] T. Takebe, M. Fujii, T. Yamamoto, K. Fujita, and T. Watanabe. "Orientation-dependent Ga surface diffusion in molecular beam epitaxy of GaAs on GaAs patterned substrates". In: *Journal of applied physics* 81.11 (1997), pp. 7273–7281.

[134] S. Koshiba, Y. Nakamura, M. Tsuchiya, H. Noge, H. Kano, Y. Nagamune, T. Noda, and H. Sakaki. "Surface diffusion processes in molecular beam epitaxial growth of GaAs and AlAs as studied on GaAs (001)-(111) B facet structures". In: *Journal of applied physics* 76.7 (1994), pp. 4138–4144.

[135] A. Richter, G. Behme, M. Süptitz, C. Lienau, T. Elsässer, M. Ramsteiner, R. Nötzel, and K. H. Ploog. "Real-space transfer and trapping of carriers into single GaAs quantum wires studied by near-field optical spectroscopy". In: *Physical review letters* 79.11 (1997), p. 2145.

[136] C. Lienau, A. Richter, G. Behme, M. Süptitz, D. Heinrich, T. Elsaesser, M. Ramsteiner, R. Nötzel, and K. H. Ploog. "Nanoscale mapping of confinement potentials in single semiconductor quantum wires by near-field optical spectroscopy". In: *Physical Review B* 58.4 (1998), p. 2045.

[137] M. B. Whitwick. "Surface evolution during gallium arsenide homoepitaxy with molecular beam epitaxy". PhD thesis. University of British Columbia, 2009. Chap. 5, pp. 79–98.

[138] G. Bastard, C. Delalande, M. H. Meynadier, P. M. Frijlink, and M. Voos. "Low-temperature exciton trapping on interface defects in semiconductor quantum wells". In: *Physical Review B* 29.12 (1984), p. 7042.

[139] J. Tignon, O. Heller, P. Roussignol, J. Martinez-Pastor, P. Lelong, G. Bastard, R. C. Iotti, L. C. Andreani, V. Thierry-Mieg, and R. Planel. "Excitonic recombination dynamics in shallow quantum wells". In: *Physical Review B* 58.11 (1998), p. 7076.

[140] E. O. Göbel, H. Jung, J. Kuhl, and K. Ploog. "Recombination enhancement due to carrier localization in quantum well structures". In: *Physical review letters* 51.17 (1983), p. 1588.

[141] J. Fricke, R. Nötzel, U. Jahn, Z. Niu, H.-P. Schönherr, M. Ramsteiner, and K. H. Ploog. "Patterned growth on GaAs (311)A substrates: Engineering of growth selectivity for lateral semiconductor nanostructures". In: *Journal of applied physics* 86.5 (1999), pp. 2896–2900.

[142] W. Bludau and E. Wagner. "Impact ionization of excitons in GaAs". In: *Physical Review B* 13.12 (1976), p. 5410.

[143] C. Rocke, A. O. Govorov, A. Wixforth, G. Böhm, and G. Weimann. "Exciton ionization in a quantum well studied by surface acoustic waves". In: *Physical Review B* 57.12 (1998), R6850.

[144] Z. Vörös, R. Balili, D. W. Snoke, L. Pfeiffer, and K. West. "Long-distance diffusion of excitons in double quantum well structures". In: *Physical review letters* 94.22 (2005), p. 226401.

[145] P. V. Santos, M. Ramsteiner, and F. Jungnickel. "Spatially resolved photoluminescence in GaAs surface acoustic wave structures". In: *Applied physics letters* 72.17 (1998), pp. 2099–2101.

[146] R. L. Gunshor. "The interaction between semiconductors and acoustic surface waves — A review". In: *Solid-State Electronics* 18.12 (1975), pp. 1089–1093.

[147] E. Blackwood, M. J. Snelling, R. T. Harley, S. R. Andrews, and C. T. B. Foxon. "Exchange interaction of excitons in GaAs heterostructures". In: *Physical Review B* 50.19 (1994), p. 14246.

[148] L. C. Andreani and A. Pasquarello. "Accurate theory of excitons in GaAs-$Ga_{1-x}Al_xAs$ quantum wells". In: *Physical Review B* 42.14 (1990), p. 8928.

[149] A. Vinattieri, J. Shah, T. C. Damen, D. S. Kim, L. N. Pfeiffer, M. Z. Maialle, and L. J. Sham. "Exciton dynamics in GaAs quantum wells under resonant excitation". In: *Physical Review B* 50.15 (1994), p. 10868.

[150] A. Malinowski, R. S. Britton, T. Grevatt, R. T. Harley, D. A. Ritchie, and M. Y. Simmons. "Spin relaxation in $GaAs/Al_xGa_{1-x}As$ quantum wells". In: *Physical Review B* 62.19 (2000), p. 13034.

[151] J. Lee, T. W. Saucer, A. J. Martin, D. Tien, J. M. Millunchick, and V. Sih. "Photoluminescence imaging of focused ion beam induced individual quantum dots". In: *Nano letters* 11.3 (2011), pp. 1040–1043.

[152] J. S. Kim, M. Kawabe, and N. Koguchi. "Ordering of high-quality InAs quantum dots on defect-free nanoholes". In: *Applied physics letters* 88.7 (2006), p. 072107.

[153] J. Liang, H. Luo, R. Beresford, and J. Xu. "A growth pathway for highly ordered quantum dot arrays". In: *Applied physics letters* 85.24 (2004), pp. 5974–5976.

[154] K. Biermann, P. L. J. Helgers, A. Crespo-Poveda, A. S. Kuznetsov, A. Tahraoui, B. Röben, X. Lü, L. Schrottke, P. V. Santos, and H. T. Grahn. "In-situ control of molecular beam epitaxial growth by spectral reflectivity analysis". In: *Journal of Crystal Growth* 557 (2021), p. 125993.

List of Figures

List of Tables

Acknowledgements

I would like to thank Dr. Paulo Santos and Prof. Dr. Henning Riechert for providing me the opportunity to pursue my PhD research in a very interesting field of physics, at the Paul-Drude-Institut in Berlin. The good facilities at the PDI were crucial for the experiments conducted in this thesis. Being part of the PDI, I did not only gain experiences relevant for my project, but as well about many other topics of physics through the many seminars, discussions outside the labs and the many conferences I got to visit.

I express my special thanks to Dr. Paulo Santos for your guidance, which was key to the successful completion of my project. Your knowledge about acoustics, spintronics and photonics is amazing. Not only have I learned from this knowledge, but also did I get to learn to work as a scientist: keeping eye for details, having patient in discovering the truth, but always taking a pragmatic attitude for progress. You also always encouraged me to take part in activities meant to broaden my horizon outside the scope of my exact PhD project, which contributed a lot to my general development.

I am also grateful to Dr. Klaus Biermann for, together with Dr. Paulo Santos, giving directions in my project and for taking care of the MBE growth involved in the fabrication process. Your expertise of MBE is incredible and without you this project would not have been possible at all. The discussions about the other topics were always helpful and interesting. I thank you as well for the assistance in translating my English abstract to the German version.

Part of the experimental work is carried out at NTT Basic Research Labs in Atsugi (Japan), which would have been impossible without the support of Dr. Haruki Sanada, Dr. Yoji Kunihashi, Dr. Tetsuomi Sogawa and Dr. Hideki Gotoh. Especially, I would like to express my gratitude towards Dr. Haruki Sanada, who has been very important for providing guidance and directions for my research during my stay at NTT BRL. I learned a lot from both your understanding of spin dynamics and your experimental skills. You always tried to provide the best conditions for both my work-related activities, as well as to make me feel at home. I would like to thank the team of technicians (via Dr. Yoji Kunihashi) for taking care of scanning transmission electron microscopy images. Additionally, I am very thankful to Mizuki Otani for taking care of the administrative part, providing the good atmosphere among the exchange students and introducing me to the many different, interesting, aspects of the Japanese culture.

Next, I wish to thank all the people who are, or have been, part of Dr. Paulo Santos'

group at the PDI. Dr. Alberto Hernández-Mínguez, you have been of crucial importance for all my experimental work: additionally to your knowledge on acoustics, spintronics, photonics and outstanding teaching skills, your experimental skills taught me a lot. Dr. Alexander Kuznetsov, I have learned a lot from your knowledge and experimental skills as well. Both of you, thank you for always being interested in my works and for the many fruitful discussions we had. Prof. Dr. James Stotz, thank you for the useful discussions on spin dynamics and providing additional clues with your experimental results. Dr. Snežana Lazić, I learned a lot from your knowledge and, especially, your alignment skills. Alexander Stramma, thank you for giving me the opportunity to gain some experiences in providing support to a student. I would like to thank also Yi-Ting Liou, Colin Hubert, Dr. Mingyun Yuan, Prof. Dr. Madeleine Msall, Diego Machado, Dr. Antonio Crespo-Poveda and Dr. Nicolás Ulloa Castillo. Thanks to all of you for providing such a pleasant and interesting environment for my research.

This work has been carried out in the framework of the SAWtrain network. Therefore, I would like to thank all people who have been involved in the network: all the PIs, PhD students and supportive people. Being part of the network has been a very pleasant and learnful experience and I would encourage any prospective PhD students to participate in such a network. Special thanks go to Antonio Rubino and Prof. Dr. Chris Ford for providing me the opportunity to conduct a secondment at the Cavendish Laboratory at the University of Cambridge. My project has benefited from our works during this secondment, as well as from the collaboration afterwards.

I thank the cleanroom team, Dr. Abbes Tahraoui, Sander Rauwerdink, Sebastian Meister and Walid Sanders, for introducing me to the cleanroom activities and partly taking care of the sample fabrication. I thank Anne-Kathrin Bluhm and Dr. Uwe Jahn for taking care of the scanning electron microscopy images. I am grateful to Dr. Jonas Lähnemann for taking care of the cathodoluminescence measurements and help with the interpretation and discussions. Claudia Hermann, thank you for introducing me to the atomic force microscopy, which has been a crucial part for the structural analysis provided in this thesis. I would also like to express my gratitude towards Andreas Hartung for taking care of the administrative part for my stay at the PDI, and helping me with official matters.

Additionally, I greatly appreciated the presence of my office mates Miriam Oliva, Irene Ayuso Pérez, Colin Hubert and Benjamin Röben for the very pleasant daily atmosphere. The many discussions and after-work beers, either work-related or not, have been very helpful and joyful.

Then, there are my friends whom I met during my stay in Berlin. I believe it is important to be able to set aside your mind for a moment and recharge your batteries. Thanks to all my Berlin friends for the great moments of enjoyment enabling me to stay motivated for my PhD project.

Als laatste wil ik graag mijn Nederlandse vrienden en familie bedanken voor hun interesse in mijn project en hun grote steun gedurende de afgelopen vier jaren. Zelfs op een afstand stonden jullie altijd klaar en tijdens mijn vele korte vakanties in Nederland waren jullie altijd van de partij om een klein feestje te vieren. Het was misschien niet altijd even gemakkelijk op afstand, maar weet dat jullie cruciaal zijn geweest voor dit werk. Speciale dank gaat uit naar mijn ouders voor het geven van de goede condities waarin ik dit werk kon starten en afmaken.

Selbständigkeitserklärung

Ich erkläre, dass ich die Dissertation selbständig und nur unter Verwendung der von mir gemäß § 7 Abs. 3 der Promotionsordnung der Mathematisch-Naturwissenschaftlichen Fakultät, veröffentlicht im Amtlichen Mitteilungsblatt der Humboldt-Universität zu Berlin Nr. 42/2018 am 11.07.2018 angegebenen Hilfsmittel angefertigt habe.

Berlin, den 14.01.2021 Paulus Leonardus Joseph Helgers